

Calcium phosphate nanoparticle surface modification by
click chemistry and applications in biomedicine

Dissertation

zur Erlangung des akademischen Grades eines
Doktors der Naturwissenschaften
Dr. rer. nat.

vorgelegt von

Leonardo Rojas Sánchez

Fakultät für Chemie
Institut für Anorganische Chemie
Universität Duisburg-Essen

2019

Diese Dissertation wird über DuEPublico, dem Dokumenten- und Publikationsserver der Universität Duisburg-Essen, zur Verfügung gestellt und liegt auch als Print-Version vor.

DOI: 10.17185/duepublico/70699

URN: urn:nbn:de:hbz:464-20191115-092416-1

Alle Rechte vorbehalten.

To Irene and my parents

Die vorliegende Arbeit wurde im Zeitraum von Juni 2016 bis Juni 2019 im Arbeitskreis von Prof. Dr. Matthias Epple am Institut für Anorganische Chemie der Universität Duisburg-Essen angefertigt.

Gutachter: Prof. Dr. Matthias Epple
Prof. Dr. Jens Voskuhl

Vorsitzender: Prof. Dr. Eckart Hasselbrink

Tag der Disputation: 24. Oktober 2019

1 Table of contents

1	TABLE OF CONTENTS	II
2	TABLE OF FIGURES	VI
3	ABBREVIATIONS	XII
4	INTRODUCTION AND MOTIVATION	1
5	THEORETICAL BACKGROUND	5
5.1	CALCIUM PHOSPHATE	5
5.2	NANOPARTICLES	6
5.3	CLICK CHEMISTRY	9
5.4	BIOLOGICAL APPLICATIONS	14
5.4.1	<i>Nanoparticles uptake</i>	14
5.4.2	<i>Cellular transfection</i>	16
5.4.3	<i>Immune system and viral infections</i>	18
6	METHODS	21
6.1	DYNAMIC LIGHT SCATTERING (DLS) AND Z-POTENTIAL	21
6.2	SPECTROSCOPY METHODS	22
6.2.1	<i>UV-Vis spectroscopy</i>	22
6.2.2	<i>Fluorescence spectroscopy (FS)</i>	23
6.2.3	<i>Transmission infrared spectroscopy (FT-IR)</i>	24
6.2.4	<i>Atomic absorption spectroscopy (AAS)</i>	25
6.3	THERMOGRAVIMETRIC ANALYSIS (TGA)	26
6.4	ELECTRON MICROSCOPY	26
6.4.1	<i>Scanning electron microscopy (SEM) and Energy dispersive X-ray spectrometry (EDX)</i>	26
6.4.2	<i>Transmission electron microscopy (TEM)</i>	28
6.5	LIGHT FLUORESCENCE MICROSCOPY	29
6.5.1	<i>Widefield fluorescence microscopy (WF)</i>	30
6.5.2	<i>Confocal laser scanning microscopy (CLSM)</i>	31
6.5.3	<i>Structured illumination microscopy (SIM)</i>	32
6.5.4	<i>Stochastic Optical Reconstruction Microscopy (STORM)</i>	32
6.5.5	<i>Sample preparation for fluorescence microscopy</i>	36

6.6	CELL CULTURE RELATED METHODS	38
6.6.1	<i>Cell viability (MTT Test)</i>	38
6.6.2	<i>Endotoxin assay</i>	39
6.6.3	<i>Enzyme-linked immunosorbent assay (ELISA)</i>	40
7	EXPERIMENTAL SECTION	41
7.1	MATERIALS AND REAGENTS.....	41
7.1.1	<i>Chemical Reagents</i>	41
7.1.2	<i>Labelling Dyes</i>	42
7.1.3	<i>Cell culture reagents</i>	42
7.1.4	<i>Adjuvants, plasmids and siRNA</i>	43
7.1.5	<i>Cell staining reagents</i>	43
7.1.6	<i>Instruments and devices</i>	44
7.2	CALCIUM PHOSPHATE NANOPARTICLE SYNTHESIS	45
7.2.1	<i>Synthesis of silica terminate calcium phosphate nanoparticles (CaP/PEI/SiO₂)</i>	45
7.2.2	<i>Synthesis of azide terminate calcium phosphate nanoparticles (CaP/PEI/SiO₂-N₃)</i>	46
7.3	CLICK CHEMISTRY SURFACE MODIFICATION	46
7.3.1	<i>CuAAC click reaction with alkyne terminated molecules</i>	46
7.3.2	<i>SPAAC click reaction</i>	49
7.4	M _{CHERRY} PLASMID LOADED CALCIUM PHOSPHATE NANOPARTICLES	49
7.5	SYNTHESIS OF CALCIUM PHOSPHATE NANOPARTICLES FOR THE EXPERIMENTS DISCUSSED IN SECTION 8.4	50
7.5.1	<i>Env-Monomer and Env-Trimer coupled nanoparticles</i>	50
7.6	SYNTHESIS OF LOADED CALCIUM PHOSPHATE NANOPARTICLES FOR EXPERIMENTS DISCUSSED IN SECTION 8.5	52
7.7	SYNTHESIS OF CALCIUM PHOSPHATE NANOPARTICLES FOR THE EXPERIMENTS DISCUSSED IN SECTION 8.6	53
7.8	CELL CULTURE EXPERIMENTS.....	54
7.8.1	<i>HeLa cells culture</i>	54
7.8.2	<i>Cell viability test (MTT test)</i>	55
7.8.3	<i>Nanoparticles cellular uptake</i>	55
7.8.4	<i>Transfection experiments</i>	55

7.9	J774.2 CELL CULTURE.....	56
7.9.1	<i>Nanoparticles cellular uptake</i>	56
7.9.2	<i>Cell viability test (MTT test)</i>	57
7.9.3	<i>Gene silencing efficiency</i>	57
8	RESULTS AND DISCUSSION	59
8.1	CALCIUM PHOSPHATE NANOPARTICLES	59
8.2	AZIDE TERMINATED CALCIUM PHOSPHATE NANOPARTICLES	64
8.3	CLICK REACTION WITH AZIDE-TERMINATE CALCIUM PHOSPHATE NANOPARTICLES ...	68
8.3.1	<i>CuAAC reaction with calcium phosphate nanoparticles</i>	69
8.3.2	<i>Aggregation-induced emission clickable luminophore</i>	85
8.3.3	<i>BSA as a general protein model for click reaction</i>	90
8.3.4	<i>Strain-promoted cycloaddition (SPAAC) click reaction</i>	93
8.3.5	<i>Nanoparticles studies by fluorescence microscopy</i>	97
8.3.6	<i>Calcium phosphate nanoparticle cellular uptake</i>	98
8.3.7	<i>Transfection study with labelled nanoparticles by click reaction</i>	109
8.3.8	<i>Azide-terminated and clicked calcium phosphate nanoparticles cell viability by MTT test</i>	114
8.3.9	<i>Section Summary</i>	116
8.4	SPECIFIC COUPLING OF BIOMOLECULES	118
8.4.1	<i>HIV-1 envelope glycoprotein</i>	118
8.4.2	<i>Env-Protein coupling to the calcium phosphate nanoparticle</i>	119
8.4.3	<i>In vivo and in vitro studies with Env-coupled calcium phosphate nanoparticles</i>	128
8.4.4	<i>Section Summary</i>	135
8.5	DELIVERY OF PLASMIDS <i>IN VITRO</i> AND <i>IN VIVO</i> BY CALCIUM PHOSPHATE NANOPARTICLES.....	136
8.5.1	<i>Plasmid loading in calcium phosphate nanoparticles</i>	136
8.5.2	<i>Hepatitis B antigen plasmid (pHBsAg) loaded calcium phosphate nanoparticles</i>	140
8.5.3	<i>Section summary</i>	147
8.6	TNF- α GENE SILENCING <i>IN VITRO</i> AND <i>IN VIVO</i> WITH CALCIUM PHOSPHATE NANOPARTICLES.....	148
8.6.1	<i>siRNA loaded calcium phosphate nanoparticles</i>	148

8.6.2	<i>In vitro</i> studies with J774.2 macrophages.....	150
8.6.3	<i>In vivo</i> studies on a periodontitis model in rats	155
8.6.4	Triple functional active paste	162
8.6.5	Section summary.....	165
9	SUMMARY AND CONCLUSIONS	167
10	ZUSAMMENFASSUNG	170
11	REFERENCES.....	174
12	APPENDIX.....	202
12.1	PUBLICATIONS.....	202
12.2	CONTRIBUTIONS TO CONFERENCES.....	203
12.3	CURRICULUM VITAE	204
12.4	ACKNOWLEDGEMENTS	204
12.5	EIDESSTÄTTLICHE ERKLÄRUNG.....	207

2 Table of figures

FIGURE 1: ENERGY-DISTANCE PLOT ACCORDING TO DLVO THEORY	8
FIGURE 2: GENERAL REACTION SCHEMES OF HUISGEN 1,3-DIPOLAR CYCLOADDITION REACTION AND COPPER CATALYZED CLICK REACTION (CUAAC).....	10
FIGURE 3: COPPER CATALYZED AZIDE-ALKYNE CYCLOADDITION PROPOSED MECHANISM BY FOKIN <i>ET AL</i>	11
FIGURE 4: GENERAL REACTION SCHEME OF THE STRAIN-PROMOTED AZIDE-ALKYNE CYCLOADDITION (SPAAC)	12
FIGURE 5: STRUCTURES OF REPRESENTATIVE CYCLOOCTYNE BASED LIGANDS DEVELOPED FOR STRAIN-PROMOTED AZIDE-ALKYNE CYCLOADDITION (SPAAC).....	13
FIGURE 6: GENERAL REPRESENTATION FOR PHAGOCYTOSIS, MACROPINOCYTOSIS AND CAVEOLIN-DEPENDENT ENDOCYTOSIS.....	14
FIGURE 7: JABLONSKI DIAGRAM FOR FLUORESCENCE.....	24
FIGURE 8: COMPARISON OF THE RESOLUTION CAPACITY OF DIFFERENT FLUORESCENCE MICROSCOPY TECHNIQUES.	30
FIGURE 9: SIMPLIFIED GENERAL REPRESENTATION OF THE STOCHASTIC OPTICAL RECONSTRUCTION MICROSCOPY (STORM) METHOD	34
FIGURE 10: DESCRIPTION DIAGRAM OF A SELF-MADE FLOW CHAMBER FOR IMAGING.	35
FIGURE 11: REPRESENTATIVE A) SCANNING ELECTRON MICROGRAPH (SEM), B) EDX SPECTRA, C) DLS OF SILICA TERMINATED CALCIUM PHOSPHATE NANOPARTICLES	60
FIGURE 12: SILICA TERMINATE CALCIUM PHOSPHATE NANOPARTICLES OBSERVED BY CRYOGENIC TRANSMISSION ELECTRON MICROSCOPY (CRYO-TEM)	61
FIGURE 13: TRANSMISSION ELECTRON MICROSCOPY (TEM) MICROGRAPH OF SILICA TERMINATE CALCIUM PHOSPHATE NANOPARTICLE	62
FIGURE 14: STEM-HAADF IN SEM MAPPING OF SILICA TERMINATE CALCIUM PHOSPHATE NANOPARTICLE	63
FIGURE 15: LINE PROFILE FOR CALCIUM AND SILICON FOR ONE NANOPARTICLE FROM THE STEM-HAADF IN SEM MAPPING.....	63
FIGURE 16: A: SCANNING ELECTRON MICROGRAPH (SEM), B: DLS SIZE DISTRIBUTION OF CALCIUM PHOSPHATE NANOPARTICLES WITH AZIDE-TERMINATED SURFACE	65
FIGURE 17: FT-IR SPECTRA BEFORE AND AFTER CALCIUM PHOSPHATE NANOPARTICLE SURFACE FUNCTIONALIZATION WITH AZIDE GROUPS	65

FIGURE 18: HYDRODYNAMIC DIAMETER SIZE, POLYDISPERSITY INDEX (PDI) AND ζ -POTENTIAL MEASURED OVER 9 DAYS FOR CALCIUM PHOSPHATE AZIDE-TERMINATED NANOPARTICLE (CAP/PEI/SiO ₂ -N ₃) DISPERSED IN WATER	68
FIGURE 19: CLICK REACTION GENERAL SCHEME WITH AN AZIDE-TERMINATED CALCIUM PHOSPHATE NANOPARTICLE	69
FIGURE 20: STRUCTURES OF THE DYES USED: FLUORESCEIN (FAM) ALKYNE, 5-ISOMER; TETRAMETHYLRHODAMINE (TAMRA) ALKYNE, 5-ISOMER; SULFO-CYANINE5 ALKYNE (CY5); AGGREGATION-INDUCED EMISSION (ATE) ACTIVE AROMATIC THIOETHER (ATE); DIBENZYLCCYCLOOCTYNE-PEG4-5/6-FLUORESCEIN (DBCO-PEG4-5/6-FAM); ALEXAFLUOR® 488	71
FIGURE 21: A) UV-VIS AND B) FLUORESCENCE SPECTRA BEFORE (CAP/PEI/SiO ₂ -N ₃) AND AFTER CLICK REACTION WITH FAM-ALKYNE (CAP/PEI/SiO ₂ -FAM)	74
FIGURE 22: UV-VIS SPECTRA OF CAP/PEI-CY5/SiO ₂ -FAM NANOPARTICLES	75
FIGURE 23: NANOPARTICLE CORE AND COUPLED DYE CO-LOCALIZATION OBSERVATION BY CONFOCAL LASER SCANNING MICROSCOPY (CLSM) ON CAP/PEI-CY5/SiO ₂ -FAM NANOPARTICLES.	76
FIGURE 24: DYE MOLECULES PER NANOPARTICLE AFTER CUAAC CLICK REACTION AT DIFFERENT ALKYNE MOLAR CONCENTRATIONS AND REACTION TEMPERATURES.....	77
FIGURE 25: COMPARISON OF THE NUMBER OF FAM MOLECULES PER NANOPARTICLE AT DIFFERENT FAM-ALKYNE WHEN USING FRESH AND LYOPHILIZED CAP/PEI/SiO ₂ -N ₃ FOR THE CLICK REACTION	79
FIGURE 26: UV-VIS (UPPER ROW), FLUORESCENCE SPECTRA (MIDDLE ROW) AND SEM IMAGES FOR SINGLE (CAP/PEI/SiO ₂ -FAM) AND DUAL LABELLED (CAP/PEI/SiO ₂ -FAM-TAMRA, CAP/PEI/SiO ₂ -FAM-CY5) CALCIUM PHOSPHATE NANOPARTICLES.....	84
FIGURE 27: ALKYNE-TERMINATED AROMATIC THIOETHER EMISSION AT DIFFERENT DMSO:H ₂ O RATIOS.	85
FIGURE 28: CAP/PEI/SiO ₂ -ATE NANOPARTICLE DISPERSION AT DIFFERENT SOLVENT CONDITIONS ILLUMINATED WITH A UV LAMP AT 366 NM.	86
FIGURE 29: NORMALIZED INTENSITY FOR ATE MOLECULE AFTER THE ADDITION OF DIFFERENT CONCENTRATIONS OF A) NaCl AND B) BSA	87
FIGURE 30: NORMALIZED INTENSITY OF THE ATE MOLECULE AND CAP/PEI/SiO ₂ -ATE NANOPARTICLES WITH DIFFERENT NaCl AND BSA CONCENTRATIONS	89
FIGURE 31: PROPARGYL-N-HYDROXSUCCINIMIDYL ESTER STRUCTURE	90

FIGURE 32: A) SCANNING ELECTRON MICROSCOPY MICROGRAPH AND B) DLS SIZE DISTRIBUTION OF CAP/PEI/SiO ₂ -BSA-647 NANOPARTICLE.	92
FIGURE 33: A) SEM MICROGRAPH, B) DLS SIZE DISTRIBUTION, C) UV-VIS SPECTRA, D) FLUORESCENCE SPECTRA OF CAP/PEI/SiO ₂ -FAM BY SPAAC CLICK REACTION.....	94
FIGURE 34: COMPARISON OF CUAAC AND SPAAC REACTIONS AT DIFFERENT INITIAL DYE MOLECULE CONCENTRATIONS AT ROOM TEMPERATURE.	95
FIGURE 35: SPAAC REACTION WITH A CONSTANT INITIAL DYE CONCENTRATION OF 0.06 μMOL FAM-DBCO AT DIFFERENT REACTION TIMES	96
FIGURE 36: SIZE DISTRIBUTION COMPARISON OF CAP/PEI/SiO ₂ -AF488 NANOPARTICLES BY CONFOCAL LASER SCANNING MICROSCOPY (CLSM) AND STRUCTURED ILLUMINATION MICROSCOPY (SIM)	98
FIGURE 37: CLSM IMAGES OF HELA CELLS AFTER 24 H INCUBATION WITH CAP/PEI/SiO ₂ -AF488 NANOPARTICLES.....	99
FIGURE 38: CLSM IMAGES OF HELA CELLS AFTER 24 H INCUBATION WITH CAP/PEI/SiO ₂ -AF488 NANOPARTICLES AND A 3D REPRESENTATION OF Z-STACK IMAGES.....	99
FIGURE 39: CLSM IMAGES OF HELA CELLS AFTER 24 H INCUBATION WITH CAP/PEI/SiO ₂ -ATE NANOPARTICLES.	100
FIGURE 40: CLSM IMAGES OF HELA CELLS AFTER 24 H INCUBATION WITH DUAL-LABELLED CAP/PEI/SiO ₂ -FAM-TAMRA AND CAP/PEI/SiO ₂ -FAM-CY5 NANOPARTICLES	101
FIGURE 41: CONFOCAL SCANNING MICROSCOPY Z-STACK IMAGING OF DUAL LABELLED CAP/PEI/SiO ₂ -AF488-AF647 NANOPARTICLES AFTER CELLULAR UPTAKE (24 H) BY HELA CELLS.....	102
FIGURE 42: PARTICLE SIZE DISTRIBUTION OF CAP/PEI/SiO ₂ -AF-488 NANOPARTICLES AFTER INCUBATION OF HELA CELLS FOR 24 H WITH NANOPARTICLES BY CLSM, SIM, AND SEM	103
FIGURE 43: STORM IMAGING OF HELA CELLS AFTER 24 H INCUBATION WITH CAP/PEI/SiO ₂ -AF-488 NANOPARTICLES.....	104
FIGURE 44: STORM MICROSCOPY SIZE DISTRIBUTION HISTOGRAM FOR NANOPARTICLES A) CAP/PEI/SiO ₂ -AF488 AND CAP/PEI/SiO ₂ -BSA647.....	105
FIGURE 45: STORM MICROSCOPY IMAGES OF THE ENDOCYTOSIS OF LABELLED CALCIUM PHOSPHATE NANOPARTICLES IN A HELA CELL.....	106
FIGURE 46: STORM IMAGING OF HELA CELLS AFTER 16 H INCUBATION WITH CAP/PEI/SiO ₂ -AF-488 NANOPARTICLES.....	107

FIGURE 47: ENLARGE IMAGE OF DIFFERENT LYSOSOME REGIONS OF A HELA CELL AFTER NANOPARTICLE UPTAKE	107
FIGURE 48 SCHEMATIC REPRESENTATION OF A CAP/PEI/SiO ₂ -AF488 NANOPARTICLE OBSERVED AVERAGE SIZE MEASURED BY DIFFERENT FLUORESCENCE MICROSCOPY TECHNIQUES AND BY SCANNING ELECTRON MICROSCOPY.	108
FIGURE 49: REPRESENTATIVE SEM IMAGES OF A) CAP/PEI/M _{CHERRY} /SiO ₂ , B) CAP/PEI/M _{CHERRY} /SiO ₂ -N ₃ , C) CAP/PEI/M _{CHERRY} /SiO ₂ -AF488 (CUAAC), D) CAP/PEI/M _{CHERRY} /SiO ₂ -FAM (SPAAC).....	111
FIGURE 50: FLUORESCENCE MICROSCOPY IMAGES OF HELA CELLS AFTER 24H AND 48H TRANSFECTION WITH DIFFERENT CALCIUM PHOSPHATE NANOPARTICLES LOADED WITH M _{CHERRY} PLASMID	112
FIGURE 51: CELL VIABILITY DETERMINED BY MTT ASSAY FOR CAP/PEI/SiO ₂ -N ₃ NANOPARTICLES AFTER INCUBATION WITH HELA CELLS FOR 24 H.....	114
FIGURE 52: CELL VIABILITY DETERMINED BY MTT ASSAY FOR CAP/PEI/SiO ₂ -FAM LABELLED NANOPARTICLES BY A) CUAAC AND B) SPAAC CLICK REACTION	115
FIGURE 53: HYDRODYNAMIC DIAMETER BY DLS COMPARISON FOR ENV PROTEIN COUPLED “SPECIFICALLY” AND “NON-SPECIFICALLY” TO THE CALCIUM PHOSPHATE NANOPARTICLE SURFACE.	122
FIGURE 54: SCANNING ELECTRON MICROSCOPY COMPARISON FOR ENV-PROTEIN COUPLED “SPECIFICALLY” AND “NON-SPECIFICALLY” TO THE CALCIUM PHOSPHATE NANOPARTICLE SURFACE.	123
FIGURE 55: CLSM IMAGES OF A DIRECT OBSERVATION OF CALCIUM PHOSPHATE NANOPARTICLE STABILIZED WITH PEI-CY5 AND COUPLED TO ENV-TRIMER-AF488 BY CUAAC CLICK CHEMISTRY	123
FIGURE 56: TRANSMISSION ELECTRON MICROSCOPY OF CAP/PEI/SiO ₂ -ENV NANOPARTICLE (LEFT) WITH POSITIVE STAINING AND (RIGHT) WITH NEGATIVE STAINING	124
FIGURE 57: CAP/PEI/SiO ₂ -ENV SIZE DISTRIBUTION DETERMINED BY TEM WITH NEGATIVE STAINING.....	125
FIGURE 58: NEGATIVE STAINED TEM MICROGRAPH OF CAP/PEI/SiO ₂ -ENV AT HIGHER MAGNIFICATION	126
FIGURE 59: REPRESENTATIVE TEM TOMOGRAM SECTIONS OF CAP/PEI/SiO ₂ -ENV	127
FIGURE 60: DLS SIZE DISTRIBUTION OF THE NANOPARTICLES IN WATER BEFORE AND AFTER LYOPHILIZATION A) NON-SPECIFIC COUPLED AND B) SPECIFICALLY COUPLED.	128

FIGURE 61: SEM MICROGRAPHS OF THE PREPARED CAP NPs FOR IMMUNIZATION EXPERIMENTS. A) CAP/PEI/SiO ₂ -ENV-MONOMER, B) CAP/PEI/P30/SiO ₂ -ENV-MONOMER, C) CAP/PEI/SiO ₂ -ENV-TRIMER, D) CAP/PEI/P30/SiO ₂ -ENV-TRIMER, E) CAP/PEI/P30+CpG/SiO ₂ -ENV-TRIMER, F) CAP/PEI/CpG/SiO ₂ -ENV-TRIMER, G) CAP/PEI/SiO ₂ -ENV-TRIMER (SC) AND H) CAP/PEI/CpG/SiO ₂ -ENV-TRIMER (SC).	131
FIGURE 62: DOSE FINDING IMMUNIZATION SCHEME FOR BALB/C AND C57BL/6 MICE.....	132
FIGURE 63: ENV-SPECIFIC IGG SUBTYPE A) IGG1 AND B) IGG2C RESPONSES AFTER ENV-COUPLED NANOPARTICLE IMMUNIZATIONS BY INTRASTRUCTURAL HELP	134
FIGURE 64: EGFP EXPRESSION <i>IN VITRO</i> IN HELA CELLS AS DETERMINED BY FLOW CYTOMETRY (A) AND FLUORESCENCE MICROSCOPY (B) AFTER 48 H OF INCUBATION WITH NANOPARTICLES OR LIPOFECTAMINE AS CONTROL.....	139
FIGURE 65: SEM MICROGRAPHS OF THE PREPARED NANOPARTICLES: CAP/PEI/PEGFP/SiO ₂ (A), CAP/PEI/PHBsAg/SiO ₂ (B), CAP/PEI/PHBsAg+CpG/SiO ₂ (C), CAP/PEI/PHBsAg+SF/SiO ₂ (D).....	140
FIGURE 66: HBsAg EXPRESSION <i>IN VITRO</i> IN HELA (A) AND C2C12 (B) CELLS DETERMINED BY ELISA	142
FIGURE 67: HBsAg EXPRESSION <i>IN VITRO</i> IN BHK-21 CELLS AFTER 24 H AND 48 H OF INCUBATION WITH NANOPARTICLES (CAP/PHBsAg/SiO ₂ AND CAP/PHBsAg+CpG/SiO ₂), LIPOFECTAMINE OR PEI DETERMINED BY ELISA.....	143
FIGURE 68 ACTIVATION OF DENDRITIC CELLS AND EXPRESSION OF COSTIMULATORY SIGNALS (CD80 AND CD86) BY CAP/PEI/PHBsAg/SiO ₂ , CAP/PEI/PHBsAg+CpG/SiO ₂ , CAP/PEI/PHBsAg+SF/SiO ₂	145
FIGURE 69: HBsAg EXPRESSION <i>IN VIVO</i> IN C57BL/6 MICE 5 DAYS POST INJECTION DETECTED BY ELISA	146
FIGURE 70: ANTIBODY RESPONSE AFTER 14 DAYS POST THE 3RD IMMUNIZATION WITH PHBsAg LOADED NANOPARTICLES.....	147
FIGURE 71 A: PARTICLE SIZE DISTRIBUTION BY DYNAMIC LIGHT SCATTERING (DLS) AND B: SCANNING ELECTRON MICROGRAPH (SEM) OF CAP/PEI/TNF- α -SIRNA/SiO ₂ NANOPARTICLES.	150
FIGURE 72: CLSM IMAGE OF J774.2 CELLS INCUBATED WITH FLUORESCENT CAP/PEI/SiO ₂ -AF488 NANOPARTICLES FOR 10 H	151
FIGURE 73: CLSM Z-STACK IMAGE OF J774.2 CELLS INCUBATED WITH FLUORESCENT CAP/PEI/SiO ₂ -AF488 NANOPARTICLES FOR 10 H	151

FIGURE 74: J774.2 MACROPHAGE TNF-A EXPRESSION AFTER 4 H INCUBATION WITH DIFFERENT LPS CONCENTRATION (<i>ESCHERICHIA COLI</i> O55:B5).....	152
FIGURE 75: A: CELL VIABILITY OF J774.2 MONOCYTES AFTER 9 HOURS INCUBATION AT DIFFERENT NANOPARTICLES PER WELL CONCENTRATIONS. B: GENE SILENCING EFFICIENCY FOR J774.2 MONOCYTES AFTER 6 H INCUBATION WITH THE NANOPARTICLES OR LIPOFECTAMINE 2000 AND 4 H LPS (1 μ G ML ⁻¹) STIMULATION.....	153
FIGURE 76: A: THERMOGRAVIMETRIC ANALYSIS (TGA) OF THE CAP/CMC PASTE MATRIX. B: SEM MICROGRAPH OF THE DRIED CAP/CMC PASTE MATRIX PARTICLES.	154
FIGURE 77 CALCIUM PHOSPHATE PASTE PHOTOGRAPH AFTER ADDING THE NANOPARTICLES DISPERSION TO THE PASTE MATRIX.	155
FIGURE 78: TIMELINE PROTOCOL OF THE <i>IN VIVO</i> EXPERIMENT WITH A RAT PERIODONTITIS MODEL.....	156
FIGURE 79: BIOCHEMICAL ANALYSES AFTER IMPLANTATION OF CAP-POSITIVE OR CAP-NEGATIVE PASTE OR SURGERY-ONLY, RESPECTIVELY, IN THE EXPERIMENTAL PERIODONTITIS SITE.....	157
FIGURE 80: IMMUNOHISTOCHEMICAL STAINING OF PERIODONTAL TISSUE AT A: 7 D, B AND C: 21 D AFTER IMPLANTATION.	159
FIGURE 81: REPRESENTATIVE μ CT IMAGES OF THE CAP-POSITIVE GROUP (A, D), THE CAP-NEGATIVE GROUP (B, E), AND THE SURGERY-ONLY GROUP (C, F) AT 21 D AFTER IMPLANTATION INTO PERIODONTAL TISSUE.	161
FIGURE 82: SCANNING ELECTRON MICROSCOPY MICROGRAPH OF CALCIUM PHOSPHATE LOADED NANOPARTICLES. A) CAP/PEI/SiO ₂ , B) CAP/PEI/TNF-A-siRNA/SiO ₂ , C) CAP/PEI/pBMP-7/SiO ₂ , D) CAP/PEI/pVEGF-A/SiO ₂	163

3 Abbreviations

AAS	Atomic absorption spectroscopy
Ab	Antibody
AF	AlexaFluor®
Ag	Antigen
βME	β-mercaptoethanol
BMP	Bone morphogenetic protein
BSA	Bovine serum albumin
CaP	Calcium phosphate
CLSM	Confocal laser scanning microscopy
CMC	Carboxymethyl cellulose
Cryo-TEM	Cryogenic transmission electron microscopy
CuAAC	Copper(I)-catalyzed azide-alkyne cycloaddition
Da	Dalton
DAPI	4',6-diamidin-2-phenylindol
DC	Dendritic cell
DLS	Dynamic light scattering
DLVO	Derjagin, Landau, Verwey, Overbeek
DMEM	Dulbecco's Modified Eagle Medium
DMSO	Dimethyl sulfoxide
DNA	Deoxyribonucleic acid
DPBS	Dulbecco's phosphate buffered saline
EDX	Energy dispersive X-ray spectroscopy
EDC	1-ethyl-3-(3-dimethylaminopropyl)carbodiimide hydrochloride
EGFP	Enhanced green fluorescent protein
ELISA	Enzyme-Linked Immunosorbent Assay
ENV	Envelope glycoprotein
FAM	Carboxyfluorescein
FCS	Fetal calf serum
FS	Fluorescence spectroscopy
FTIR	Fourier-transform infrared spectroscopy
HAADF	High-angle annular dark field

HA	Hydroxyapatite
HBSS	Hank's Balanced Salt Solution
HBV	Hepatitis B virus
HeLa	Henrietta Lacks cervix carcinoma
HIV	Human immunodeficiency virus
i.m.	Intramuscular
IgG	Immunoglobulin
LPS	Lipopolysaccharides
MEA	Mercaptoethylamine
MHC	Major histocompatibility complex
MTT	3-(4,5-dimethylthiazol-2-yl)-2,5-diphenyltetrazolium bromide
MW or Mw	Molecular weight
NPs	Nanoparticles
PDI	Poly dispersity index
pDNA	Plasmid DNA
PEG	Polyethylene glycol
PEI	Polyethylenimine
RNA	Ribonucleic acid
ROS	Reactive oxygen species
SC	Specific coupled
SEM	Scanning electron microscopy
SIM	Structured illumination microscopy
siRNA	Small interfering RNA
SPAAC	Strain-promoted azide-alkyne cycloaddition
STEM	Scanning transmission electron microscopy
STORM	Stochastic optical reconstruction microscopy
Sulfo-SMCC	Sulfosuccinimidyl 4-(N-maleimidomethyl)cyclohexane-1-carboxylate
TAMRA	5-Carboxytetramethylrhodamine
TEM	Transmission electron microscopy
TGA	Thermogravimetric analysis
THPTA	Tris(3-hydroxypropyltriazolylmethyl)amine
TLR	Toll-like receptors
TNF	Tumor necrosis factor

UV-Vis	Ultraviolet-visible
VEGF-A	Vascular endothelial growth factor A
Wt.%	Weight percent

4 Introduction and Motivation

Calcium phosphate nanoparticles are a well-established biomaterial and numerous applications *in vivo* and *in vitro* demonstrate its huge potential [1]. Different synthetic approaches and methodologies for the synthesis of these nanoparticles give rise to a large variety of calcium phosphate nanoparticles with diverse sizes, morphologies, and composition [2-4].

The recognition process of a nanoparticle by a biological system, depends not only on the core composition or morphology but also on the surface properties [5]. Different methodologies for surface modification of nanoparticles can be found in the literature, some of them based on physical interactions and others in a chemical bond formation [6-9].

To this end, targeting or labelling molecules can be attached or absorbed to the surface of a nanoparticle to modify the specific affinity of the material [10]. For example, antibodies or antibody-fragments have been typically used as targeting agents, and have been coupled to different nanoparticles such as: gold nanoparticles [11, 12], iron oxide nanoparticles [13-15], mesoporous silica nanoparticles [16, 17], calcium phosphate nanoparticles [18, 19], among others. In a different way to labelling, a coating with poly(ethylene glycol) has been used to reduce further molecular adsorptions on the nanoparticle surface and to increase its hydrophilicity and circulation time in the organism [20-23]. In general, chemical surface modification methods are preferred because a covalent modification provides a more stable binding than a physical interaction that is not reliable enough for complex environments [24].

In the case of calcium phosphate nanoparticles, as the material is ionic, it is not possible to make a direct covalent reaction on its surface. For this reason, Neumeier *et al.* [25] and Kozlova *et al.* [26] developed a method to coat the calcium phosphate nanoparticle with a thin silica shell. The silica coating can then be used as starting point for further chemical reactions via siloxane chemistry [27].

Modifications of silica-terminated nanoparticles with (3-aminopropyl)triethoxysilane (APTES) and (3-mercaptopropyl)trimethoxysilane (MPS) have been reported [26] as a method to introduce an amine or thiol terminal group on the surface. These functional groups can later be used for coupling of biomolecules on the surface usually with the help of an activating crosslinker (e.g. sulfo-SMCC, EDC). For example, the following biomolecules have been coupled to calcium phosphate nanoparticles using this method: anti-CD11c and anti-IgG antibodies [18], anti-CD146, anti-IgG1, and anti-IgG2 antibodies [28], antigen Hen Egg Lysozyme (HEL) [29, 30], and synthetic antigen for HSV-1 (Herpes simplex virus) [31]. As an alternative, van der Meer *et al.* [19] have developed a different modification approach based on the avidin-biotin-complex. For this, avidin was added to the surface of the nanoparticle, so that it could react with any biotinylated molecule. This method was tested *in vitro* and *in vivo* using anti-CD11c coupled-nanoparticles.

Although the above mentioned examples showed the successful modification and application of the calcium phosphate nanoparticles, those methods can be limited for further applications. First, related to the fact that within a molecule more than one binding site can be found especially with biomolecules that often contain thiol, amine, and carboxyl groups and can react in multiple positions. Second, additional crosslinkers or intermediate molecules are required and consequently the number of molecules that can be attached per area are reduced. Third, the application of crosslinkers involves the need of additional purification steps that can induce aggregation of the molecule and generate random orientations with the coupling on the nanoparticle surface [32].

To overcome these issues an alternative method for the surface modification of calcium phosphate nanoparticles is required. Taking into account the *click chemistry* conditions established by Sharpless *et al.* [33], reactions that require simple conditions are preferred for the calcium phosphate nanoparticles surface modification. From the various available click reactions, the azide-alkyne cycloaddition click reaction is of interest because of its high efficiency, simplicity and specificity as both functional groups are not naturally found in biomolecules [34] *i.e.*, is possible to synthetically control the position of the group within the molecule. Moreover, these functional groups are suitable for bioorthogonal reactions [35, 36] and produce a stable triazole

covalent bond after the reaction [37]. One aim of this thesis is to develop the methodology for the surface modification of calcium phosphate nanoparticles based on the azide-alkyne cycloaddition click chemistry as a new and versatile method for the surface modification of the calcium phosphate nanoparticle.

The second part of this work is developed within biomedical applications using calcium phosphate nanoparticles. The biomedicine concept is an interdisciplinary field for which the application of nanotechnology is used to effectively diagnose and solve medical issues [38]. The synthesized calcium phosphate nanoparticle has the advantage, as mentioned previously, that an internal loading can be added and when required also an external surface modification. Kopp *et al.* have attached two different synthetic peptides to the surface of a calcium phosphate nanoparticle that mimic a neutralizing antigen of HSV-1/2 gB [31] and the nanoparticle contained an internal loading of CpG adjuvant to stimulate the immune response. The functionalized nanoparticles were able to activate the immune response and protect the mice from a lethal HSV-1 infection. Moreover, Zilker *et al.* [29] and Temchura *et al.* [30] used HEL protein surface-bonded nanoparticles to successfully induce a humoral immune response *in vitro* and *in vivo*. On those examples the coupling interaction on the nanoparticle was not further studied.

It is of relevance to further investigate the influence that the coupling method has on the protein binding because it can affect the biomolecule conformation and interaction after the attachment. For example, Ma *et al.* studied the effect that the coupling and the spacer arm have on the Glutathione S-Transferase after attachment to the surface of gold nanoparticles [39]. Regarding the calcium phosphate nanoparticles, and especially for immunization applications, in the literature neither a comparison at this level nor the influence the coupling method has on the protein activity has been reported.

As part of the aims of this thesis, nanoparticles will be synthesized to investigate at the surface-environment interaction the influence the protein coupling method has on the immune response using HIV envelope glycoproteins.

Additionally, changing the scope from the nanoparticle surface to the internal loading, calcium phosphate nanoparticle has been used as carrier of different loadings for immune response with peptides [40, 41], proteins for imaging [42, 43] and with siRNA and DNA plasmid for transfection and gene silencing [44-46]. Additionally, the transfection in 3D cell culture and co-culture has been also studied for this type of nanoparticle [47].

Kopp *et al.* [31] and Zilker *et al.* [29] have studied the use of antigen loaded calcium phosphate nanoparticles for vaccination applications using calcium phosphate nanoparticles. In both cases a direct loading of the antigen into the nanoparticles was used. Using a different approach, instead of carrying the required protein, it is possible to deliver the plasmid of interest that encodes the required protein into the cell to induce an immune response (*i.e.*, genetic immunization [48]). Within the aims of this thesis, an optimization of the calcium phosphate nanoparticle internal loading will be studied and applied for HBsAg transfection *in vitro* and *in vivo* to further extend the application of this material as a potential tool for nanoparticle plasmid vaccination.

In contrast to the biomedical vaccination applications mentioned before, a direct application of calcium phosphate nanoparticle to induce a healing effect is also of interest. A direct application *in vivo* of active calcium phosphate nanoparticles have been reported by Schlickewei *et al.* [49, 50] for the *in-situ* transfection of BMP-7 and VEGF-A in a critical-size bone defect. The application of the calcium phosphate paste material can be extended, for example, to dental applications as it can be locally applied during a dental procedure. As part of the aims of this thesis, the efficiency of a direct application of an active calcium phosphate nanoparticle paste will be investigated as a gene silencing or gene expression agent *in vitro* and *in vivo* for dental applications.

5 Theoretical background

5.1 Calcium phosphate

Calcium orthophosphates are composed of calcium (+II), phosphorus (+V) and oxygen (-II) in the orthophosphate anion [51]. Depending on factors such as the molar ratio, protonation, and substitution degree, different calcium orthophosphates are obtained. In general, calcium orthophosphates crystalize in triclinic and monoclinic crystal systems, although formation in rhombohedral or hexagonal lattices also occurs. Table 1 lists the most common calcium orthophosphates [51, 52].

Table 1: Common calcium orthophosphates [51, 52]

Compound	Formula	Ca/P	Crystal system	Space group
Monocalcium phosphate monohydrate (MCPM)	$\text{Ca}(\text{H}_2\text{PO}_4)_2 \cdot \text{H}_2\text{O}$	0.5	triclinic	$P\bar{1}$
Monocalcium phosphate anhydrate (MCPA)	$\text{Ca}(\text{H}_2\text{PO}_4)_2$	0.5	triclinic	$P\bar{1}$
Dicalcium phosphate dihydrate (DCPD)	$\text{CaHPO}_4 \cdot 2\text{H}_2\text{O}$	1.0	monoclinic	la
Dicalcium phosphate anhydrate (DCPA)	CaHPO_4	1.0	triclinic	$P\bar{1}$
Octacalcium phosphate (OCP)	$\text{Ca}_8(\text{HPO}_4)_2(\text{PO}_4)_4 \cdot 5\text{H}_2\text{O}$	1.33	triclinic	$P\bar{1}$
α -tricalcium phosphate (α -TCP)	$\alpha\text{-Ca}_3(\text{PO}_4)_2$	1.5	monoclinic	$P2_1/a$
β -tricalcium phosphate (β -TCP)	$\beta\text{-Ca}_3(\text{PO}_4)_2$	1.5	rhombohedral	$R3cH$
Hydroxyapatite (HA)	$\text{Ca}_{10}(\text{PO}_4)_6(\text{OH})_2$	1.67	monoclinic Hexagonal	$P2_1/b$ $P6_3/m$
Tetracalcium phosphate (TTCP)	$\text{Ca}_4(\text{PO}_4)_2\text{O}$	2.0	monoclinic	$P2_1$

In mammals, calcium orthophosphates are the main inorganic component that are predominantly found in bones and teeth. From these, hydroxyapatite (HA) is of relevant importance, as it is the most abundant form present in the body. Within the organism, hydroxyapatite is not likely to be found in the stoichiometric form but rather as calcium deficient hydroxyapatite with a less crystalline structure and substituted with other ions. Ca^{2+} positions can be substituted by Na^+ , K^+ , Mg^{2+} , Sr^{2+} ions; PO_4^{3-} positions by CO_3^{2-} , HPO_4^{2-} ions and OH^- positions by F^- , Cl^- and CO_3^{2-} ions [51].

For this reason calcium phosphate compounds (especially HA) are considered to have a natural biocompatibility and low toxicity for mammals (e.g. humans) [53]. Calcium phosphate compounds have been extensively used for research for biological applications since decades until today. Initially, the main focus for this materials was for implants and biomineralization [52, 54-58]; although applications in molecular biology and biomedicine have been also intensively developed [1, 59].

Many synthetic approaches to prepare calcium phosphates can be found in the literature, such as precipitation, hydrothermal, sol-gel, solid state, among others methods [2, 4, 60]. With the development of methods to obtain calcium phosphate in the nanoscale dimension (*i.e.*, at least one dimension is $1 < 100$ nm, although the definition varies among authors and organizations [61-63]), the material application scope was broadened, especially in the biological field [1, 3].

5.2 Nanoparticles

When moving from the macro- or microscale to the nanoscale, some of the materials properties can change (e.g., optical, hardness, solubility, electrical) [64, 65]. Additionally, as the size decreases, the relationship surface area to volume ratio is higher, and the surface becomes more relevant for the interaction with the environment.

Nanoparticles in a colloidal dispersion will tend to aggregate to reduce the surface energy and stabilize the system [66]. The stability of a colloidal system is generally described by the theory developed by Deryaguin and Landau [67], and Verwey and

Overbeek [68], known as the DLVO theory. This model takes into consideration two contributing forces (one attractive and one repulsive) for the total energy of interaction (G_T):

$$G_T = G_A + G_{el} \quad (1)$$

where G_A is the van der Waals energy of attraction and G_{el} is the electrostatic energy of repulsion between two particles, which are described as:

$$G_A = -\frac{A_{11}}{6} \left[\frac{2}{s^2 - 4} + \frac{2}{s^2} + \ln \left(\frac{s^2 - 4}{s^2} \right) \right] \quad (2)$$

$$G_{el} = \frac{4\pi\epsilon_0\epsilon_r R^2 \Psi_d^2 \exp(-kh)}{2R + h} \quad (3)$$

where R is the particle radius, h is the distance between them, A_{11} is the Hamaker constant ($A_{11} = \pi^2 q^2 \beta_{11}$, q is the number of atoms per volume and β_{11} the London dispersion constant), $s = (2R+h)/R$, ϵ_0 is the permittivity of free space, ϵ_r is the relative permittivity, Ψ_d is the potential at the center of the specifically adsorbed counter ions, and k is the Boltzmann constant [5].

A representative energy-distance curve is shown in Figure 1. In blue is the contribution of only the G_A , which has an inverse power law with h , and in red G_{el} , which has an exponential decay approaching to zero when increasing h . The DLVO curve shown with the black dash line has two minima and one maximum. The secondary minimum, which is reversible, occurs at higher h and is related to a slight particles aggregation.

The secondary and primary minimum are separated by a maximum (G_{max}) and represents the required energy barrier that keeps the colloidal system stable. Above this maximum, the repulsion between the particles becomes bigger than the attraction. This value also depends on the surface potential (ζ -potential) and electrolyte concentration [69]. Normally, with a ζ -potential higher than 30 mV (absolute value) the dispersion is considered stable [70, 71].

When this maximum is overpassed at closer distances, the primary minimum is reached and the particles will aggregate causing the dispersion to collapse.

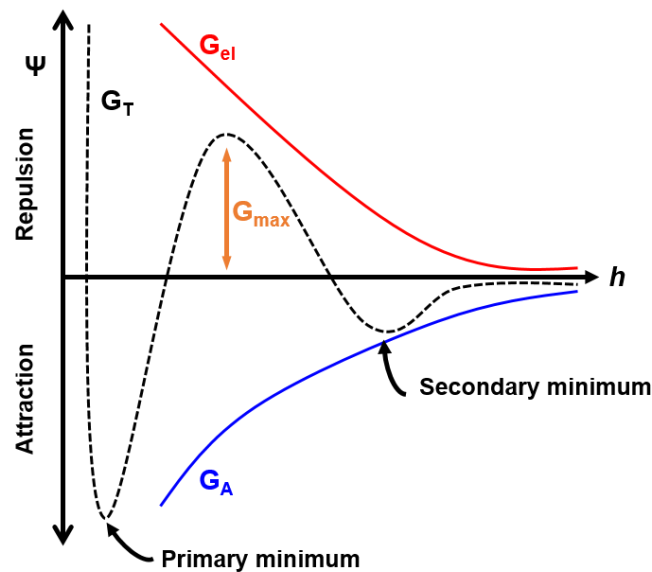


Figure 1: Energy-distance plot according to DLVO theory, imaged based on [69].

An extended version of the DLVO theory has been also developed for cases in which the classical model does not provide an appropriate adjustment [72]. In the extended version, in addition to the G_A and G_{el} forces the model takes into account repulsive forces at short distances ($G_{solv, str}$) that are mostly attributed to solvent structured induced forces.

To reduce the aggregation of the particles in dispersion two main ways can be used, by electrostatic, and steric stabilization. With the electrostatic stabilization, a charged surface is needed so that the particles are repelled from each other when they come close enough due to its surface charge. With the steric stabilization, ligands on the particles surface or free polymers (depletion mode) are used to keep the particles separated. When two particles get closer, two phenomena can occur: a) an osmotic repulsion, caused by the increase in osmotic pressure due to the overlap of polymer chains that changes the density in the interaction zone and, b) entropy reduction for the polymer chains due to the volume decrease caused by the overlap [69].

Having a stable colloidal system is required for a successful application of nanoparticles. These materials are of interest for biological applications, because at this scale, the nanoparticles can interact in a different way with biological systems, due to the similarity in the size range [73]. For example, nanoparticles can be taken up by cells, interact with proteins or have similar sizes as other biological agents like viruses. Therefore, nanoparticles can then be used as an active (functional) or passive (carrier) agent.

In a colloidal dispersion, the nanoparticles will be surrounded by the Stern double layer and hydration layer. When changing from pure water to a cell culture medium or to a biological fluid, the molecules and ions in the medium like the proteins will form a coating around the particles surface that is referred as protein corona. The interaction of the nanoparticles with the protein corona is important as it will influence the materials performance (*e.g.*, cellular uptake, targeting, and distribution) and stability *in vitro* and *in vivo* [74, 75].

The protein corona can be divided into two sections, the inner corona (hard shell) and the outer corona (soft shell) [76]. In the first, the proteins have a stronger affinity with the nanoparticles and are not likely to be desorbed. In the latter, surrounding proteins can interact with the proteins of the hard corona and will exhibit a higher exchange with the medium making the outer corona more labile. Although with this definition it seems that the corona is somehow fixed. Its formation and evolution is a dynamic process that is influenced by factors such as concentration, affinity, temperature and time [77, 78] and reflects, in a simplified way, the classical model of protein-protein competition interaction and displacement steps (the so-called Vroman effect [76, 79]).

5.3 Click chemistry

Click chemistry concept was introduced in 2001, as a way to group reactions with high selectivity and reliability that work under simple conditions (non water nor oxygen sensitive) [33]. Sharpless *et al.* described several conditions that the reactions should fulfil to be considered a click reaction. In general, besides requiring simple reaction

conditions, the reaction should be stereospecific and give a high product yield that can be isolated with simple methods like non-chromatographic approaches.

One of the most used and good example of click reaction is the copper catalyzed click reaction (CuAAC) that was described by Meldal *et al.*[80] and Sharpless *et al.* [81] in 2002. The chemical foundations of such reaction goes back to the work of Huisgen in 1963 [82, 83]. The Huisgen 1,3-dipolar cycloaddition allows to have a large variety of five-membered heterocycles by reacting an alkyne containing molecule with an azide containing molecule as shown in Figure 2.

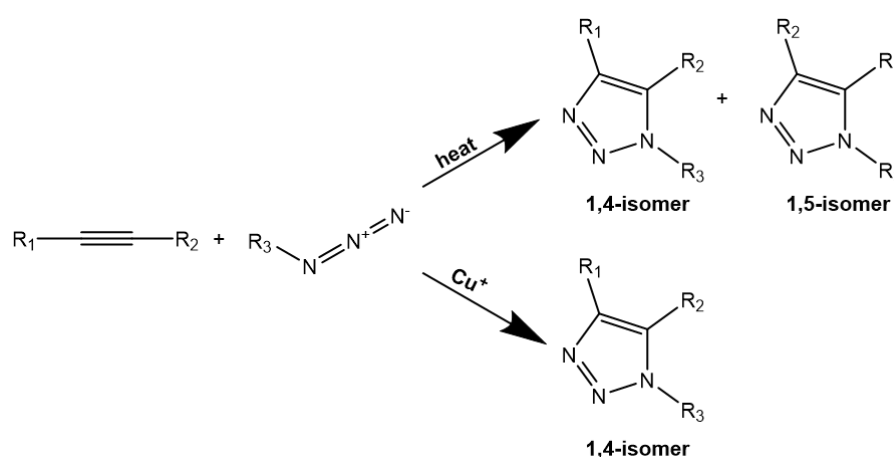


Figure 2: General reaction schemes of Huisgen 1,3-dipolar cycloaddition reaction and copper catalyzed click reaction (CuAAC).

The applicability of this reaction was limited by its high endothermic requirement, which needs high temperatures and long reaction times, and at the end two isomers were obtained, the 1,4 and 1,5 regioisomers. With the introduction of the copper (I) catalyst, the reaction conditions become milder (water or other solvents, room temperature) and only the 1,4 isomer is obtained (Figure 2). Thus, this reaction is a good example for click chemistry.

The CuAAC reaction mechanism has been described by Fokin *et al.* initially in 2002 [81] and updated in 2013 (Figure 3) [37]. For this reaction, the initial step is the formation of an σ -bond between the copper and the alkyne group. Next, a second copper atom forms a π interaction with the acetylide. The azide group will then coordinate with π -bound copper forming the active complex, which enables the β -

carbon to make a nucleophilic attack to the N-3 of the azide and generates an intermediate. The second C-N bond is formed, and one copper atom is released followed by a hydrogenation step where the triazolide is obtained. Based on the copper isotopic enrichment analysis the presence of two different copper atoms in the intermediate state was confirmed.

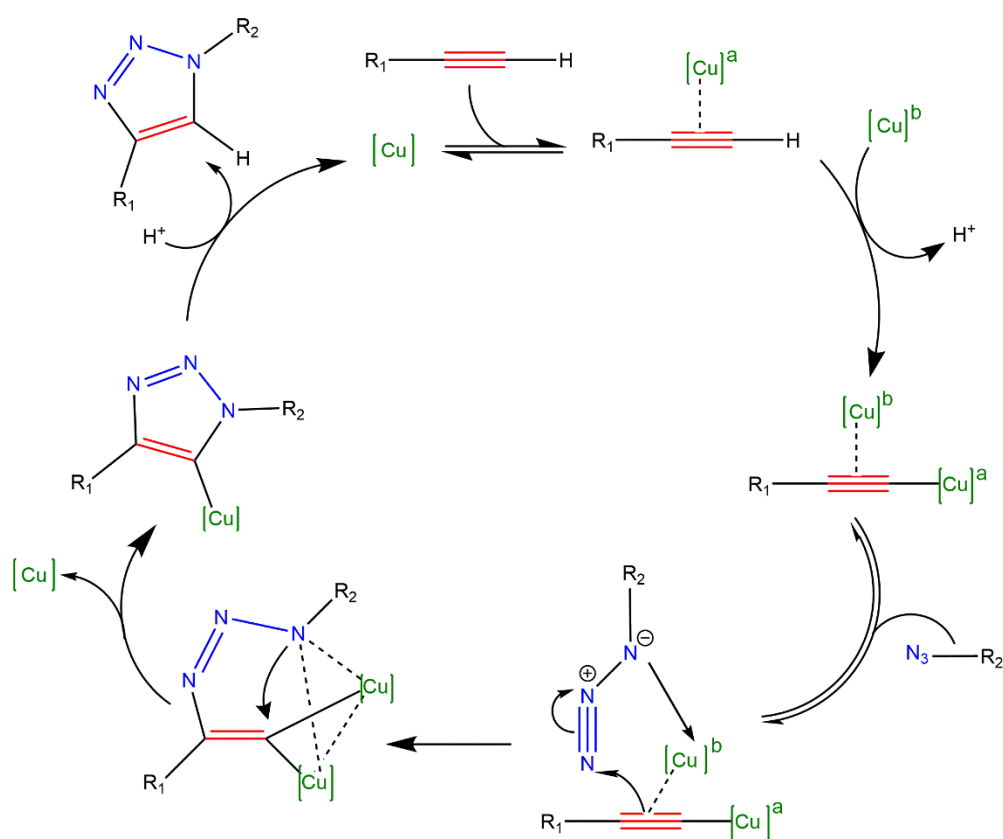


Figure 3: Copper catalyzed azide-alkyne cycloaddition proposed mechanism by Fokin *et al.* Figure based on [37].

After its introduction, the CuAAC reaction was rapidly adopted and further applications were developed. In the field of bioorthogonal reactions this method broadened the possibilities, as both functional groups, alkyne and azide, are not normally naturally found in biomolecules (*e.g.*, amino acids, peptides, proteins). For example, the azide functional group can be introduced into biomolecules (or metabolically) causing a minimal influence in the biomolecule environment [84]. Thus, this reaction for bioorthogonal applications becomes very prominent for modification, reporting or labelling [35, 85].

When moving into the biological applications like reactions in live cells, the toxicity issue of using copper as a catalyst is of relevance [86-88]. Although, the copper concentration for the reaction is relatively small, for sensitive or repetitive applications it can have detrimental effects.

For this reason, an alternative for CuAAC was introduced by Bertozzi *et al.* [89]. In a different way, the reaction approach is based on the cycloaddition of a highly constrained cyclooctyne and the azide group. These types of spontaneous reactions were first studied back in the 1950-1960 by Blomquist [90], Wittig and Krebs [91].

As no copper or other catalyst is needed for this reaction, the ring tension is the reaction inducer. This reaction was termed strain-promoted azide-alkyne cycloaddition (SPAAC), which is also known as copper-free click reaction. Figure 4 shows a representative reaction scheme.

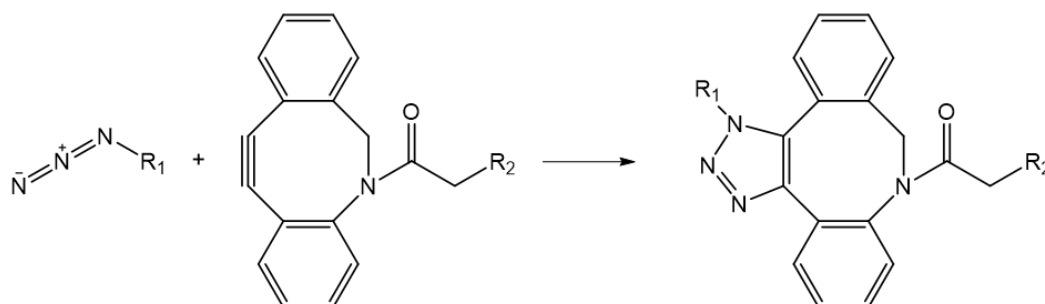


Figure 4: General reaction scheme of the strain-promoted azide-alkyne cycloaddition (SPAAC).

The limiting factor for this reaction is the alkyne reactivity towards the azide molecule. To increase the reactivity of the cyclooctyne molecule, modifications have been developed by controlling the ring strain with the angle of distortion, and electronics effect of the substituents using electron-withdrawing or electron-donor groups [92]. Figure 5 shows representative cyclooctyne derivate compounds, DIFO [93], BNC [94], DIBO [95], DIBAC [96], and BARAC [97] with different reaction rate constants according to the structure modification.

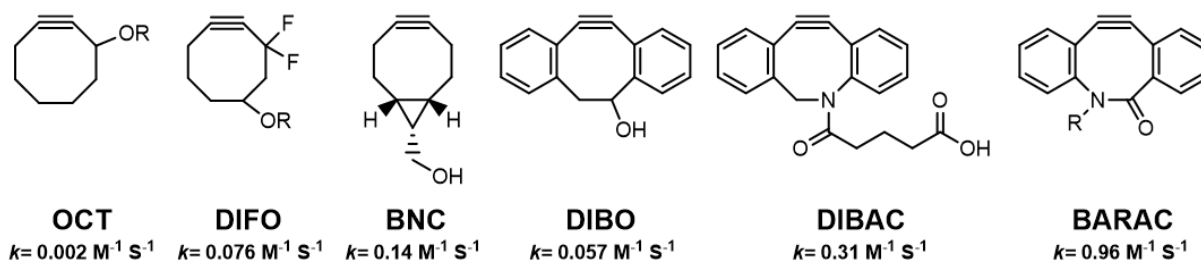


Figure 5: Structures of representative cyclooctyne based ligands developed for strain-promoted azide-alkyne cycloaddition (SPAAC).

One of the initial structures modification was DIFO molecule that has two fluorine atoms near the alkyne that work as electron withdrawing elements and increase the alkyne reactivity. When DIFO is compared to OCT it has a reaction rate near 40 times higher. In a different way, DIBO, DIBAC and BARAC uses a dibenzo system on both sides of the cyclooctyne group, which can increase the strain [98] but a steric hindrance, during the transition state with the azide group, affects its reactivity [99] if no further modifications are performed. With the introduction of a nitrogen group (sp^2 center) in DIBAC and BARAC ring its reactivity increases considerably [92]. Moreover, at this position further modifications can be performed to attach molecules of interest (e.g., dyes, hydrophilic linker, active molecule) making it also valuable from a synthetic point-of-view.

From Figure 5, molecules based on DIBO and DIBAC are the most used compounds as they provide a balance between reactivity, stability and synthetic feasibility [100]. Moreover, some of them are commercially available.

Many applications for CuAAC and SPAAC can be found in literature [36]. Most of them were developed for in-solution reactions [101], although applications for surface modification [102-105], polymerization [106-110], solid-phase synthesis [111, 112], nucleic acids modification [113-115] and live cell assays [89, 93, 98, 116, 117] are also found. Reactions with different nanoparticles substrates, like iron oxides [118-123], silica [124, 125] and gold [126, 127] are also reported.

5.4 Biological applications

As mentioned in the previous sections the use of nanoparticles for biological applications is a highly active research field. Some general and basic concepts related to this topic and important for the following chapters will be described in this section.

5.4.1 Nanoparticles uptake

When nanoparticles are given to a biological system at the end the nanoparticles come into contact with cells. Depending on its size, charge, chemical and biological properties the material's interaction with the cell membrane will differ. The mechanism by which the nanoparticles are taken by the cells has been studied by several authors and evaluated for different types of nanoparticles [128, 129].

Most Eukaryotic cells take up nanoparticles by endocytosis [130]. In general, this procedure can be described as the nanoparticle internalization caused by an initial membrane invagination, which ends with endocytic vesicles inside the cell. Depending on the material's size and properties, the mechanism can follow a macroscale or a microscale endocytosis. When particles are larger than 500 nm, it normally follows a macroscale endocytosis [131]. These mechanisms are summarized in Figure 6.

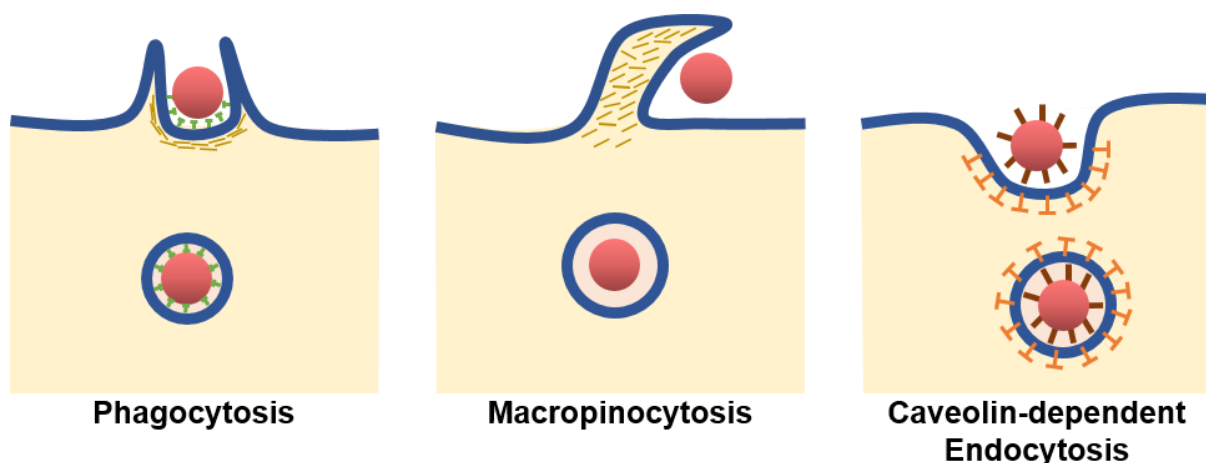


Figure 6: General representation for phagocytosis, macropinocytosis and caveolin-dependent endocytosis. Image adapted from [128].

Macroscale endocytosis comprise phagocytosis and macropinocytosis. Phagocytosis is the uptake procedure normally found in phagocytes, like macrophages, monocytes, dendritic cells, etc. [132]. This mechanism starts with an opsonisation procedure, in which the particle surface absorbs opsonins (immunoglobulins) that will interact with the specific membrane receptors. This induces the particle engulfing which ends with the phagosome that contains the internalized particle [129].

On the other hand, macropinocytosis takes the particles and other extracellular components via an encapsulation induced by the extension of the cell membrane, which surrounds the extracellular fluid until the cavity is completely enclosed, and is followed by its internalization [129].

Smaller particles (< 200 nm) internalization follow usually a microscale endocytosis [131], which can be divided in clathrin-mediated, caveolin-mediated and clathrin/caveolae-independent endocytosis. For these mechanisms specific molecular regulators and modules are required for its functionality.

Clathrin-mediated endocytosis can occur following a receptor-specific or non-specific adsorptive uptake. In the case of receptor-specific, clathrin protein mediates the process in which the clathrin rich cavity is formed after the particle recognition, and it is followed by an invagination. With the help of adaptors and other accessory proteins the membrane internalization is stabilized [128, 131]. Usually vesicles of 100-150 nm size are obtained, and it has been observed that this route normally ends up in lysosome degradation [129].

Caveolin-mediated endocytosis occurs in the caveolae membrane invaginations (with a size of 50-80 nm) normally found in regions that anchors with the cytoskeleton [129]. The caveolin protein is responsible for cavity shape and once the particle is recognized secondary proteins help in the membrane stabilization and the vesicle encapsulation. Compared to clathrin-mediated endocytosis, caveolin-mediated route tend to lead to a lysosomal degradation escape [130, 131].

The uptake mechanism is dependent in the cell type and the nanoparticles properties. Calcium phosphate nanoparticles uptake route by HeLa cell line was studied by

Sokolova *et al.* using positive and negatively charge nanoparticles [133]. With the application of endocytosis inhibitors, the route was followed by confocal microscopy and FACS analysis. The authors concluded that calcium phosphate nanoparticles were taken up by a macropinocytosis mechanism.

5.4.2 Cellular transfection

The introduction of foreign nucleic acids into a cell is known as transfection, and is a way to generate modified cells or organisms [134, 135]. The modification can be permanent by the integration into the host genome (known as stable transfection) or temporal in which the modify genes are not integrated into the host genome and are only expressed or inhibited for a limited period of time (mainly performed with mRNA) [136]. Different transfection methods exists and can be grouped in physical, chemical or biological methods.

Physical methods can be highly selective, but time consuming, for example with micro injection or laser-mediated transfection one cell at a time is transfected giving a very high selectivity. With micro injection the nucleic acids are directly added into the cytoplasm or nucleus. In a less specific way, electroporation involves the application of an electrical potential that induces the temporal destabilization of the membrane generating pores in which the nucleic acids can penetrate the cell [136, 137].

Biological transfection approaches involve the application of a virus as the transfecting agent. Due to its capacity as nucleic acid carriers, different viruses' strands like lentivirus, adenovirus, herpes simplex virus and poxvirus has been used and studied as transfection vectors, some of them also in clinical trials [138, 139]. With this mechanism, the DNA incorporation into the genome is likely to occur with high efficiency [136].

On a different way chemical methods involve the application of molecules or ions that can form a stable electrostatic interaction with the nucleic acids, and thus the particle-like material is taken by the cell following any of the described mechanisms in the previous section. Lipid-based complexes (Lipoplexes), Polymer-based complexes

(Polyplexes) and with calcium phosphate are the most common ones [140]. With this methods, many cells can be transfected at once given a high throughput, but the transfection efficiency and viability will have a higher dependence on the cell type and conditions (*i.e.*, not all cells are transfected the same or experiences the same toxicity) compared to other methods [136].

The transfection approach can also be used for a gene knock-down that is also known as gene silencing [141]. The generated inhibition is reflected only for a limited time and does not generate a permanent modification expression [142]. Two main approaches of using short RNA duplexes with non-coding RNA has been developed, the small interfering RNAs (siRNAs, usually with 21-23 nucleotides) and the microRNAs (miRNAs, usually with 18-25 nucleotides) [143]. For siRNA to be effective a complete complementarity with mRNA strand is required, but for miRNA only a partial complementarity is needed. This difference causes that for siRNA only one target is reached but for miRNA multiple targets can happen and decreases the targeting specificity [144]. Additional differences between both are observed in the silencing mechanism. In general, siRNA mechanism follows a RNA cleavage while miRNA follows a translational repression and mRNA a degradation [145].

For siRNA, after the dsRNA is released into the cytoplasm the Ribonuclease-III enzyme (“Dicer”) divides the dsRNA into small fragments (siRNA), which then activates the RNA-induced silencing complex (RISC). In this complex, the siRNA passenger strand is cleaved by endonuclease Argonaute 2 (AGO2) and the guide strand stays in the RISC, which then targets the complementary mRNA. After the siRNA binds the corresponding mRNA, the fragment cleavage is induced by AGO2, and will be followed by a degradation pathway via cellular exonucleases [146, 147].

In miRNA pathway, once the pre-miRNA is released from the nucleus into the cytoplasm, it is divided by the “Dicer” enzyme into smaller fragments of 18-25 nucleotides. The fragments then form the miRISC complex where the double strand is unwound and the passage strand removed without further cleavage [145, 148]. The single-stranded miRNA in the miRISC targets partially and binds the complementary bases in the mRNA. After this step, the gene silencing happens due to translational repression, degradation and/or cleavage [143, 149].

5.4.3 Immune system and viral infections

The immune response can be divided according to the type of response in the innate and the adaptive one [150]. The former constitutes a faster response that is based on the activation of neutrophils, macrophages and other hematopoietic cells (cells from the bone marrow that can differentiate into different blood cell types [151-153]) that are directed by the release of cytokines, chemokines and complementary proteins. The latter, as the name suggests, responds to a precise antigen-specific reactions but takes a longer time to be developed [154, 155]. Naturally, both immune responses communicate and function together.

In the innate response most of the elimination activity takes place at the infection site, and several elimination mechanism can occur depending in the involved cells (*e.g.*, macrophages, dendritic cells, mast cells, neutrophils, natural killer cells) [156]. For example, neutrophils can destroy the foreign agent by reduction of the aerobic conditions with formation of toxic species (like H_2O_2 , OH^- and $^1\text{O}_2$) inside de cell and with the help of cationic proteins and enzymes that induces apoptosis.

On the other hand, killer cells act by a lysis process to eliminate the foreign agent when the surface receptors for immunoglobulin or major histocompatibility complex (MHC) class I are not fulfilled. Additionally, pathogens can also be recognized by the host system with pattern recognition receptors (Toll-like receptors, TLRs) which can identified highly conserve chemical structures from bacteria or other microorganisms [157], like the lipopolysaccharides (LPS) from gram negative bacteria cell walls. After the recognition different pathways can happen, for example: endocytosis and antigen expression, and nuclear factor kappa-light-chain-enhancer (NF- κ B) transduction and cell activation [154].

The adaptive immune response allows to have specific responses mainly based by antigen-specific receptors found on the surface of T and B cells. T lymphocytes mature in the thymus and B lymphocytes within the bone marrow [158]. After a gene rearrangement, the cell develops the specific receptors, B cells produce IgM in its membrane, while T cells receptor complexes with a CD3 molecule.

For a T-cell to respond to an antigen first it requires an activation process in which a major histocompatibility complex (MHC) is involved. The MHC can be expressed as class I when an antigen has been formed endogenously within the cell, or as MHC class II where the antigen has been previously processed after uptake by a dendritic cell, B cell or macrophage [158]. Each class varies depending on the cell type, for example, CD8 cells identifies antigen within MHC class I and CD4 cells for MHC class II. Once CD4 is activated, cytokines are released inducing further cellular activations, while activated CD8 cells carry removal by cytotoxicity [154].

T cells can be further divided according to its functionality into T helper (Th) for CD4 carrying cells and T cytotoxic (Tc) cells that has CD8 molecule in its surface (this molecule also functions as a coreceptor for MHC class I). Once activated, Th cells are separated into Th1 and Th2 cells. The former produces interleukin 2 that prompts T cells proliferation and stimulates CD8+ T cell division and cytotoxicity effect. Interferon γ is also released and activates macrophages for removal of intracellular pathogens. The latter improves antibodies formation by the release of interleukin 4, interleukin 5, interleukin 6 and interleukin 10 [158]. Additionally, Tc cells act by a direct apoptosis induction of the target cell, and they can be subdivided similarly to Th cells, into Tc1 and Tc 2 according to the released cytokines [154].

In the organism there are different types of immunoglobulins (antibodies) according to its localization and function [159], for example IgM (vascular), IgD (receptor for B cells activation) [160], IgG (blood and tissues) [161, 162], IgA (secretions) [163, 164], and IgE (allergic reactions) [165], and from each one there are different subclasses.

These antibodies are generated by B cells after its activation and differentiation [166]. The following described pathway represents the most common one [167]. After a B cell has been recognized and internalized an antigen (primary response), it further processes and expresses the antigen in the MHC class II complex that can then activate a T cell. As mentioned before, activated Th cells help in the B cell division and maturation where the originally expressed IgM/IgD is transformed into IgA, IgE or IgG by a recombination process, or stay as IgM/IgD [168]. Once activated the B cell, it can be released as a plasma cell or a memory cell that will then enable a faster response when the antigen is again recognized (secondary response).

For a virus infection, the virus needs first to bind the target cell to start the cell membrane penetration. Two common pathways are normally followed by a direct penetration and by endocytosis [169]. For the direct penetration, the virus undergoes a conformational transformation that activates the membrane fusion machinery that will enable the transportation of the virus capsid into the cytosol. Enveloped viruses like HIV-1 Env virus, Influenza virus HA, Ebola virus GP are common examples of viruses that follow this pathway [170]. In a different way, other viruses use endocytosis that follows any of the mechanisms described in section 5.4.1., followed by pH-dependent or independent fusion from the endocytic compartments for release [171]. This second pathway allows the virus to avoid the plasma membrane, actin cortex and other cytoplasmic barriers. Also it helps to overpass at the entry level the immune detection system [172].

Once inside the cell, the viral genome is uncoated and transferred into the host cell cytosol or nucleus. The innate immune system is able to detect foreign DNA or RNA inside the cytosolic regions usually mediated by nucleotide oligomerization domain-like receptors (NLRs), RIG-I-like receptors (RLRs), and extracytosolic by TLRs receptors [173]. Although, many immune system inhibitors and viral elusion mechanisms allow the virus survival and propagation.

Taking the viral structure as a model, virus-like particles (VLPs) are self-assembled (usually viral envelope or capsid proteins) within 20 to 100 nm that mimic the native viral structure but without the genetic material [174]. These materials have the advantage that are capable to stimulate the immune system, which make them of relevance for vaccination applications [175, 176]. By surface modification the VLPs can be derivatized to include the required functional groups to enable the coupling of other molecules of interest [177].

In this field, nanoparticles are of interest due to its similarity in size to VLPs, the high chemical and physical properties variability and also to its capacity for further modifications. Different types of nanoparticles have been developed based on silica, gold and calcium phosphate, as well as soft-nanoparticles like polymeric and lipids (liposomes) based [178, 179].

6 Methods

6.1 Dynamic Light Scattering (DLS) and ζ -Potential

One of the most popular methods to determine the nanoparticles size in dispersion is Dynamic Light Scattering (DLS). Particles in a dispersion are subject to Brownian motion and this movement is related to the diffusion coefficient of the particle that follows the Stokes-Einstein equation.

$$D = \frac{k_b T}{6\pi\eta R_h} \quad (4)$$

where k_b is the Boltzmann constant, T the absolute temperature, η de viscosity and R_h the hydrodynamic radius [180]. From this equation is possible to conclude that smaller particles will have a higher diffusion coefficient compared to larger particles.

When the sample is illuminated by a laser beam, the beam is then scattered by the particles following the Rayleigh light scattering principles. The time variation of the scattered light intensity and frequency is detected and correlated to the Brownian motion. As smaller particles diffuse faster, the intensity fluctuation will be larger compared to bigger particles. The autocorrelation function $g_2(\tau)$ relates the normalized integration of the initial intensity ($I(t)$) and after a given time ($I(t + \tau)$) [181].

$$g_2(\tau) = \frac{\langle I(t) I(t + \tau) \rangle_t}{\langle I(t) \rangle_t^2} \quad (5)$$

Experimentally, what is measured is the normalized electrical field generated by the particles with the incident beam. For a monodisperse distribution the autocorrelation function is then adjusted to [182]:

$$g_2(\tau) = B + \beta e^{-2\Gamma\tau} \quad (6)$$

$$A\Gamma = Dq^2 \quad (7)$$

$$q = \frac{4\pi n_0}{\lambda} \sin \frac{\theta}{2} \quad (8)$$

where B is the baseline, β factor corresponds to the amplitude of the autocorrelation function and depends on the detector area, optical alignment, and scattering

properties of the materials. D is the diffusion coefficient and q the scattering factor that varies with the medium refractive index (n_0), source wavelength (λ), and detector angle (θ). From these relationships the particle radius can be determined.

The nanoparticle ζ -potential is the potential difference of the particles electric double layer (EDL, *i.e.*, Stern layer and diffusive layer) and the layer of dispersant around it. This parameter can be measured by an electrophoretic mobility method [180]. When an electrical field is applied, the nanoparticle will move to the opposite charged electrode. The electrophoretic mobility is described by Henry's equation [71]:

$$\mu_e = \frac{2\varepsilon_r\varepsilon_0\zeta f(ka)}{3\eta} \quad (9)$$

where ε_r is the relative permittivity/dielectric constant, ε_0 the permittivity of vacuum, $f(ka)$ the Henry's function and η the viscosity. For $f(ka)$ a value of 1.5 can be used when the EDL is significantly smaller than the particle radius. The equation is then simplified and known as the Helmholtz-Smoluchowski equation [183].

The measurements of the hydrodynamic radius and ζ -potential were performed in a Malvern Nano ZS ZEN 3600 device with a disposable folded capillary cuvette (DTS1070). The data were analyzed with the instrument software without further treatment.

6.2 Spectroscopy methods

6.2.1 UV-Vis spectroscopy

UV-Vis spectroscopy is a general characterization technique that is based on the electronic transitions a molecule has. When the specific wavelength (energy) is applied, the excitation of an electron from the ground level to the excitation state occurs (*i.e.*, moving from a π bonding orbital to an anti-bonding orbital) and a photon is absorbed. The wavelength at which this happens depends on the energy difference between the energy levels. When this occurs between wavelengths of 190 – 800 nm is possible to measure the absorbance with a UV-Vis spectrophotometer.

The lineal relationship between the absorbance (A) and concentration (c) of a sample is given by the Beer-Lambert Law

$$A = \epsilon lc \quad (10)$$

where ϵ is the molar extinction constant and is the proportionality factor. This value depends on the molecule's chemical structure. l is the optical path length (usually 1 cm). A linear relationship is obtained when plotting the absorbance as a function of the concentration and makes it suitable for quantitative analysis. Therefore, a calibration curve was prepared to calculate the concentration of the sample.

This method was used to quantify the amount of the coupled dye after the click reaction. A five point calibration curve was prepared for each dye used with the following concentrations and corresponding wavelength maximum: 0.5 to 8 μM for FAM-alkyne (498 nm), TAMRA-alkyne (550 nm), FAM-DBCO (498 nm), AF-488 (498 nm), between 0.3 and 5 μM for Cy5-Alkyne (646 nm), and between 2.5 and 20 μM for ATE (395 nm). When it was not possible to prepare a 5-point calibration (due to material availability), a single point calibration was performed.

The measurements were performed with a Varian Cary 300 Bio and a 400 μL Suprasil® quartz cuvette (10 mm pathway).

6.2.2 Fluorescence spectroscopy (FS)

When a molecule reaches an excite state (S_1 , S_2) after the absorption of a photon different pathways exist to return to the ground state. A graphical representation of this phenomenon is clearly illustrate with a Jablonski diagram (Figure 7).

Once in a higher excitation state (S_2), the molecule loses its vibrational energy excess by internal conversions, vibrational relaxations, and collisions with other molecules, and reaches the lowest vibrational level of excited state (S_1). From this state, the molecule can reach the ground state by a) radiationless internal conversion and vibrational relaxation, or by b) losing a fluorescence photon at a higher wavelength (lower energy) [184]. This difference between the excitation and emission wavelengths

is known as the Stokes shift and it depends on the molecular structure and environment [185].

Fluorescence spectra were measured with an Agilent Cary Eclipse spectrophotometer using a 400 μL Suprasil® quartz cuvette for fluorescence or with a 96-well plate.

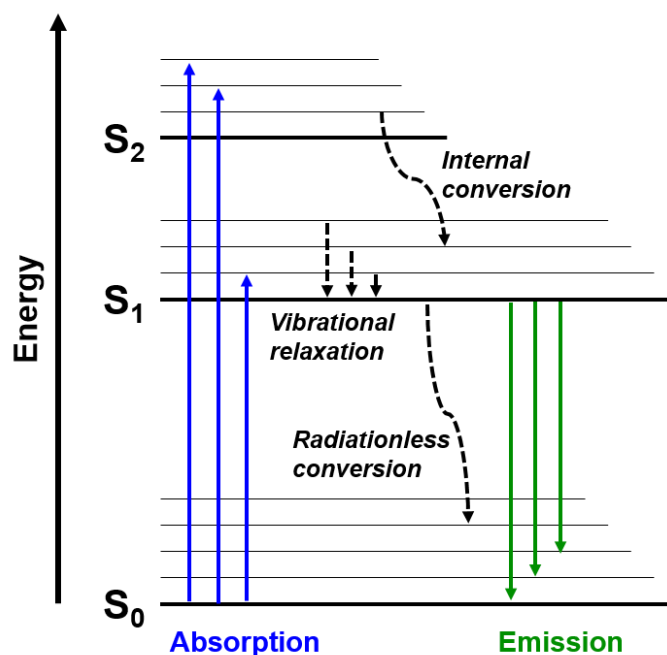


Figure 7: Jablonski diagram for fluorescence, imaged based on [184]

6.2.3 Transmission infrared spectroscopy (FT-IR)

With infrared spectroscopy, the asymmetric molecular vibration (stretching and bending modes) of covalent bonds can be analyzed as a function of the wavelength within the IR region. For ease of representation of the spectra, the wavelength is expressed as wavenumber (cm^{-1}).

The wavenumber at which the bond absorbs depend on the bond polarizability, geometry and environment. This property enables a characteristic absorption wavelength for each functional group and each molecule will exhibit a unique infrared spectra [186].

Similar to other spectroscopic methods, FT-IR spectroscopy can be used in a qualitative approach to identify functional groups or quantitative after the measurement of a proper calibration curve for a specific vibrational band.

The measurements were performed in FT-IR transmission mode to achieve a higher sensitivity. A 500-700 μL aliquot of the nanoparticles dispersion was first lyophilized to remove the water from the sample. Then 150 mg KBr (FT-IR Grade) was added to the lyophilized sample. The powders were mixed in an agate mortar, followed by the pellet pressing step, and hundred scans were recorded for the measurement.

6.2.4 Atomic absorption spectroscopy (AAS)

The elemental quantification of metals can be performed by atomic absorption spectroscopy. As each element has a unique electron configuration, it absorbs radiation at a specific wavelength. For this, the sample has to be first atomized. In this process, the metal elements found in the sample are released in an ionized vapor state into the optical pathway of the spectrophotometer. In the same pathway, the radiation of the required wavelength is emitted with a hollow cathode lamp or electrodeless discharge lamp and thus absorbed by the atoms from the sample. Similar to UV-VIS, a linear relationship between the sample absorbance and concentration is given by the Beer-Lambert Law, making it possible to perform quantitative analyses.

The calcium analysis was performed by Mrs. Kerstin Brauner and Mr. Robin Meya from the Microanalytic Lab (Labor für Mikroanalytik) of the Chemistry Faculty. The determinations were measured on a Thermo Electron AAS M-Series Spectrometer.

Prior to the measurement, an aliquot of the nanoparticles dispersion was first dissolved with HCl (1+3) and diluted with ultrapure water to an appropriate volume.

6.3 Thermogravimetric analysis (TGA)

Thermogravimetric analysis is based on the controlled heating of the sample and its simultaneous weight measurement at a high sensitivity (0.1 μg) [187]. The sample heat rate and atmosphere is also controlled by a gas flow, which can be oxidative, reductive or inert. The sample decomposition is reflected in the weight loss as the component is released from the sample. Complementary analysis from the evolved gas can be performed with a coupled FT-IR spectroscopy or MS-spectrometry.

From the thermogram (weight loss vs temperature plot) is possible to identify the sample decomposition steps, as each step will be reflected as a weight loss. In general terms, a weight loss up to 200 $^{\circ}\text{C}$ is associate to absorbed water, between 200-400 $^{\circ}\text{C}$ to organic content and above 400 $^{\circ}\text{C}$ to inorganic components transformation and decomposition. Within each of these general ranges it is possible to have more than one transition depending in the materials properties. By this method is easy to determine the organic content in an inorganic core nanoparticle like for example the amount of polymer..

The TGA analysis was performed with a Netzsch STA-449 F3 Jupiter device. The sample was heated from 30 $^{\circ}\text{C}$ to 1000 $^{\circ}\text{C}$ with a rate of 3 $^{\circ}\text{C}/\text{min}$ under an oxidative atmosphere of 254 mL min^{-1} O_2 flow. A mass near 15-20 mg was placed in an Al_2O_3 crucible holder.

6.4 Electron microscopy

Electron microscopy techniques allow to work at higher resolution compared to light or fluorescence microscopes. With these techniques an electron beam is accelerated and focused with electromagnetic lenses onto the sample.

6.4.1 Scanning electron microscopy (SEM) and Energy dispersive X-ray spectrometry (EDX)

With scanning electron microscopy an electron beam is raster scanned over the sample surface. From the scanning beam different signals can be detected and

measured: secondary electrons (SE), backscattered electrons (BSE), electron beam-induced current, cathodoluminescence, Auger electrons and X-rays [188].

Secondary electrons provides topographical information of the sample. As the electrons are emitted closer to the surface, they allow a higher resolution. On the other hand, backscattered electrons are generated from elastic scattering and originated from a deeper position of the sample reducing the achievable resolution. One advantage of BSE electrons is that the signal intensity is related to the atomic number. Elements with a higher atomic mass give a higher intensity compared to elements with lower atomic mass.

Energy dispersive x-ray spectroscopy (EDS/EDX) measures the energy of the emitted X-rays. The X-rays are generated after the incident high-energy beam removes an inner-shell electron from the sample. To fill the empty orbit an outer-shell electron transfers into the empty position. Due to the energy difference, the energy excess is emitted as an X-ray. As every element has characteristic energies, the sample composition can be analyzed.

An alternative method for SEM microscopes is to work in scanning transmission electron microscopy (STEM) mode. With this approach, the sample in a TEM grid is scanned in an equivalent way to SEM, but besides of detecting only transmitted electrons (like in TEM) other signals such, as secondary and scattered beam electrons, can be measured. A high angle annular dark field detector (HAADF) measures the scattered beam electrons at a very close position, which enables a high resolution imaging of atomic contrast [189].

An aliquot from the sample dispersion was placed on an aluminum sample holder with or without a silicon wafer. The sample was dried at room temperature and sputtered with gold-palladium to increase the sample conductivity. The images and EDX spectra were taken with a FEI Quanta 400 ESEM microscope or a Thermo Electron Corporation Apreo S microscope. The scanning electron microscopy imaging was performed by Mr. Smail Boukercha, Mrs. Ursula Giebel and Dr. Kateryna Loza from Chemistry Scanning Electron Microscopy Central Lab at the University of Duisburg-Essen.

6.4.2 Transmission electron microscopy (TEM)

In transmission electron microscopy the sample is illuminated with the electron beam. In a different way to SEM, the electron beam passes through the sample and the transmitted electrons are focused to form the image or the diffraction pattern. To produce the contrast in the image, different methods based on absorption contrast, amplitude contrast and phase contrast are available. For absorption contrast, an aperture ring after the sample is placed and it allows to detect only the electrons that have very low scattering. In phase contrast mode, the contrast is obtained from the phase change in the incident electron beam caused by the sample. Amplitude contrast is generated by the scattering of the beam caused by the material. For an amorphous material is caused by variations in the thickness and for a crystalline material by the atomic lattices planes [188]. Additionally, from the inelastic scattered electrons chemical composition of the sample can be measured [190].

To increase the sample contrast different staining methods can be used such as positive or negative staining with the help of heavy metals. With positive staining the sample structure is stained to give a better contrast with the lighter background. On the other hand, with negative staining the background near the sample is stained with heavy metal ions (caused by the repulsion of the heavy metals ions by the charged groups in the sample [191]) generating a darker background due to electron absorption [192]. Usually 1% phosphotungstic acid (pH 7.2) is used for negative staining. For positive staining solutions like uranyl acetate (pH 4) or lead citrate (pH 12) are mostly used as they react with soft or cellular structures (e.g., proteins, lipids, nucleic acids). Another approach, especially for biological material containing samples, is to perform immunostaining with antibodies coupled to metals which provides a higher contrast like gold nanoparticles [193].

With a TEM tomography is possible to create a 3D reconstruction image based on a 2D tilt series frames, which provides further tridimensional information about the sample. For this, during the imaging the sample holder is rotated, usually between $\pm 70^\circ$, and at each angle a 2D TEM projection image is captured [194, 195].

Alternatively, with cryogenic TEM (cryo-TEM) the sample drying on the TEM grid is avoided during sample preparation. With this method, drying artifacts are avoided and the sample, for example a nanoparticle dispersion, can be observed in the same state as in the dispersion.

For cryo-TEM, a sample dispersion drop is placed on the grid, and after removing the water excess by blotting with filter paper, the grid is shock frozen in a cryogenic liquid, like liquid ethane, so that the solvent stays in an amorphous form. Afterwards, the sample, sample holder and microscope are held at cryogenic temperature, usually with liquid nitrogen, to avoid the formation of ice or other artifacts due to higher temperatures [196, 197].

The transmission electron microscopy imaging was performed by Mr. Bernd Walkenfort and Dr. Mike Hasenberg from the Electron Microscopy Unit of Imaging Center Essen (IMCES), University Hospital of the University of Duisburg-Essen.

6.5 Light fluorescence microscopy

Fluorescence microscope techniques are widely used in biological applications as well in materials research, and takes advantage of fluorescent molecules or staining on the sample. These microscopes can be divided in two main categories, the widefield based microscopes and the laser confocal scanning microscopes.

Light microscopy resolution is limited by the Abbe diffraction limit [198] which is expressed as:

$$d = \frac{\lambda}{2n\sin(\alpha)} \quad (11)$$

where λ is the illumination wavelength, n is the refractive index of the medium, α is the half opening angle of the objective lens. The term $n\sin(\alpha)$ is also known as the lens aperture number (NA).

As observed from the previous expression the resolution depends on the wavelength of the source, so when moving to lower wavelengths the resolution limit decreases

although there is a physical limit. In best conditions, a resolution near half of the wavelength used is the possible maximum [198].

Further developments to overcome the classical light refraction limit lead to the so-called super-resolution microscopy (sub-diffraction). Stimulated emission depletion microscopy (STED) based in confocal scanning technique, structured illumination microscopy (SIM) and stochastic optical reconstruction microscopy (STORM) are based on wide-field microscopy systems [199]. Figure 8 shows a comparison of the resolution limits for these techniques.

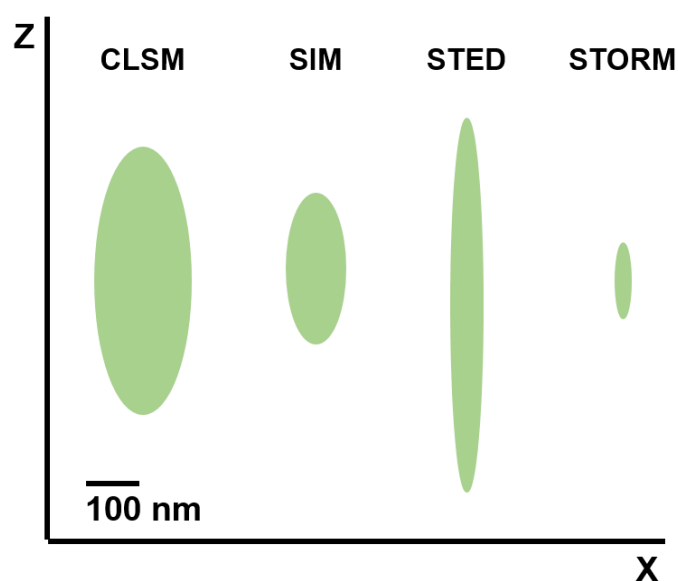


Figure 8: Comparison of the resolution capacity of different fluorescence microscopy techniques. Image based on the resolution limits from [198].

For the development of this work the following light fluorescence microscopic techniques were used: widefield fluorescence microscopy (WF), confocal laser scanning microscopy (CLSM), structured illumination microscopy and stochastic optical reconstruction microscopy. In the next sections each of these are briefly described.

6.5.1 Widefield fluorescence microscopy (WF)

Widefield fluorescence microscopes are the most common fluorescent microscopes. The main components are: the source, filter set, optical system and camera based

detector. A white light and fluorescence source is used to illuminate the sample and the working wavelength is further limited by a filter set. One important characteristic of this system is that the sample is completely illuminated at the working wavelength range and all the signals from the sample are detected simultaneously in a camera. This mechanism allows faster imaging times compared to other techniques like CLSM, although this type of illumination, detection, and filter sets have the limitation that it can cause an overlap in the detected fluorescence, when there is not enough spectral separation between the dyes. Additionally, the fluorescence detection of out of focus planes decrease the achievable resolution.

A Keyence Biorevo BZ-9000 with filters GFP-B (Ex. 470/40 nm, DM 495, BA 535/50 nm), TRITC (Ex. 540/25 nm, DM 565 nm, BA 605/55 nm), Cy5 (Ex. 628/40 nm, DM 660 nm, BA 692/40 nm), DAPI (Ex. 360/40 nm, DM 400, BA 460/50 nm), ND Filter 10 (Transmission 10%) were used. A Plan Fluor ELWD DM 20x/0.45 objective was used.

6.5.2 Confocal laser scanning microscopy (CLSM)

This type of microscope involves a laser punctual illumination system. Specific wavelengths lasers or white-lasers (tunable wavelength within the UV-Vis region) are used. As the illumination is punctual, the illumination and detection depths are also controlled [200]. By scanning the sample on a line by line basis (raster), the information of the complete sample is achieved pixel by pixel. Beside these aspects, the fundamental factor in CLSM, is the confocal aperture (pinhole) before the detector, which allows only the plane in-focus to be detected and removes the out-of-focus fluorescence coming from the sample. This aspect improves significantly the capable resolution compared to wide-field microscopy.

Another benefit from this technique is the capability to perform optical sectioning of the sample (z-stack). Due to the good depth precision control is possible to image at different levels in the sample by a precise movement of the stage at a determined step size [201]. Then from the z-stack images is possible to generate a projection of the slides or a tridimensional reconstruction.

A Leica TCS SP8 AOBS Confocal Microscope and Leica TCS SP8X FALCON Microscope were used from the Imaging Centre Campus Essen (ICCE). The following laser wavelengths were available: 405 nm, 488 nm, 514 nm, 561 nm, 633 nm and a pulsed laser WLL (470-670 nm). A HCX PL Apo 63X/1.4 oil immersion objective and a HC PL APO UVIS CS2 63X/1.2 water immersion objective were used.

6.5.3 Structured illumination microscopy (SIM)

SIM super-resolution microscopy is based on a wide-field microscope and it applies a patterned illumination during the sample illumination, which is generated by two laser beams that go through the objectives back-focal aperture [202]. By imaging at different positions and orientations the pattern illumination will produce moiré fringes caused by the illumination interference with the fine structures of the sample [203, 204]. This allows that the higher spatial frequency information from the details moves to lower frequencies becoming detectable [205]. The image reconstruction process involves the Fourier transformation of the data and the image frequencies are then processed to separate the lower frequencies from higher frequencies (higher resolution) contribution to apply the corrections. After processing usually a two factor improvement compared to CLSM is achieved by this method [202].

A Zeiss Elyra PS.1 Microscope was used from the Imaging Center Essen (IMCES). The following laser wavelengths were available: 405 nm, 488 nm, 561 nm, 642 nm and filter sets BP 420-480 nm LP 750 nm, BP 495-575 nm LP 750 nm, BP 570-650 nm LP 750 nm and BP 642 LP 655. An alpha Plan-Apochromat 100x/1.46 oil immersion objective was used.

6.5.4 Stochastic Optical Reconstruction Microscopy (STORM)

A different approach for super-resolution microscopy are the single-molecule detection methods. These methods, as the name suggests, are based on the detection of single emitting molecules which are captured over different (thousands) frames with a high sensitivity camera, like an EMCCD camera.

As the imaging is based on a molecule localization basis, the achievable precision is then dependent on the number of photons that the molecule emits before getting into the dark state. Thus theoretically higher emitting dyes allow to have a better localization precision when compared to lower emitting molecules [206].

One important aspect that makes these methods applicable is that the emitting molecules should not emit all at the same time, so that the positions of each one can be correctly localized (resolved). Different approaches to control emitting process to have an on/off state of the dye lead to the development of slightly different techniques. Stochastic optical reconstruction microscopy (STORM) is a technique within the molecule localization microscopy methods (SMLM).

With the STORM approach the dye is usually induced into the dark state using a high power laser. To control the activation and blinking state of the dye once it reactivates from the dark state, the sample is usually contained with an imaging buffer solution. An oxygen scavenging system based on glucose oxidase with catalase is used with a primary thiol additive (usually MEA or β ME). The composition of imaging buffer influences the number of photons and switching cycle events of the dyes and its effect varies with the dye structure and buffer composition [207].

The detected intensity spots are then adjusted by a Gaussian fit to find the localization position. This procedure is repeated over the different frames of the dye switching cycle to generate the reconstructed image with a sub-diffraction resolution [208]. Figure 9 shows a simplified general representation of the STORM method.

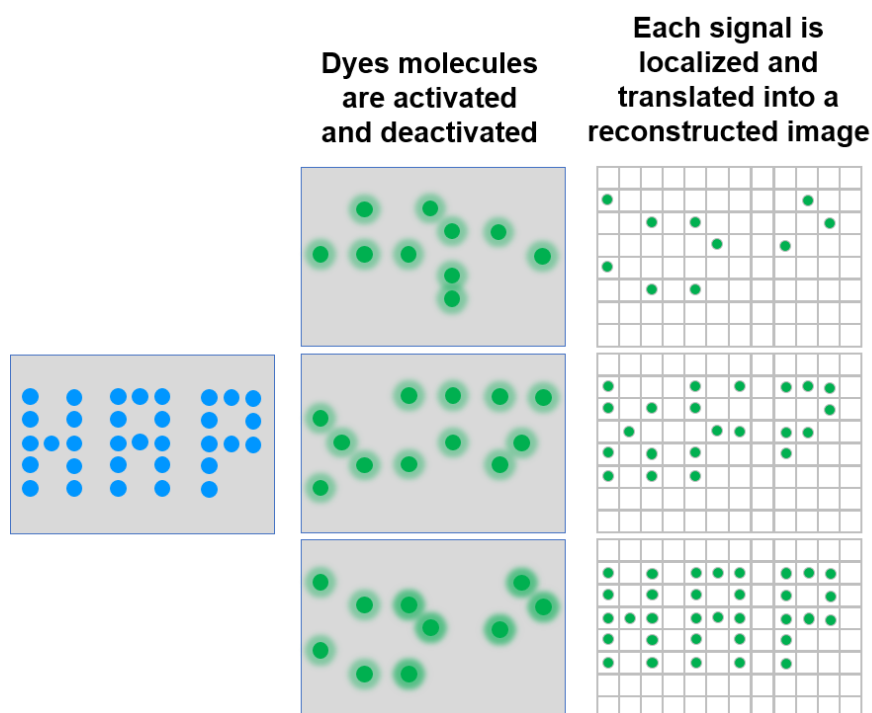


Figure 9: Simplified general representation of the stochastic optical reconstruction microscopy (STORM) method.

A Zeiss Elyra PS.1 Microscope was used from the Imaging Center Essen (IMCES). The following laser wavelengths were available: 405 nm, 488 nm, 561 nm, 642 nm and filter sets BP 420-480 nm LP 750 nm, BP 495-575 nm LP 750 nm, BP 570-650 nm LP 750 nm and BP 642 LP 655. An alpha Plan-Apochromat 100x/1.46 oil immersion objective was used.

To make the oxygen scavenging imaging buffer the following solutions were prepared [207, 209].

Buffer 1 (10 mM Tris (pH 8) + 50 mM NaCl)

To a 1 mL of Buffer (Tris Buffer 50 mM, pH 8 + 10 mM NaCl) was added 14.6 mg NaCl and diluted to 5 mL with H₂O.

Buffer 2 (50 mM Tris (pH 8) + 10 mM NaCl + 10% Glucose)

To 10 mL of Buffer (Tris Buffer 50 mM, pH 8 + 10 mM NaCl) were added 1 g Glucose.

Mercaptoethylamine (MEA) 0.1 M solution

MEA (11.3 mg, 0.097 mmol) was measured and dissolved with 1 mL DPBS.

Glox-solution

To prepare 100 μL solution, in an Eppendorf tube 5.6 mg Glucose Oxidase was measured and 20 μL catalase (17 mg/mL) was added. Then 80 μL of Buffer 1 was added. The solution was centrifuged with a mini table top centrifuge (4,000 rpm) for 2 minutes and the supernatant was used.

Imaging buffer

To prepare the imaging buffer 1.4 μL Glox Buffer were added into an Eppendorf tube, followed by 14 μL 0.1 MEA solution. Finally, 124 μL Buffer B was added. The solution was vortexed gently and immediately used. The preparation volume can be adjusted according to the imaging required volume.

For imaging self-made flow chamber were prepared according to the procedure described in [210]. The cover slide and slide were washed according to section 6.5.5. Figure 10 shows a representative diagram. In general, the stained cover slide was taken from the storage solution (DPBS) and attached to the adhesive band on the slide. The slide was then washed three times with the imaging buffer, and filled one more time for imaging. No bubbles should be inside the chamber.

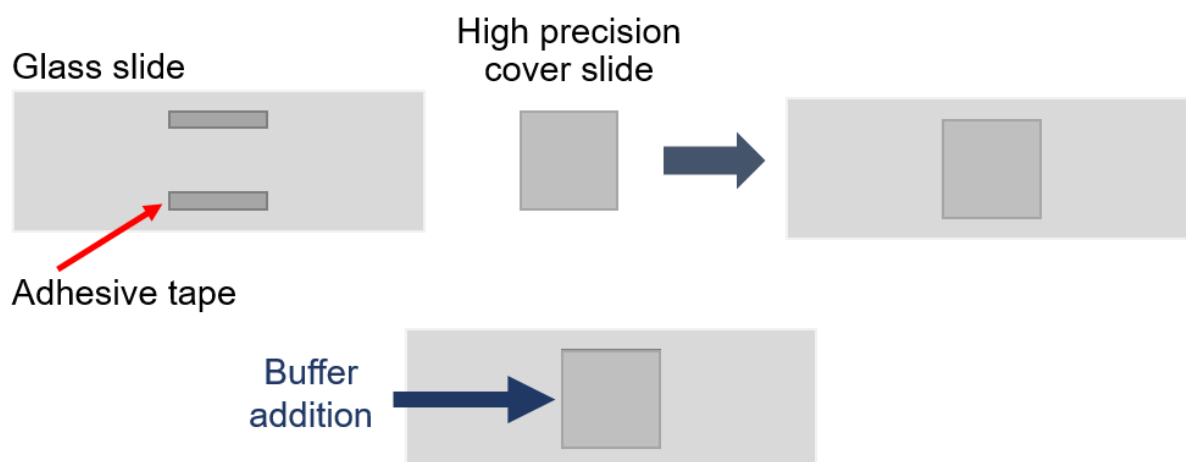


Figure 10: Description diagram of a self-made flow chamber for imaging.

As an alternative to the self-made flow chambers commercial imaging chambers or dishes were used. In this case, the storage solution was removed and washed three times with the imaging buffer. Then it was filled one more time with the imaging buffer and the lid was placed to reduce additional air to come into contact with the sample.

6.5.5 Sample preparation for fluorescence microscopy

Cover slides and slides cleaning step

High precision cover slides (170 ± 5) μm were used for all the experiments to provide a uniform surface at the microscope illumination. Before their application the slides and cover slides are washed with an alkaline basis method according to [210]. The used procedure is described here.

The slides or cover slides were placed in the slides holder inside a Beaker, ethanol (99.8%) was added until covering all the surface, and then put for 10 minutes in a sonicator bath. Afterwards, the ethanol was removed and KOH 1M was added until all the surface was covered. The materials were sonicated for 10 minutes and then rested for 60 min. Finally, the KOH solution was removed and the slides were fully washed with filtered Millipore water. The slides were kept in a covered holder and then dried in a vertical position at 60 °C. The slides were stored at RT. Alternatively, the slides were also stored under filtered ethanol (99.8%) to protect from the dust.

For the imaging chambers (glass bottom) used for super-resolution imaging, the wells were washed three times with filtered Millipore water, followed by 500 μL HCl (3+1) for 15 minutes. Then five washing steps were performed with 500 μL Millipore water. Finally, the wells were rinse with ethanol 70% for 10 minutes.

The glass surface was coated with poly-D-lysine to increase the cell adherence. For this, 200 μL of 0.2% poly-D-lysine in 150 mM NaCl solution (sterile filtered) were given to the cover slide or well for 15 minutes at room temperature. Then it was washed 3 times with sterile H₂O before seeding the cells.

Sample fixation and staining

Cell were fixed with 4% paraformaldehyde at room temperature for 10 min followed by three times washing with DPBS. The following staining procedures were performed depending on the application.

Cell nucleus

The cell nucleus was stained with DAPI or Hoechst solutions. The Hoechst 33342 stock solution (Cat. H3570, Invitrogen) was diluted 0.5 μL in 100 μL DPBS. From this solution, 8 μL was added to the well with 400 μL DPBS and incubated for 10 min or 5 min with permeabilized membrane. DAPI stock solution (1 mg/mL, Cat. 62248, Thermo Scientific), was diluted 0.5 μL in 500 μL DPBS. From this solution 10 μL was added to the well with 400 μL DPBS and incubated for 10 min. After incubation, the cells were washed 3 times with DPBS with 2 minutes each washing step.

Cell membrane

The cell membrane was stained with Wheat Germ Agglutinin (WGA-CF568). The cells were washed with Hank's balanced salt solution (HBSS) two times. Then 2 μL WGA-CF568 stock solution (1 mg/mL) was diluted with 400 μL HBSS buffer and added to the well. Cells were incubated 10 minutes and then washed twice with HBSS buffer.

Actin filaments (F-actin)

To stain the filaments AlexaFluor® 488 or 647 phalloidin was used. The cell was permeabilized with Triton X-100 0.1% in DPBS for 5 minutes. Then the wells were washed two times with DPBS. The phalloidin stock solution was diluted 5 μL of the stock solution into 180 μL DPBS + 20 μL BSA 10% and added to the well. The staining was done for 20 minutes followed by two washes with DPBS.

Lysosome

To stain for lysosomes a two-step immunostaining was performed, first with anti-Lamp1 antibody (host mouse, ab25630, abcam) that detects Lamp1 protein in the lysosome membrane, second with Goat anti-mouse IgG H&L AlexaFluor® 647 (ab150115, abcam) as labelled antibody.

The cells were permeabilized with 0.5% saponin for 10 min followed by three washings with DPBS of 5 minutes each. To block for unspecific binding a blocking solution was prepared, which contained: 1% BSA, 22.52 mg/mL glycine, and 0.1% Tween 20 in DPBS. The cells were incubated for 30 minutes with the blocking solution, and after this time the solution was removed.

To stain with the first antibody, the stock anti-Lamp1 antibody was diluted 1:250 with a DPBS solution that contained 1% BSA and 0.1% Tween 20. The diluted antibody was added to the well and incubated for 1 hour at room temperature. After the incubation the well was washed 3 times with DPBS for five minutes each.

To stain with the second antibody, the stock anti-mouse IgG-AF647 antibody was diluted 1:500 with a DPBS solution that contained 1% BSA and 0.1% Tween 20. The diluted antibody was added to the well and incubated for 1 hour at room temperature. After the incubation the well was washed 3 times with DPBS and 5 minutes per wash.

Sample mounting

After the last staining step the cover slide with the sample was mounted on the slide with Fluoromount-G™ mounting media. The slide was dried at room temperature protected from light during 4-6 hours and later sealed with nail polish. The slides were stored at 4 °C until imaging. Additionally, fixed samples in well-chambers, dishes or slides for STORM were kept with DPBS buffer at 4 °C.

6.6 Cell culture related methods

6.6.1 Cell viability (MTT Test)

Cell viability can be determined quantitatively by the MTT test [211]. This method is based on the metabolic reduction of (3-(4,5-dimethylthiazol-2-yl)-2,5-diphenyltetrazolium bromide (MTT) by NADH and NADPH dependent enzymes in living cells. MTT compound is yellow and after reduction becomes purple (formazan) and insoluble. The formazan crystals are dissolved with a solvent, usually DMSO, and the absorbance measured [212]. Due to this change color is possible to follow and quantify the cell viability.

The experimental parameters for this assay with the samples are described in sections 7.8.2 and 7.9.2.

6.6.2 Endotoxin assay

Endotoxins are found in the outer membrane of gram-negative bacteria (*e.g.*, *E. coli*, *P. aeruginosa*), and are also called lipopolysaccharides (LPS) because of its chemical structure [213]. They are composed of three linked regions, the lipid A and the oligosaccharide core which are highly conserve within the bacterial strains, and the O-specific polysaccharide, that determines the serological specificity [214]. LPS can bind to CD14 and activate TLR4 receptor in cells, which induces the secretion of pro-inflammatory cytokines [215].

Limulus Amebocyte Lysate (LAL) assay is frequently used for endotoxin quantification and different detection methods are available *e.g.*, gel clot, turbidimetric, and chromogenic [216].

In the chromogenic method, the LPS in the sample activates the proenzymes in LAL that can cleavage the p-nitroaniline (pNA) from the chromogenic substrate (Ac-Ile-Glu-Ala-Arg-pNA) generating a yellow color. The measured absorbance is proportional to the amount of endotoxin in the sample, and with an appropriate calibration curve the concentration can be determined. Two different detection approaches are suitable for this method by endpoint or kinetic. With the first one, the reaction is stopped after the acidification of the medium or a preset time and the absorbance is measured. With the second one, the reaction is followed until an absorbance value is reached. In this case the time required is inversely proportional to the amount of endotoxins in the sample [217].

The endotoxin assay were performed with a Pierce™ LAL Chromogenic Endotoxin Quantitation Kit (Thermo Scientific, P/N 88282) and with an Endosafe® nexgen-PTS spectrophotometer (Charles River). In both cases the manufacturer procedure was followed.

To prepare endotoxin-free materials the following clean-up procedures were followed:

Glassware

- Clean glassware was heated for 4 hours at 200 °C. Endotoxins are heat resistant, so a higher temperature than the 121 °C autoclave method is required.

Plastic and other materials

- Preferentially new endotoxin-free plastic materials were used.
- For cleaning the peristaltic pump lines and ultracentrifuge tubes, the following procedure was used:
 - First, the lines or tubes were rinsed with 10 mL endotoxin-free water. A washing solution of 15 mL (or 25 mL for tubes) of NaOH 2M solution during 30-60 minutes were applied. Followed by rinsing with endotoxin-free water.
 - Next, 3.5% H₂O₂ in water solution was given under the same previous conditions. Followed by rising with endotoxin-free water.
 - Finally, the materials were rinsed with 70% ethanol and let them dry.

6.6.3 Enzyme-linked immunosorbent assay (ELISA)

ELISA assays are a widespread technique that is based on the antigen-antibody interaction for the detection and quantification of proteins, antibodies, etc. Different ELISA methods are available, such as indirect, competitive, antibody-sandwich, among others [218].

Antibody-sandwich method has the advantage to be more sensitive and selective. In this case, the specific antibody is first adhered to the surface of a 96-well plate. The antigen in the sample will be recognized by the antibody, and the protein is then captured. Unbound antigens are washed out and a second antigen-specific antibody conjugated to an enzyme is added and binds the already captured antigen. Then, the substrate for enzyme is given, and after the incubation the substrate hydrolysis degree is measured. Thus, the more hydrolyzed substrate is measured the larger the amount of antigen in the sample [219]. With an appropriate calibration curve the concentration can be calculated.

The ELISA assays were performed according to the manufacturer procedure.

7 Experimental section

7.1 Materials and reagents

7.1.1 Chemical Reagents

Reagent	Company	Purity
(3-Azidopropyl)triethoxysilane (APTES)	SelectLab Chemicals	97 %
(3-Mercaptopropyl)trimethoxysilane (MPS)	Sigma-Aldrich	95 %
Aminoguanidine hydrogen carbonate	Alfa Aesar	98 %
Ammonia solution 30%	Carl Roth	p.a.
Branched polyethyleneimine (PEI), Mw= 25,000 g/mol	Sigma-Aldrich	-
Calcium lactate pentahydrate	Sigma-Aldrich	p.a.
Copper sulfate pentahydrate	Sigma-Aldrich	p.a.
Diammonium hydrogenphosphate	VWR Life Science	p.a.
Dimethyl sulfoxide (DMSO)	Carl Roth	≥ 99.5 %
Ethanol (absolute)	Fischer Chemicalr	≥ 99.8%
Polyethyleneimine-Cy5 (PEI-Cy5), Mw= 25,000 g/mol	Surflay	-
Propargyl-N-hydroxysuccinimidyl ester	Sigma-Aldrich	≥ 88 %
Sodium Azide	Sigma-Aldrich	99 %
Sodium carboxymethyl cellulose (CMC), Mw=90,000 g/mol	Sigma-Aldrich	-
Sodium L-ascorbate	Sigma-Aldrich	≥ 99 %
Sulfosuccinimidyl-trans-4-(N- maleimidomethyl)cyclohexane-1-carboxylate (Sulfo-SMCC)	Merck	≥ 94 %
Tetraethoxysilane (TEOS)	Sigma-Aldrich	98 %
Trehalose	VWR Life Science	≥ 98 %
Tris(3-hydroxypropyltriazolylmethyl)amine (THPTA)	Sigma-Aldrich	95 %

Reagents were used as received without further purification.

7.1.2 Labelling Dyes

Dye	Short Name	Company
3',6'-Dihydroxy-3-oxo-N-(prop-2-yn-1-yl)-3H-spiro[isobenzofuran-1,9'-xanthene]-5-carboxamide. Fluorescein alkyne, 5-isomer	FAM-alkyne	Lumiprobe
5-carboxytetramethylrhodamine alkyne	TAMRA-alkyne	Lumiprobe
AlexaFluor™ 488 alkyne (Invitrogen)	AF488-alkyne	Invitrogen
AlexaFluor™ 647 alkyne (Invitrogen)	AF647-alkyne	Invitrogen
Dibenzylcyclooctyne-PEG4-5/6-fluorescein	DBCO-PEG4-5/6-FAM	Jena Bioscience
Sodium 3,3-dimethyl-1-[6-oxo-6-(prop-2-yn-1-ylamino)hexyl]-2-[(1E,3E,5E)-5-(1,3,3-trimethyl-5-sulfonatoindolin-2-ylidene)penta-1,3-dien-1-yl]-3H-indol-1-ium-5-sulfonate. Sulfo-cyanine5 alkyne	Cy5-alkyne	Lumiprobe

7.1.3 Cell culture reagents

Reagent	Company
(4,5-dimethylthiazol-2-yl)-2,5diphenyl-tetrazolium bromide (MTT)	Invitrogen
Bovine serum albumin (BSA)	SERVA Electrophoresis
Dulbecco's modified Eagle's medium (DMEM)	Invitrogen
Dulbecco's phosphate-buffered saline (DPBS)	Invitrogen
Elisa Kit TNF-a (ab100747)	abcam
Fetal bovine serum (FBS)	Invitrogen
Glycine	Biomol
Hank's balanced salt solution (HBSS)	Invitrogen
Lipofectamine 2000	Invitrogen
Penicillin	Invitrogen
Poly-L-lysine	Sigma-Aldrich
Saponin	Sigma-Aldrich
Sodium pyruvate	Invitrogen
Streptomycin	Invitrogen
Triton® X-100	Sigma-Aldrich
Tween 20®	Sigma-Aldrich
Ultrapure distilled water (DNase/RNase free)	Invitrogen

7.1.4 Adjuvants, plasmids and siRNA

Reagent	Company
BMP-7-pCMV6-XL4	OriGene
CpG (ODN 1826) (5'-TCCATGACGTTCTGACGTT-3')	InvivoGen Microsynth
Flagellin	Provided by Dr. Huimin Yan Lab
p30 peptide (FNNFTVSFWLRVPKVASHLE-COOH)	Peptides and Elephants
pcDNA3-eGFP	-
pcDNA3-mCherry	-
pHBsAg-DNA	Provided by Dr. Huimin Yan Lab
TNF- α^* -siRNA (non-Target) (5'-UGGUUUACAUGUUGUGUGA-3')	Dharmacon
TNF- α -siRNA (Target) (5'-GCCGAUGGGUUGUACCUUG-3')	Dharmacon
VEGF-A-pCMV6-XL5	OriGene

7.1.5 Cell staining reagents

Reagent	P/N	Company
Alexa Fluor™ 488 Phalloidin	A12379	Invitrogen
Alexa Fluor™ 647 Phalloidin	A22287	Invitrogen
Anti-Lamp1 antibody	ab25630	abcam
DAPI	62248	Thermo Scientific
Fluoromount-G™	00-4958-02	Invitrogen
Goat anti-mouse IgG H&L AlexaFluor® 647	ab150115	abcam
Hoechst	33342	Invitrogen
Wheat Germ Agglutinin (WGA-CF568)	29077	Biotium

7.1.6 Instruments and devices

Instrument	Model	Company
Atomic absorption spectrometer	M-Series AA	Thermo Electron Corporation
Centrifuge	Heraeus Fresco 21	Thermo Scientific
Centrifuge	Heraeus Multifuge X1R	Thermo Scientific
Centrifuge	5430 R	Eppendorf
Centrifuge	Rotofix 32A	Hettich
Confocal laser scanning microscope	TCS SP8 AOBS	Leica
Confocal laser scanning microscope	TCS SP8X FALCON	Leica
Dynamic light scattering (DLS) and ζ - potential	Nano ZS ZEN 3600	Malvern
Endotoxin spectrophotometer	Endosafe nexgen-PTS	Charles River
Fluorescence microscope	BZ 9000	Keyence
Fluorescence spectrophotometer	Cary Eclipse	Agilent Technologies
Infrared spectrophotometer	Vertex 70	Bruker
Lyophilizer	Alpha 2-4 LSC	Christ
Microplate photometer	Multiskan FC	Thermo Fischer Scientific
Microvolume UV-Vis spectrophotometer ("Nanodrop")	DS-11 FX+	DeNovix
pH-meter	pH340	WTW
Scanning electron microscope	Quanta 400 ESEM	FEI
Scanning electron microscope	Apreo S	Thermo Electron Corporation
Sonotrode	UP50H	Heilscher
Super-resolution microscope	ELYRA PS.1	Zeiss
Thermogravimetric analyzers	STA-449 F3 Jupiter	Netzsch
Transmission electron microscope	JEM-1400+ 120KV TEM with cryo and tomographic goniometer	JEOL

Ultracentrifugation	Sorvall Series	WX	Ultra	Thermo Electron Corporation
Ultrapure water system	Purelab			ELGA
Ultrasonic bath	S10			Elmasonic
Ultraviolet-visible spectrophotometer (UV-Vis)	Cary 300 Bio			Varian

In the following section are described the procedures for the calcium phosphate nanoparticles synthesis used in the following sections.

7.2 Calcium phosphate nanoparticle synthesis

7.2.1 Synthesis of silica terminate calcium phosphate nanoparticles (CaP/PEI/SiO₂)

The synthesis of calcium phosphate nanoparticles and the silica coating is based on the method described by Kozlova et. al. [26]. This method corresponds to the precipitation of calcium phosphate and its stabilization using polyethyleneimine.

To a stirred vessel with 20 mL ultrapure water, calcium lactate (18 mM, pH 10), diammonium phosphate (10.8 mM, pH 10) and PEI (2 g/L) solutions were simultaneously pumped for one minute with a volume ratio of 5 mL: 5 mL: 7 mL with a peristaltic pump. The dispersion was stirred for 20 min.

The silica coating on the nanoparticle is based on the Stöber method [220] and adapted by Kozlova et. al. [26]. From the previous dispersion, 10 mL were taken and added to a mixture of 40 mL ethanol, 50 μ L tetraethoxysilane and 100 μ L aqueous ammonia solution (7.8 wt.%). The reaction was stirred at room temperature for 14 - 16 h (overnight). After this reaction time and to isolate the nanoparticles, the dispersion was ultracentrifugated at 66,000 g for 30 min. The supernatant was removed and the nanoparticles were redispersed in 10 mL water with ultrasonication (Cycle 0.8, amplitude 70%, 30s).

7.2.2 Synthesis of azide terminate calcium phosphate nanoparticles (CaP/PEI/SiO₂-N₃)

To the silica terminate nanoparticles a further silanization reaction was performed to introduce the azide groups into the nanoparticles surface.

For this, 10 mL of silica-modified nanoparticle dispersion was taken and added to a mixture of 40 mL ethanol, either 50, 100 or 150 μ L (3-azidopropyl)triethoxysilane and 50 μ L aqueous ammonia solution (7.8 wt.%). This reaction was stirred for 8 h, and after this time the nanoparticles were isolated by ultracentrifugation (66,000 g, 30 min) and redispersed in 5 mL water.

7.3 Click Chemistry surface modification

7.3.1 CuAAC click reaction with alkyne terminated molecules

CaP/PEI/SiO₂-FAM and CaP/PEI/SiO₂-Alexa-488

100 μ L FAM-alkyne or Alexa-488-alkyne in DMSO (200 μ M), 307 μ L H₂O, 1.6 μ L NaOH (0.1 M in H₂O), 8 μ L of an aqueous solution containing CuSO₄ (40 μ M) and THPTA (200 μ M), 83 μ L aqueous aminoguanidine (1 mg mL⁻¹), and finally 83 μ L sodium ascorbate (100 mM) were added to 1 mL nanoparticle dispersion contained in a 2.0 mL Eppendorf Tube. The tube was closed and stirred for 60 min.

To isolate the nanoparticles, the reaction mixture was centrifuged at 30,000 g, and the product was washed once with 1 mL 1:3 DMSO:H₂O (v.v) and then once with 1 mL H₂O. The nanoparticles were then redispersed in 1 mL water.

CaP/PEI/SiO₂-FAM-TAMRA

100 μ L TAMRA-alkyne in DMSO (200 μ M), 307 μ L DMSO, 1.6 μ L NaOH (0.1 M in H₂O), 8 μ L of an aqueous solution containing CuSO₄ (40 μ M) and THPTA (200 μ M), 83 μ L aqueous aminoguanidine (1 mg mL⁻¹) and finally 83 μ L aqueous sodium ascorbate (100 mM) were added to 0.9 mL of previously FAM-labelled nanoparticles. The tube was closed and stirred for 60 min.

To isolate the nanoparticles the reaction mixture was centrifuged at 30,000 g, and the product was washed once with 1 mL 1:3 DMSO:H₂O (v.v) and once with 1 mL H₂O. The nanoparticles were redispersed in 1 mL water.

CaP/PEI/SiO₂-FAM-Cy5

100 μ L Cy5-alkyne in DMSO (200 μ M), 307 μ L H₂O, 1.6 μ L NaOH (0.1 M in H₂O), 8 μ L of an aqueous solution containing CuSO₄ (40 μ M) and THPTA (200 μ M), 83 μ L aqueous aminoguanidine solution (1 mg mL⁻¹) and finally 83 μ L aqueous sodium ascorbate solution (100 mM) were added to 1 mL of previously FAM-labelled nanoparticles. The tube was closed and stirred for 60 min.

To isolate the nanoparticles, the reaction mixture was centrifuged at 30,000 g, and the product was washed once with 1 mL 1:3 DMSO:H₂O (v.v) and once with 1 mL H₂O. The nanoparticles were redispersed in 1 mL water.

CaP/PEI/SiO₂-AF488-AF647

100 μ L AF-647 in DMSO (200 μ M), 307 μ L H₂O, 1.6 μ L NaOH (0.1 M in H₂O), 8 μ L of an aqueous solution containing CuSO₄ (40 μ M) and THPTA (200 μ M), 83 μ L aqueous aminoguanidine solution (1 mg mL⁻¹) and finally 83 μ L aqueous sodium ascorbate solution (100 mM) were added to 1 mL of previously AF488-labelled nanoparticles. The tube was closed and stirred for 60 min.

To isolate the nanoparticles, the reaction mixture was centrifuged at 30,000 g, and the product was washed once with 1 mL 1:3 DMSO:H₂O (v.v) and once with 1 mL H₂O. The nanoparticles were redispersed in 1 mL water.

CaP/PEI/SiO₂-ATE

100 μ L ATE in DMSO (200 μ M), 307 μ L DMSO, 1.6 μ L NaOH (0.1 M in H₂O), 8 μ L of an aqueous solution containing CuSO₄ (40 μ M) and THPTA (200 μ M), 83 μ L aqueous aminoguanidine (1 mg mL⁻¹), and finally 83 μ L sodium ascorbate solution (100 mM in H₂O) were added to 0.9 mL of the nanoparticle dispersion. The reaction flask was closed and stirred for 60 min.

To isolate the nanoparticles, the reaction mixture was centrifuged at 30,000 g, and the product was washed once with 1 mL 1:1 DMSO:H₂O (v:v) and then once with 1 mL H₂O. The nanoparticles were redispersed in 1 mL of water.

CaP/PEI/SiO₂-BSA

To include the alkyne functional group into BSA, the protein was first reacted with Propargyl-N-hydroxysuccinimidyl.

To 1.1 mg Propargyl-N-hydroxysuccinimidyl were added 420 μ L H₂O. Then 40 μ L DMSO was added to dissolve completely the molecule. From this solution, 60 μ L were taken and added to 500 μ L BSA-647 solution in DPBS (1 mg mL⁻¹). The tube was closed, mixed and incubated at 4 °C for 2h. After this time, the protein was purified using a 3 kDa Amicon® Filter.

In brief the procedure with the Amicon® Tube purification is described. The filter was first washed with 400 μ L DPBS solution and centrifuged at 14,000 g for 10 min. Then the BSA-crosslinker solution was added and centrifuged for 15 min at 14,000 g. The filter was washed with 400 μ L DPBS and centrifuged again at 14,000 g for 10 min. Finally, the protein was recovered in a new tube after 2 min centrifugation at 1,000 g. The volume was diluted to 500 μ L with DPBS.

50 μ L activated BSA-647-crosslinker in H₂O (1 mg mL⁻¹), 0.8 μ L NaOH (0.1 M in H₂O), 10 μ L of an aqueous solution containing CuSO₄ (40 μ M) and THPTA (200 μ M), 100 μ L aqueous aminoguanidine (1 mg mL⁻¹), and finally 100 μ L sodium ascorbate (100 mM) were added to 1.5 mL nanoparticle dispersion contained in a 2.0 mL Eppendorf Tube. The tube was closed and stirred for 60 min.

To isolate the nanoparticles, the reaction mixture was centrifuged at 30,000 g, and the product was washed twice with 1 mL H₂O. The nanoparticles were then redispersed in 1.1 mL water.

7.3.2 SPAAC click reaction

CaP/PEI/SiO₂-FAM (SPAAC)

100 μL DBCO-PEG4-5/6-FAM in DMSO (200 μM), 330 μL DMSO, 1.5 μL NaOH (0.1 M in H_2O) were added to 1 mL nanoparticle dispersion contained in a 2.0 mL Eppendorf Tube. The tube was closed and stirred for 60 min.

To isolate the nanoparticles the reaction mixture was centrifuged at 30,000 g, and the product washed once with 1 mL 1:3 DMSO: H_2O (v:v) and then once with 1 mL H_2O .

7.4 m_{cherry} plasmid loaded calcium phosphate nanoparticles

To 1 mL of CaP/PEI nanoparticles were added either 100 μL of plasmid m_{cherry} (1 mg mL^{-1}) dissolved in water, and stirred for 30 min at room temperature. After the 30 min, the supernatant was measured by UV microvolume spectroscopy to determine the amount of plasmid m_{cherry} loaded on the nanoparticle. Next, a silica coating was added to the nanoparticle. For this, 1 mL of nanoparticle dispersion were added to 4 mL ethanol, 5 μL TEOS and 10 μL aqueous ammonia solution (7.8 wt.%). The reaction was stirred for 16 h at room temperature. After this time, the nanoparticles were isolated by ultracentrifugation at 66,000 g for 30 min and redispersed in 1 mL water with 4 s ultrasonication (cycle 0.8 and amplitude 70%).

To couple the dye to the surface by click reaction the procedures described in 7.3.1 and 7.3.2 were followed using AF-488 alkyne and DBCO-PEG4-5/6-FAM dyes.

7.5 Synthesis of calcium phosphate nanoparticles for the experiments discussed in section 8.4

7.5.1 Env-Monomer and Env-Trimer coupled nanoparticles

Env-Monomer and Env-Trimer were provided by the research group of Prof. Dr. Klaus Überla and PD Dr. Vladimir Temchura, from the Institute of Clinical and Molecular Virology from University Hospital Erlangen of Friedrich-Alexander University Erlangen-Nürnberg (FAU). The material was used as received.

Non-specific coupling

To couple the Env-Monomer or Env-Trimer non-specifically to calcium phosphate nanoparticles Sulfo-SMCC (sulfosuccinimidyl 4-(N-maleimidomethyl)cyclohexane-1-carboxylate) crosslinker was used. This crosslinker reacts with the amine groups found in the protein and at the other end with the thiol functional group located on the nanoparticle surface. To modify the protein and synthesize the nanoparticles the following procedure was used.

Thiol terminate calcium phosphate nanoparticle (CaP/PEI/SiO₂-SH)

10 mL of silica-modified nanoparticle dispersion (from section 7.2.1) was taken and added to a mixture of 40 mL ethanol and 50 μ L (3-mercaptopropyl)trimethoxysilane. The reaction was stirred for 8 h, and after this time the nanoparticles were isolated by ultracentrifugation (66,000 g, 30 min) and redispersed in 10 mL water.

Crosslinker conjugation to protein

2.5 mg sulfo-SMCC were dissolved with 1.4 mL H₂O. From this solution, 300 μ L were taken and added to 600 μ L Env-Trimer or Env-Monomer solution in DPBS (1 mg mL⁻¹). The tube was closed, vortexed and incubated at 4 °C for 2 h. After this time, the protein was purified using a 3 kDa Amicon® Filter as previously described.

Protein coupling to nanoparticles

330 μL activated protein (1 mg mL^{-1}) was given to 4 mL CaP/PEI/SiO₂-SH nanoparticles in an Eppendorf Tube (1.5 mL), mixed and incubated for 24 h at 4 °C. After this time, the tube was centrifuged at 21,000 g at 8 °C, and the nanoparticles washed once with 1 mL H₂O. The nanoparticles were redispersed in 4 mL of water.

Specific coupling

An alkyne-terminate Env-Trimer was bonded to azide terminate calcium phosphate nanoparticles by CuAAC click chemistry. The CaP/PEI/SiO₂-N₃ were prepared according to 7.2.2.

50 μL Env-PEG3-Alkyne in H₂O (1 mg mL^{-1}), 0.7 μL NaOH (0.1 M in H₂O), 7.3 μL of an aqueous solution containing CuSO₄ (40 μM) and THPTA (200 μM), 77 μL aqueous aminoguanidine (1 mg mL^{-1}), and finally 73 μL sodium ascorbate (100 mM) were added to 1 mL azide-terminate calcium phosphate nanoparticle dispersion contained in a 2.0 mL Eppendorf Tube. The tube was closed and stirred for 60 min.

To isolate the nanoparticles, the reaction mixture was centrifuged at 21,000 g at 8 °C and the product was washed with 1 mL H₂O. The nanoparticles were then redispersed in 0.8 mL water.

CpG or p30 loaded nanoparticles

CpG (5'-TCCATGACGTTCTGACGTT-3') or p30 (FNNFTVSWLVRPKVASHLE-COOH) loading was added into the nanoparticles before the silica coating. To 1 mL of CaP/PEI nanoparticles were added 40 μL CpG (1 mg mL^{-1}) or 60 μL p30 (1 mg mL^{-1}) dissolved in water, and stirred for 30 min at room temperature. After this time an aliquot was taken to determine the adjuvant concentration in the supernatant by Nanodrop.

To make the silica coating, 1 mL of the previous dispersion was added to a mixture with 4 mL ethanol, 5 μL tetraethoxysilane and 10 μL aqueous ammonia solution (7.8 wt.%). The reaction was stirred at room temperature for 14-16 h (overnight). After this reaction time and to isolate the nanoparticles the dispersion was centrifuged at

21,000 g for 30 min. The supernatant was removed and the nanoparticles were redispersed in 1 mL water with ultrasonication (Cycle 0.8, amplitude 70%, 4s).

The SH-terminated or N₃-terminated calcium phosphate nanoparticles were prepared using the previous procedure.

7.6 Synthesis of loaded calcium phosphate nanoparticles for experiments discussed in section 8.5

Calcium phosphate nanoparticle were prepared according to the precipitation method described in 6.2.1. The following plasmids, pEGFP, pcDNA3-EGFP (abbreviated as pEGFP), $M_w=4,056.4$ kDa, 6,146 bp, and pHBsAg-DNA (abbreviated as pHBsAg), $M_w=25.4$ kDa, 681bp [221], and adjuvants CpG (ODN 1826, InvivoGen) sequence 5'-TCCATGACGTTCTGACGTT-3' and flagellin (SF, $M_w=53.2$ kDa, 1521bp [222]) were used.

CaP/PEI/pEGFP/SiO₂

To 1 mL of CaP/PEI nanoparticles were added either 100, 150 or 200 μ L of pEGFP (1 mg mL⁻¹) dissolved in water, and stirred for 30 min at room temperature. After the 30 min, the supernatant was measured by UV microvolume spectroscopy to determine the amount of pEGFP-loading on the nanoparticle. Next, a silica coating was added to the nanoparticle. For this, 1 mL of nanoparticle dispersion were added to 4 mL ethanol, 5 μ L TEOS and 10 μ L aqueous ammonia solution (7.8 wt.%). The reaction was stirred for 16 h at room temperature. After this time, the nanoparticles were isolated by ultracentrifugation at 66,000 g for 30 min and redispersed in 1 mL water with 4 s ultrasonication (cycle 0.8 and amplitude 70%).

pHBsAg loaded nanoparticles

To 1 mL of CaP/PEI nanoparticles were added 150 μ L of pHBsAg (1 mg mL⁻¹) dissolved in water, and stirred for 30 min at room temperature. For nanoparticles carrying adjuvants, 7.5 μ L (1 mg mL⁻¹) dissolved adjuvant (CpG or Flagellin) were added afterwards.

After 30 min, the supernatant was measured by UV microvolume spectroscopy to determine the amount of pHBsAg-loading on the nanoparticle. Next, a silica coating was added to the nanoparticle. For this, 1 mL of nanoparticle dispersion was added to 4 mL ethanol, 5 μ L TEOS and 10 μ L aqueous ammonia solution (7.8 %). The reaction was stirred for 14-16 h at room temperature. After this time, the nanoparticles were isolated by ultracentrifugation at 66,000 g for 30 min and redispersed in 1 mL water with 4 s ultrasonication (cycle 0.8 and amplitude 70%).

7.7 Synthesis of calcium phosphate nanoparticles for the experiments discussed in section 8.6

CaP/PEI/TNF- α -siRNA/SiO₂ and CaP/PEI/scrambled-siRNA/SiO₂

Calcium phosphate nanoparticles were prepared according to the precipitation method described in 6.2.1. To add the siRNA loading into the nanoparticle, TNF- α -siRNA, target sequence 5'-GCCGAUGGGUUGUACCUUG-3' ($M_w=13,459.9$ g mol⁻¹), and non-target TNF- α^* -siRNA, sequence 5'-UGGUUUACAUGUUGUGUGA-3' were used.

To 1 mL of CaP/PEI nanoparticles were added 100 μ L of TNF- α -siRNA (1 mg mL⁻¹) dissolved in water, and stirred for 30 min at room temperature under RNase-free conditions. After 30 min, the supernatant was measured by nanodrop to determine the amount of siRNA-loading on the nanoparticle. Next, a silica coating was added to the nanoparticle. For this, 1 mL of nanoparticle dispersion was added to 4 mL ethanol, 5 μ L TEOS and 10 μ L aqueous ammonia solution (7.8 wt.%). The reaction was stirred for 16 h at room temperature. After this time, the nanoparticles were isolated by ultracentrifugation at 66,000 g for 30 min and redispersed in 1 mL water with 4 s ultrasonication (cycle 0.8 and amplitude 70%).

The same procedure was followed for the non-target TNF- α^* -siRNA sequence, plasmid-DNA BMP-7 and plasmid-DNA VEGF.

CaP/CMC paste matrix

The calcium phosphate base matrix was based on the previous developed method by Chernousova et. al. [223]. In a stirred glass vessel with 20 mL ultrapure water, calcium lactate solution (18 mM, pH 10), diammonium hydrogen phosphate solution (10.8 mM, pH 10) and carboxymethyl cellulose solution (2 mg mL⁻¹) were simultaneously pumped at a rate 7.5 mL : 7.5 mL : 2.5 mL for 30 minutes with a peristaltic pump. The dispersion was stirred for five additional minutes and then centrifuged at 5,000 rpm for 30 min. The particles were redispersed in 50 mL ultrapure water and centrifuged again. Finally, the sample was shock-frozen with liquid nitrogen and lyophilized at 0.31 mbar and -10 °C.

7.8 Cell culture experiments

7.8.1 HeLa cells culture

HeLa (human cervical epithelial carcinoma) cell line were cultivated in Dulbecco's Modified Eagle's medium (DMEM) supplemented with 10% fetal bovine serum, 100 U mL⁻¹ penicillin, 100 U mL⁻¹ streptomycin, and 1 mM sodium pyruvate at 37 °C in 5 % CO₂ atmosphere. Every two to three days the cells were transferred to a new flask or the media was changed.

Cells were detached from the culture flask (T-25 flask) by adding 0.5 mL Trypsin-EDTA solution after washing with 10 mL DPBS, and incubated for 2 min at 37 °C. After this time, the flask was shaken and 5 mL of fresh media was added and mixed. The cell dispersion was transferred to a centrifuge tube and centrifuged at 900 RPM for 3 min. The supernatant was aspirated and to the cell pellet was added 2 mL of fresh media. An aliquot was taken for the new culture flask and the cell concentration was adjusted according to the needed amounts for seeding.

7.8.2 Cell viability test (MTT test)

The cell viability was determined by the MTT assay. Cells were incubated with nanoparticles at (0.1 to 1.6) 10^7 nanoparticles per well for 24 h. After the incubation time, the medium was removed and 300 μL MTT solution (1 mg mL^{-1} 4,5-dimethylthiazol-2-yl)-2,5-diphenyl-tetrazolium bromide in DMEM media) was added to each well. The cells were incubated with the MTT solution for 1 h at 37 °C under 5% CO_2 in humidified atmosphere. Then, the MTT solution was removed from the wells, and 300 μL DMSO were added to dissolve the precipitate. The plate was incubated at 37 °C and after 30 min, a 100 μL aliquot was placed into a 96-well plate and the absorbance at 570 nm was measured. The absorption was normalized to the absorption of untreated cells to determine the viability ratio.

7.8.3 Nanoparticles cellular uptake

One day before the addition of nanoparticles, the cells were trypsinized and seeded on a cover slip in a 24-well plates or imaging chambers at a density of $5 \cdot 10^4$ or $2 \cdot 10^4$ cells per well with 0.4 mL medium. After the incubation with the nanoparticles (6h, 12h or 24h), the whole cell culture medium was removed and the cells were washed twice with DPBS. Then the cells were fixed and stained according to the procedure described in section 6.5.5.

7.8.4 Transfection experiments

One day before the transfection experiments, HeLa cells were trypsinized and seeded in a 24-well plate with a cell density of $5 \cdot 10^4$ cells per well with 0.4 mL supplemented DMEM medium. After 24 h of incubation, a nanoparticle aliquot per well was given and a final concentration of plasmid (pDNA-mCherry) per well of near 7 μg were obtained. As positive control, Lipofectamine 2000 was used. Lipofectamine (2 μL) was mixed with 50 μL DMEM (without supplements) and incubated for 20 min at room temperature. Then, 1 μg pDNA-mCherry was added to 50 μL DMEM. After the 20 min of incubation both solutions were mixed. Then 50 μL of this solution was added to the control cells. After 7 hours of incubation, the medium was changed with fresh one and the cells were further incubated for 24 h and 48 h.

After each incubation period and before imaging, the cells were fixed using 4% paraformaldehyde at room temperature for 10 min followed by three times washing with DPBS. The cells were then stained with DAPI for the cell nucleus and washed three times with DPBS. For imaging using fluorescence microscopy the wells were left with DPBS.

7.9 J774.2 cell culture

J774.2 monocyte macrophages (BALB/C) were cultured in Dulbecco's modified Eagle's medium (DMEM), supplemented with 10% fetal bovine serum (Invitrogen), 100 U mL⁻¹ penicillin, 100 mg mL⁻¹ streptomycin, and 1 mM sodium pyruvate at 37 °C in humidified atmosphere with 5% CO₂. Every two to three days the cells were transferred to a new flask or the media was changed.

To transfer the cells to a new flask (T-25 flask), the cells were first washed with DPBS for 2 minutes (DPBS buffer helps to detach the cells). Then 3 mL fresh media was added and the flask was fully washed by repeated pipetting (as an alternative, a cell scraper can be used). The cell dispersion was then transferred to a centrifuge tube and centrifuged at 900 RPM for 3 minutes. The supernatant was aspirated and 2 mL of fresh media was added to the cell pellet. An aliquot was taken for the new culture flask and the cell concentration was adjusted according to the needed amounts.

7.9.1 Nanoparticles cellular uptake

One day before the addition of nanoparticles, the cells were seeded on an imaging chamber at a density of 5·10⁴ cells per well with 0.4 mL medium. Then, 20 µL of the nanoparticle dispersion was added to each well and incubated for 10 h. After this time, the cell culture medium was removed and the cells were washed with Dulbecco's phosphate-buffered saline (DPBS). Then the cells were fixed and stained according to the procedure described in section 6.5.5.

7.9.2 Cell viability test (MTT test)

The cell viability was determined by an MTT assay. Cells were incubated with nanoparticles at $(0.5 \text{ to } 8.2) \cdot 10^{10}$ nanoparticles per well for 9 h. For LPS-stimulated cells, $1 \mu\text{g mL}^{-1}$ LPS (*Escherichia coli* O55:B5) was added to the cells after 7 h incubation and incubated for another 2 h. After the incubation time, the medium was removed and 300 μL MTT solution (1 mg mL^{-1} 4,5-dimethylthiazol-2-yl)-2,5diphenyl-tetrazolium bromide in DMEM media) was added to each well. The cells were incubated with the MTT solution for 1 h at 37 °C under 5 % CO₂ in humidified atmosphere. Then, the MTT solution was removed from the wells, and 300 μL DMSO were added to dissolve the precipitate. The plate was incubated at 37 °C and after 30 min, a 100 μL aliquot was placed into a 96-well plate and the absorbance at 570 nm was measured. The absorption was normalized to the absorption of untreated cells to determine the viability ratio.

7.9.3 Gene silencing efficiency

Cells were seeded in a 24-well plate for 24 h before adding the nanoparticles at a density of $5 \cdot 10^4$ cells per well in 500 μL supplemented DMEM medium. To each well, either 4, 8 or 15 μL of the nanoparticle dispersion was given. After 6 h incubation, the cells were stimulated with $1 \mu\text{g mL}^{-1}$ LPS (*Escherichia coli* O55:B5) and incubated for additional 4 h. After this time, the supernatant was collected and frozen at -80 °C and later analyzed for secreted TNF- α by ELISA (ab100747, Abcam). ELISA analysis was performed following the manufacturer instructions.

8 Results and Discussion

8.1 Calcium phosphate nanoparticles

Calcium phosphate nanoparticles can be prepared using a precipitation method by mixing solutions of calcium and phosphate ions. By controlling the molar ratio and pH of the solutions at the precipitation moment it is possible to control the calcium phosphate face that will preferentially be formed. This preparation methodology has been previously described by Kozlova *et al.* [18]. With the addition of a polymer, such as polyethyleneimine, the nanoparticles dispersion is stabilized and the nanoparticle size is kept. Additionally, polyethyleneimine has the advantage to be active for biological applications such as transfection [224-227].

In material sciences the surface modification of materials, especially for nanoparticles due to the high relationship surface area to volume ratio, is a way to manipulate the material's properties and interactions with the environment. Due to the ionic nature of calcium phosphate, its modification is limited to electrostatic interactions or physical absorption that can lead to a not very stable modification. To overcome this limitation Neumeier *et al.* [25] and Kozlova *et al.* [26] developed a methodology to grow a silica coating on the calcium phosphate nanoparticle surface. This coating allows to extend the possible chemical modification of the nanoparticle surface by siloxane chemistry.

The addition of other functional groups to the nanoparticle surface was demonstrated by Kozlova *et al.* Functional groups such as amines and thiols were introduced by their corresponding organosilane precursors, and further coupling to biomolecules were performed [26]. An additional surface modification was developed by van der Meer *et al.* [19], in which the material was developed as a modular building block for avidin-biotin interactions.

Although these modifications methods were successfully applied, for other applications its versatility can be limited due to the number of bonding sites and selectivity, and specificity for coupling positions within a biomolecule. For these

reasons a new approach based on azide terminated nanoparticles for click chemistry was developed [228] and will be demonstrated in the following sections.

Silica terminated calcium phosphate nanoparticles were used as starting material for the following azide modification. Figure 11 shows a representative SEM, EDX and DLS for this material. With this method silica terminated calcium phosphate nanoparticles with a hard core in the range 40-100 nm and with a spherical morphology were obtained. A hydrodynamic radius determined by DLS between the range 140-250 nm was usually measured. By EDX analysis a Ca/P molar ratio of 1.41 – 1.60 was determined, which agrees with the Ca/P of 1.52 – 1.64 determined by Ca^{2+} (AAS) and PO_4^{3-} wet chemical analysis. These values are in the range expected for precipitated hydroxyapatite that has a Ca/P molar ratio between 1.33-1.67 and a stoichiometry of $\text{Ca}_{10-x}(\text{HPO}_4)_x(\text{PO}_4)_{6-x}(\text{OH})_{2-x}$ (X can vary between 0 and 2) [1, 52]. For following calculations, hydroxyapatite stoichiometry ($\text{Ca}_{10}(\text{PO}_4)_6(\text{OH})_2$) will be used with a density of $3,140 \text{ kg/m}^3$.

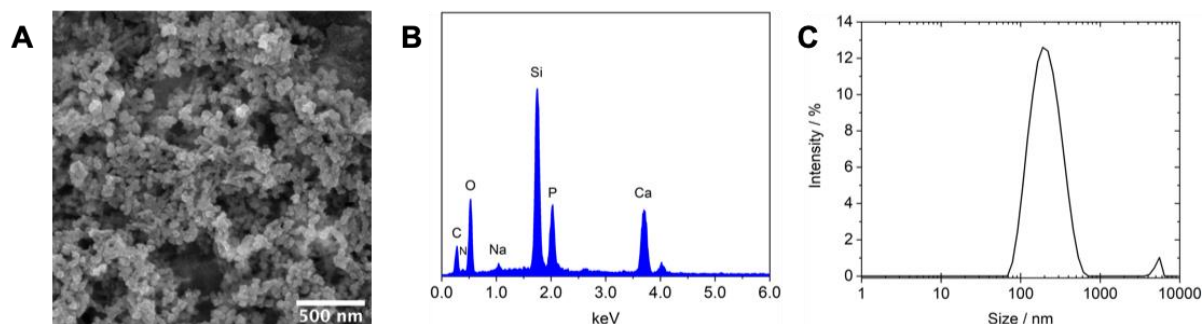


Figure 11: Representative **A)** Scanning electron micrograph (SEM), **B)** EDX spectra, **C)** DLS of silica terminated calcium phosphate nanoparticles.

Figure 12 shows representative images for the calcium phosphate silica terminate nanoparticles by cryogenic transmission electron microscopy (cryo-TEM), in which the spherical morphology is further confirmed. Rather than having a flat crystalline surface, the nanoparticle surface is rough, due to the presence of the silica coating and polymer in the internal structure. For this example, an average diameter of 89 nm was determined by this technique and had a good agreement to the average diameter by SEM, which was 90 nm. Due to the low contrast obtained with cryo-TEM is not possible to distinguish the composition difference within the nanoparticle.

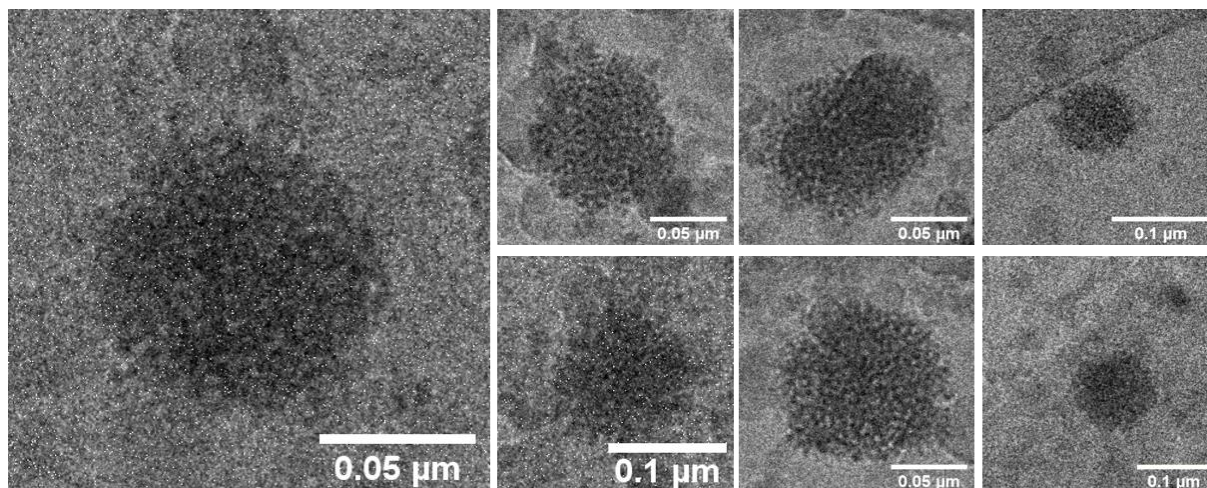


Figure 12: Silica terminate calcium phosphate nanoparticles observed by cryogenic transmission electron microscopy (cryo-TEM).

Additionally, Figure 13 shows an electron transmission micrograph of a silica terminate calcium phosphate nanoparticles. As observed from the image, around the nanoparticle an external ring is noticed due to the contrast difference with the inner core. This difference is related to the elemental composition caused by the variation in element density. Heavier elements will absorb more electrons from the electron beam and produce a darker area compared to lighter elements [190]. Between Si and Ca, a higher electron absorption is expected for calcium, thus the inner core looks darker compared to the external SiO_2 coating. To enhance the contrast the sample core was also stained with uranyl acetate, which is absorbed by the nanoparticle core (CaP/PEI), and gives a better contrast to differentiate the silica coating.

With a line intensity profile analysis, it is possible to observe the variation in the intensity as a function of the measured distance of an object. From the plotted profile in Figure 13, three regions are observed within the nanoparticle. The internal region with lower intensity, related to the calcium phosphate core has a diameter between 60-80 nm, which is consistent with the size measured with other methods like SEM and Cryo-TEM. Additionally, the silica coating has a diameter near 12-20 nm and based in the observed intensity and contrast a thin layer is most likely to be expected rather than a thicker coating. The size ratio between the calcium phosphate core and silica coating is mostly kept as the core diameter varies for example for smaller particles.

Silica particles networks with a plate-like morphology were also observed in the grid and have an average size between 10-20 nm. These particles networks near the calcium phosphate nanoparticles were generated during the Stöber method procedure and in those cases the silica particle nucleation did not occur directly on the calcium phosphate surface.

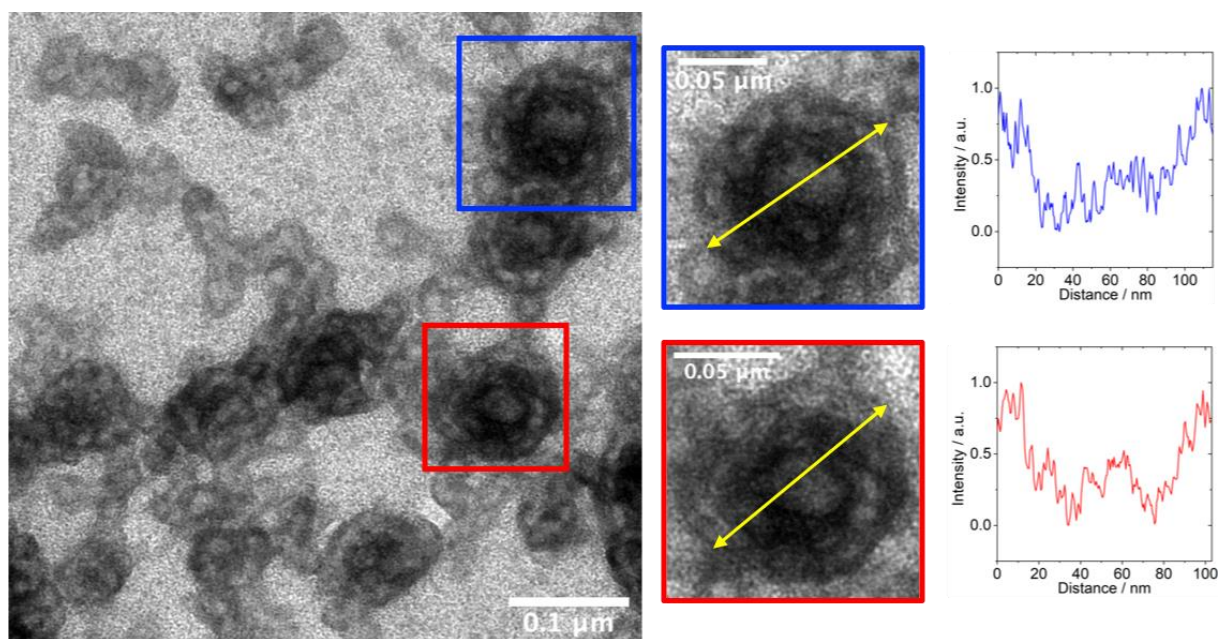


Figure 13: Transmission electron microscopy (TEM) micrograph of silica terminate calcium phosphate nanoparticles after uranyl acetate staining. The line profile analysis of the nanoparticle shows an intensity variation across the nanoparticle because of the electron absorption difference that is related to a composition change. The outer shell is associate to silica and the inner core to the calcium phosphate.

With STEM-HAADF imaging is possible to determine the elemental composition of the nanoparticle. Figure 14 shows an elemental mapping measured by STEM-HAADF in SEM of the silica terminate calcium phosphate nanoparticle. The mapping evidences the expected composition of nanoparticles. A good correlation between the positions of calcium, phosphate and oxygen is observed corresponding to the nanoparticle core. Moreover, silicon is found in the same positions and around the identified calcium phosphate core.

Furthermore, Figure 15 shows a line profile analysis for Ca and Si analysis of one nanoparticle which reflects the silica coating around the calcium phosphate core. This

analysis confirms the previous conclusion based on the intensity profile line analysis, an external coating of SiO₂ and an internal core of calcium phosphate. Similar to Figure 13, thin silica networks around the calcium phosphate nanoparticles are also observed on the elemental mapping.

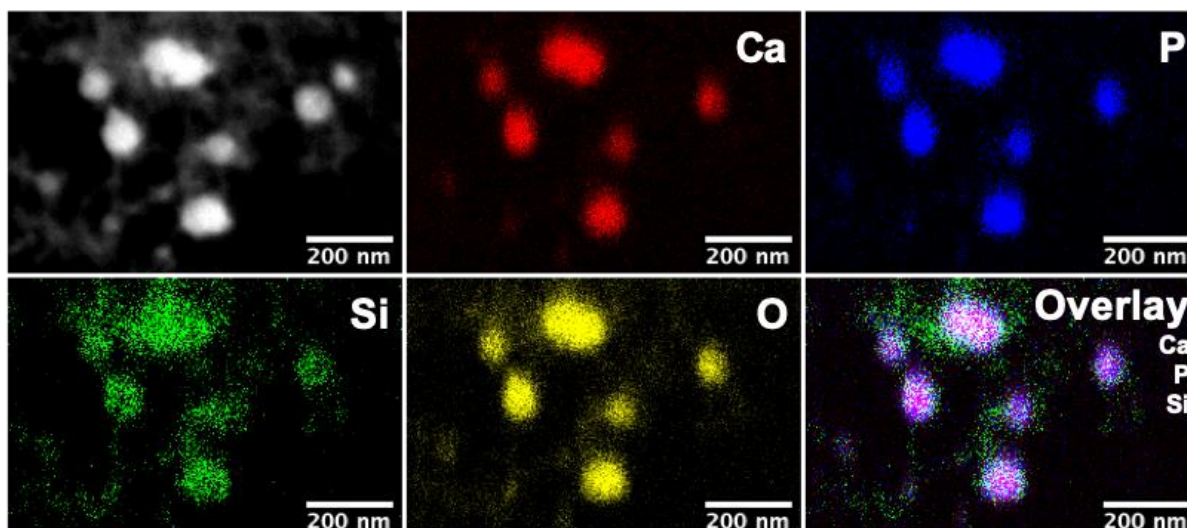


Figure 14: STEM-HAADF in SEM mapping of silica terminate calcium phosphate nanoparticle.

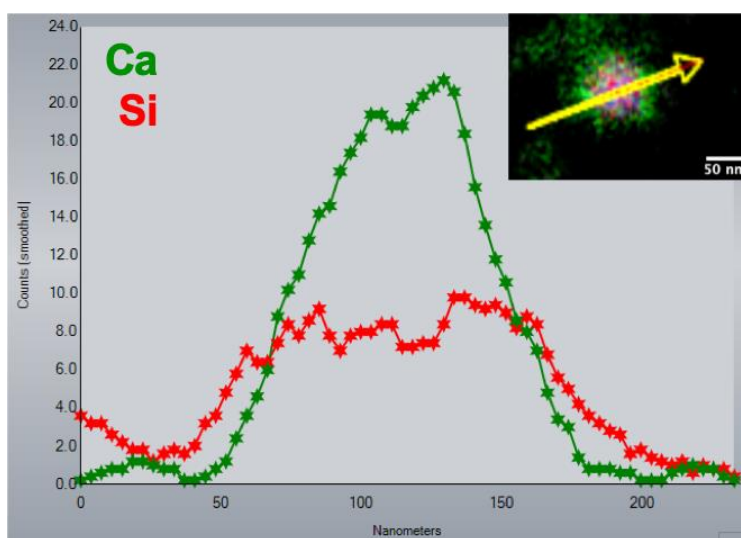
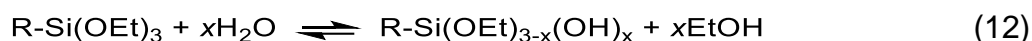


Figure 15: Line profile for calcium and silicon for one nanoparticle from the STEM-HAADF in SEM mapping of Figure 14.

8.2 Azide terminated calcium phosphate nanoparticles

Silica terminated calcium phosphate nanoparticles were used as starting material to prepare the azide terminated calcium phosphate nanoparticles following the procedure described in section 7.2.2.

The azide precursor condensation onto the silica coating starts with the hydrolysis of (3-Azidopropyl)triethoxysilane to generate $R-Si(OEt)_2(O^-)$ and $R-Si(OEt)(OH)(O^-)$ species ($R = -CH_2-CH_2-CH_2-N_3$). At the working ammonia concentration (5.2 μM) a low hydrolysis rate is expected, which promotes the condensation on the existing siloxane networks that coat the calcium phosphate nanoparticle. Condensation reaction follows a nucleophilic attack and the siloxane networks are more active than individual monomers to perform the attack, which favors the network growing [229]. The process can be described by:



After the surface modification the particle conserved the spherical morphology and the size was not significantly altered as observed by electron microscopy. Figure 16 shows a representative SEM image of the nanoparticles after the reaction with an average solid core size of 60 nm and a DLS diameter distribution of the nanoparticles in a water dispersion.

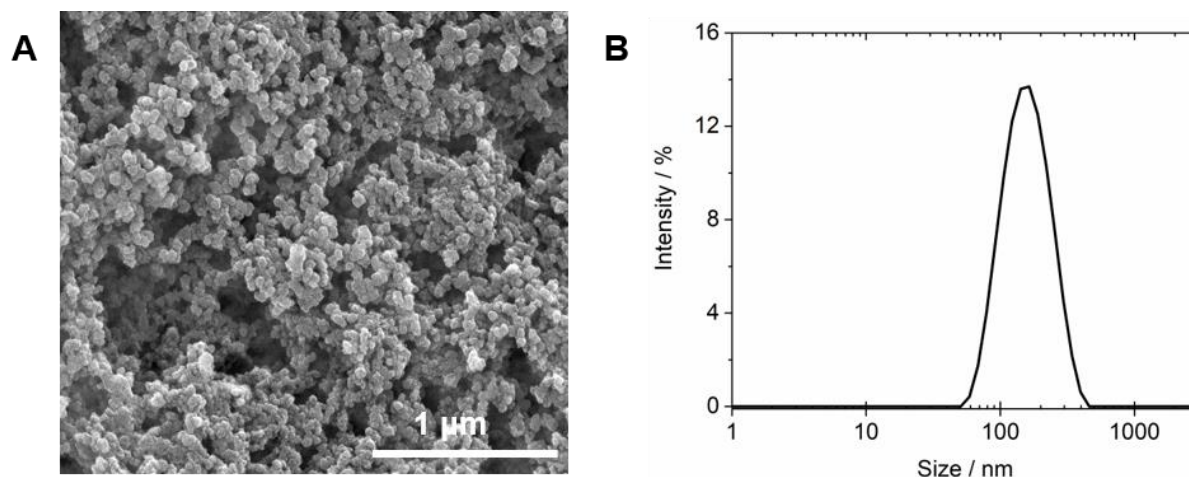


Figure 16: A: Scanning electron micrograph (SEM), B: DLS size distribution of calcium phosphate nanoparticles with azide-terminated surface.

Azide functional group has a characteristic vibrational band near 2100 cm^{-1} [230, 231] that can be detected by IR spectroscopy. Figure 17 shows a representative IR spectra of the nanoparticle before and after the incorporation of the azide groups. At 2105 cm^{-1} is detected the azide band.

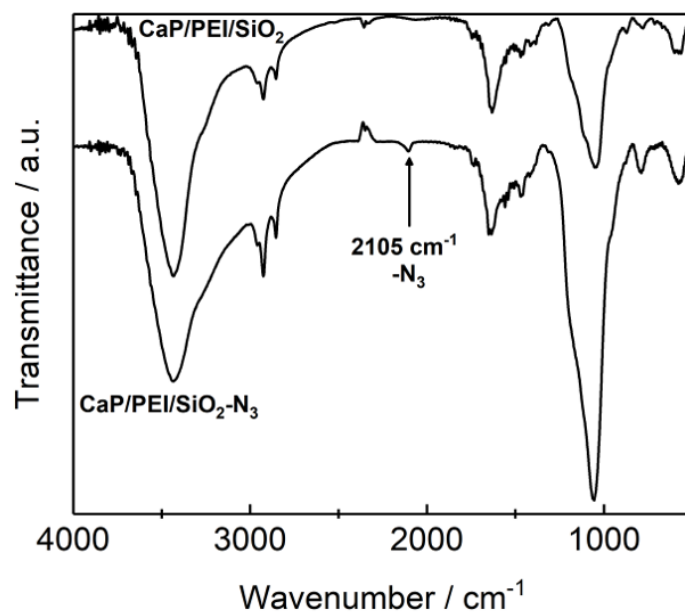


Figure 17: FT-IR spectra before and after calcium phosphate nanoparticle surface functionalization with azide groups. After the reaction, the azide signal is detected at 2105 cm^{-1} .

Other characteristic bands of the nanoparticle are found at 1058 and 577 cm^{-1} which corresponds to the ν_3 and ν_4 PO_4 ; although at 1058 cm^{-1} exists a band overlapping with the Si-O symmetric stretching band from the silica coating. A Si-O-Si bending band is also detected at 787 cm^{-1} . Signals from the C-H symmetric and asymmetric stretching are detected at 2854-2959 cm^{-1} and correspond to the methyl and methylene groups in the side chain from (3-Azidopropyl)triethoxysilane and TEOS precursors, as well as from the methylene from the polyethylenimine carbon backbone. Additional bending bands for these groups are observed at 1471-1417 cm^{-1} . The broad band near 3434 cm^{-1} is assigned to the N-H stretching of the amine groups of PEI and O-H stretching from the silica network. The identified bands are summarized in Table 2.

Table 2: Observed FT-IR bands with its corresponding vibrational assignments [186, 232-235].

Wavenumber (cm^{-1})	Assignment
3434	N-H stretching, O-H stretching
2959	C-H symmetric stretching from CH_3
2924	C-H asymmetric stretching from CH_2
2854	C-H symmetric stretching from CH_2
2105	$\text{N}\equiv\text{N}$ stretching
1634	N-H bending
1471	C-H asymmetrical bending
1417	O-H bending, C-H wagging
1058	ν_3 PO_4 , Si-O symmetric stretching
787	Si-O-Si bending
577	ν_4 PO_4

Different azide surface modification densities were studied by changing the molar concentration of the azide precursor during the silanization reaction. With quantitative FT-IR spectroscopy the amount of azide groups on the nanoparticles was determined.

For the quantification, a solid calibration curve using NaN_3 was prepared and measured. As the azide group in the inorganic salt has a different absorption coefficient compared to the azide in the organosilane molecule, due to the chemical

environment, a correction factor was determined. For this two additional calibration curves using NaN_3 and (3-azidopropyl)triethoxysilane were prepared (from 0 to 2 μmol) and measured using a NaCl liquid cell. The ratio of both absorption coefficients was calculated and an absorbance factor of $\epsilon(3\text{-azidopropyl)triethoxysilane} = 1.2 \epsilon(\text{NaN}_3)$ was established. This factor was then used to correct the interpolated absorbance within the NaN_3 solid calibration curve.

For the sample FT-IR measurements, the nanoparticles dispersion was first lyophilized to remove the water and to concentrate the sample before preparing the sample pellet with KBr. Table 3 summarizes the obtained values after different synthesis conditions. With this procedure different azide groups densities on the nanoparticle can be adjusted.

Table 3: Calcium phosphate nanoparticle characterization after surface modification with terminal azide groups. Nanoparticles had an average core diameter of 60 nm as measured by SEM (solid core).

Condition	$N(\text{N}_3)$ per nanoparticle / $\cdot 10^5$	$-\text{N}_3$ groups per nm^2	Reaction yield / %	Hydrodynamic diameter by DLS / nm	Pdl by DLS	Zeta potential by Doppler micro-electrophoresis / mV
C1	1.73	15	6.7	169	0.13	+24
C2	2.59	23	4.9	197	0.30	+27
C3	3.34	30	4.4	204	0.44	+27

For further experiments the first condition was chosen as it enables enough binding sites for further reactions. In all cases the reaction yield (incorporation of azide groups into the nanoparticles vs the initial amount) was similar between (4.4-6.7)%.

The nanoparticles hydrodynamic diameter was determined by DLS giving typical values between 160-200 nm. The surface was positively charged due to the presence of polyethyleneimine (cationic polymer) in the nanoparticle. The nanoparticles dispersion stability was analyzed during 9 days for the C1-type nanoparticles (Figure 18). For this, two sample aliquots in water were stored one at room temperature and one at 4 °C. A size around 200 nm and a polydispersity index (Pdl)

near 0.3 within this period was measured, thus the nanoparticles were considered to be stable during this timeframe.

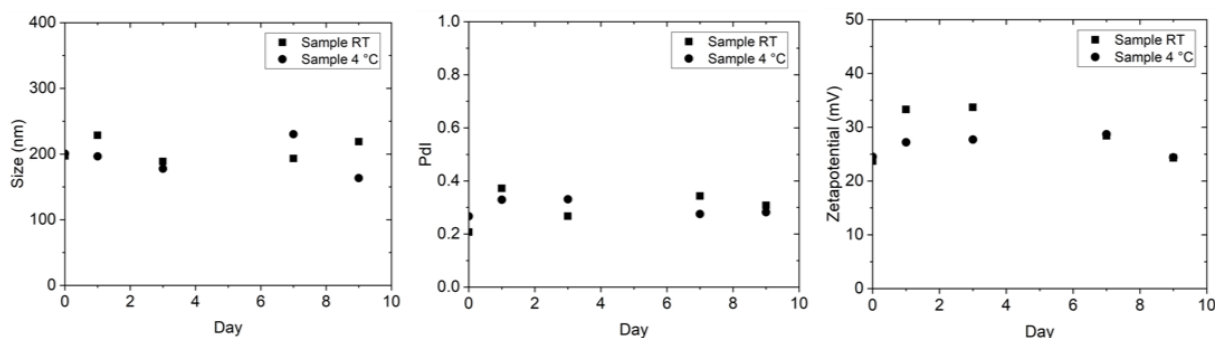


Figure 18: Hydrodynamic diameter size, polydispersity index (PDI) and ζ -potential measured over 9 days for calcium phosphate azide-terminated nanoparticle (CaP/PEI/SiO₂-N₃) dispersed in water.

8.3 Click reaction with azide-terminate calcium phosphate nanoparticles

Click reactions are a group of chemical reactions that allow a straightforward reaction with specific functional groups as described in section 5.3. This approach will be used to modify the calcium phosphate nanoparticle surface, so that a chemical bond (*i.e.*, triazole ring) between the nanoparticle surface and the coupling molecule will be formed. With the surface modification is possible to extent the properties and applications of the calcium phosphate nanoparticles. A general reaction scheme with an azide-terminated calcium phosphate nanoparticle is shown in Figure 19.

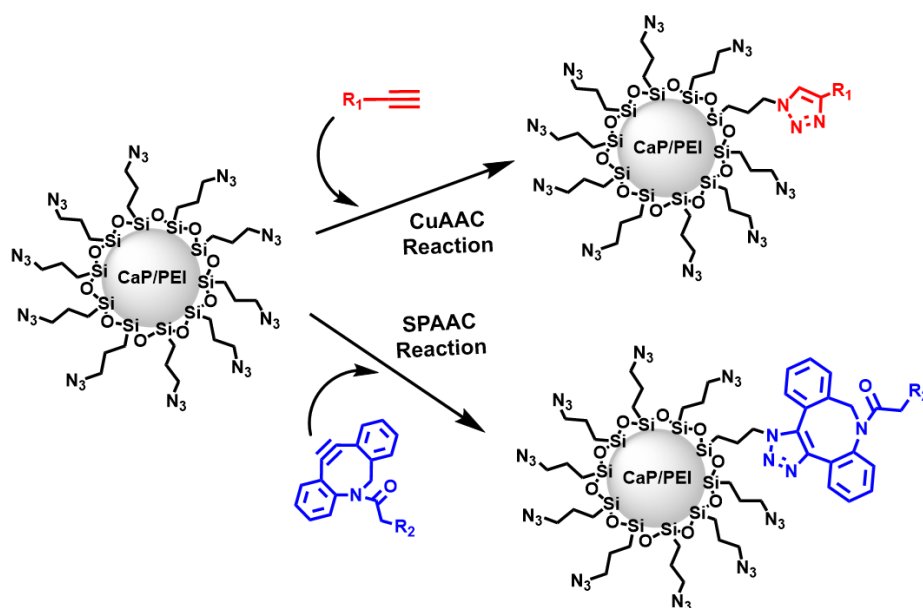


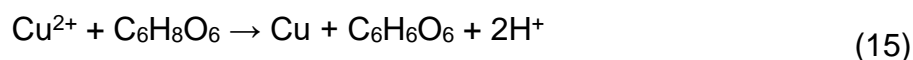
Figure 19: Click reaction general scheme with an azide-terminated calcium phosphate nanoparticle.

8.3.1 CuAAC reaction with calcium phosphate nanoparticles

pH evolution, pH control and reaction time

Copper catalyzed click reaction is one of the most commonly used and efficient click reactions. For the reaction, copper (I) is generated *in situ* using sodium ascorbate as reducing agent and a copper (II) salt precursor like $\text{CuSO}_4 \cdot 5\text{H}_2\text{O}$. This redox reaction can cause an acidity issue for our system because calcium phosphate nanoparticles are dissolved at $\text{pH} < 6$.

In a general way, the copper (II) complete reduction by ascorbic acid can be described by the following equation:



As observed from equation 15, with the copper reduction the reaction solution is acidified. The reaction pH of the copper (II) reduction by sodium ascorbate was monitored up to 24h and the results are shown in Table 4.

Table 4: Solution pH evolution during the copper (II) reduction with sodium ascorbate reaction up to 24 h.

Initial pH	+2 h	+ 4 h	+ 6 h	+24 h
7.3	6.7	6.1	5.9	4.3

As observed from Table 4, after two hours of reaction the pH drops below 7 and at longer times the pH acidity is enough to dissolve the calcium phosphate nanoparticles. Similar pH values (near pH 4.5) are obtained for the nanoparticles after 24 h reaction. An easy way to avoid the solution acidification is to perform the reaction in a buffer solution, although another problem due to the nanoparticles can appear. When performing the reaction in a buffer solution, the stability of the calcium phosphate nanoparticle dispersion will be affected by the high ionic strength, thus affecting the long term stability of the nanoparticles. For this reason is not viable to perform the reaction with a buffer. An alternative solution is to decrease the reaction time.

Reaction with FAM-Alkyne as model molecule

To further study the reaction with the nanoparticles, FAM-Alkyne was chosen as a model molecule to be coupled to the calcium phosphate nanoparticle. This molecule can be easily detected by UV-Vis and fluorescence spectrophotometry (structure shown in Figure 20). The usual procedure for the reaction is described in the experimental section.

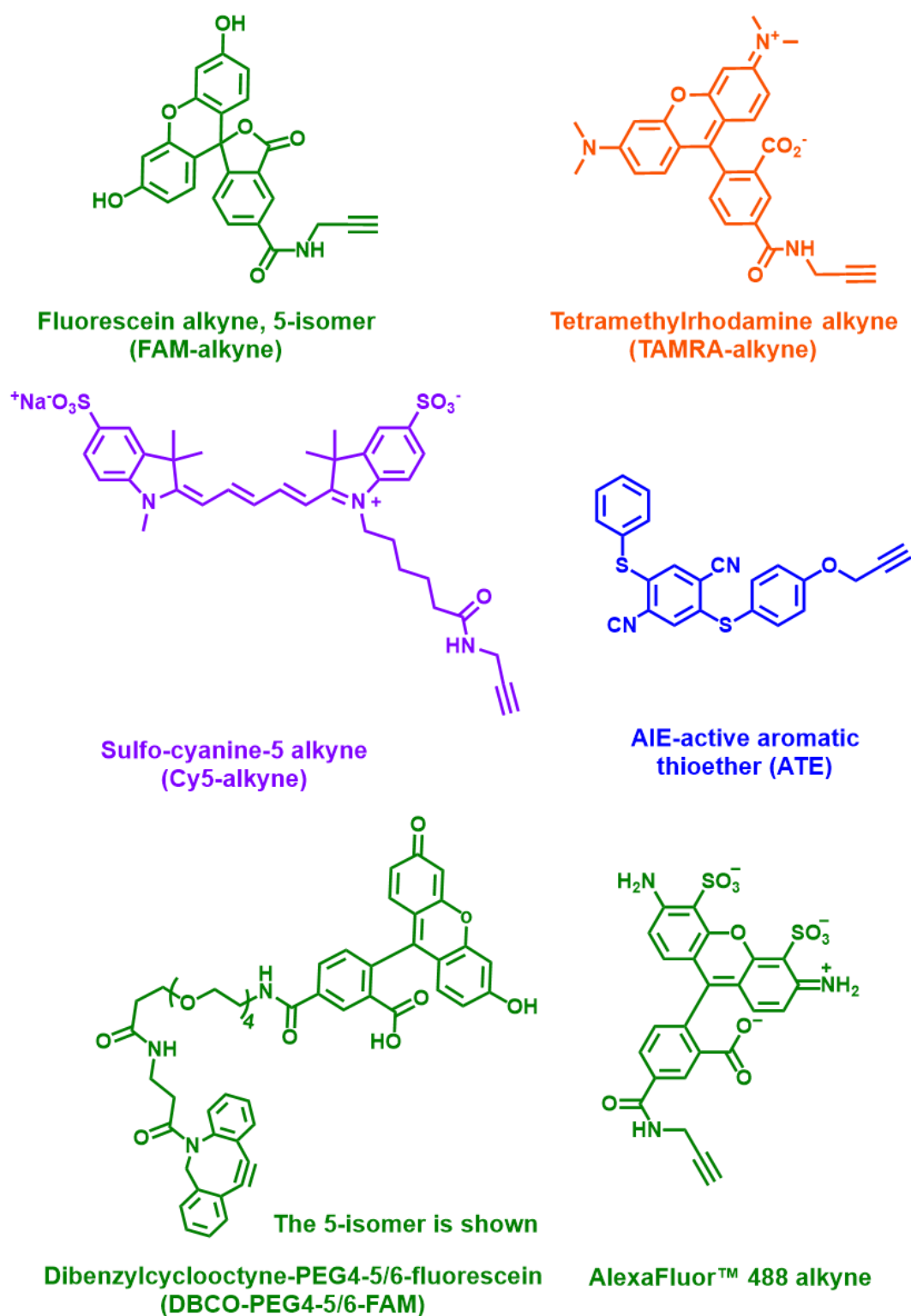


Figure 20: Structures of the dyes used: Fluorescein (FAM) alkyne, 5-isomer; tetramethylrhodamine (TAMRA) alkyne, 5-isomer; sulfo-cyanine5 alkyne (Cy5); aggregation-induced emission (ATE) active aromatic thioether (ATE); dibenzylcyclooctyne-PEG4-5/6-fluorescein (DBCO-PEG4-5/6-FAM); AlexaFluor® 488.

By decreasing the reaction time to one hour and adjusting the reaction initial pH, the reaction conditions can be controlled to avoid the dissolution of the calcium phosphate nanoparticles. Using FAM-alkyne for the reaction, the effect of the initial pH over the nanoparticle labeling was evaluated. Table 5 summarizes the results for three different initial pH at 9.13, 8.80 and 8.44. The pH was adjusted by adding NaCl 0.1 M. From these results, is possible to observe that for an initial pH below 9 the reaction yield was slightly improved.

Table 5: Summary of CaP nanoparticles labeled with FAM-alkyne by CuAAC with different initial reaction pH.

Sample	Initial pH	Final pH	Solid core		DLS / nm	PDI	ζ -potential / mV
			diameter by SEM / nm	N (FAM) per nanoparticle			
Click A1	9.13	7.65	52	$2.5 \cdot 10^3$	205	0.36	+27
Click A2	8.80	7.58	51	$3.2 \cdot 10^3$	196	0.35	+27
Click A3	8.44	7.55	52	$3.7 \cdot 10^3$	173	0.32	+29

By adding 5 μ L of 0.1 M NaOH to a 3 mL NPs based reaction media the pH is adjusted within 8.5-9.0, and after one hour reaction a final pH near 7.6 is obtained. With this parameters the nanoparticles dissolution (due to an acidic pH) is avoided during the CuAAC click reaction. For the following reactions an initial pH adjustment was performed.

As mentioned before, Cu (I) is the catalyst for the CuAAC reaction. With a higher availability of Cu (I) during the reaction it is expected an increase in the reaction efficiency. A common Cu (I) stabilizing agent for this reaction is the ligand Tris(3-hydroxypropyltriazolylmethyl)amine (THPTA) [236]. This molecule helps to keep a high Cu (I) availability, but also protects from hydrolysis byproducts and intercept radicals from further ascorbate oxidations [237]. This ligand structure allows to have a

high availability of binding positions for copper with constant access to open coordination sites [238]. The effect of this reagent in our system was evaluated and the click reaction with and without this ligand was performed and summarized in Table 6.

As shown in Table 6, a significant improvement in the nanoparticle labeling (a factor of near 2.5 times) is achieved when performing the reaction with THPTA ligand. Additionally, as the physical absorption of the labelling molecule on the nanoparticles surface can occur, a control reaction was set to determine the physical absorption of FAM. For this, the same volume of calcium phosphate nanoparticles dispersion was mixed with FAM-Alkyne at the same molar concentration.

Table 6: Click reaction with FAM-alkyne comparison with and without adding THPTA ligand for the reaction.

Sample	Solid core diameter by SEM / nm	N (FAM) per nanoparticle	Reaction yield	DLS / nm	PDI	ζ -potential / mV
Without THPTA	51	$3.2 \cdot 10^3$	30.9%	196	0.35	+27
With THPTA	54	$9.3 \cdot 10^3$	75.5%	157	0.37	+27
Physical absorption control	34	$0.27 \cdot 10^3$	8.9%	227	0.41	+26

The amount of physically absorbed molecules on the surface is much smaller than the number of molecules obtained after the click reaction (almost 10 times lower than with THPTA ligand). From this comparison is possible to conclude that the reaction between the particles and FAM-alkyne actually occurs and is not only a physisorption process.

Figure 21 shows a representative UV-Vis and Fluorescence spectra of the nanoparticles before and after the click reaction with FAM-Alkyne, in which a clear signal of the dye is detectable. From the UV-Vis absorbance and with the appropriate calibration curve (see 6.2.1 section) the concentration of the dye is calculated. Then the number of molecules per particle can be computed from the dye concentration (from UV-Vis), nanoparticles amount (from Ca^{2+} analysis), particle size (from SEM) and density of hydroxyapatite. The following relationship was used assuming a complete spherical particle, one layer formation and a hydroxyapatite stoichiometry:

$$N_{(\text{molecules per nanoparticle})} = \frac{w_{\text{dye}} \cdot N_A}{M_{\text{dye}}} \times \frac{10 \cdot M_{\text{Ca}}}{w_{\text{Ca}} \cdot M_{\text{Ca}_{10}(\text{PO}_4)_6(\text{OH})_2}} \times \frac{4\pi r^3 \rho \cdot 10^{-27}}{3} \quad (16)$$

where w_{dye} is the dye concentration in $\mu\text{g mL}^{-1}$, w_{Ca} is the calcium concentration in g L^{-1} , r is the particle radius in nm, M_{dye} is the dye molecular weight in g mol^{-1} , M_{Ca} is the calcium molecular weight (40.08 g mol^{-1}), $M_{\text{Ca}_{10}(\text{PO}_4)_6(\text{OH})_2}$ is the hydroxyapatite molecular weight ($1,004.62 \text{ g mol}^{-1}$), ρ is the hydroxyapatite density ($3,140 \text{ kg m}^{-3}$), and N_A the Avogadro constant.

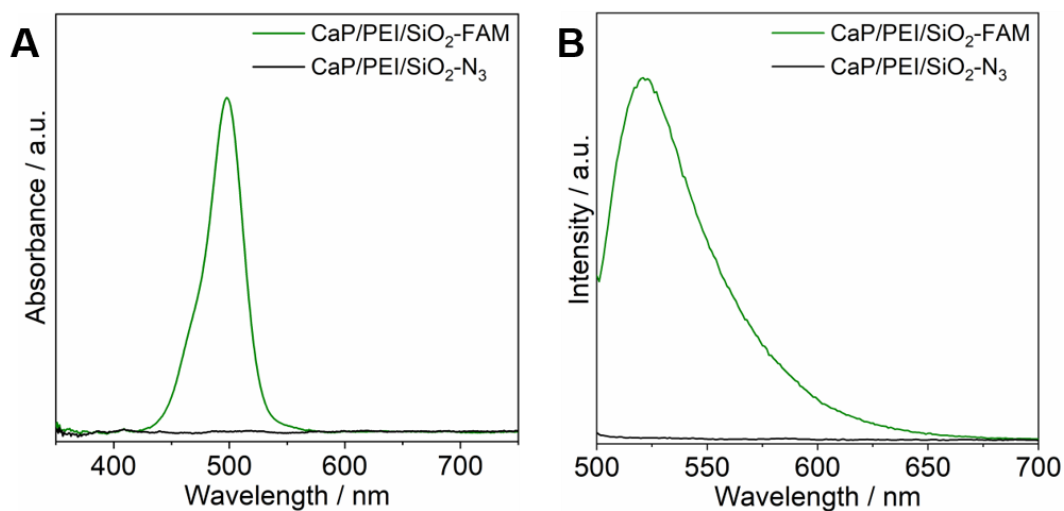


Figure 21: A) UV-Vis and B) fluorescence spectra before (CaP/PEI/SiO₂-N₃) and after click reaction with FAM-Alkyne (CaP/PEI/SiO₂-FAM). Fluorescence excitation wavelength at 490 nm.

As the reaction takes place on the nanoparticle surface, after the click reaction the nanoparticle core diameter is not expected to change as confirmed by scanning electron microscopy (Figure 16, Figure 26).

An additional experiment to confirm that the click reaction happened on the nanoparticle was performed. Core labelled calcium phosphate nanoparticles were prepared using PEI-Cy5 instead of unlabeled PEI. In this case, the nanoparticle had a purple fluorescence due to the Cy5 in the stabilizing polymer and after clicking FAM-alkyne, a green fluorescent signal should also be detected. Both colors should colocalize when the reaction is successful.

Using UV-Vis the absorption of both molecules (FAM and Cy5) can be detected (Figure 22), but is not possible to confirm that it comes from the same particle as it is a measurement of the complete dispersion. Using fluorescence microscopy, the particles can be imaged and the fluorescence detected making it a suitable method for this purpose.

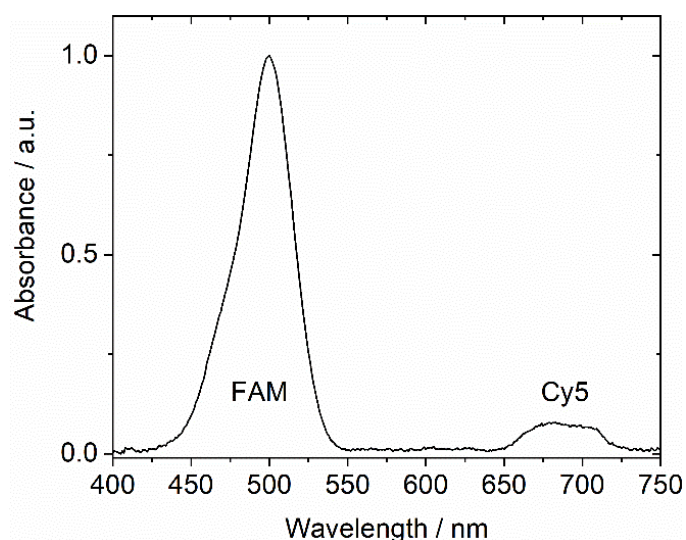


Figure 22: UV-Vis spectra of CaP/PEI-Cy5/SiO₂-FAM nanoparticles. Two maxima are detected, the first one for FAM dye and the second one for Cy5 dye.

Figure 23 shows representative images for the colocalization of both dyes on the calcium phosphate nanoparticle by confocal laser scanning microscopy (CLSM), the core is in purple and the labelling dye is in green. The colocalization was identified as a white spot (green + purple = white) and an overall colocalization was detected. As observed in Figure 23 not all green positions are colocalized. This is because not all the applied polymer was labelled with Cy5, a dilution 1:2:PEI:PEI-Cy5 was made. With

this comparison is possible to confirm that the reaction had taken place on the nanoparticle.

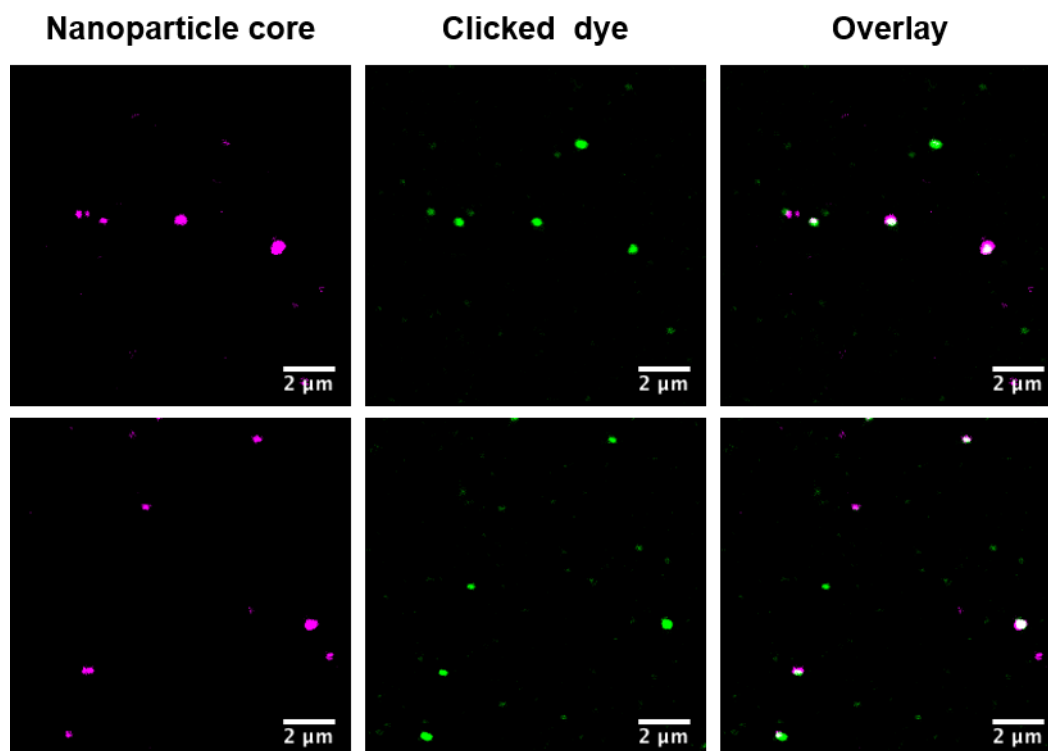


Figure 23: Nanoparticle core and coupled dye co-localization observation by confocal laser scanning microscopy (CLSM) on CaP/PEI-Cy5/SiO₂-FAM nanoparticles. Calcium phosphate nanoparticles are purple (PEI-Cy5), and the coupled dye (FAM) is green.

The reaction with FAM-alkyne at different initial molar concentration of the dye was evaluated in the range (6.9 – 41) μM . For the given amount of azide-terminate nanoparticles and according to the number of azide groups per nanoparticle in the reaction an azide concentration of near 90 μM is estimated. For the click reaction is recommended that the azide group be in excess compared to the alkyne [237]. Table 7 and Figure 24 show the labelling results at four different alkyne concentrations.

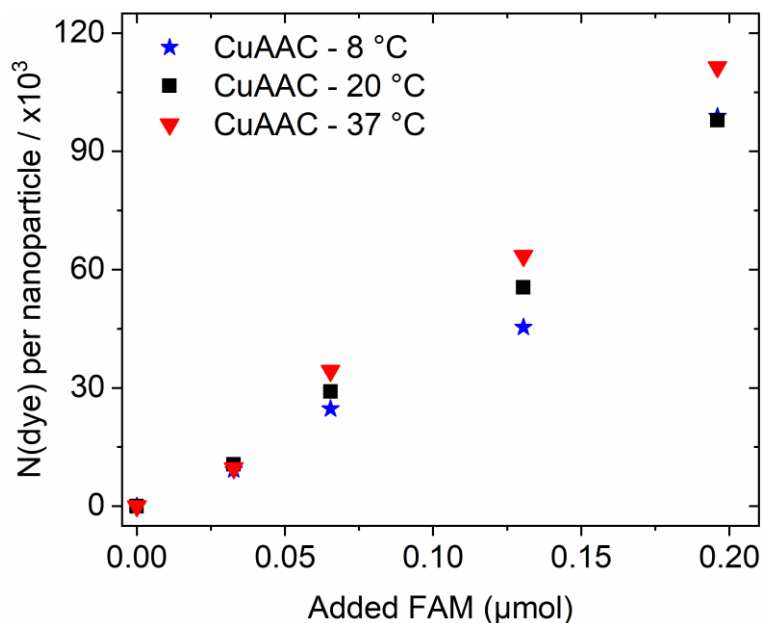


Figure 24: Dye molecules per nanoparticle after CuAAC click reaction at different alkyne molar concentrations and reaction temperatures (8, 20 and 37 °C).

As observed from Table 7 at higher initial concentrations the number of labelling molecules in the surface increases. This means that the initial alkyne-molecule concentration or alkyne – azide ratio exerts a positive influence over the reaction rate within this range. At higher concentrations an equivalent reaction yield was observed, although a higher residue percentage (unreacted dye) was obtained (*i.e.*, as more initial dye was given a higher amount remains unreacted).

The reaction yield is defined as the ratio between the number of bonded molecules on the nanoparticle and the initial given dye amount normalized to the total number of nanoparticles available in the system. On the other hand, the residue percentage is based on the measured dye concentration in the supernatant after the reaction and the initial given amount. By controlling the initial alkyne concentration or the ratio between alkyne-azide is possible to adjust the coupling number on the nanoparticles surface.

Table 7: Calcium phosphate nanoparticle labelling after click reaction with different FAM-Alkyne initial molar concentration and 1 h reaction time. A nanoparticle average core size of 60 nm was used as determined by SEM.

FAM initial concentration / μM	$N(\text{FAM})$ per nanoparticle	Dye molecules per nm^2	Yield / %	Residue / %	DLS / nm	Pdl	ζ -Potential / mV
6.89	$3.04 \cdot 10^3$	0.3	38.1	60	335	0.48	+25
13.8	$8.16 \cdot 10^3$	0.7	51.1	70	290	0.40	+24
27.5	$1.90 \cdot 10^4$	1.7	59.8	74	335	0.44	+24
41.3	$3.01 \cdot 10^4$	2.7	62.9	81	497	0.47	+24

Lyophilization is an appropriate and frequently use method for the nanoparticles long-term storage [239-241]. In this process, the colloidal dispersion is frozen with liquid nitrogen and the water is removed by sublimation under vacuum. To analyze the influence in the nanoparticles reactivity after lyophilization, azide-terminated calcium phosphate nanoparticles were lyophilized. Then, CuAAC reaction with FAM-Alkyne was performed and the number of labelling molecules was compared to the nanoparticles without lyophilization.

Figure 25 shows a comparison of the number of molecules per nanoparticle using fresh and lyophilized nanoparticles. A higher number of molecules are detected with lyophilize nanoparticles which suggests a higher surface reactivity or accessibility. Between both types, lyophilize nanoparticles increase by a factor of near 3.1 the number of bonded molecules per nanoparticle.

The rise in the number of molecules per nanoparticle after lyophilization can be related to the water removal process, which influences the nanoparticle structure, especially the siloxane network covering the calcium phosphate nanoparticles. After lyophilization more azide groups on the network can become accessible probably due to a change in the surface porosity or roughness [240, 242, 243].

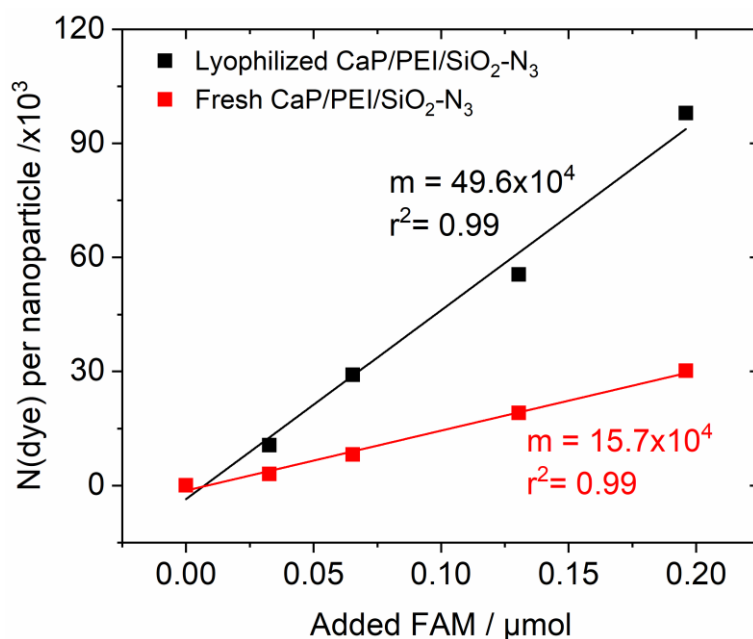


Figure 25: Comparison of the number of FAM molecules per nanoparticle at different FAM-alkyne when using fresh and lyophilized CaP/PEI/SiO₂-N₃ for the click reaction.

Additionally, CuAAC reaction was evaluated at two more temperatures, 8 °C and 37 °C, as shown in Figure 24. In all cases, a good lineal relationship, within the studied range, was observed when increasing the initial alkyne concentration. When performing the reaction at different temperatures a slight influence on the slope was observed as shown in Table 8.

When decreasing the reaction temperature from 20 °C to 8 °C the influence in the reaction was negligible (ratio 1.02). However when increasing the temperature to 37 °C a slightly higher rate was obtained with a 1.15 ratio between the 20 °C and 37 °C reaction temperatures. In general, the rate of variation between these temperatures was approximately 15%. As the reaction was already catalyzed, a slight variation within a small temperature range is expected to occur.

For these three temperatures (8, 20, and 37 °C) is possible to achieve an equivalent nanoparticle labelling. This is of importance, as those temperatures are representative of usual working temperature ranges. Moreover for potential further biological applications or labelling with thermal sensitive materials (e.g. proteins).

For further experiments, the second condition (13.8 μM alkyne initial concentration) at room temperature was chosen as it allowed to have a high labeling density (near 1 molecule per nm^2) with an acceptable reaction yield.

Table 8: Slope comparison after a lineal fitting of the labelling number of calcium phosphate nanoparticles after 1 h CuAAC reaction with different FAM-Alkyne initial molar concentration and temperature (8, 20 and 37 °C).

Temperature / °C	Slope / $\cdot 10^4$	R-Square (COD)	Ratios
8	48.9	0.96	T20 and T8: 1.02
20	49.6	0.99	T37 and T8: 1.17
37	56.9	0.99	T37 and T20: 1.15

For imaging purposes, nanoparticles labelled with AlexaFluor®-488 alkyne derivate were prepared following the procedure described in the experimental section and equivalent results were obtained for this dye. The results are shown in Table 9.

When computing the number of bonded azide groups per nanoparticles the obtained percentage is relatively low between 2-20% from the total azide groups. For heterogeneous reactions different efficiencies are expected when compared to in-solution reactions. In our system, the azide groups are located in the nanoparticles surface and the labelling molecules are in solution. Factor such as the surface orientation of the azide groups and steric hindrance between the approaching molecules limits the reaction effectivity [244].

Table 9: Calcium phosphate nanoparticles characterization after surface modification by click chemistry for nanoparticles used in imaging experiments.

Sample	CaP/PEI/SiO ₂ -FAM	CaP/PEI/SiO ₂ -Alexa-488	CaP/PEI/SiO ₂ -FAM	CaP/PEI/SiO ₂ -ATE	CaP/PEI/SiO ₂ -FAM-TAMRA	CaP/PEI/SiO ₂ -FAM-Cy5
Click reaction method	CuAAC	CuAAC	SPAAC	CuAAC	CuAAC	CuAAC
Solid core diameter by SEM / nm	62	120	70	54	81	106
$V(\text{one nanoparticle}) / \text{m}^3$	$1.25 \cdot 10^{-22}$	$9.04 \cdot 10^{-22}$	$1.80 \cdot 10^{-22}$	$8.24 \cdot 10^{-23}$	$2.78 \cdot 10^{-22}$	$6.23 \cdot 10^{-22}$
$A(\text{one nanoparticle}) / \text{m}^2$	$1.21 \cdot 10^{-14}$	$4.52 \cdot 10^{-14}$	$1.54 \cdot 10^{-14}$	$9.16 \cdot 10^{-15}$	$2.06 \cdot 10^{-14}$	$3.53 \cdot 10^{-14}$
$m(\text{one nanoparticle}) / \text{kg}$	$3.92 \cdot 10^{-19}$	$2.84 \cdot 10^{-18}$	$5.64 \cdot 10^{-19}$	$2.59 \cdot 10^{-19}$	$8.73 \cdot 10^{-19}$	$1.96 \cdot 10^{-18}$
$w(\text{Ca}^{2+}) \text{ by AAS} / \text{kg} \cdot \text{m}^{-3}$	0.0067	0.0728	0.0498	0.0707	0.0322	0.0110
$w(\text{Ca}_5(\text{PO}_4)_3\text{OH}) / \text{kg} \cdot \text{m}^{-3}$	0.0168	0.1825	0.1249	0.1772	0.0807	0.0274
$N(\text{nanoparticles}) / \text{m}^{-3}$	$4.29 \cdot 10^{16}$	$6.43 \cdot 10^{16}$	$2.22 \cdot 10^{17}$	$6.85 \cdot 10^{17}$	$9.24 \cdot 10^{16}$	$1.40 \cdot 10^{16}$
$w(\text{dye}) / \text{kg} \cdot \text{m}^{-3}$	$3.58 \cdot 10^{-4}$	$3.38 \cdot 10^{-3}$	$1.05 \cdot 10^{-3}$	$3.22 \cdot 10^{-3}$	FAM: $1.29 \cdot 10^{-3}$ TAMRA: $3.59 \cdot 10^{-4}$	FAM: $9.35 \cdot 10^{-4}$ Cy5: $1.50 \cdot 10^{-3}$
$N(\text{dye}) / \text{m}^{-3}$	$5.22 \cdot 10^{20}$	$2.63 \cdot 10^{21}$	$7.16 \cdot 10^{20}$	$4.88 \cdot 10^{21}$	FAM: $1.88 \cdot 10^{21}$ TAMRA: $4.63 \cdot 10^{20}$	FAM: $1.36 \cdot 10^{21}$ Cy5: $1.26 \cdot 10^{21}$
$N(\text{dye}) \text{ per nanoparticle}$	$1.22 \cdot 10^4$	$4.10 \cdot 10^4$	$3.23 \cdot 10^3$	$7.12 \cdot 10^3$	FAM: $2.04 \cdot 10^4$ TAMRA: $5.01 \cdot 10^3$	FAM: $9.71 \cdot 10^4$ Cy5: $9.00 \cdot 10^4$
Dye molecules per nm ²	1.01	0.91	0.21	0.78	FAM: 0.99 TAMRA: 0.24	FAM: 2.75 Cy5: 2.55
Surface area per dye molecule / nm ²	0.99	1.10	4.76	1.29	FAM: 1.01 TAMRA: 4.11	FAM: 0.36 Cy5: 0.39
Hydrodynamic diameter by DLS / nm	178	215	173	288	193	186
PDI by DLS	0.40	0.33	0.31	0.41	0.49	0.46
Zeta potential / mV	+26	+24	+26	+24	+27	+27

To take advantage of the free binding sites after the first reaction a second surface reaction was performed using FAM-Alkyne or other dyes such as TAMRA-Alkyne and Cy5-Alkyne. Both dyes have complementary absorption and emission wavelengths and differ structurally [245]. TAMRA-Alkyne has a rhodamine type structure similar in size to the FAM-Alkyne structure, and Cy5-Alkyne has a more lineal structure, which is based on a polymethine conjugate chain system [246, 247]. At the working pH, TAMRA-alkyne is likely to be neutral and Cy5-alkyne negatively charged. The structures of the used dyes are shown in Figure 20.

A simultaneous click reaction using two dye molecules was performed and a preference for one of the dyes was observed by UV-Vis. Under these conditions both dye molecules will compete and the one with a higher affinity and more reactive will be the one to be coupled first to the surface. An example of this behavior is shown in Table 10.

Table 10: Number of molecules per particle after CuAAC click reaction with two simultaneous molecules.

System	Solvent	N (dye) per nanoparticle
FAM-TAMRA	H ₂ O	FAM: $1.5 \cdot 10^3$, TAMRA: 370
FAM-Cy5	65% H ₂ O - 35% DMSO	FAM: $6.2 \cdot 10^3$, Cy5: 500

A two-step reaction is then preferred, *i.e.*, the nanoparticles are first labelled using FAM-Alkyne and as a second step after the first work-up the second click reaction is performed using a different dye. The second dye will react with the free azide positions that are found on the nanoparticle surface after the first reaction. Figure 26 shows a representative UV-Vis and Fluorescence spectra for the dual labelled nanoparticles and Table 9 shows the complete characterization.

TAMRA molecules have a lower water solubility compared to FAM and Sulfo-Cy5 dyes. A mixture of 70% H₂O - 30% DMSO was used for the click reaction to increase TAMRA solubility (TAMRA is soluble in DMSO). At higher DMSO percentages the click

reaction did not work, *i.e.*, no dye molecules were detected on the nanoparticles by UV-Vis or fluorescence. When increasing the DMSO concentration, the click reaction efficiency was affected as the stabilization effect from THPTA ligand was reduced [248].

When comparing the number of TAMRA bonded molecules to Cy5 a lower amount was detected. It is more likely that TAMRA molecules will exhibit a higher steric hindrance to reach the free azide groups on the FAM-labelled calcium phosphate nanoparticle. Also, Cy5 with a more lineal structure has a higher flexibility to reach those groups.

As the obtained particles are highly fluorescent, further microscopy and cellular uptake experiments were performed. In section 8.3.5 these results are shown and discussed.

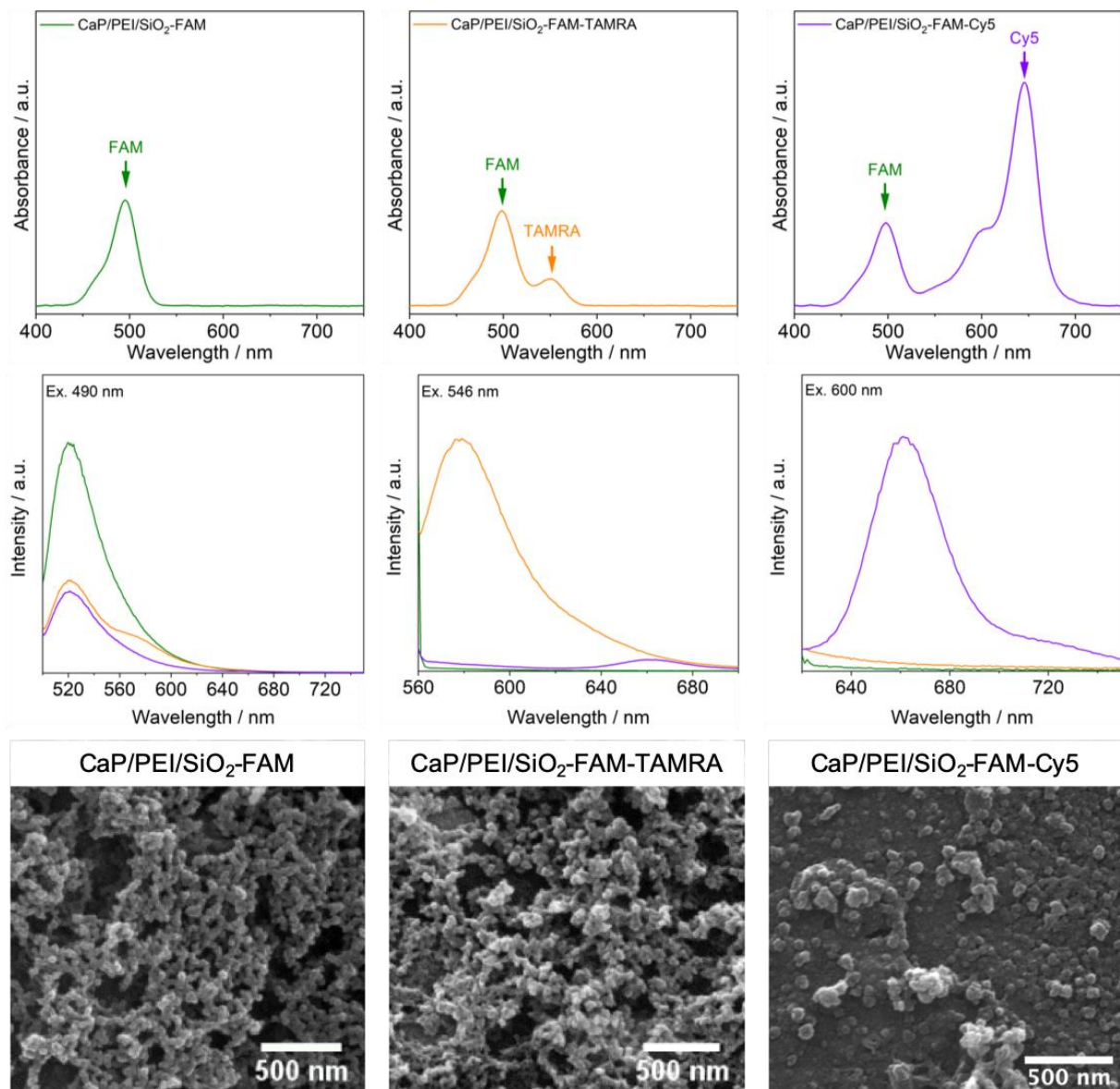


Figure 26: UV-Vis (upper row), fluorescence spectra (middle row) and SEM images for single (CaP/PEI/SiO₂-FAM) and dual labelled (CaP/PEI/SiO₂-FAM-TAMRA, CaP/PEI/SiO₂-FAM-Cy5) calcium phosphate nanoparticles.

8.3.2 Aggregation-induced emission clickable luminophore.

Traditional dyes are usually fluorescent in solutions and when aggregated or highly concentrated the emission decreases due to aggregation quenching [249, 250]. In a different way, luminophores that exhibit aggregation induced emission (AIE) based their emission on the restriction of intramolecular motion or rotation. When constrained, the absorbed light cannot be translated into intramolecular motion that causes the emission [251, 252].

An alkyne-terminated aromatic thioether (ATE, structure shown in Figure 20) was developed and synthesized by Prof. Voskuhl research group. This molecule was clicked on the calcium phosphate nanoparticle surface and its properties were evaluated.

ATE molecule is soluble in DMSO with an absorption maximum at 395 nm. When dissolved in DMSO no emission was detected (*i.e.*, no aggregation occurs) and with > 36% H₂O content an emission near 450 nm is observed (Figure 27). This behavior is reversible when moving from higher water content to lower amounts (< 36% H₂O). A shift in the emission maximum to lower wavelengths was observed when the water content increases due to the formation of aggregates that cannot longer interfere with the surrounding solvent molecules [253].

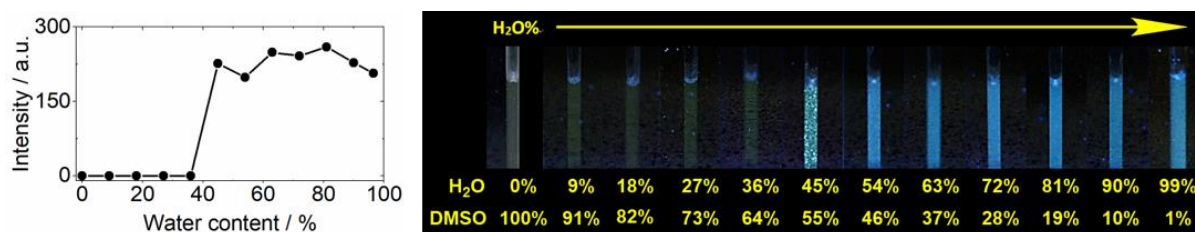


Figure 27: Alkyne-terminated aromatic thioether emission at different DMSO:H₂O ratios. Left, measured fluorescence intensity, Right, sample solution illuminated with a 366 nm UV lamp. The emission is detected at higher water contents.

This molecule was clicked to calcium phosphate nanoparticles using the procedure described in 7.3.1. After the reaction, near 7,120 molecules were measured on the

nanoparticles by UV-vis spectroscopy, which corresponds to an anchoring surface area of 1.29 nm^2 per molecule. The nanoparticles had a hydrodynamic diameter of 288 nm with a PDI of 0.41 determined by DLS and a ζ -Potential of +24 mV. The complete characterization data is shown in Table 9.

Aggregation induced emission properties were tested for the modified nanoparticles. For this, the nanoparticles (CaP/PEI/SiO₂-ATE) were redispersed in solutions of different DMSO:H₂O ratios (25% DMSO, 50% DMSO, 75% DMSO, and 100% DMSO). As shown in Figure 28 the modified nanoparticles exhibit the same AIE properties of the luminophore, at higher amounts of water the emission was observed (“on”), while at lower amounts no fluorescence emission was detected (“off”).

From these results, it is possible to conclude that the coupling on the surface does not affect the dye molecular rotation as no permanent emission was observed and it is still dependent on the dispersant properties (Water:DMSO ratio).

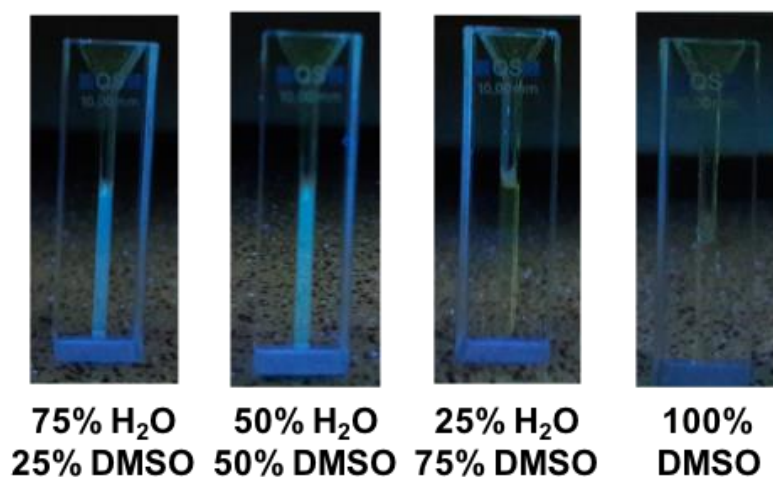


Figure 28: CaP/PEI/SiO₂-ATE nanoparticle dispersion at different solvent conditions illuminated with a UV lamp at 366 nm. The fluorescence occurs only at higher water contents similar to the behavior of ATE molecule alone.

ATE molecule emission is sensitive to the environment, which can influence the molecular rotation and interactions. The effect in the emission of the ionic strength and protein content were evaluated. For this purpose different NaCl and BSA concentrations were used as ion strength modifier and model protein respectively.

First, the fluorescence influence on ATE molecule at different NaCl and BSA concentrations were measured. Figure 29 shows the normalized measured intensity for each type of additive at different concentrations.

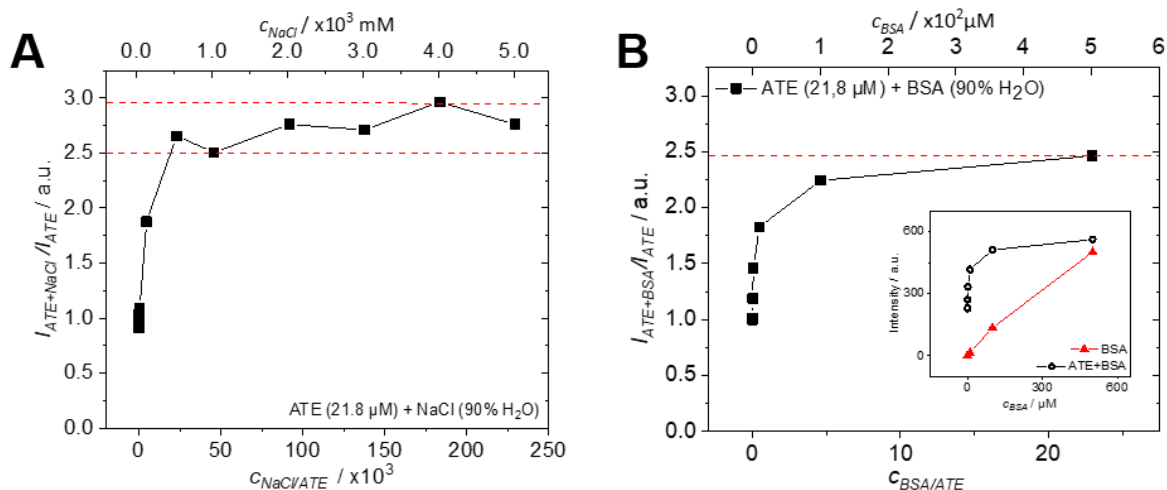


Figure 29: Normalized intensity for ATE molecule after the addition of different concentrations of a) NaCl and b) BSA. The intensity is normalized to the sample intensity without additives.

From Figure 29 it can be seen that the intensity can increase up to 2.5-3.0 times from the original ATE molecule intensity with the addition of NaCl. Regarding the addition of BSA at higher concentrations, an intensity near 2.5 times was also observed. This ratio (~ 2.5 times) based on both systems can be related to the induced fluorescence intensity maximum for this molecule at the studied concentration. Additionally, the effect the protein had over ATE emission was higher than with NaCl, as with a lower amount of protein an equivalent fluorescence emission increment was observed at higher salt concentrations.

This significant difference between both additives suggests that the reason that induces a higher emission is related to the molecular constraint, as the protein generates steric constraint on the molecule, rather than the effect of the additions of ions. This behavior is in agreement with the AIE properties.

The application of BSA as an additive has the limitation that at higher concentrations this protein exhibits autofluorescence at the working emission conditions [254, 255]. As shown in the insert of Figure 29 B, at lower BSA concentrations, the protein

autofluorescence does not interfere with the ATE emission as the detected fluorescence is not due to BSA, and at $< 1 \mu\text{M}$ no significant fluorescence was detected.

For the application of nanoparticles an additional consideration has to be taken into account to test the additive conditions. A higher ion strength and protein content will destabilize the nanoparticle dispersion limiting its application, thus a maximum additive concentration has to be established.

Nanoparticles dispersed in 10 mM and 100 mM NaCl were measured by DLS to analyze the aggregation and stability of the dispersion. The dispersion at 100 mM NaCl showed a higher aggregation and polydispersity index, 3 and 2 times higher than the nanoparticles in water respectively. On the other hand, at 10 mM the results were comparable with the nanoparticles dispersed in water. For this reason, a maximum of 10 mM NaCl concentration was used for the analysis with the nanoparticles.

Regarding the BSA maximum concentration, a dispersion with up to $2 \mu\text{M}$ BSA was viable with the nanoparticles. However, with a $5 \mu\text{M}$ BSA concentration the protein was no longer completely dissolved after the addition of the nanoparticles, a higher turbidity was observed. For this reason a maximum concentration of $2 \mu\text{M}$ BSA was used with the nanoparticles.

Figure 30 shows the effect the additives had on the nanoparticles dispersion emission at three different additive concentrations and with a mixture of both. As observed from the graph, the influence the additives had at the working concentrations was small, and both ATE molecule and CaP-ATE exhibited the same trend. The addition of BSA caused an intensity increment of near 20 %, and with NaCl the change was negligible. With the mixture of both additives, the detected intensity growth was mostly caused by the BSA influence rather than by NaCl as a similar intensity ratio was obtained with only BSA.

To discard any influence of the nanoparticles on the detected emission with BSA additive system (*i.e.*, nanoparticles can potentially interact with the protein and induce

an emission), nanoparticles without ATE molecule (CaP/PEI/SiO₂) were assayed at the same conditions and no fluorescence signal was detected at the region of interest.

The effect in a double concentrated ATE or CaP-ATE dispersion was also evaluated. The same trend was observed, *i.e.*, a higher intensity ratio was detected when BSA was added compared to NaCl. It is important to take into account that due to the solvent exchange step the final ATE and CaP-ATE concentrations are slightly different (not an exact double concentration).

In general, at these concentrations the influence was practicable negligible. As observed before, with a higher concentration of additives or additive/molecule ratios the influence in the intensity becomes near 250% higher and at these ratios the system can have potential for fluorescence applications. Due to the nanoparticles dispersion stability or ATE concentration within the nanoparticle, the working range became very narrow reducing the additives effect on the fluorescence emission. Still the nanoparticles dispersed in water showed the ATE characteristic emission that can be easily detected.

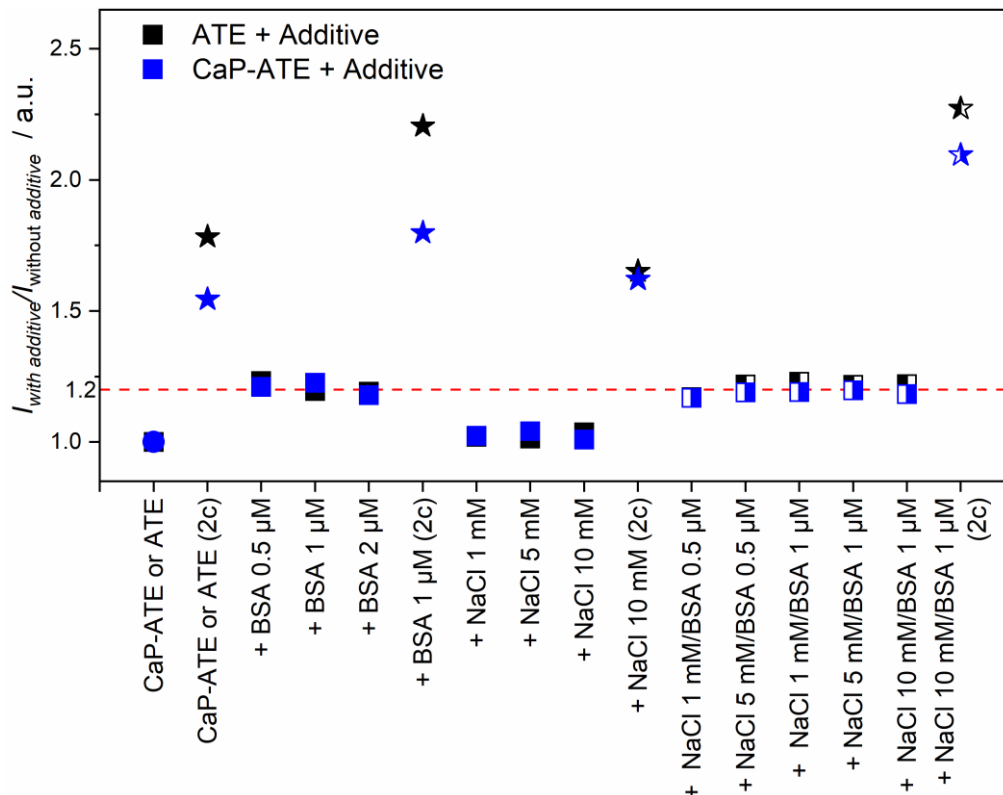


Figure 30: Normalized intensity of the ATE molecule and CaP/PEI/SiO₂-ATE nanoparticles with different NaCl and BSA concentrations. The intensity was normalized to the sample without additives.

8.3.3 BSA as a general protein model for click reaction.

Albumin protein is one of the most abundant proteins in the mammalian plasma [256]. This globular protein is relatively small (66 kDa) and stable, which makes it useful as a general model of a protein. Bovine serum albumin (BSA) consists of 583 amino acids from which 60 are lysine residues [257, 258]. To make this protein appropriate for click reaction, a crosslinker is needed to introduce an alkyne functionality into it. Additionally, the crosslinker works as a spacer between the surface and the protein reducing the direct biomolecule-nanoparticle interactions [244].

For this purpose, propargyl-N-hydroxysuccinimidyl ester crosslinker was used (Figure 31). The NHS ester reacts with the primary amine groups found in the protein, like in the lysine amino acid side chain [259]. The reaction between the NHS ester and the amine group proceeds under near neutral pH generating a stable amide bond between both species and with inclusion of the propargyl functional group.

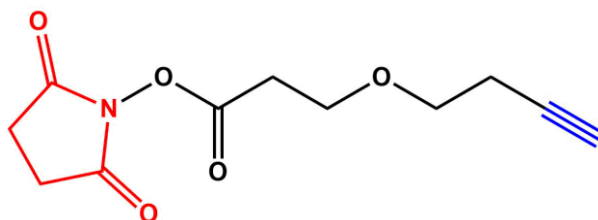


Figure 31: Propargyl-N-hydroxysuccinimidyl ester structure.

By CuAAC click reaction, the modified protein was coupled to the surface of calcium phosphate nanoparticles. To determine the number of BSA units on the nanoparticle surface, the extinction coefficient for the labelled protein was measured, by preparing and measuring a solution of known concentration, and determined to be $5.89 \cdot 10^4 \text{ L} \cdot \text{mol}^{-1} \cdot \text{cm}^{-1}$.

After the click reaction the nanoparticle had an average core size of 50 nm. (Figure 32), a hydrodynamic diameter of 352 nm (Pdl 0.40), and a zeta potential of +35 mV. The number of protein units per nanoparticle was measured by UV-Vis and

near 5,290 proteins were calculated. When taking into account the nanoparticle surface area and the number of protein units an anchor size on the surface of 1.5 nm² or 0.7 proteins per nm² were calculated.

When comparing this value to the literature a higher protein density was obtained with the prepared system. It has been reported: for calcium phosphate particles 0.014 proteins per nm² [260]; for SiO₂ 0.002 proteins per nm² [261]; porous and non-porous SiO₂ NP 0.001-0.020 proteins per nm² [262]; TiO₂ 0.017 proteins per nm² [261] and 0.006-0.032 proteins per nm² on a gold surface with self-assembled monolayers [263]. All these values corresponded to the physical absorption of the protein with the surface and no chemical reaction was performed, which is likely to be lower.

As observed from previous examples and as expected, a positively charge surface will have higher absorption due to the better affinity to the negatively charged BSA (at neutral pH). This tendency was also observed for gold nanoparticles with different crosslinkers [264]. Additionally, Phan *et al.* observed that a higher BSA protein packing density is obtained for charged surfaces compared to neutral ones [263].

In our system, as the chemical reaction occurs it is expected to have a higher number of proteins per particle, which react and increase the protein density in the surface. Additionally, the used crosslinker (one PEG spacer measures approx. 0.28 nm [265]) with BSA allowed a higher rotation flexibility. Thus more molecules can access and fit onto the surface.

Another factor to take into consideration with our nanoparticle system is the surface roughness. Due to the presence of PEI and the silica coating around the nanoparticle, and as observed from electron microscopy, the synthesized nanoparticles have a degree of roughness on the surface and is not a perfect flat surface. This aspect contributes to a higher binding of molecules in different orientations and positions on the surface.

Naturally, there exists a physical limitation on the number of proteins that can bind to the surface and this value depends on the protein size. BSA in solution can exhibit two shapes, a triangular one (N form) at pH near 4-9, with a footprint area of 27.6 nm² or

36.7 nm² depending on the side, and an elongated (E form) at acid pH (<4) with a footprint area of 53.1 or 4.4 nm² depending on the orientation [266]. These values also agree with the previously reported dimensions of BSA in solution with an ellipsoid shape of 14 nm x 4 nm (area of 16 or 56 nm²) [263, 267].

From these dimensions, a theoretical maximum number of molecules per particle can be calculated for the nanoparticle surface assuming a regular surface. A number between 210 and 490 proteins for the N form, and from 150 to 1800 proteins with the E form can theoretically be found. These values do not take into account any hydration effect on the protein. In our case, due to the solution pH, the protein N form is more likely to occur during the reaction.

Our labelled nanoparticle shows near 10-20 times more units as theoretically expected for N form and between 3-40 times for E form. As mentioned before, different factors can influence a higher protein density, although a multilayer (even with some physically absorbed proteins) is likely to happen and cannot be excluded due to the high affinity the protein has to the surface.

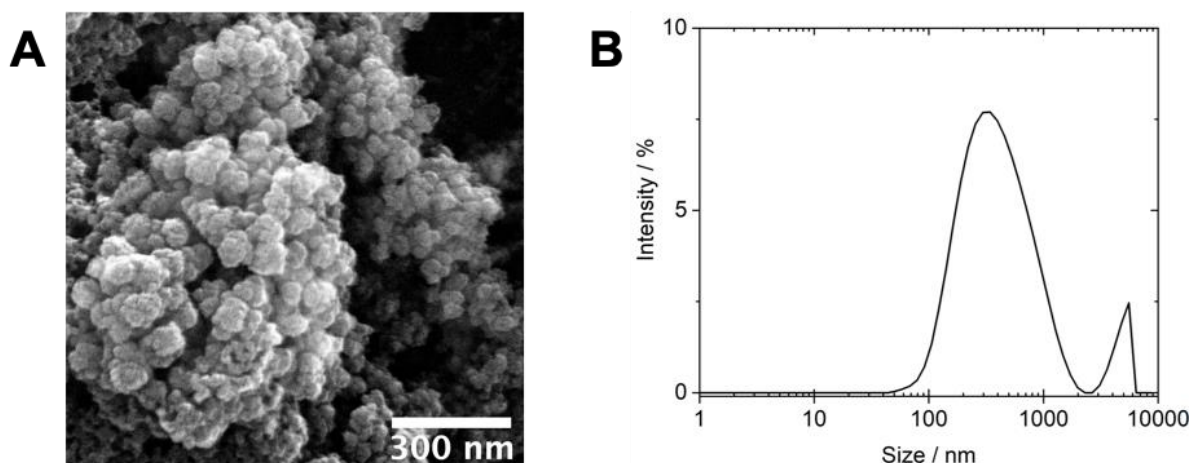


Figure 32: A) Scanning electron microscopy micrograph and B) DLS size distribution of CaP/PEI/SiO₂-BSA-647 nanoparticle.

8.3.4 Strain-promoted cycloaddition (SPAAC) click reaction

The strain-promoted cycloaddition represents an alternative to the copper catalyzed cycloaddition. The alkyne functional group is contained in a highly constraint ring which makes it react spontaneously with an azide to produce a triazole ring. This approach has the advantage of not requiring copper as catalyst, so no reducing agent (ascorbic acid), stabilization ligand (THPTA), nor protectant (aminoguanidine) are needed. Additionally, it eliminates any potential toxicity due to copper absorption into the nanoparticles.

This reaction was studied with the azide terminated calcium phosphate nanoparticles and DBCO-PEG4-5/6-FAM as model molecule (structure is shown in Figure 20). In this case, the molecule has four polyethylene glycol units as spacer between the FAM dye and the DBCO reactive functional group that helps to reduce the steric hindrance between both sections and the surface.

The nanoparticles were prepared following the procedure described in the experimental section. Figure 33 shows a representative SEM image, UV-Vis spectra, fluorescence spectra and DLS size distribution. Table 9 has the complete characterization data.

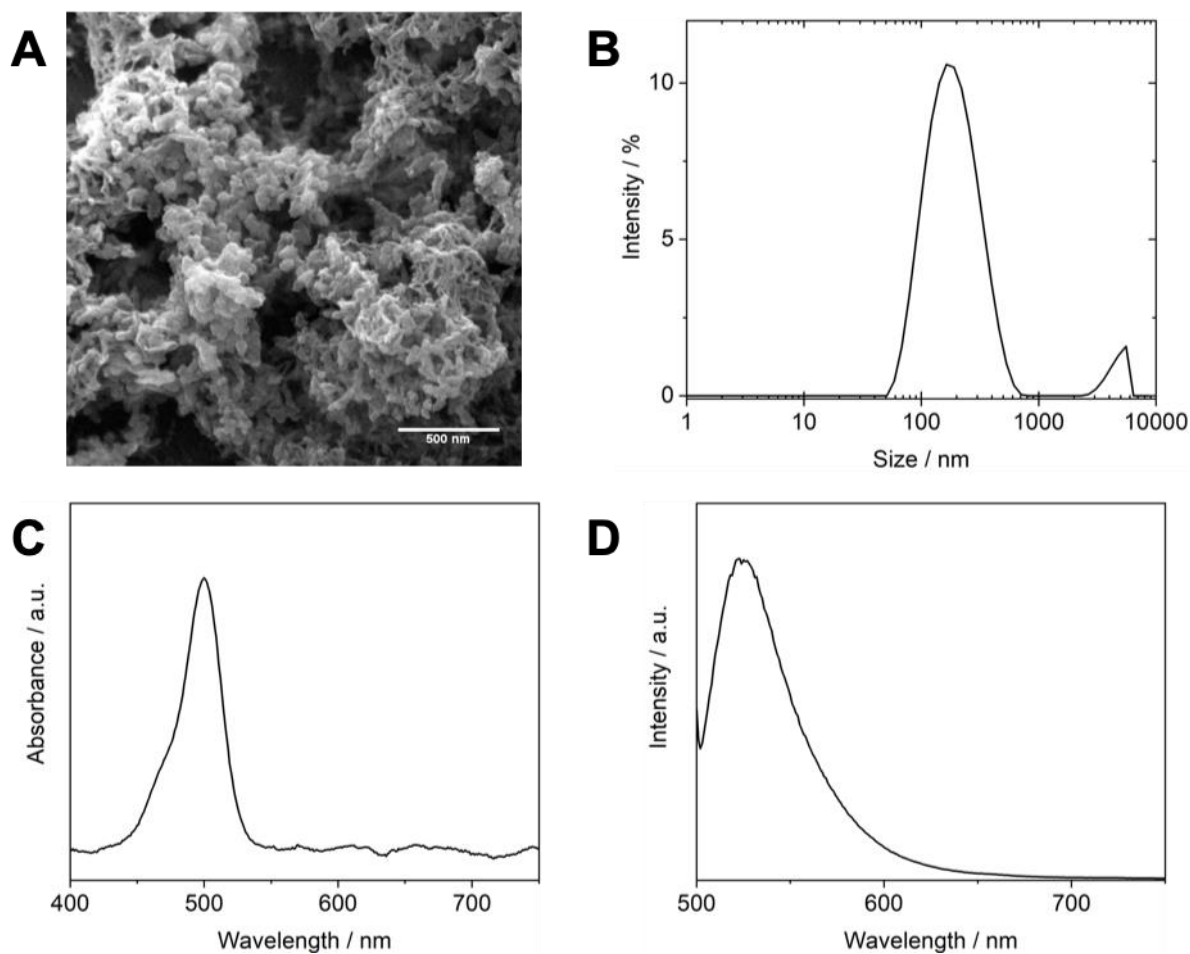


Figure 33: A) SEM micrograph, B) DLS size distribution, C) UV-Vis spectra, D) fluorescence spectra of CaP/PEI/SiO₂-FAM by SPAAC click reaction.

For this system after one hour reaction time, when compared to CuAAC reaction, the SPAAC reaction at 20 °C is near 17 times slower as shown in Figure 34. This behavior was expected because previous studies have reported a slower reaction rate constant for SPAAC in solution (usually 10-100 times slower than CuAAC) [35].

To compensate the lower reaction speed for SPAAC (*i.e.*, less amount of coupled molecules onto the surface) a longer reaction time with the nanoparticles can be performed. SPAAC reaction does not have the 1 hour reaction limitation like CuAAC, no pH acidification occurs with the reaction. A comparison of different reaction times was performed with observation points after 1 h, 4 h, 6 h, and 12 h. As observed in Figure 35, with longer incubation times the number of dye molecules per nanoparticle increases. After a 24 h reaction time, it was not possible to fully redisperse the

nanoparticles, thus this longer reaction time is not recommended and was not used in the calculations.

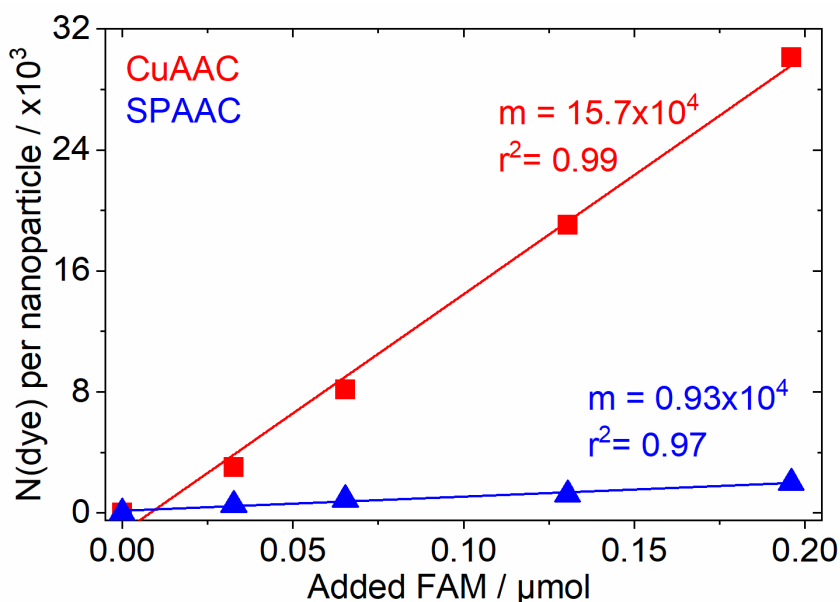


Figure 34: Comparison of CuAAC and SPAAC reactions at different initial dye molecule concentrations at room temperature and 1 hour reaction time.

Table 11 shows a comparison between the obtained number of dye molecules per nanoparticle for SPAAC and CuAAC. After 4 hours of reaction time with SPAAC method, it was possible to reach a similar surface labelling as with CuAAC (with a one hour reaction). This overcomes the lower coupling observed after 1 hour with still a reasonable reaction time. Moreover, this time dependence labelling approach permits to adjust the surface modification density in a controllable way and allows to adjust the molecule density from a lower to higher density with an initial constant dye concentration.

Additionally, when performing the SPAAC reaction at 8 °C and 37 °C a variation of near 32% was observed between both slopes. A higher number of labelling molecules were obtained at 37 °C. In this range the temperature influence for SPAAC was almost the double compared to the 15.3% of CuAAC. This temperature effect is reasonable, as SPAAC reaction energetic barrier can be better overcome when the reaction temperature is increased. This situation is attenuated for CuAAC because the reaction is already catalyzed by Cu(I).

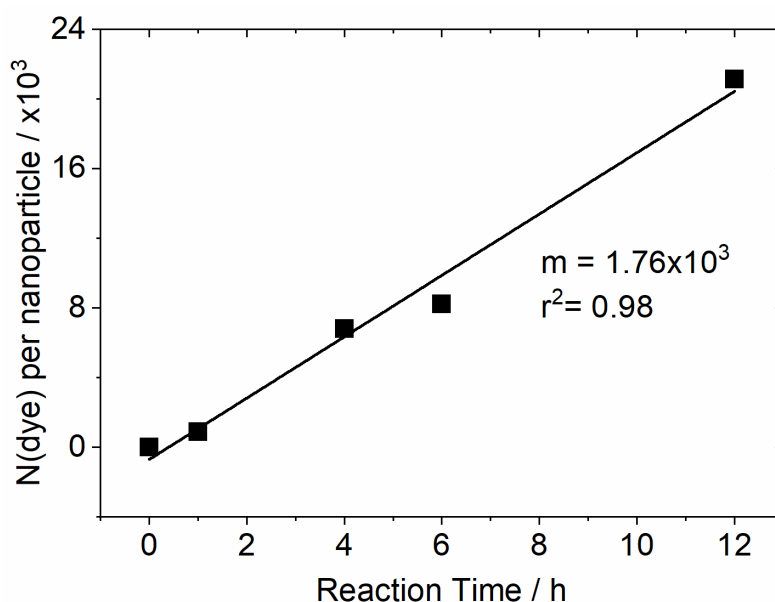


Figure 35: SPAAC reaction with a constant initial dye concentration of 0.06 μmol FAM-DBCO at different reaction times (1, 4, 6, and 12 h).

Table 11: Number of dye molecules on the calcium phosphate nanoparticles surface after different reaction times by SPAAC click reaction after the addition of 0.06 μmol FAM. As comparison CuAAC with 1 hour reaction time is shown.

Reaction Time / h	$N(\text{FAM})$ per nanoparticle	Dye molecules per nm^2
1	$8.83 \cdot 10^2$	0.08
4	$6.79 \cdot 10^3$	0.60
6	$8.21 \cdot 10^3$	0.36
12	$2.11 \cdot 10^4$	1.87
CuAAC (1 h)	$8.16 \cdot 10^3$	0.72

8.3.5 Nanoparticles studies by fluorescence microscopy

After the surface modification by click reaction described in the previous sections, highly fluorescent calcium phosphate nanoparticles were obtained and were suitable for fluorescence microscopy.

To start, green fluorescent nanoparticles (CaP/PEI/SiO₂-AF488) were observed directly by Confocal Laser Scanning Microscopy (CLSM) and Structured Illumination Microscopy (SIM). Figure 36 shows representative images of the direct observation of the nanoparticles by both techniques. For this, an aliquot of a dilute nanoparticles dispersion was placed on a cover slide, and let it dry. Then the cover slide was mounted on the slide using the mounting media and sealed (further details of the preparation are in the Methods section).

The used nanoparticles had an average core size of 120 nm determined by scanning electron microscopy. With this size the particle diameter is below the resolution limit of CLSM and close to the limit for SIM, although the particles might not be perfectly resolved it is still possible to identify them.

As observed in the distribution histograms from Figure 36, the determined average size reflects indirectly the resolution capacity of both techniques. A lower value and narrower distribution is obtained by SIM, due to a better capacity to distinguish adjacent nanoparticles. The average size of 180 nm (by SIM), although somehow higher, is still in agreement with the dimension observed by SEM.

These average diameters (260 nm CLSM, 180 nm SIM) will be later used as the reference size of the nanoparticle for these microscopy techniques (CLSM and SIM).

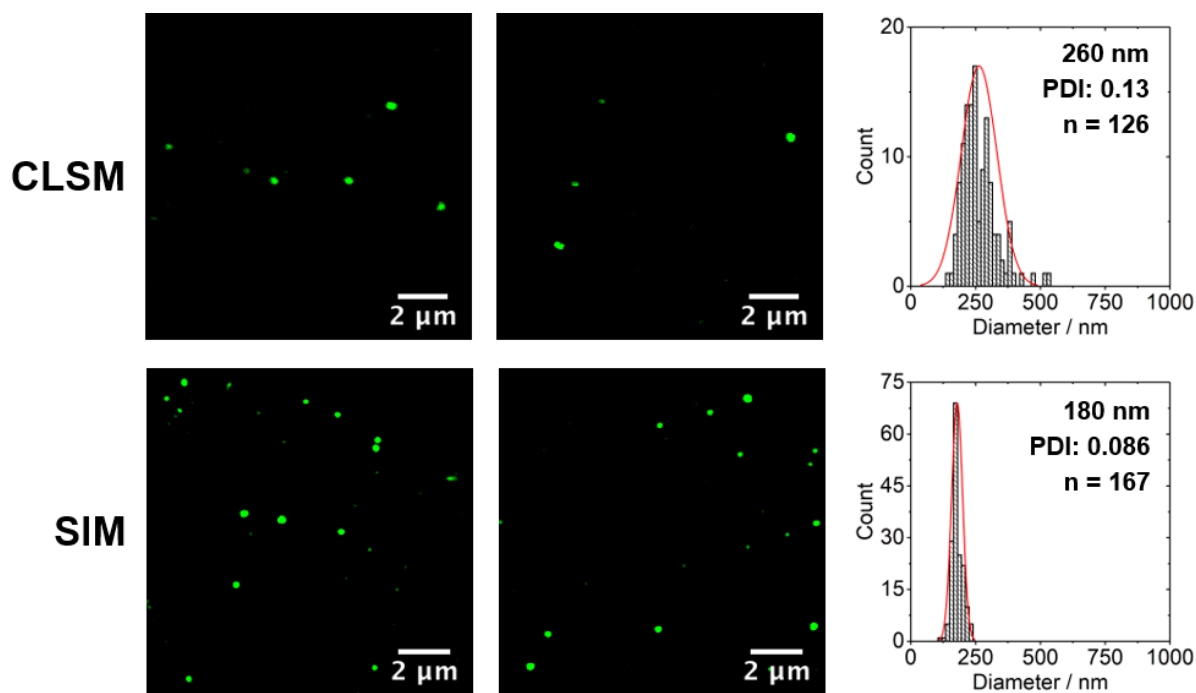


Figure 36: Size distribution comparison of CaP/PEI/SiO₂-AF488 nanoparticles by confocal laser scanning microscopy (CLSM) and structured illumination microscopy (SIM). Nanoparticles are shown in green color.

8.3.6 Calcium phosphate nanoparticle cellular uptake

It is of interest to study the cellular uptake of the synthesized calcium phosphate nanoparticles by click chemistry using higher resolution microscopy techniques and to evaluate the performance of the labelling method under cellular uptake conditions. For this purpose HeLa cell line was used.

On previous works [44], it has been demonstrated that for this cell line the cellular uptake of calcium phosphate nanoparticles starts after three hours of incubation. Figure 37 shows a CLSM image after a 24h cellular uptake of CaP/PEI/SiO₂-AF488 nanoparticles. The nanoparticles are shown in green color and can be identified inside the cell.

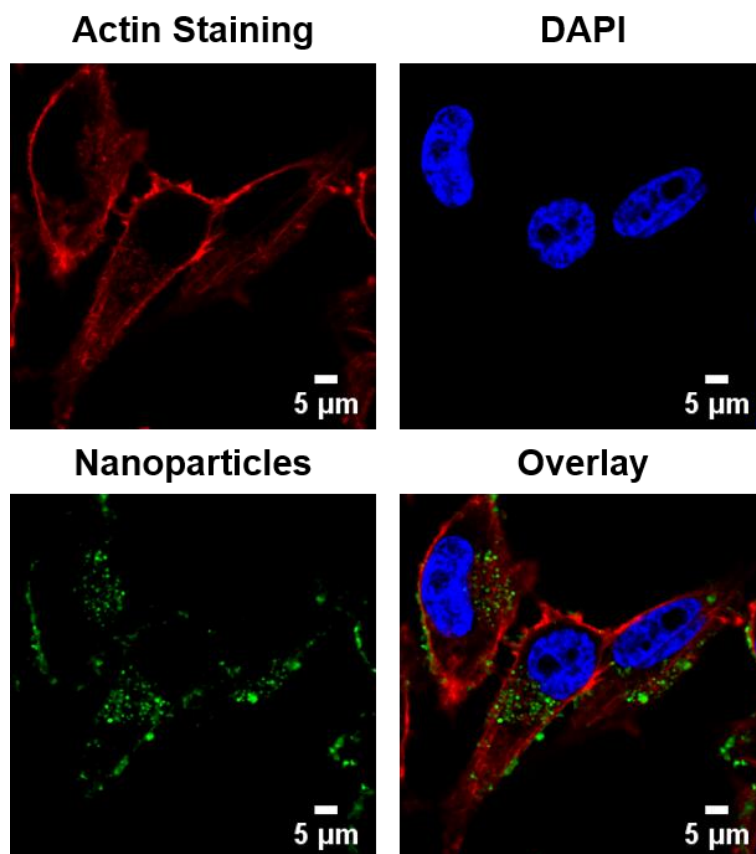


Figure 37: CLSM images of HeLa cells after 24 h incubation with CaP/PEI/SiO₂-AF488 nanoparticles. Labeled nanoparticles are shown in green (AF-488). The cell nucleus is stained blue by DAPI and actin staining for the cytoskeleton is shown in red.

To further confirm that the nanoparticles are inside the cell and do not lay on its surface a z-stacking with CLSM was used, as shown in Figure 38. As observed in these images, the nanoparticles can be clearly identified inside the cell volume and it confirms the uptake of the prepared nanoparticles. The cell nucleus was stained with DAPI as localization and height reference.

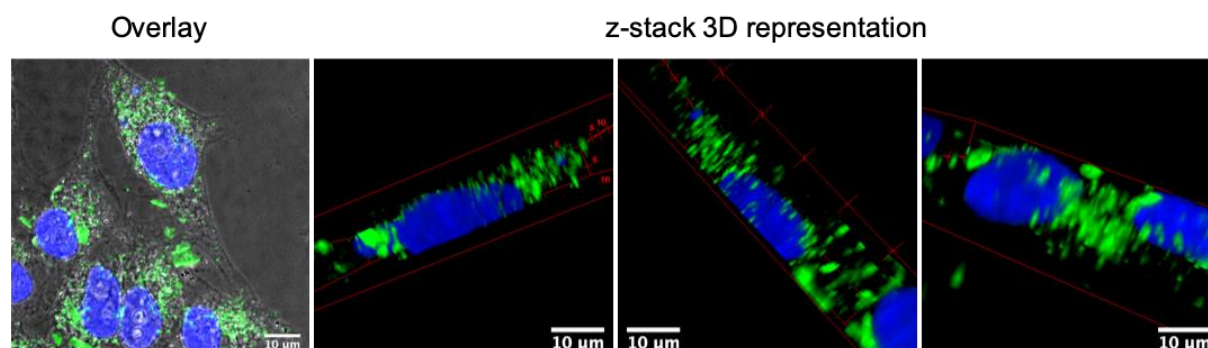


Figure 38: CLSM images of HeLa cells after 24 h incubation with CaP/PEI/SiO₂-AF488 nanoparticles and a 3D representation of z-stack images to confirm that the nanoparticles are inside the cells. Nanoparticles are shown in green (AF-488) and the cell nucleus in blue (DAPI).

Additionally, Figure 39 shows representative images of the cellular uptake of CaP/PEI/SiO₂-ATE nanoparticles. As described in the previous sections, in aqueous environment the coupled ATE molecule will exhibit its emission due to rotational constraint and can therefore be detected. With the coupling to the nanoparticle the dye can be transported to the cell.

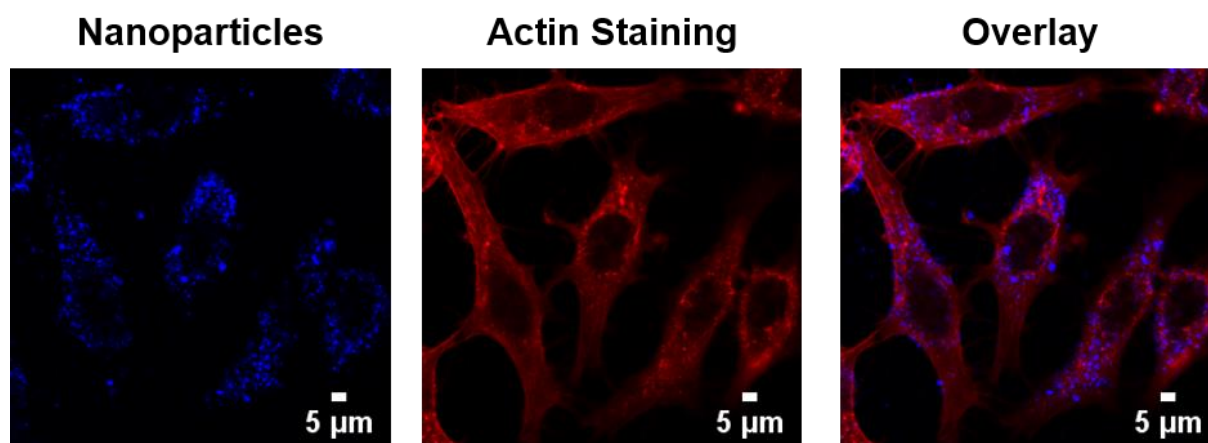


Figure 39: CLSM images of HeLa cells after 24 h incubation with CaP/PEI/SiO₂-ATE nanoparticles. Labeled nanoparticles are shown in blue (ATE). Actin staining for the cytoskeleton is shown in red. Cells were not stained for DAPI as ATE has an excitation and emission wavelength similar to DAPI.

The synthesized dual labeled nanoparticles were also observed by CLSM after cellular uptake. Figure 40 shows representative images and evidences a good colocalization of both dyes even after cellular uptake. A yellow color indicates colocalization of FAM-TAMRA (green + red = yellow) and white of FAM-Cy5 (green + purple = white).

Furthermore, with CLSM z-stack imaging the colocalization in different planes was observed. Figure 41 shows a z-stack maximum projection and 3D representation for the dual labelled nanoparticle (CaP/PEI/SiO₂-AF488-AF647), for which is possible to confirm also a good colocalization in the 3D reconstruction. The nanoparticle was labelled in green (AF488) and purple (Cy5), the colocalization is observed as whitish spots (due to an intensity variation between both channels the whitish intensity is opaque by the green channel in the overlay).

In all cases, the coupling method allows to have a strong covalent bond between the labelling molecule and the nanoparticle surface. Additionally, for the dual labeled nanoparticles it can be confirmed that the labelling occurred in the sample particle as evidenced with the CLSM images. In general, the labelling (*i.e.*, chemical bond) survives the cellular uptake process making it suitable for transportation in cellular applications.

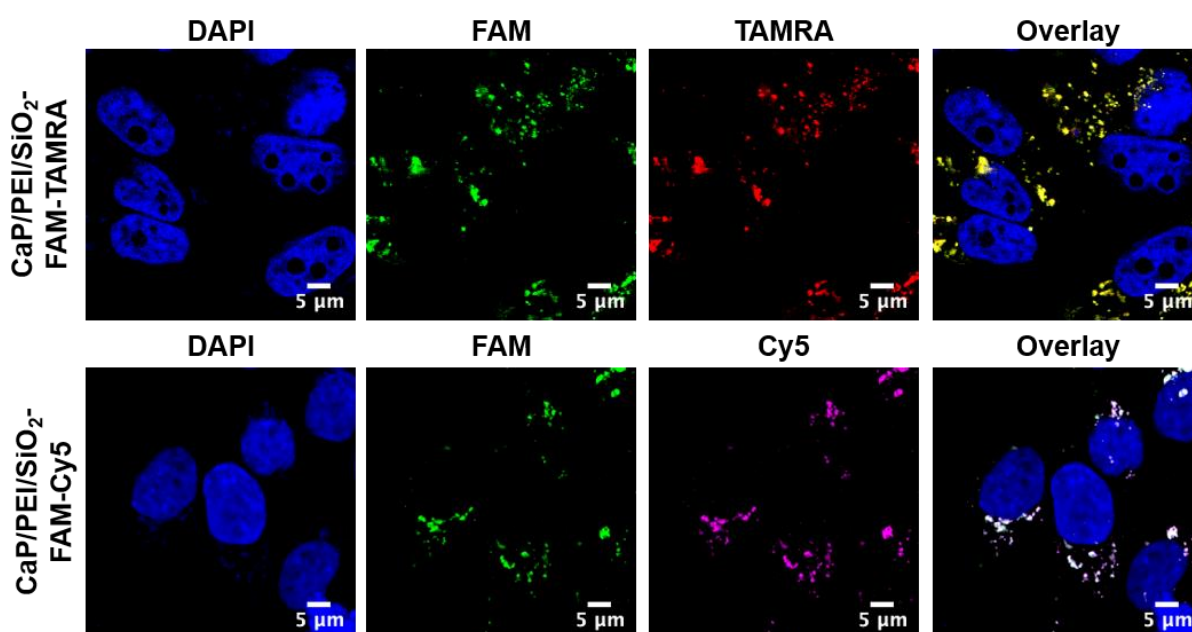


Figure 40: CLSM images of HeLa cells after 24 h incubation with dual-labelled CaP/PEI/SiO₂-FAM-TAMRA and CaP/PEI/SiO₂-FAM-Cy5 nanoparticles. The nucleus is stained with DAPI (blue), labelled nanoparticles are shown in green (FAM), red (TAMRA) and purple (Cy5).

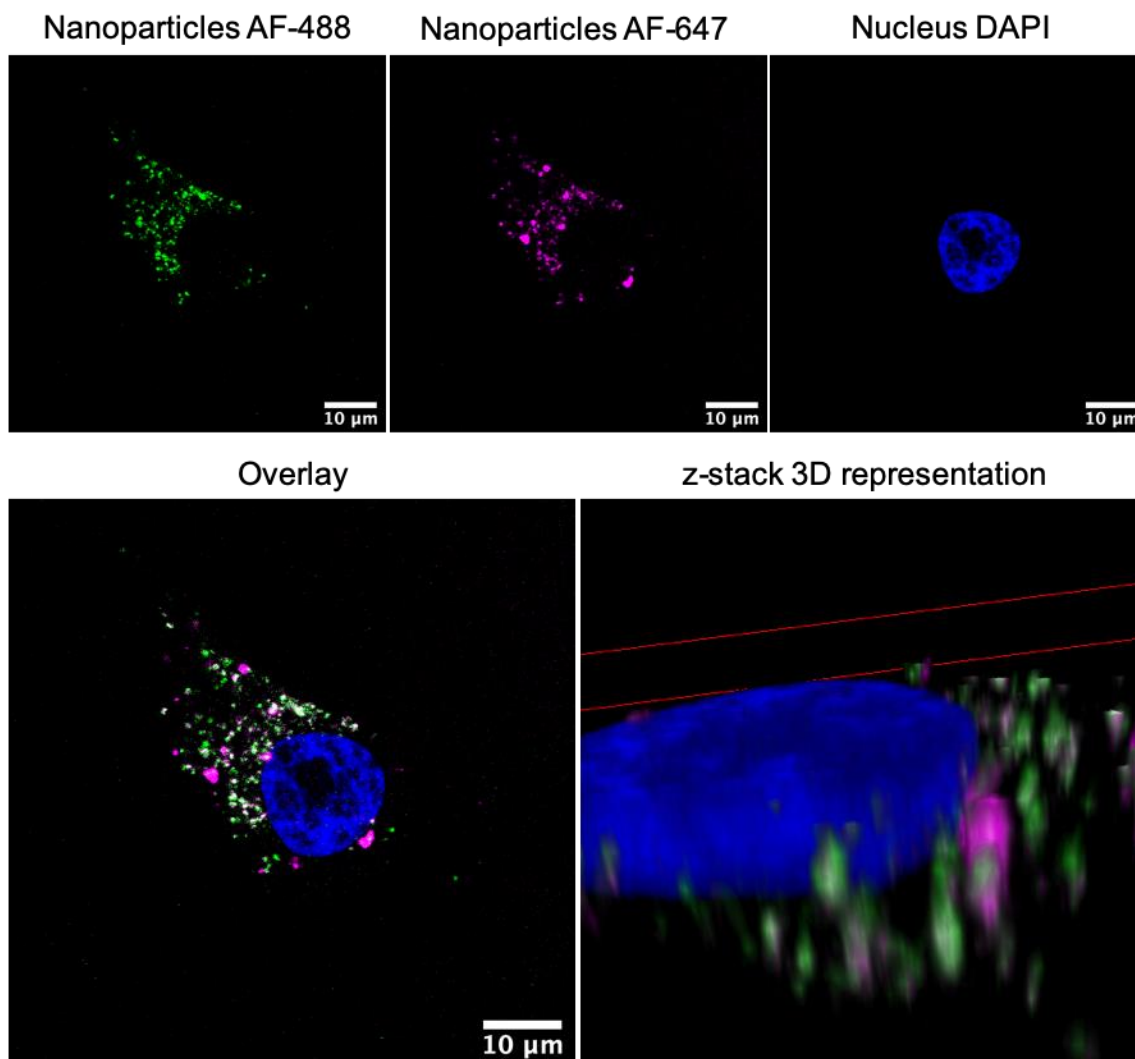


Figure 41: Confocal scanning microscopy z-stack imaging of dual labelled CaP/PEI/SiO₂-AF488-AF647 nanoparticles after cellular uptake (24 h) by HeLa cells. A z-stack maximum projection and 3D representation is shown. Nanoparticles are shown in green (AF-488) and purple (AF-647) and nucleus in blue (DAPI). Colocalization is shown in white.

The nanoparticle size after cellular uptake was also determined by CLSM and SIM using CaP/PEI/SiO₂-AF488 labelled nanoparticles. AF488 labelled nanoparticles (Ex. 488 nm) were chosen among the others because the green excitation laser allows to have a better achievable resolution when compared to larger wavelengths (e.g., Cy5, AF647, Ex. 647nm) as the optical resolution is dependent of the used wavelength.

Figure 42 shows the nanoparticle size distribution after uptake. When comparing the size after cellular uptake using CLSM and SIM microscopy a similar value is obtained like for the nanoparticles alone (without cellular uptake, Figure 36). From the results

obtained with these techniques, it is possible to conclude that these nanoparticles are likely to be individually inside the cell instead of highly aggregated after cellular uptake, *i.e.*, one nanoparticle per endosome-lysosome.

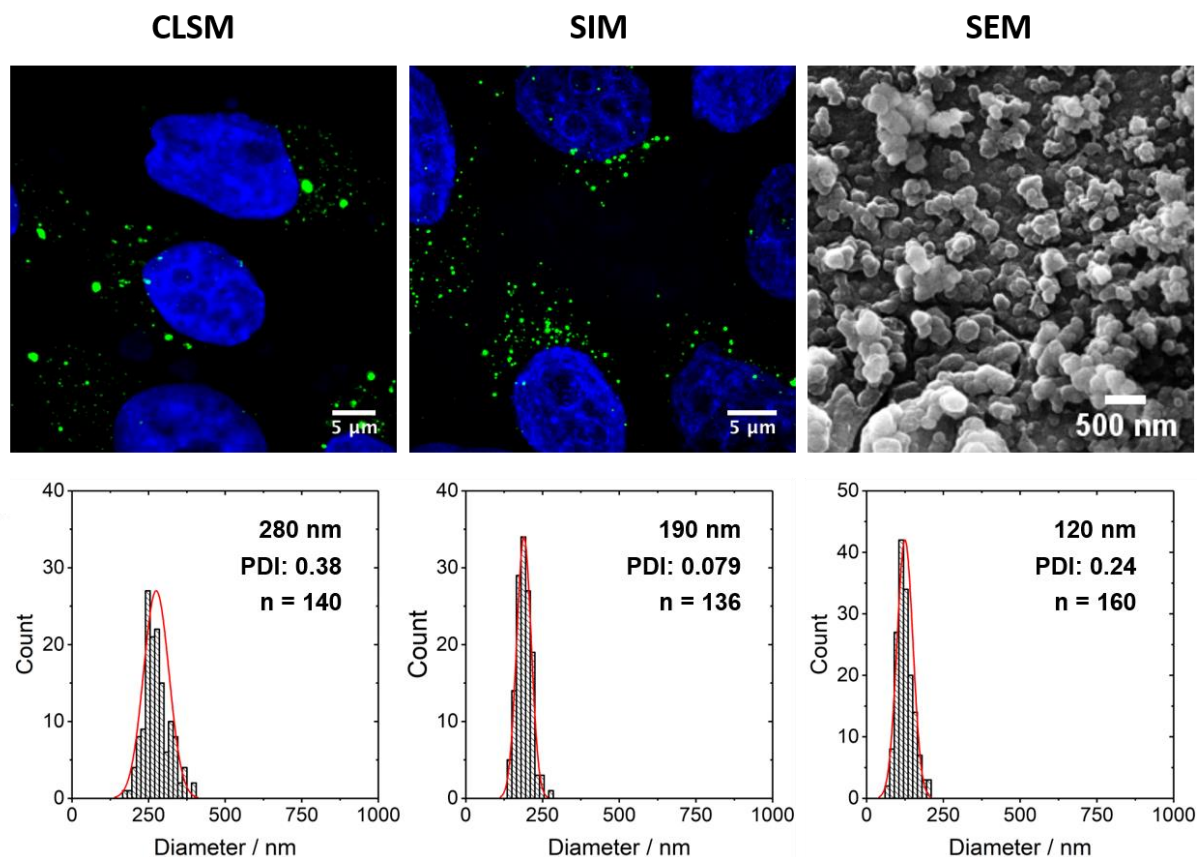


Figure 42: Particle size distribution of CaP/PEI/SiO₂-AF-488 nanoparticles after incubation of HeLa cells for 24 h with nanoparticles by CLSM, SIM, and SEM (pure nanoparticles without cells for comparison). The green channel shows the labelled nanoparticles, and the blue channel shows the nucleus stained with DAPI.

To further study these nanoparticles, stochastic optical reconstruction microscopy (STORM) was used. This microscopy localization based method has a resolution capability of near 20-40 nm [199, 268], that corresponds to almost four times the resolution capacity of SIM, making it suitable for our nanoparticles system.

Nanoparticles cell uptake by HeLa cell line using STORM microscopy and CaP/PEI/SiO₂-AF488 nanoparticles (with an average core diameter of 52 nm by SEM) was studied. Figure 43 shows an STORM reconstruction image of the nanoparticles after 24 hours of cellular uptake and its comparison view with widefield microscopy at

lower resolution. As observed the nanoparticles can be clearly detected inside the cell membrane. The nanoparticle average diameter size was calculated and found to be near 96 nm within the cell. Figure 44 shows the size distribution histogram for CaP/PEI/SiO₂-AF488 and CaP/PEI/SiO₂-BSA647 nanoparticles. Between both labelled nanoparticles equivalent results were obtained, although BSA-647 modified nanoparticles showed a higher variation in the histogram distribution related to a higher nanoparticle aggregation caused by the protein coupling.

The obtained average size by STORM method has an improvement factor close to two when compared with the previous value measured by SIM (190 nm, Figure 42) and agrees with the better resolution capacity of this technique.

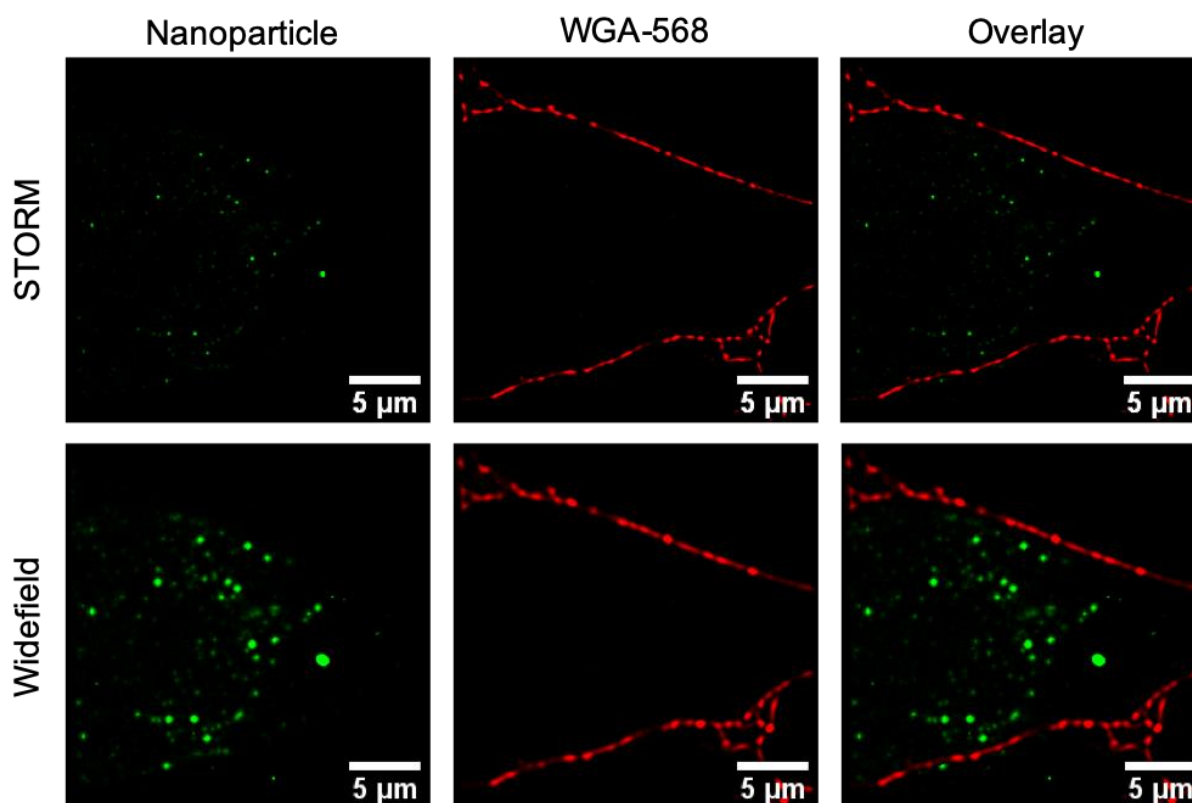


Figure 43: STORM imaging of HeLa cells after 24 h incubation with CaP/PEI/SiO₂-AF-488 nanoparticles. The green channel shows the labelled nanoparticles, and the red channel cell membrane stained with WGA-568.

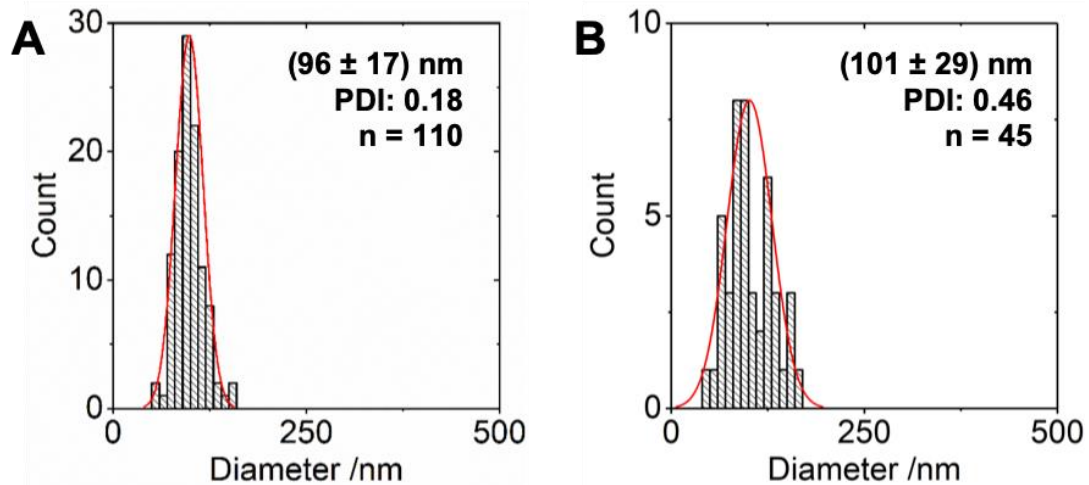


Figure 44: STORM microscopy size distribution histogram for nanoparticles a) CaP/PEI/SiO₂-AF488 and CaP/PEI/SiO₂-BSA647.

The nanoparticles are usually taken up by the cells following a micropinocytosis [228]. In this case, the cell membrane is extended to form an encapsulating cavity around the extracellular fluid in which the nanoparticles are trapped and the endosome formed [129, 133]. Figure 45 shows an example of this process from a STORM reconstructed image which allows a better resolution to detect the calcium phosphate nanoparticle. From the image it can be observed that on the outside part of the cell membrane where the micropinocytosis takes place a small aggregate of nanoparticles is observed, but after the endosome formation (inside the cell) the nanoparticles are mostly detected as independent particles or lightly aggregated. This agrees with the previous observation based on the nanoparticle size comparison between SIM and CLSM techniques.

Later in the process, the endosomes with the NPs are likely to fusion with lysosomes to continue into the degradation pathway. As the nanoparticles contain PEI in its core, they are mostly able to escape from the endosomes-lysosome compartment by the so-called proton sponge effect [224]. This means that not necessarily all the up taken nanoparticles end up in the lysosomes until degradation. For the sake of transfection or gene silencing applications the lysosomal escape is of importance otherwise the nucleic acid loading would be degraded.

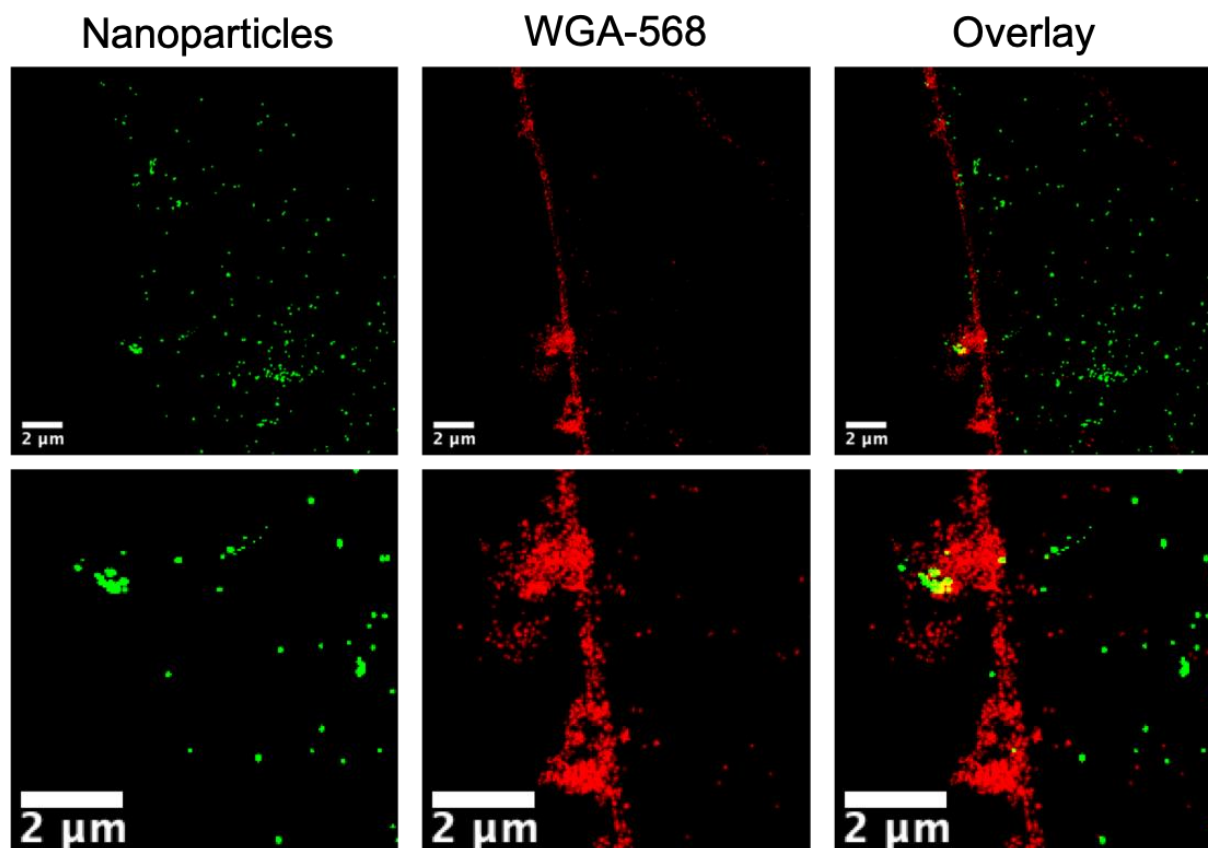


Figure 45: STORM microscopy images of the endocytosis of labelled calcium phosphate nanoparticles in a HeLa cell. The green channel shows the nanoparticles and the red channel the cell membrane. The lower row shows a magnified region.

Calcium phosphate nanoparticles localization detection inside lysosomes or early endosomes have been performed by other authors with immunostaining [42] or by LysoTracker™ [47, 133] using CLSM, although with confocal microscopy its resolution limits the capacity to clearly identify separate nanoparticles (if any) in the detected region.

For this purpose, STORM super-resolution microscopy and the highly fluorescent calcium phosphate nanoparticles were used. By immunostaining, the lysosomes were stained with LAMP-1 antibody and an AF-647 labelled secondary antibody for imaging. Figure 46 shows a representative STORM image with colocalization between the nanoparticles and lysosomes.

From the image, single nanoparticles can be identified where some of them are localized in the lysosomes. The measured size of the nanoparticle in the lysosomes

mostly agrees with the average size previously obtained for this technique. An enlarge image of the lysosome region is shown in Figure 47.

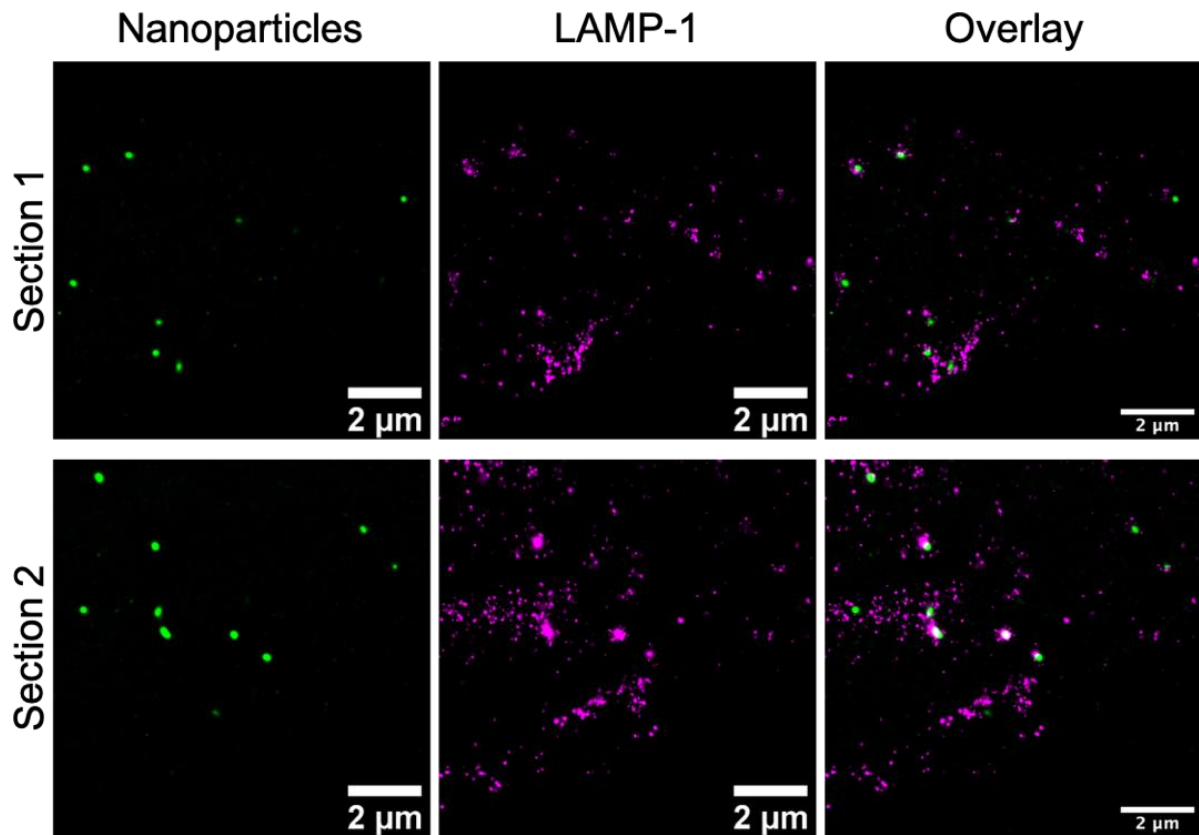


Figure 46: STORM imaging of HeLa cells after 16 h incubation with CaP/PEI/SiO₂-AF-488 nanoparticles. Green channel (AF-488) shows the labelled nanoparticles and the magenta channel (AF-647) stained LAMP-1.

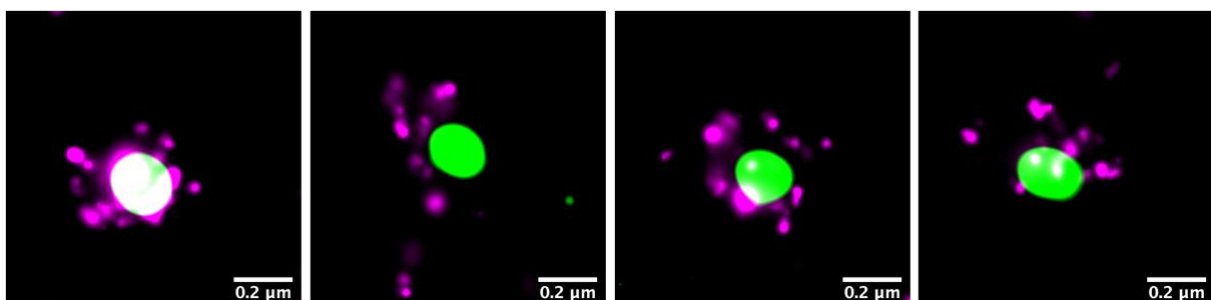


Figure 47: Enlarge image of different lysosome regions of a HeLa cell after nanoparticle uptake. In green (AF-488), a single calcium phosphate nanoparticle was identified. The magenta channel (AF-647) corresponds to the stained LAMP-1.

The improvement in the resolution capacity moving from the general widefield microscopy, confocal microscopy to STORM allows the detection and better identification of the nanoparticles. A schematic scale representation of the measured average size of CaP/PEI/SiO₂-AF488 nanoparticle by different fluorescence microscopy techniques is shown in Figure 48. With the lower resolution methods the nanoparticles are observed near 3 times bigger causing a significant overlap in the detection. Furthermore, the better capacity to distinguish adjacent nanoparticles is also reflected in a lower size deviation (almost the half) for higher resolution methods such as STORM and SIM compared to widefield or CLSM.

Although electron microscopy allows a higher resolution compared to fluorescence microscopy methods, the sample preparation requirements (*e.g.*, no water content, fixation, contrast agents) limits its direct application. On the other hand, as demonstrated with our nanoparticle system, STORM microscopy allows to detect and follow the synthesized nanoparticles at the required resolution. From our results comparable nanoparticle sizes determined by STORM and SEM evidenced the potential of this system for further studies, grounded in a stable nanoparticle labelling technique.

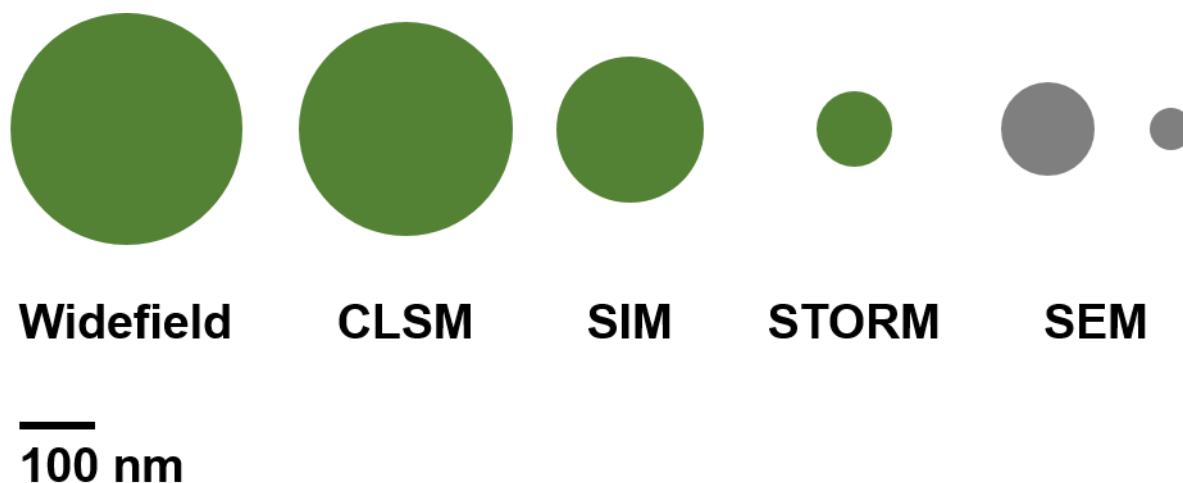


Figure 48 Schematic representation of a CaP/PEI/SiO₂-AF488 nanoparticle observed average size measured by different fluorescence microscopy techniques and by scanning electron microscopy.

8.3.7 Transfection study with labelled nanoparticles by click reaction

Using m_{cherry} plasmid as model

Calcium phosphate nanoparticles have been successfully used as transfection agents for different cell lines [44]. For this material, the nucleic acids (anionic compounds) are usually absorbed within the calcium phosphate core by electrostatic interactions until released inside the cell.

The protection of the nanoparticle internal loading (e.g., plasmids, biomolecules) from the environment can be performed by synthetic approaches. In our case, by applying the silica shell coating the internal loading is protected, for example for enzymatic degradation as demonstrated by previous publications [26, 31, 44, 47].

When the nanoparticle surface modification takes place, e.g., by click chemistry, the internal loading can be affected by the procedure. Due to this reason it is of importance to evaluate the functional integrity of the internal loading after the click reaction and discard or confirm any affectation. For this purpose, and as a model application, the transfection activity of the nanoparticles after the click reaction was evaluated.

To assay the bioactivity of the loading after the surface modification by CuAAC and SPAAC, plasmid loaded nanoparticles with m_{cherry} plasmid as model loading were prepared. The nanoparticles were further labelled with AF488-Alkyne and DBCO-(PEG)₄-FAM by CuAAC and SPAAC click reactions respectively. Table 12 has the characterization summary of the nanoparticles and Figure 49 shows representative SEM images. Plasmid m_{cherry} loading amount was determined by nanodrop measurement and calculated by difference between the amount found in the supernatant and the added one.

The nanoparticles were incubated with HeLa cells for 7 hours and after this time the medium exchanged with fresh one. Transfection was detected by fluorescence microscopy after 24 h and 48 h of incubation, as described in the experimental section. Figure 50 shows the fluorescence microscopy images. Lipofectamine 2000 was used as a transfection positive control [269, 270].

Table 12: Characterization summary of calcium phosphate nanoparticles loaded with *m_{cherry}* plasmid and surface modified by click chemistry.

Sample	CaP/PEI/ <i>m_{cherry}</i> /SiO ₂	CaP/PEI/ <i>m_{cherry}</i> /SiO ₂ - N ₃	CaP/PEI/ <i>m_{cherry}</i> /SiO ₂ - AF488 (CuAAC)	CaP/PEI/ <i>m_{cherry}</i> /SiO ₂ - -FAM (SPAAC)
Solid core diameter by SEM / nm	61	64	52	74
<i>V</i> (one nanoparticle; only CaP) / m ³	1.19·10 ⁻²²	1.37·10 ⁻²²	7.36·10 ⁻²³	2.12·10 ⁻²²
<i>A</i> (one nanoparticle; only CaP) / m ²	1.17·10 ⁻¹⁴	1.29·10 ⁻¹⁴	8.49·10 ⁻¹⁵	1.72·10 ⁻¹⁴
<i>m</i> (one nanoparticle; only CaP) / kg	3.73·10 ⁻¹⁹	4.31·10 ⁻¹⁹	2.31·10 ⁻¹⁹	6.67·10 ⁻¹⁹
<i>w</i> (Ca ²⁺) by AAS / kg m ⁻³	0.0435	0.0521	0.0211	0.0334
<i>w</i> (Ca ₅ (PO ₄) ₃ OH) / kg m ⁻³	0.1090	0.1307	0.0528	0.0837
<i>N</i> (nanoparticles) / m ⁻³	2.92·10 ⁺¹⁷	3.03·10 ⁺¹⁷	2.29·10 ⁺¹⁷	1.26·10 ⁺¹⁷
<i>w</i> (plasmid) / kg m ⁻³	0.060	0.060	0.060	0.060
<i>N</i> (loading) / m ⁻³	8.89·10 ⁺¹⁸	8.89·10 ⁺¹⁸	8.89·10 ⁺¹⁸	8.89·10 ⁺¹⁸
<i>m</i> (loading) per nanoparticle / kg	2.05·10 ⁻¹⁹	1.98·10 ⁻¹⁹	2.62·10 ⁻¹⁹	4.77·10 ⁻¹⁹
<i>N</i> (loading) molecules per nanoparticle	30.4	29.3	38.9	70.1
wt. ratio plasmid to calcium phosphate	1:0.55	1:0.46	1:1.14	1:0.72
Hydrodynamic diameter by DLS / nm	265	254	398	316
PDI by DLS	0.31	0.24	0.37	0.36
Zeta potential by DLS / mV	+23	+22	+25	+23

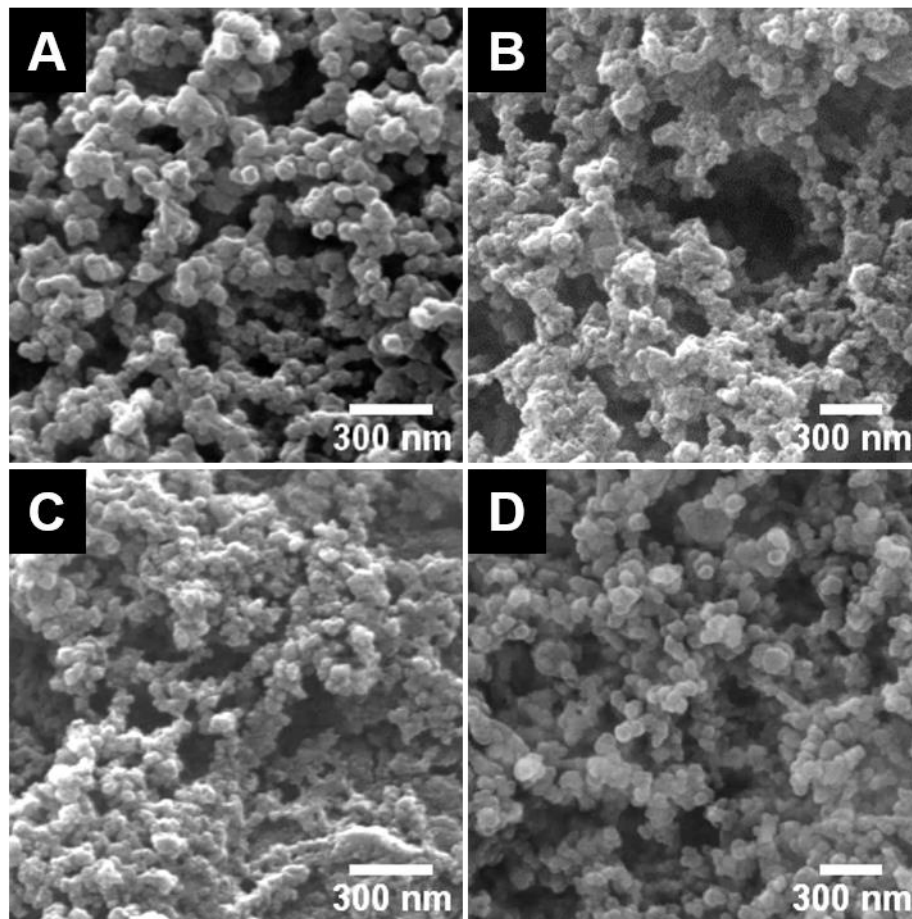


Figure 49: Representative SEM images of A) CaP/PEI/m_{cherry}/SiO₂, B) CaP/PEI/m_{cherry}/SiO₂-N₃, C) CaP/PEI/m_{cherry}/SiO₂-AF488 (CuAAC), D) CaP/PEI/m_{cherry}/SiO₂-FAM (SPAAC).

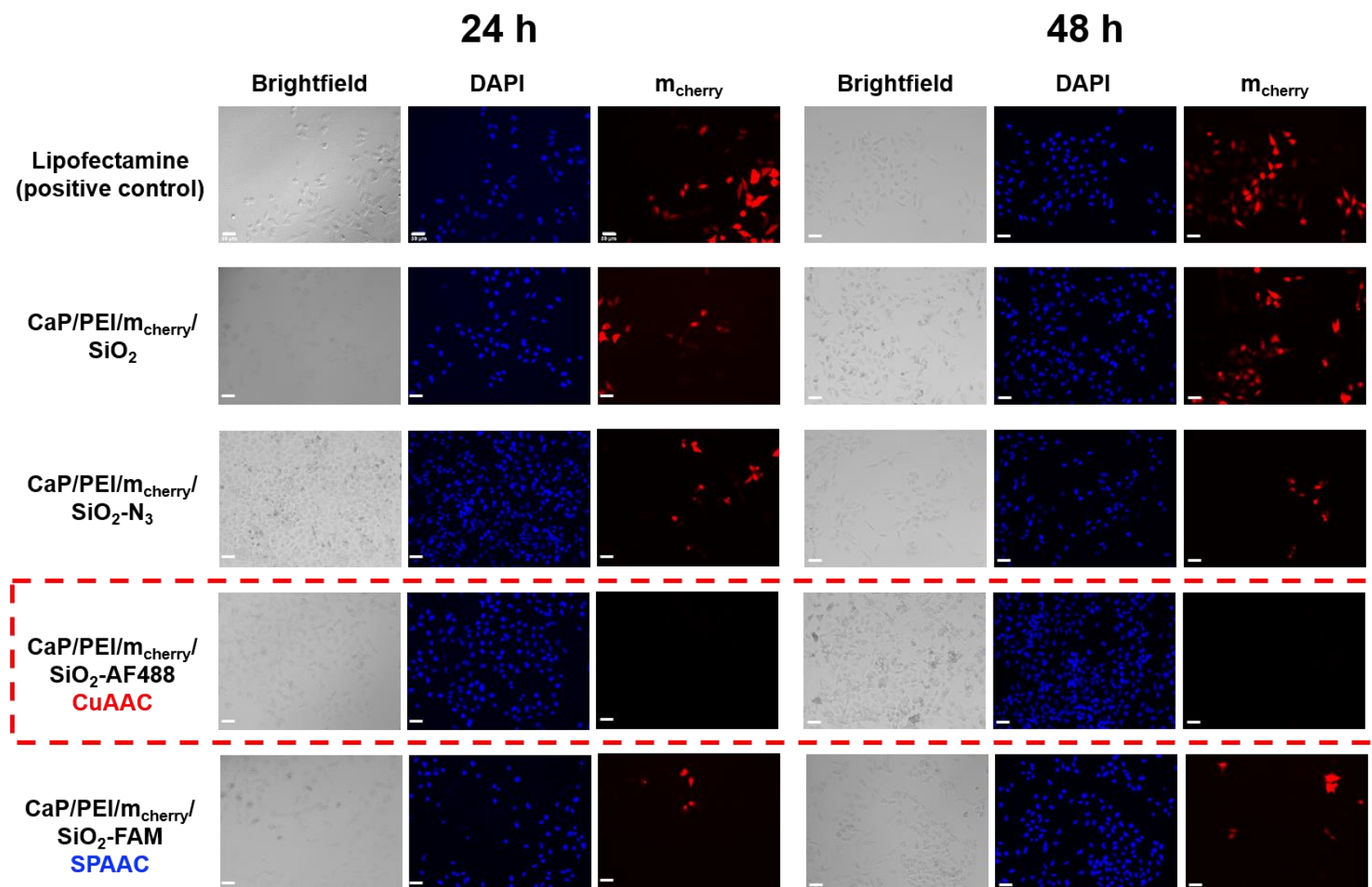


Figure 50: Fluorescence microscopy images of HeLa cells after 24h and 48h transfection with different calcium phosphate nanoparticles loaded with m_{cherry} plasmid. Lipofectamine was used as positive control. A 20X objective was used. Scale bar is 50 μ m.

As observed in Figure 50 for CuAAC labelled nanoparticles no transfection was detected. For the SPAAC labelled nanoparticles, transfection is detected after 24h, as well as for the azide terminated nanoparticles and the positive control sample with Lipofectamine. Transfection detection means that the plasmid loading was not damaged or lost after the surface modification steps. Thus the internal loading of calcium phosphate nanoparticles labelled by CuAAC seems to be damaged.

In the CuAAC reaction, the oxidative conditions during the reaction can become harmful for nucleic acids or other sensitive loading. The issue can be related to the *in situ* copper (I) reduction, where sodium ascorbate is used as reducing agent.

Sodium ascorbate oxidation can generate reactive oxygen species (ROS) that can damage the organic loading. THPTA ligand was added in the reaction to protect from the potential side effect damage caused by these species. This molecule stabilizes Cu (I) but also intercepts and reduces ROS generated during the ascorbate reduction of dissolved O₂. Additionally, aminoguanidine was added into the reaction mixture to work as a protective molecule for byproducts of ascorbate oxidation that can further crosslink to biomolecules [236]. Although, both molecules were added during the reaction, for a sensitive loading like m_{cherry} plasmid, the loading was still affected and altered after the CuAAC reaction as no cellular transfection was detected.

Abel *et al.* had studied the oxidative damage of DNA during CuAAC click reaction [271]. The authors had found that after a few minutes of the copper catalyzed click reaction the DNA damage was observed. Additionally, the frequency of damage is related to the reaction time and to the copper, ascorbate and THPTA ligand concentration. This work is in agreement with the observations from our experimental results using plasmid DNA loaded calcium phosphate nanoparticles.

Additionally, Cai *et al.* have evaluated the oxidative damage of peptides and proteins when using CuAAC reaction [88]. They found that the degree of oxidation damage is dependent on the presence of copper coordination sites within a biomolecule (*i.e.*, copper coordinating amino acids) and solvent accessibility. Moreover, when a stabilizing ligand like THPTA is applied, it is still not enough to completely protect from oxidation of strong copper coordinating sites.

8.3.8 Azide-terminated and *clicked* calcium phosphate nanoparticles cell viability by MTT test

The cell viability of the azide terminated calcium phosphate nanoparticles and clicked nanoparticles was assayed by the MTT test. Figure 51 and Figure 52 show the cell viability after 24 hour incubation at different nanoparticle concentration before and after click reaction. The cell viability is expressed as the percentage ratio between the cells incubate with the nanoparticles and the mock (without nanoparticles).

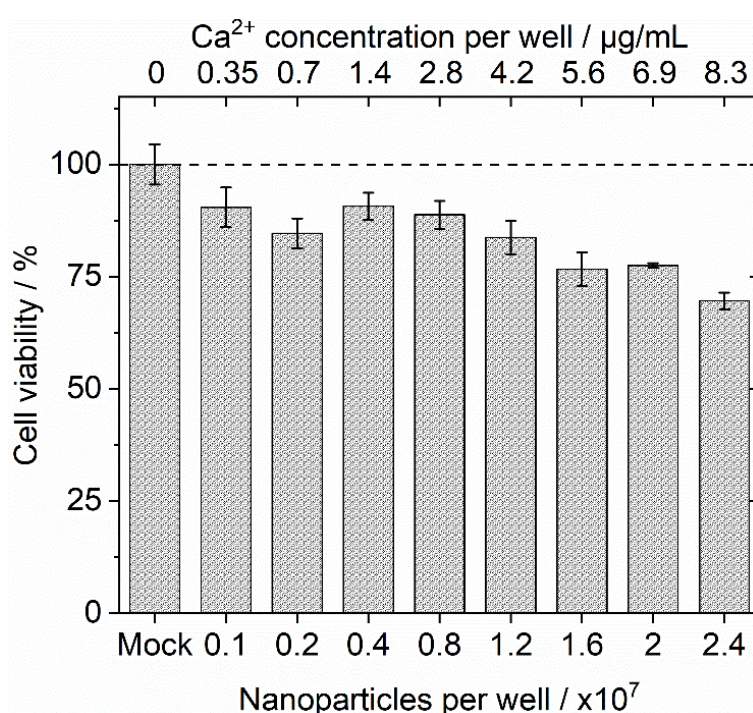


Figure 51: Cell viability determined by MTT assay for CaP/PEI/SiO₂-N₃ nanoparticles after incubation with HeLa cells for 24 h.

In general, the nanoparticles at the studied concentrations had a low toxicity with this cell line. At higher concentrations a lower cell viability is expected and observed. This is mainly related to the higher PEI concentration as polyethyleneimine is known to be cytotoxic at higher concentrations [272, 273].

For the labelled nanoparticles after click reaction by CuAAC and SPAAC a good cell viability was also obtained. Although at a higher nanoparticle concentration the cell viability was lower compared to the precursor nanoparticle (CaP/PEI/SiO₂-N₃). With a

nanoparticle number of 1.2×10^7 the cell viability was near 60% for labelled nanoparticles and around 80% for CaP/PEI/SiO₂-N₃. This lower viability can be related to the modification procedure (e.g. copper and DMSO absorption). Within the different dye labeling densities for each click reaction method (1 hour reaction) equivalent cell viabilities are obtained, thus the labelling density does not affect the cell viability.

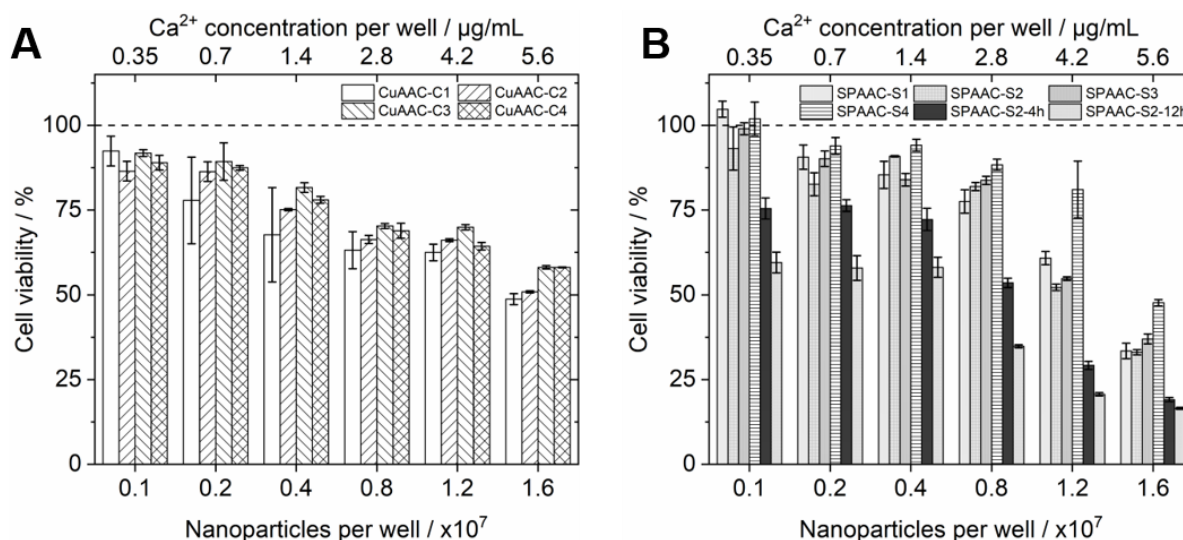


Figure 52: Cell viability determined by MTT assay for CaP/PEI/SiO₂-FAM labelled nanoparticles by A) CuAAC and B) SPAAC click reaction. Nanoparticles were incubated with HeLa cells at different concentrations for 24 h.

In the usual *in vitro* experiments, after giving the nanoparticles to the cell culture an equivalent calcium concentration of near 2.8 $\mu\text{g/mL}$ was obtained. At this specific point the cell viability for CaP/PEI/SiO₂-N₃ was near 90 %, for CaP/PEI/SiO₂-FAM (CuAAC) 65 % and for CaP/PEI/SiO₂-FAM (DBCO) 80 % were observed. This tendency reflects the influence the click reaction approach has on the nanoparticles even after the purification steps.

The cell viability difference (near 15%) between CuAAC and SPAAC method can be related to the use of copper during the click reaction and a potential absorption on the nanoparticle. The concentration of copper in the nanoparticles was analyzed by AAS, although a non-detected value (ND, < 0.35 $\mu\text{g/mL}$) was obtained. This does not mean or confirm that there is no copper absorbed, but the quantity is small enough to not be detected by AAS. Furthermore, by EDX analysis the detection range for copper was between (ND to 4)% wt.% for CuAAC modified samples.

For the SPAAC reaction after longer incubation steps like 4h and 12 h a lower cell viability was observed. This tendency is related not to the labelling density but to the longer exposition of the nanoparticles during the reaction to DMSO that can be absorbed by the nanoparticle and not completely removed after the washing steps.

In general, the nanoparticles have a good cell viability under the usual experimental conditions (*i.e.*, nanoparticle concentration per well). Moreover, the observed tendencies provided valuable information about how the click reaction approach can influence in the final nanoparticle cell viability.

For further applications with other molecules and synthetic conditions, the cell viability has to be evaluated and assayed for each case as the molecule in the surface and methodology can affect the cell viability, as well as the used cell line because each cell line has different cytotoxicity tolerance.

8.3.9 Section Summary

Azide-terminate calcium phosphate nanoparticles were synthesized with a usual core diameter within 50-100 nm. The nanoparticles were colloidal stable, and suitable for CuAAC and SPAAC click reactions. Using different alkyne terminate dyes (*i.e.*, FAM-Alkyne, TAMRA-Alkyne, Cy5-Alkyne, AF488-Alkyne, ATE, DBCO-PEG4-FAM) the reaction was established. Moreover, it was possible to synthesize a dual labelled nanoparticle, which opens the possibility to anchor two different molecules to the nanoparticle with a two-step reaction. Additionally, a molecule with AIE properties was reacted to the surface, and it continued to have the AIE behavior depending on the solvent medium.

CuAAC reaction enables a faster surface reaction compared to SPAAC reaction but is limited to a 1 hour reaction time, and for SPAAC the surface labelling density can be controlled as a function of time. A good cell viability is obtained for the synthesized nanoparticles, although for the CuAAC labelled nanoparticles a slightly higher

cytotoxicity is observed at greater nanoparticles concentrations. This issue can be related to the possible absorption of copper into the nanoparticles. Another potential limitation with CuAAC reaction is the oxidative damage on sensitive loadings as evidenced with the m_{cherry} plasmid, although the potential damage is dependent on the used molecule. As demonstrated, both methods (CuAAC and SPAAC) allowed a good surface modification and can be chosen according to the require conditions.

Finally, with fluorescence microscopy methods like CLSM, SIM, and STORM the nanoparticles were studied with and without cellular uptake. It was possible to determine that the nanoparticles remain mostly like individual particles or low aggregated after cellular uptake.

8.4 Specific coupling of biomolecules

The orientation of a biomolecule on the nanoparticles surface can influence the activity a molecule can have. For example, for a protein which needs to be recognized by an enzyme or antibody it should have the correct orientation and accessibility for a successful identification. Therefore, the way a molecule is coupled on the nanoparticle surface can influence the materials performance and recognition process.

In this section, two different coupling approaches on the calcium phosphate nanoparticles were prepared and evaluated using HIV-1 envelope glycoproteins.

8.4.1 HIV-1 envelope glycoprotein

HIV-1 envelope glycoprotein (Env) is the main viral B-cell antigen and is formed by a trimer of heterodimers which are non-covalently bonded subunits (subunit gp120 and gp41) [274]. The virus has a size of near 130 nm [275], and Env structure is the only one found on the HIV external surface, so it becomes the protein that is involved in the initial infection and/or recognition process. It has been demonstrated that synthetic Env structures can mimic native-like trimers and induce antibodies neutralization [276-279].

For an infection to occur, the virus membrane has to fusion with the target cell membrane [280, 281]. For this, the Env gp120 subunit binds to the CD4 receptor on the cell (normally found in the surface of T lymphocytes, monocytes, dendritic cells and brain microglia [282]), and after a conformational modification, the co-receptors (CCR5 or CXCR4) binding sites are exposed. The binding triggers a conformation change in gp41 which allows the contact between both membranes causing the fusion of the membranes [274].

Calcium phosphate nanoparticles are in the same size range as this virus which makes them a potential synthetic carrier of Env proteins on its surface, for example, for

vaccination applications. Additionally, an internal loading can be included inside the nanoparticle making it a versatile system.

To study the influence in the protein coupling and the biological activity, two different coupling approaches were studied. One based on amine – NHS chemistry and the other on copper catalyzed click chemistry (CuAAC).

For the click chemistry approach, the Env-Trimer was first modified to include a terminal aldehyde tag by mutagenesis PCR. With Bertozzi *et al.* method [283, 284], the cysteine in the His-Tag can then be transformed with the Formylglycine-generating enzyme (FGE) to an aldehyde. The introduced aldehyde is then reacted with an aminoxy-PEG3-Propargyl crosslinker to include the alkyne functionality into the protein at the specific position.

The proteins, Env-Trimer and Env-Monomer, were prepared by the research group of Prof. Dr. Klaus Überla and PD Dr. Vladimir Temchura, from the Institute of Clinical and Molecular Virology from University Hospital Erlangen of Friedrich-Alexander University Erlangen-Nürnberg (FAU). The supplied proteins were used as received for the nanoparticles surface modification.

8.4.2 Env-Protein coupling to the calcium phosphate nanoparticle

Two different approaches were used for the coupling of the Env-Protein to the surface of a calcium phosphate nanoparticle.

The “non-specific coupling” approach is based on the thiol-maleimide chemistry. For this an amine reactive crosslinker (Sulfo-SMCC) is first coupled to the Env-Trimer (140 kDa) or Env-Monomer (120 kDa). Near neutral pH the N-hydroxysuccinimide group from the crosslinker will react preferentially with the primary amines found in the protein. Env protein has 33 amino acid residues that are lysine and are expected to have the side chain exposed to the solvent [259, 285]. These sites are potential

coupling points for this protein. After the activation, the protein was purified from free crosslinker with an Amicon® Filter with a molecular weight cutoff of 3 kDa.

The other end of the crosslinker is reactive with thiols, so thiol-terminate calcium phosphate nanoparticles were prepared following the procedure described by Kozlova *et al.* [26] and the modified Env-protein was then coupled to the nanoparticles with the procedure described in section 7.5.1.

The “specific-coupling” approach is based on the copper catalyzed click reaction between the alkyne terminated Env-Trimer and the azide terminate calcium phosphate nanoparticle. This method is based on the reaction described in the previous section 7.3 [228].

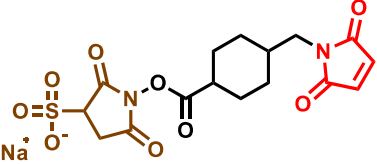
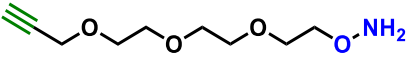
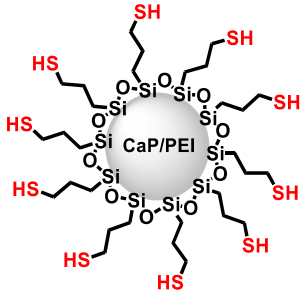
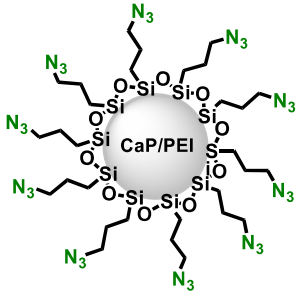
Table 13 shows a summary of the comparison for both coupling methods on calcium phosphate nanoparticles and the obtained yield values. Alexa-488 labelled Env Protein was used to determine the number of units per nanoparticle after each reaction type by UV-Vis spectroscopy.

For both cases a similar protein number on the calcium phosphate nanoparticles were obtained after the reaction. With the non-specific coupling more binding orientations are likely to occur because the crosslinker can react in different positions within the Env protein. This aspect was reflected in the occupied surface area per protein on the calcium phosphate nanoparticle. For the non-specific coupling an area of 14 nm² was obtained and for the specific coupling 23 nm². This difference is related to the orientation the protein has during and after the surface coupling that finally influences the occupied surface.

Additionally, using micro-volume UV-Vis (Nanodrop) the amount of protein coupled was also determined. With this method, after the coupling reaction the nanoparticles were centrifuged and the supernatant was measured at 280 nm. As the absorbance coefficient for the protein is known, the concentration can be calculated. Then, by subtraction the amount of bonded protein is determined, *i.e.*, the residual protein amount in the supernatant is subtracted from the initial added amount. This method is only applicable with the “non-specific coupling” method, because with the “specific

coupling” carried out by CuAAC residual reagents in the supernatant interfere with the nanoprop measurement (absorbance at 280 nm).

Table 13: Comparison between both Env Protein coupling methods on the calcium phosphate nanoparticle.

	Non-specific coupling	Specific coupling
Protein modification method with crosslinker	amine- sulfo-NHS	carbonyl-aminooxy
Crosslinker	sulfo-SMCC 	aminooxy-PEG3-Propargyl 
Calcium phosphate nanoparticle terminal group	Thiol terminate 	Azide terminate 
Chemistry with the NPs	Thiol-Maleimide	Alkyne-azide (CuAAC)
N(Env-) per nanoparticle	480	570
Env-anchor size on the nanoparticle	14 nm ²	23 nm ²
Wt.% ratio Env- to calcium phosphate	0.6	0.3
Reaction yield	85 %	80 %
Hydrodynamic diameter by DLS / nm	344	269
PDI by DLS	0.37	0.33
Zeta potential by DLS / mV	+25	+23

When comparing the amount of protein determined using the 85% reaction yield (for non-specific coupling) and by nanodrop measurements at 280 nm an average difference between both values of nearly 16% was calculated. It is important to consider that for a labeled Env Protein like Env-AF488 is not appropriate to perform the nanodrop determination at 280 nm, because most dyes have also absorption at this wavelength and will give a positive interference in the measurement.

After the surface coupling, both types of nanoparticles kept the original positive surface charge due to the polyethyleneimine and comparable hydrodynamic diameters, as shown in Figure 53. Representative SEM micrographs for both nanoparticle types are shown in Figure 54.

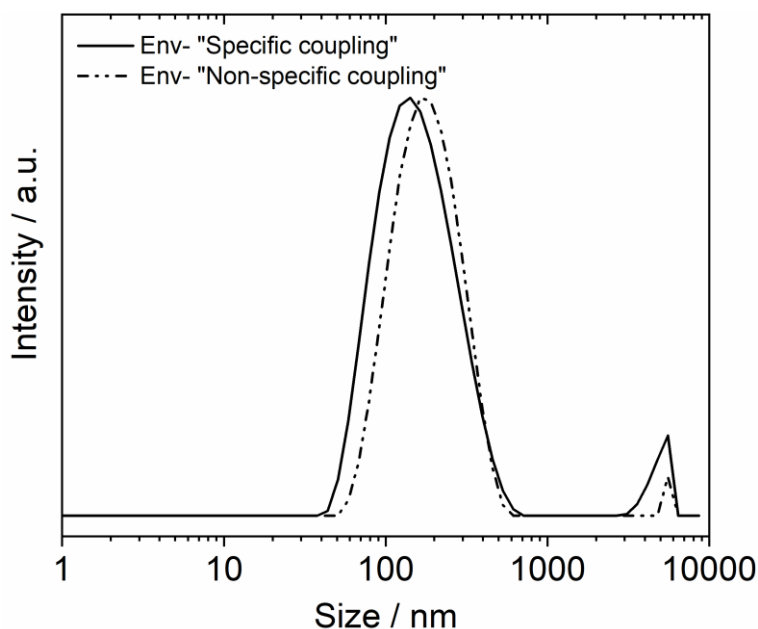


Figure 53: Hydrodynamic diameter by DLS comparison for Env protein coupled “specifically” and “non-specifically” to the calcium phosphate nanoparticle surface.

Calcium phosphate nanoparticles stabilized with PEI-Cy5 were prepared and Env-Trimer-AF488 reacted to it. When both channel signals colocalize, it means that the protein was successfully coupled to the nanoparticle. Figure 55 shows a representative image of the colocalization of both signals, which confirms that the protein is bonded to the calcium phosphate nanoparticle.

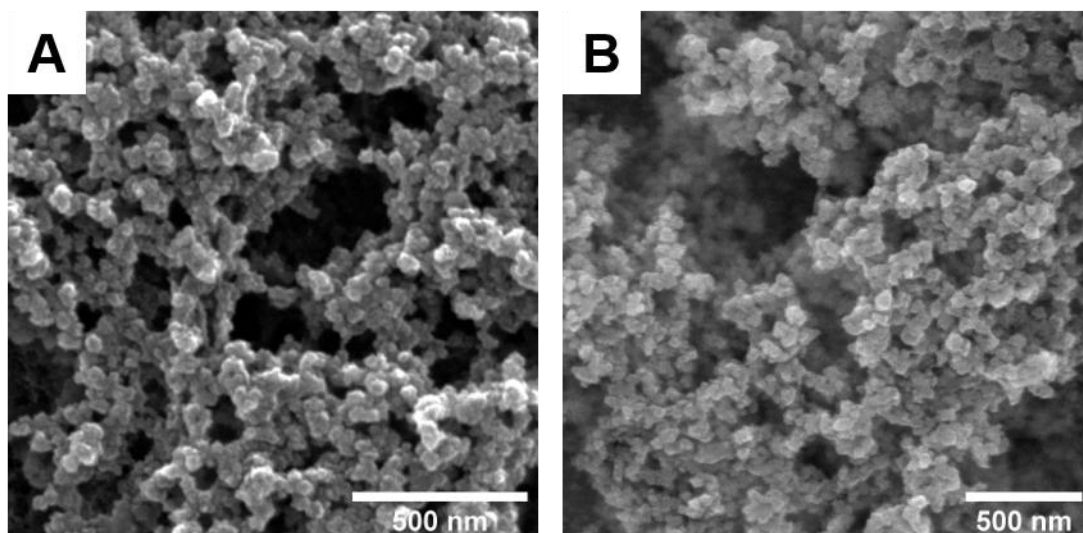


Figure 54: Scanning electron microscopy comparison for Env-protein coupled “specifically” and “non-specifically” to the calcium phosphate nanoparticle surface.

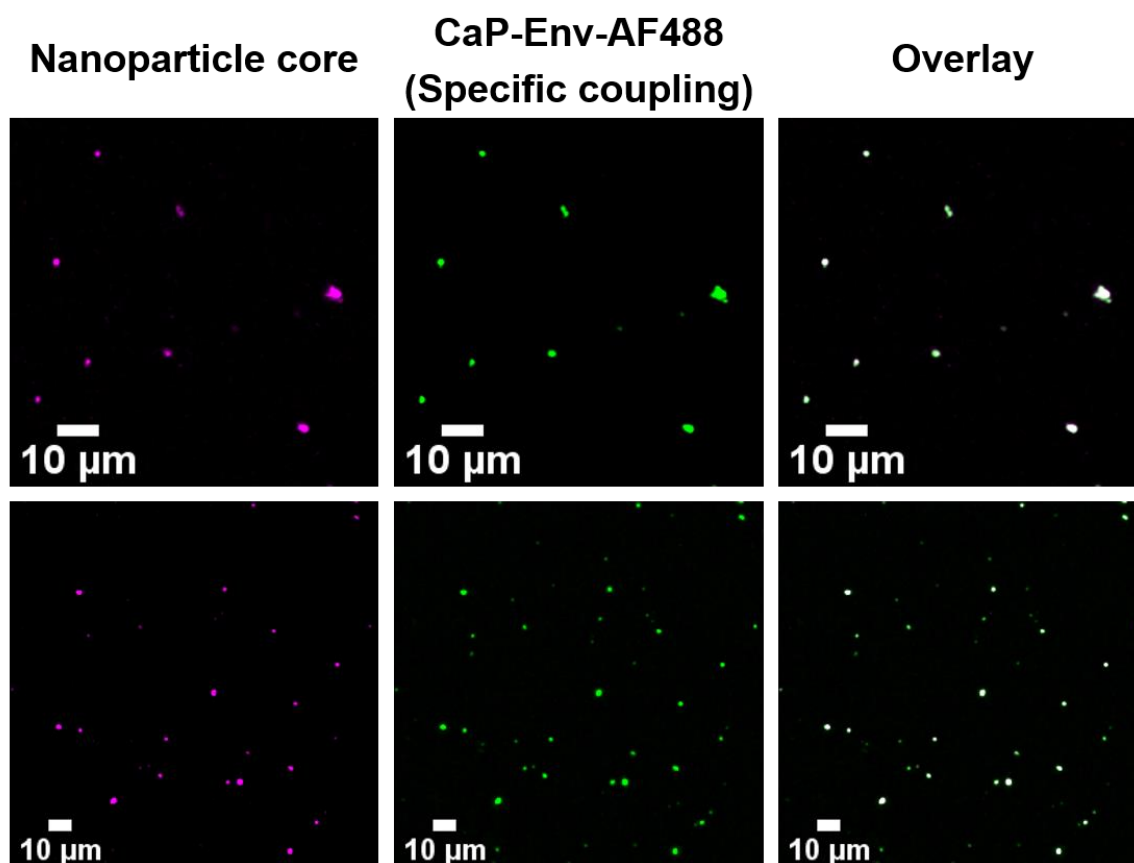


Figure 55: CLSM images of a direct observation of calcium phosphate nanoparticle stabilized with PEI-Cy5 and coupled to Env-Trimer-AF488 by CuAAC click chemistry. The nanoparticle core is shown in purple (Cy5, 647 nm), the labeled Env-Trimer in green (AF488, 488 nm) and the overlay of both channels in white.

The nanoparticles were further analyzed with transmission electron microscopy. To increase the contrast in the sample and better detect the protein on the surface, a negative staining of the sample on the grid with phosphotungstate solution (1%, pH 7) was performed. After the staining, the silica shell around the calcium phosphate nanoparticle can be distinguished easily due to the contrast difference as shown in Figure 56. This contrast enhances the protein detection, as the protein should have a lighter contrast compared to Si, Ca and W. After the negative staining it is not further possible to visualize the calcium phosphate component in the nanoparticle and the nanoparticle seems to be empty (without the core) but it is just an imaging artifact caused by the contrast similarity of the nanoparticle core and the staining. Figure 56 shows a comparison of the same sample with and without negative staining.

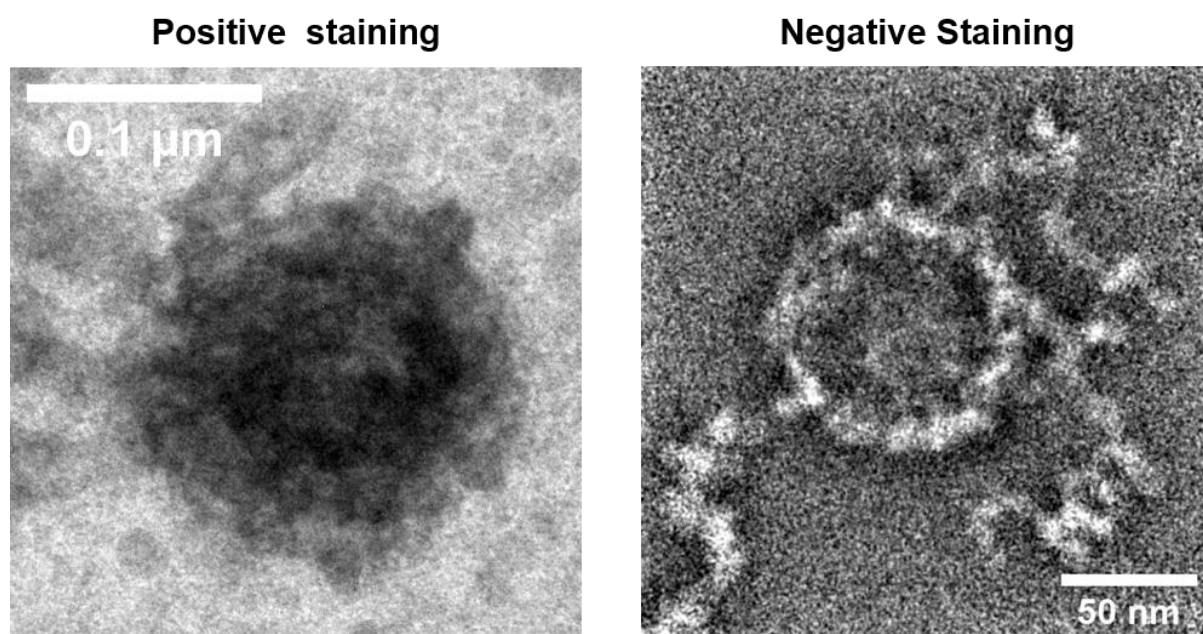


Figure 56: Transmission electron microscopy of CaP/PEI/SiO₂-Env nanoparticle (left) with positive staining and (right) with negative staining using phosphotungstate solution (1%, pH 7).

The nanoparticle size distribution determined by TEM is in agreement with the values determined by SEM. The nanoparticle had an average diameter of 80 nm and the silica coating components of 16 nm as observed for the silica terminated nanoparticles (Figure 57). When comparing no appreciable growth in the core or silica coating is observed after the additional surface reaction steps like azide group addition and Env-Protein coupling.

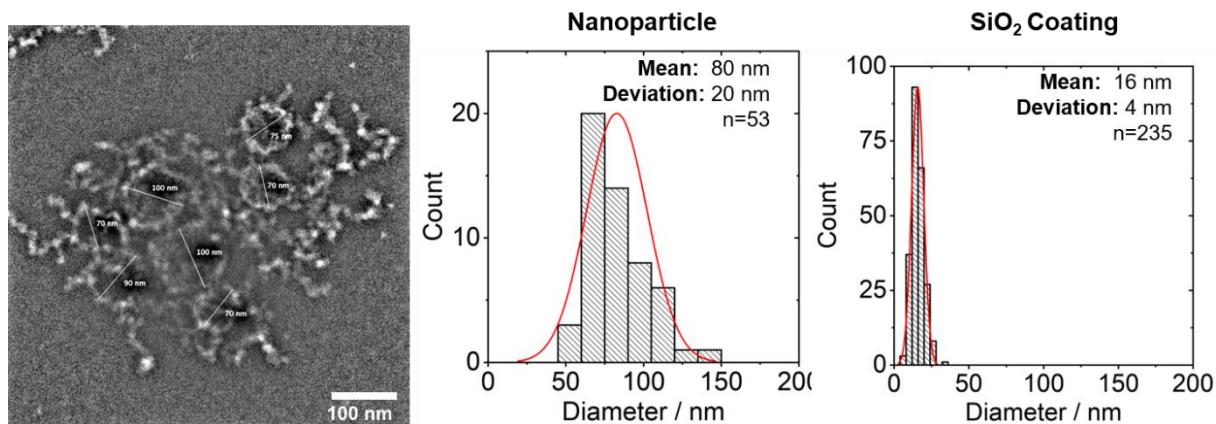


Figure 57: CaP/PEI/SiO₂-Env size distribution determined by TEM with negative staining.

The detection of the protein on the surface of the calcium phosphate nanoparticle is not trivial due to two main reasons: a) a similar contrast between the components and b) the surface roughness of the nanoparticle system. With negative staining the sample contrast is improved, especially for the lighter elements (organic components like the Env Protein).

Figure 58 shows a higher magnification negative stained TEM micrograph of CaP/PEI/SiO₂-Env. The arrows mark positions with a higher intensity (lighter grey) measured using the intensity line profile and these are probable positions where ENV-Trimer could be localized. Although, with this approach is not possible to really confirm the detection of the protein on the nanoparticle surface.

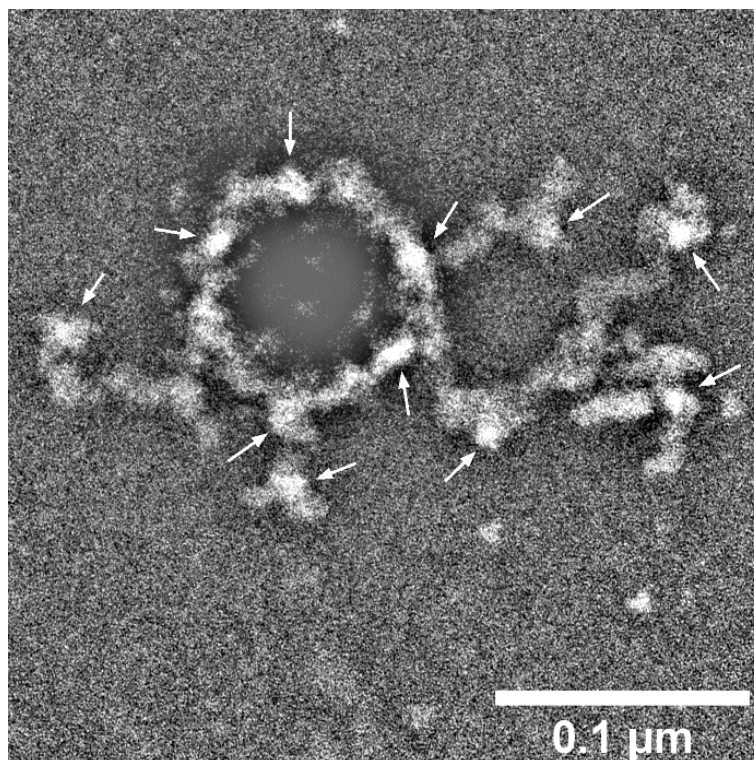


Figure 58: Negative stained TEM micrograph of CaP/PEI/SiO₂-Env at higher magnification. White arrows indicate probable positions where the Env- protein can be found.

To increase the image resolution and contrast a tomography imaging was performed. With this approach the sample is rotated (between -60° and 120°) and at each step an image is recorded. Afterwards the image is reconstructed. The sample was negative stained to increase the contrast with the protein. A side effect of this staining is that the calcium phosphate core cannot be longer identified due to the contrast similarity like previously shown in Figure 56 and thus only the empty ring and silica network coating were observed. Figure 59 shows representative tomogram sections with a 200 frames step between each one. The yellow arrows show some positions at which the Env-Trimer was identified.

According to this data, the Env-Trimer has a base size near 3 nm and a top size around 8 nm which agrees with the reported size by Zhu *et al.* [275]. Although with this technique the resolution is improved, it is not clear enough to distinguish all the proteins units and orientations on the calcium phosphate nanoparticle surface nor to detect all the proteins. The surface morphology, roughness and contrast influences the capacity to clearly distinguish the Trimers on its surface. Ingale *et al.* have reported

the analysis of Env-Trimers on a Liposomes surface using TEM microscopy [277]. In this case, the contrast difference between the liposome, protein and background allows a cleaner detection, in addition to a more regular define surface boundary of liposomes.

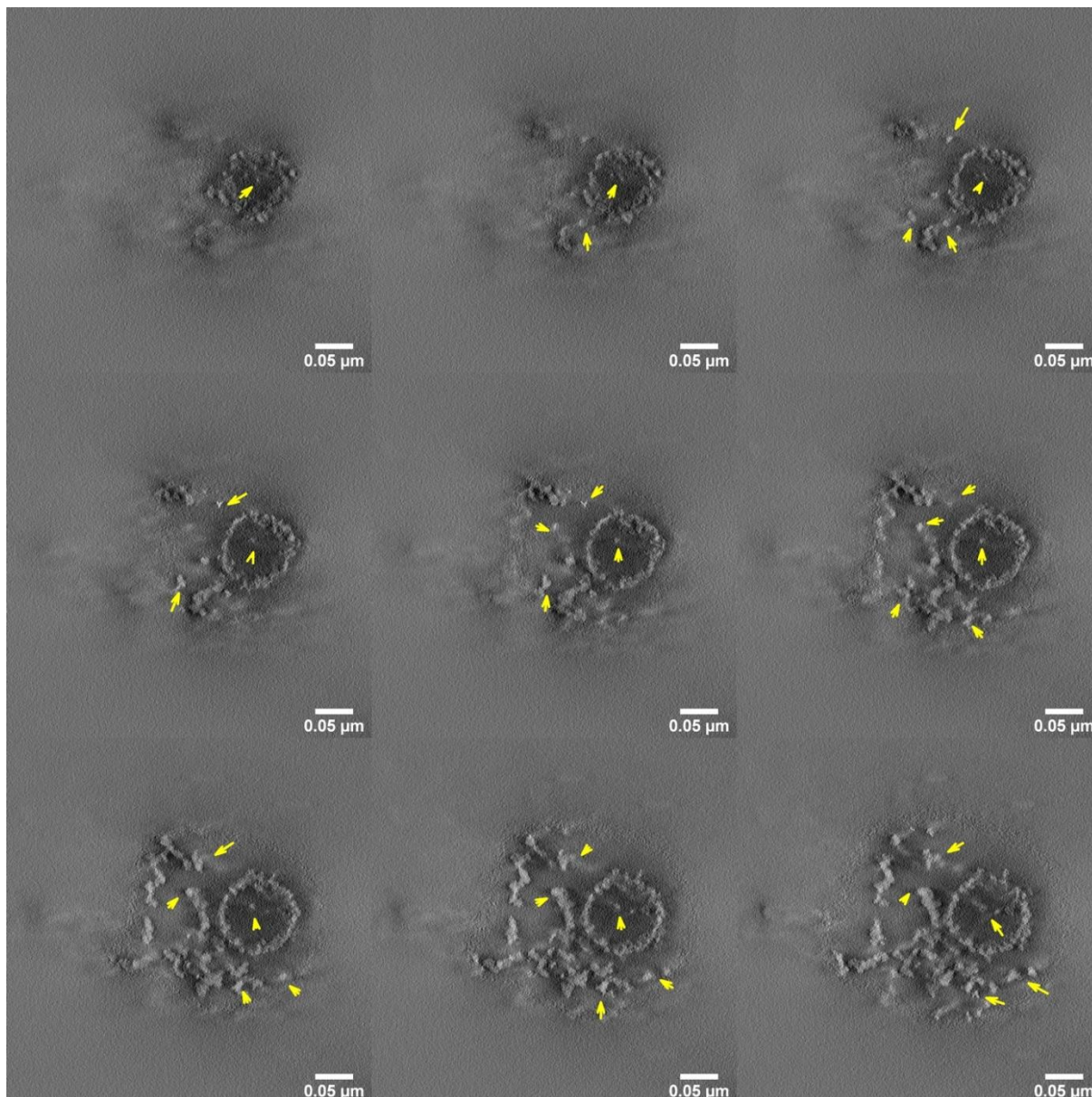


Figure 59: Representative TEM tomogram sections of CaP/PEI/SiO₂-Env. The yellow arrows indicate positions in where the Env-Trimer is observed. Each section represents a step of 200 frames.

For the nanoparticles storage for the *in vivo* and *in vitro* studies the nanoparticles dispersion was freeze-dried with trehalose as cryoprotectant according to [239]. Figure 60 shows two representative DLS measurements before and after the

nanoparticles lyophilization. The nanoparticle size distribution is equivalent before and after the treatment, although after lyophilization some higher aggregates are detected without affecting the overall nanoparticles stability.

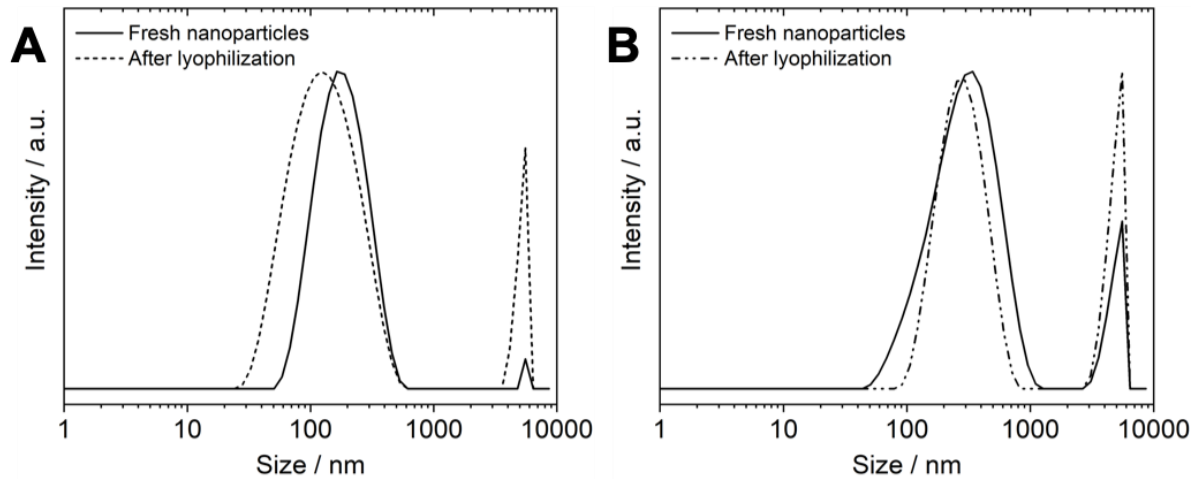


Figure 60: DLS size distribution of the nanoparticles in water before and after lyophilization A) non-specific coupled and B) specifically coupled.

8.4.3 *In vivo* and *in vitro* studies with Env-coupled calcium phosphate nanoparticles

The *in vivo* and *in vitro* studies were carried out by Mr. Dominik Damm and other members of the research group of Prof. Dr. Klaus Überla and PD Dr. Vladimir Temchura from the Institute of Clinical and Molecular Virology from University Hospital Erlangen of Friedrich-Alexander University Erlangen-Nürnberg (FAU). A summary of some obtained results are shown in the following section.

Nanoparticles bearing “specific” and “non-specific” Env- coupling on the surface were prepared. Additionally, nanoparticles with an internal loading (p30 peptide or CpG) were also synthesized for the immunization studies. Table 14 and Table 15 summarize the nanoparticles characterization and Figure 61 shows representative SEM images.

Table 14: Properties of the prepared calcium phosphate nanoparticles for the immunization experiments. Concentrations refer to stock solutions which were diluted before use in the biological experiments

Calcium phosphate nanoparticles	CaP/PEI/SiO ₂ -Env-Monomer	CaP/PEI/p30/SiO ₂ -Env-Monomer	CaP/PEI/SiO ₂ -Env-Trimer	CaP/PEI/p30/SiO ₂ -Env-Trimer	CaP/PEI/p30+CpG/SiO ₂ -Env-Trimer	CaP/PEI/CpG/SiO ₂ -Env-Trimer	CaP/PEI/SiO ₂ -Env-Trimer (SC)	CaP/PEI/CpG/SiO ₂ -Env-Trimer (SC)
Solid particle diameter by SEM / nm	61	60	45	45	45	57	60	44
<i>V</i> (one nanoparticle; only CaP) / ×10 ⁻²² m ³	1.19	1.19	0.49	0.49	0.48	0.97	1.13	0.45
<i>m</i> (one nanoparticle; only CaP) / ×10 ⁻¹⁹ kg	3.73	3.73	1.59	1.54	1.50	3.04	3.55	1.41
<i>w</i> (Ca ²⁺) by AAS / kg m ⁻³	0.043	0.012	0.026	0.031	0.019	0.023	0.075	0.041
<i>w</i> (Ca ₅ (PO ₄) ₃ OH) / kg m ⁻³	0.109	0.029	0.064	0.079	0.046	0.057	0.188	0.103
<i>N</i> (nanoparticles) / ×10 ¹⁷ m ⁻³	2.91	0.79	4.23	5.14	3.11	1.87	5.30	7.28
Hydrodynamic diameter by DLS / nm	160	439	411	386	380	362	391	236
PDI by DLS	0.36	0.42	0.43	0.41	0.40	0.38	0.48	0.34
Zeta potential by DLS / mV	+22	+22	+20	+23	+28	+27	+22	+23
Endotoxins / EU mL ⁻¹	< 0.1	< 0.1	< 0.1	< 0.1	< 0.1	< 0.1	< 0.1	< 0.1

SC= specific coupling by click chemistry.

Table 15: Properties of the prepared calcium phosphate nanoparticles for the immunization experiments. Concentrations refer to stock solutions which were diluted before use in the biological experiments

Calcium phosphate nanoparticles	CaP/PEI/ SiO ₂ - Env- Monomer	CaP/PEI/ p30/SiO ₂ Env- Monomer	CaP/PEI/ SiO ₂ - Env- Trimer	CaP/PEI/ p30/SiO ₂ - Env- Trimer	CaP/PEI/ p30+CpG/ SiO ₂ -Env- Trimer	CaP/PEI/ CpG/SiO ₂ -Env- Trimer	CaP/PEI/ SiO ₂ -Env- Trimer (SC)	CaP/PEI/ CpG/SiO ₂ - Env-Trimer (SC)
With UV-Vis factor								
w (Env) / kg m ⁻³	0.146	0.146	0.085	0.085	0.085	0.085	0.062	0.050
N (Env) / ×10 ²⁰ molecules m ⁻³	7.33	7.33	3.66	3.66	3.66	3.66	2.66	2.15
m (Env) per nanoparticle / ×10 ⁻¹⁹ kg	5.01	18.5	2.01	1.65	2.74	4.54	1.17	0.68
N (Env) molecules ×10 ³ per nanoparticle	2.52	9.30	0.87	0.71	1.18	1.95	0.50	0.30
weight ratio Env to calcium phosphate	1 : 1.3	1 : 5	1 : 1.3	1 : 1.1	1 : 1.8	1 : 1.5	1 : 0.3	1 : 0.5
With Nanodrop								
w (Env) / kg m ⁻³	0.136	0.151	0.100	0.072	0.093	0.086	-	-
N (Env) / ×10 ²⁰ molecules m ⁻³	6.83	7.58	4.30	3.10	4.00	3.70	-	-
m (Env) per nanoparticle / ×10 ⁻¹⁹ kg	4.67	0.19	2.37	1.40	2.99	4.59	-	-
N (Env) molecules ×10 ³ per nanoparticle	2.34	9.61	1.02	0.60	1.30	1.98	-	-
weight ratio Env to calcium phosphate	1 : 1.3	1 : 5	1 : 1.6	1 : 0.9	1 : 1.2	1 : 1.5	-	-
w (adjuvant)) / kg m ⁻³	-	0.060	-	0.068	0.068 p30 0.040 CpG	0.040	-	0.037
N (adjuvant) molecules ×10 ³ per nanoparticle	-	185	-	32.1	53.2 p30 12.1 CpG	20.2	-	4.8

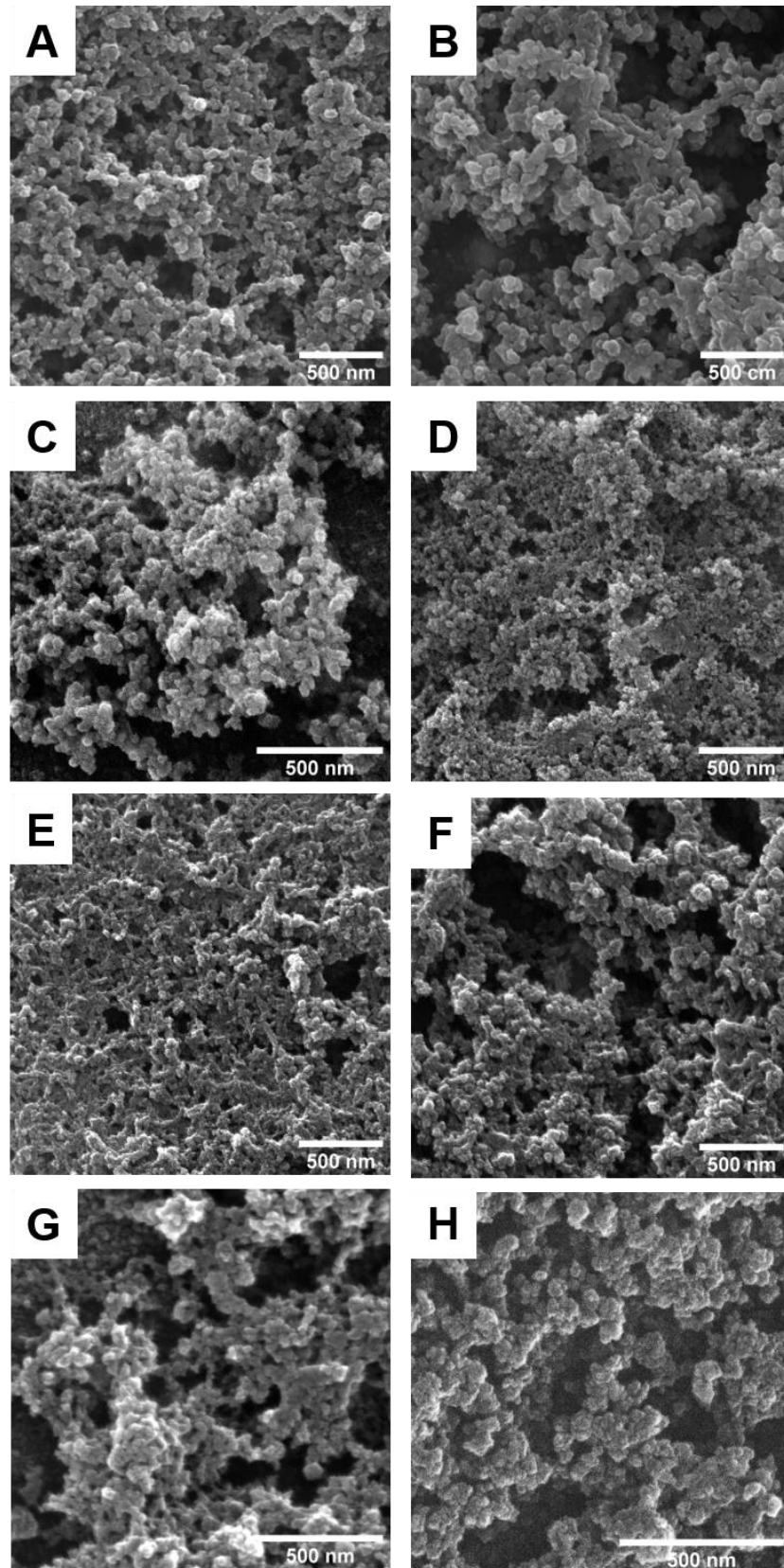


Figure 61: SEM micrographs of the prepared CaP NPs for immunization experiments. A) CaP/PEI/SiO₂-Env-Monomer, B) CaP/PEI/p30/SiO₂-Env-Monomer, C) CaP/PEI/SiO₂-Env-Trimer, D) CaP/PEI/p30/SiO₂-Env-Trimer, E) CaP/PEI/p30+CpG/SiO₂-Env-Trimer, F) CaP/PEI/CpG/SiO₂-Env-Trimer, G) CaP/PEI/SiO₂-Env-Trimer (SC) and H) CaP/PEI/CpG/SiO₂-Env-Trimer (SC).

First, the general immunization dose finding experiments were performed and for this Env-Trimer and Env-Monomer coupled non-specifically to calcium phosphate nanoparticles were used. With this assay the immune response after each dose was measured until a significant increase in the response was obtained. Initially, two different mice lines were used BALB/c and C57bl/6. For BALB/c mice the response to p30 peptide can be lower compared to C57bl/6 mice [286], and can potentially induce to a bias in the detected immune response. Both mice lines were evaluated in the assays.

Figure 62 shows the general dose finding immunization experiment time line. Two different concentrations of Env-Monomer and Env-Trimer were evaluated, a lower one with 250 ng per injection and a higher one with 2.5 μ g per injection. The first dose was applied on week zero (“prime”) and two additional doses were applied at week 4 and week 10 (“boost”).

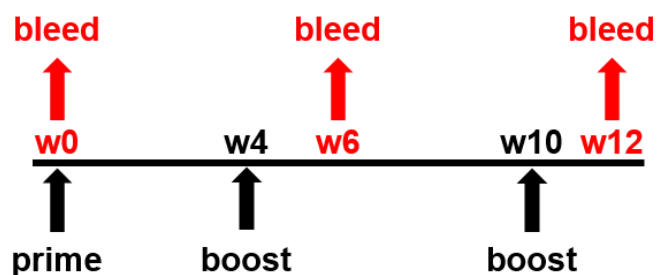


Figure 62: Dose finding immunization scheme for BALB/c and C57bl/6 mice. Nanoparticles coupled with Env-Monomer or Env-Trimer were applied on week 0, 4, and 10.

In week 6, after the second dose, the IgG, IgG1, and IgG2 response were still low but after the third boost, the immune response highly increased in week 12 for all the groups. Similar responses were obtained for both evaluated doses, although for C57bl/6 a better response was observed with a higher dose. For further experiments, a three time nanoparticle immunization design was used.

Intrastructural help (ISH) concept was introduced by S.M.Russell and F.Y. Liew in 1979 [287]. In general, it refers to the process by which envelope-specific B cell uptake a virus like particle (or virion) via the specific B-cell receptor it has on the surface. Then

the corresponding peptides are generated from the viral proteins on the MHC-II (major histocompatibility complex class II), which will then help for the protein-specific B cells recognition [288-290].

It has been observed that HIV-specific CD4⁺ T cells improve the helper activity to Env-specific B cells by ISH [291-293], which will promote their differentiation, maturation and secretion of neutralizing antibodies [292]. For this reason, to evaluate under an ISH immunization scheme using the Env-coupled calcium phosphate nanoparticles is of importance.

For the immunization trial the mice were primed twice with DPBS or Tetanol (for ISH group) and boosted three times with the nanoparticles. Env coupled to calcium phosphate nanoparticles with and without an internal loading of p30 were used for the immunizations. Peptide p30 from tetanus toxoid contain epitopes that can be recognized by different MHC-II alleles broadening its application [294]. To have an ISH effect, this fragment has to bind to the MHC-II, so that the T cells can recognize the complex. For this reason, a higher response is expected to occur for the nanoparticles containing the p30 peptide.

Figure 63 shows the Env-specific IgG subtype responses after the third nanoparticle boost. In general, a higher anti-Env IgG1 antibody response was obtained for the nanoparticles that contained the p30 peptide. In the case of anti-Env IgG2c antibody a similar response was observed. This variation in the antibody response suggests an initial suboptimal MHC-II restricted T-cell help in mice immunized with nanoparticles without p30 peptide.

This observation was further evaluated with mice that were first primed with Tetanol to provide an ISH effect. From Figure 63 it is observed that a significantly higher anti-Env antibody response was obtained for Env- coupled nanoparticles containing p30 peptide. Moreover, CD4 T-cells from the spleens of immunized mice indicated an increase potential of heterologous T-cell help for the ISH group. The Th1 cytokines like IFN- γ and TNF- α were expressed in a higher ratio for the ISH immunized mice. Likewise, Th2 cytokine IL-5 release was also higher for ISH group.

These cytokines secretion, Th1 and Th2, support respectively the IgG2a/IgG2c and IgG1 antibody subclasses formation. The significantly higher IL-5 expression for ISH group agreed with the higher antibody detection for IgG1 for the group with p30 peptide containing nanoparticles.

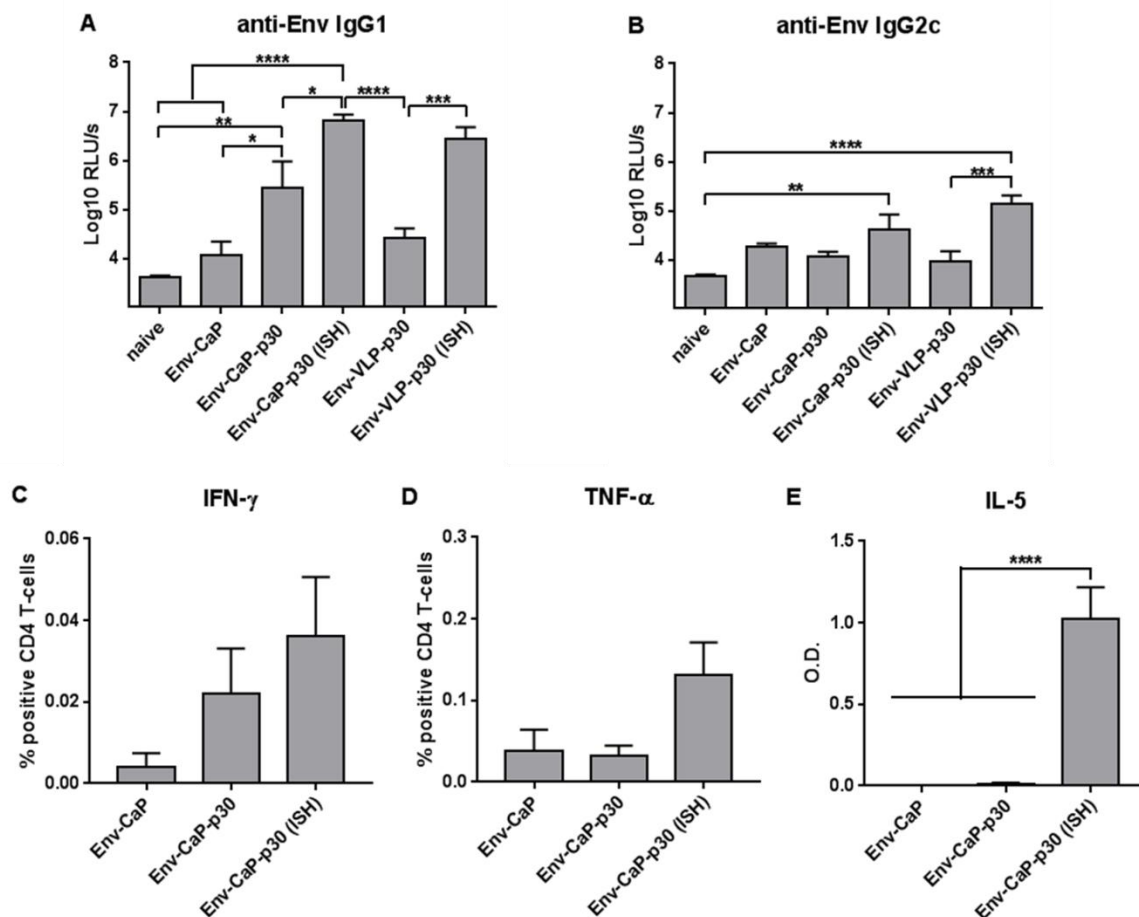


Figure 63: Env-specific IgG subtype a) IgG1 and b) IgG2c responses after Env-coupled nanoparticle immunizations by intrastructural help. Immunizations were carried out on primed mice with DPBS or Tetanol and three nanoparticles doses were given. Percentages of CD4 T-cells producing IFN- γ (C) and TNF- α (D) from differently immunized wt animals after in vitro stimulation with p30 peptide were measured by intracellular cytokine staining. (E) p30-specific IL-5 cytokine secretion as determined by ELISA. The columns represent the mean values of six animals \pm SEM. * $p < 0.05$; ** $p < 0.001$; *** $p < 0.0005$; **** $p < 0.0001$; one-way ANOVA with Tukey multiple comparison post-hoc test. Figure edited by PD Dr. Temchura *et al.*

Further *in vivo* and *in vitro* experiments are currently in progress by our collaboration partners in Erlangen for the “non-specific” and “specific” Env coupled calcium phosphate nanoparticles.

8.4.4 Section Summary

HIV envelope glycoprotein was coupled to calcium phosphate nanoparticles using two different reaction methods. One using the amine functional groups from the protein and the Sulfo-SMCC crosslinker, and the second method by click reaction with an alkyne-derivate Env protein. The first approach provides a non-specific coupling and the second one a specific coupling with the reaction at a specific position within the protein. With both methods equivalent protein number per nanoparticle and a colloidal stable system were obtained. The initial results from the immunization studies evidences the activation of the immune response with these nanoparticles. Further immunization experiments are currently in progress by our collaboration colleagues.

8.5 Delivery of plasmids *in vitro* and *in vivo* by calcium phosphate nanoparticles

As demonstrated in the previous sections and in the literature, calcium phosphate nanoparticles can be used successfully as nucleic acids carrier for transfection. This characteristic is of advantage for further applications in biomedicine, for example, for a potential DNA vaccination [179].

In the following section, an application of calcium phosphate nanoparticles for potential vaccination against Hepatitis B is described. In this case, nanoparticles loaded with encoding plasmid for Hepatitis B antigen were prepared and its effect evaluated *in vivo* and *in vitro*. For *in vivo* studies higher plasmid doses are required, therefore an initial loading optimization step was performed using pEGFP as protein model.

As part of a collaborative work, the *in vitro and in vivo* studies of the synthesized nanoparticles were performed by Dr. Maohua Zhong and Dr. Ejuan Zhang from Prof. Dr. Huimin Yan Group of Wuhan Institute of Virology of the Chinese Academy of Sciences in Wuhan, China and Prof. Dr. Mengji Lu of Institute of Virology from University Hospital Essen.

8.5.1 Plasmid loading in calcium phosphate nanoparticles

Calcium phosphate nanoparticles have been successfully used as carriers of nucleic acids. Normally in our research group a nominal plasmid input of 100 µg during the calcium phosphate nanoparticles synthesis have been used [26, 47]. With this amount, usually a high incorporation percentage (above 90%) inside the calcium phosphate nanoparticle core is obtained but for *in vivo* applications a higher amount is normally required. Seeking for a higher plasmid loading into the nanoparticles that can enhance the transfection yield different conditions were tested using EGFP as a plasmid model.

EGFP expression after transfection can be easily followed by fluorescence microscopy or FACS analysis because of the green color of transfected cells. An observation point

after a total incubation of 48 hours is selected because a better transfection rate can be obtained compared to 24 hours [46].

Calcium phosphate nanoparticles were prepared following the procedure described in section 7.6. Three different initial plasmid concentrations were used: 100, 150, or 200 $\mu\text{g mL}^{-1}$ during each nanoparticle synthesis. The incorporated amount of plasmid into the nanoparticle was calculated by subtraction of the unbound plasmid amount measured by *nanodrop* in the supernatant. Table 16 summarizes the prepared calcium phosphate nanoparticles characterization.

From Table 16 it can be observed that for the calcium phosphate nanoparticles preparation a maximum loading of near 150 $\mu\text{g mL}^{-1}$ is possible. With higher doses the plasmid excess remains in the supernatant. For the synthesis with an initial input of 150 μg , 93% of the plasmid was incorporated into the nanoparticles and with an initial input of 200 μg only 75% is retained giving a concentration near 150 $\mu\text{g mL}^{-1}$.

The plasmid, negatively charged, is electrostatically attracted to the positively charged calcium phosphate nanoparticle (due to the presence of PEI). EGFP plasmid is a relative big molecule with a molecular weight of $M_w=4,056.4$ kDa. As observed in the prepared samples, with an input of 150 μg and 200 μg a saturation of the surface is likely to occur with a loading near 150 μg . At this amount, the plasmid occupies an area close to 80 nm^2 per unit with a total of 170 molecules per nanoparticle.

The reproducibility of this loading procedure was within the $\pm 5\%$ as determined from different nanoparticles preparations.

Table 16: Characterization data for calcium phosphate nanoparticles loaded with different amounts of pEGFP. Shown concentrations refer to the stock solutions which were then diluted and applied in the biological experiments.

Sample	CaP/PEI/ pEGFP(100)/SiO ₂	CaP/PEI/ pEGFP(150)/SiO ₂	CaP/PEI/ pEGFP(200)/SiO ₂
Solid core diameter by SEM / nm	64	64	64
<i>V</i> (one nanoparticle; only CaP) / m ³	1.37·10 ⁻²²	1.37·10 ⁻²²	1.37·10 ⁻²²
<i>A</i> (one nanoparticle; only CaP) / m ²	1.29·10 ⁻¹⁴	1.29·10 ⁻¹⁴	1.29·10 ⁻¹⁴
<i>m</i> (one nanoparticle; only CaP) / kg	4.31·10 ⁻¹⁹	4.31·10 ⁻¹⁹	4.31·10 ⁻¹⁹
<i>w</i> (Ca ²⁺) by AAS / kg m ⁻³	0.0283	0.0273	0.0231
<i>w</i> (Ca ₅ (PO ₄) ₃ OH) / kg m ⁻³	0.0710	0.0683	0.0579
<i>N</i> (nanoparticles) / m ⁻³	1.65·10 ⁺¹⁷	1.59·10 ⁺¹⁷	1.34·10 ⁺¹⁷
<i>w</i> (plasmid) / kg m ⁻³	0.100	0.140	0.151
Loading yield %	100	93.3	75.4
<i>N</i> (loading) / m ⁻³	1.48·10 ⁺¹⁹	2.08·10 ⁺¹⁹	2.24·10 ⁺¹⁹
<i>m</i> (loading) per nanoparticle / kg	6.06·10 ⁻¹⁹	8.83·10 ⁻¹⁹	1.12·10 ⁻¹⁸
<i>N</i> (loading) molecules per nanoparticle	90	130	170
Loading anchor size / nm ² per molecule	143	98	77
wt ratio plasmid to calcium phosphate	1:1.4	1:2	1:2.6
Hydrodynamic diameter by DLS / nm	330	300	372
PDI by DLS	0.35	0.34	0.34
Zeta potential by DLS / mV	+38	+32	+35

For the transfection assay, the prepared nanoparticles were incubated with HeLa cells for 7 h. After this time the medium was changed with fresh one and the cells were further incubated until 48h. Figure 64 shows the transfection efficiency determined by FACS and fluorescence microscopy. The nanoparticles with a higher plasmid loading per nanoparticle gave the best transfection yield near 60%. This percentage is comparable to the one obtained for Lipofectamine. Lipofectamine was used as a positive control due to its well-known transfection efficiency [269]. Between the two nanoparticles types with the higher plasmid content no significant difference was detected in the number of transfected cells, as expected due to the similar plasmid content in the nanoparticle.

Nanoparticles carrying a higher plasmid load per particle will enable after the successful cellular uptake a greater plasmid delivery, and will provide a higher transfection efficiency. From these results, is possible to conclude that nanoparticles with a higher loading can be of advantage when a high plasmid loading is required for transfection, for example for *in vivo* applications.

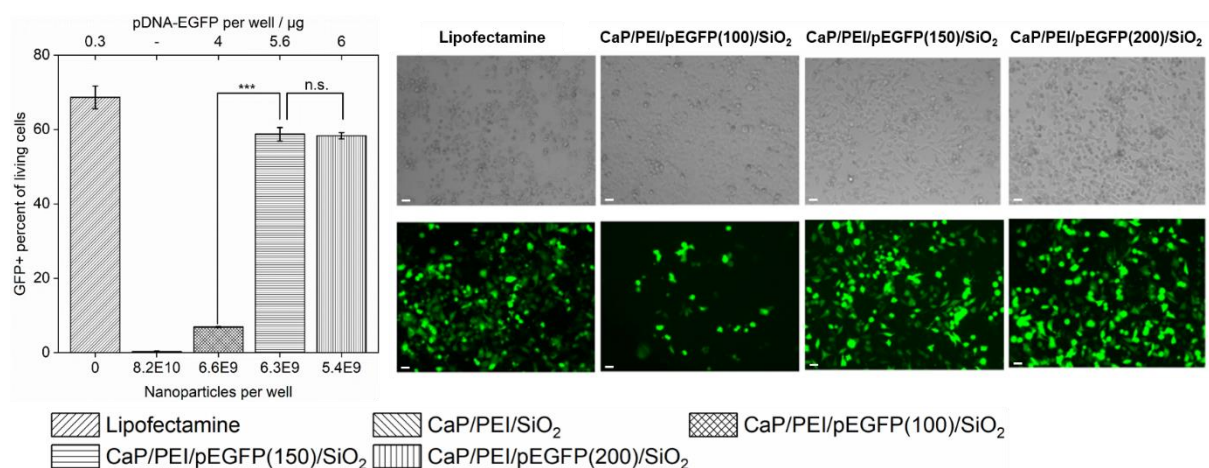


Figure 64: EGFP expression *in vitro* in HeLa cells as determined by flow cytometry (A) and fluorescence microscopy (B) after 48 h of incubation with nanoparticles or Lipofectamine as control (after the first 7 h of incubation the medium was replaced with fresh one). Scale bar is 50 μ m.

8.5.2 Hepatitis B antigen plasmid (pHBsAg) loaded calcium phosphate nanoparticles

Calcium phosphate nanoparticles with an internal load of pHBsAg plasmid were synthesized following the previous described methodology using a nominal plasmid input of 150 μg . Additionally, nanoparticles containing Toll-like receptor ligands (TLR), CpG and flagellin (SF), inside the nanoparticle core were prepared. Table 17 summarizes the nanoparticles characterization data and Figure 65 its corresponding scanning electron micrographs.

These nanoparticles were evaluated for the expression of HBsAg *in vitro* using different cell lines *i.e.*, HeLa, C2C12 and BHK-21. After 7 h incubation of the nanoparticles with the cells, the medium was exchanged with fresh one, and the cells were further incubated until 48 h. By ELISA, the expressed HBsAg concentration was measured in the supernatant. Figure 66 shows the HBsAg expression as a function of the nanoparticles concentration (different given pHBsAg concentration per well) for HeLa and C2C12 cell lines.

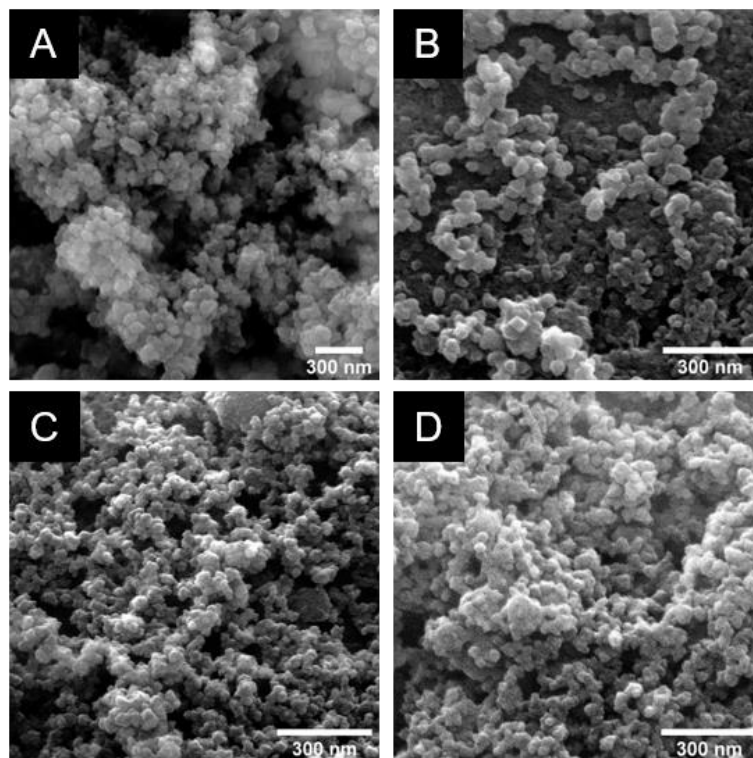


Figure 65: SEM micrographs of the prepared nanoparticles: CaP/PEI/pEGFP/SiO₂ (A), CaP/PEI/pHBsAg/SiO₂ (B), CaP/PEI/pHBsAg+CpG/SiO₂ (C), CaP/PEI/pHBsAg+SF/SiO₂ (D).

Table 17: Characterization summary of pHBsAg loaded calcium phosphate nanoparticles. These given concentrations refer to the nanoparticle stock solutions.

Sample	CaP/PEI/ SiO ₂	CaP/PEI/ pHBsAg/SiO ₂	CaP/PEI/ pHBsAg+ CpG/SiO ₂	CaP/PEI/ pHBsAg+SF/ SiO ₂
Solid core diameter by SEM / nm	36	40	32	39
$V(\text{one nanoparticle; only CaP}) / \text{m}^3$	$2.44 \cdot 10^{-23}$	$3.35 \cdot 10^{-23}$	$1.71 \cdot 10^{-23}$	$3.10 \cdot 10^{-23}$
$m(\text{one nanoparticle; only CaP}) / \text{kg}$	$7.67 \cdot 10^{-20}$	$1.05 \cdot 10^{-19}$	$5.38 \cdot 10^{-20}$	$9.75 \cdot 10^{-20}$
$w(\text{Ca}^{2+}) \text{ by AAS} / \text{kg m}^{-3}$	0.065	0.067	0.067	0.072
$w(\text{Ca}_5(\text{PO}_4)_3\text{OH}) / \text{kg m}^{-3}$	0.165	0.168	0.167	0.181
$N(\text{nanoparticles}) / \text{m}^{-3}$	$2.15 \cdot 10^{18}$	$1.60 \cdot 10^{18}$	$3.10 \cdot 10^{18}$	$1.86 \cdot 10^{18}$
$w(\text{plasmid}) / \text{kg m}^{-3}$	-	0.144	0.144	0.144
$N(\text{plasmid}) / \text{m}^{-3}$	-	$3.41 \cdot 10^{21}$	$3.41 \cdot 10^{21}$	$3.42 \cdot 10^{21}$
$m(\text{plasmid}) \text{ per nanoparticle} / \text{kg}$	-	$9.02 \cdot 10^{-20}$	$4.65 \cdot 10^{-20}$	$7.75 \cdot 10^{-20}$
$N(\text{plasmid}) \text{ molecules per nanoparticle}$	-	$2.14 \cdot 10^3$	$1.10 \cdot 10^3$	$1.84 \cdot 10^3$
weight ratio of plasmid to calcium phosphate	-	1 : 1.17	1 : 1.16	1 : 1.26
$w(\text{adjuvant}) / \text{kg m}^{-3}$	-	-	CpG: 0.0074	SF: 0.0074
$N(\text{adjuvant}) / \text{m}^{-3}$	-	-	CpG: $7.00 \cdot 10^{20}$	SF: $8.38 \cdot 10^{19}$
$m(\text{adjuvant}) \text{ per nanoparticle} / \text{kg}$	-	-	CpG: $2.39 \cdot 10^{-21}$	SF: $3.98 \cdot 10^{-21}$
$N(\text{adjuvant}) \text{ molecules per nanoparticle}$	-	-	CpG: 226	SF: 45
weight ratio of adjuvant to calcium phosphate	-	-	CpG: 1 : 22	SF: 1 : 24
Hydrodynamic diameter by DLS / nm (z-average)	137	258	289	220
PDI by DLS	0.25	0.22	0.21	0.29
Zeta potential by DLS / mV	+24	+26	+24	+23
Endotoxins / EU mL ⁻¹	< 0.1	< 0.1	< 0.1	< 0.1

With HeLa cell line an equivalent HBsAg expression for nanoparticles and Lipofectamine was obtained at 0.3 μg plasmid per well. By increasing the number of nanoparticles per well (*i.e.*, the amount of given plasmid per well) a higher HBsAg expression is achieved. With C2C12 cell line a higher HBsAg expression was obtained using the nanoparticles compared to Lipofectamine. It has been reported that for C2C12 cells Lipofectamine transfection efficiency is decreased with medium containing serum during the incubation [295, 296]. The lower transfection efficiency for C2C12 cells compared to HeLa cell line is related that in general myoblasts are considered to be a hard to transfect [297, 298]. In this way, the calcium phosphate nanoparticles are a good alternative to increase the transfection yield as observed in Figure 66. The transfection analysis with muscle cells (*e.g.* C2C12) is of importance, because with an intra muscular (*i.m.*) injection, the muscle cells are the first ones to be in contact with the delivery for uptake [299].

The influence in the transfection due to the adjuvant loading inside the nanoparticles were also evaluated. With a CpG or SF concentration of near 7.5 $\mu\text{g mL}^{-1}$ a higher HBsAg expression was obtained compared to higher adjuvant doses. It has been reported that a suppressive effect in the stimulatory pathway can occur with higher CpG doses [300]. This effect can become more significant with other cell lines or *in vivo* if higher adjuvant doses are used.

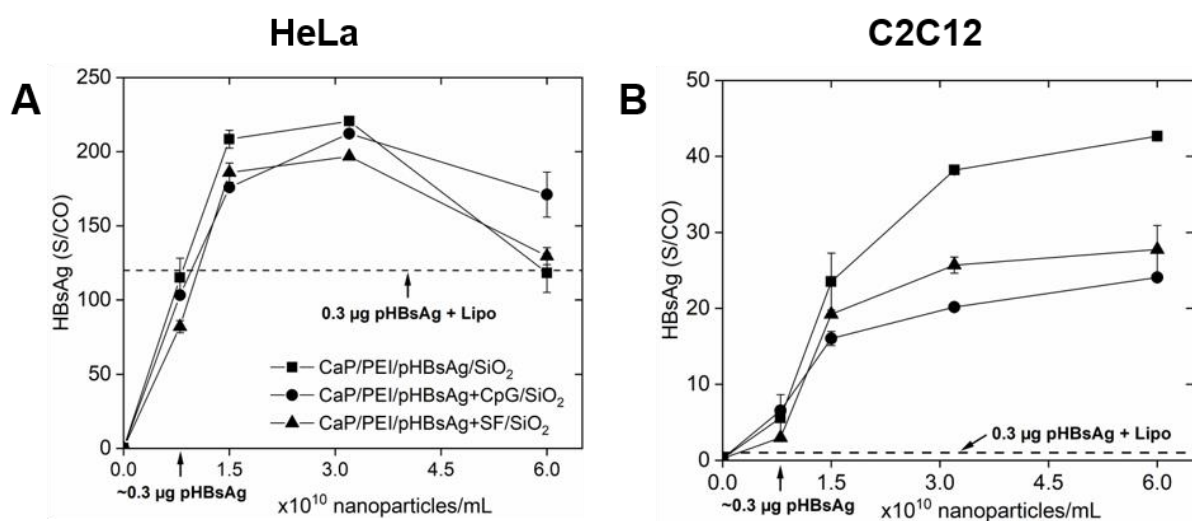


Figure 66: HBsAg expression *in vitro* in HeLa (A) and C2C12 (B) cells determined by ELISA. Different nanoparticles concentrations per well were assayed using dilutions from nanoparticles stock solutions (Table 17) and Lipofectamine was used as a control.

Transfection with baby hamster kidney cells (BHK-21) were also investigated, as this cell line is a useful model for viral studies [301-303]. Figure 67 shows the HBsAg expression measured by ELISA after 24 and 48 hours of incubation with this cell line. Different plasmid amounts per well were evaluated 0.2, 0.5, 1.5, and 2.8 μg . With the lower plasmid concentration (0.2 μg) the antigen expression was very low even after 48 h, and at the highest concentration (2.8 μg) a lower cell viability was observed by microscope, which was related to the higher amount of nanoparticles and polyethylenimine (PEI) cytotoxicity [272, 273].

After 48 hours of incubation a higher HBsAg expression was detected, and with a plasmid dose of 1.5 μg the highest expression was achieved. Between the nanoparticles with and without CpG comparable results were obtained. As positive control Lipofectamine [270] and PEI [224] were used and after 48 h similar results were obtained. From previous studies using HeLa cells it was observed that the transfection with Lipofectamine increases faster as compared with calcium phosphate nanoparticles [46], situation that is also reflected in these results.

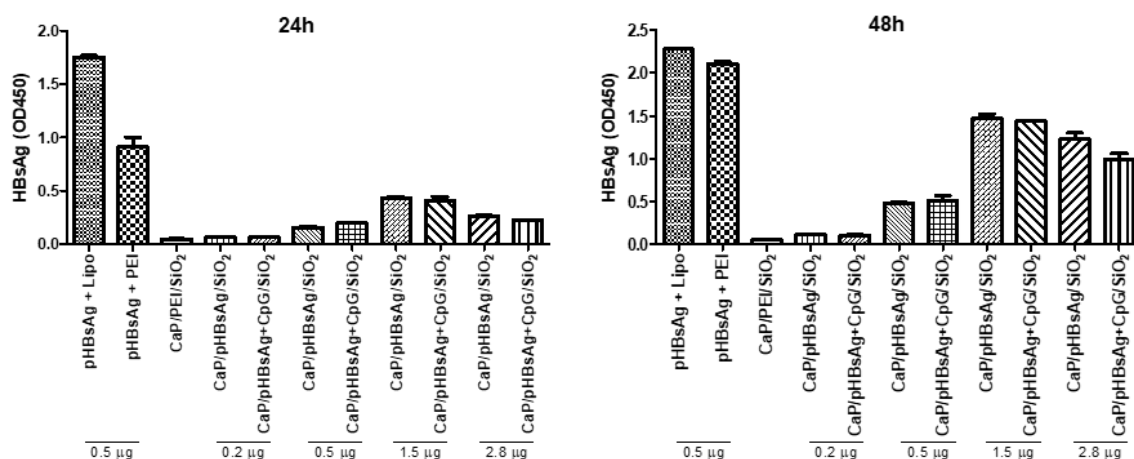


Figure 67: HBsAg expression *in vitro* in BHK-21 cells after 24 h and 48 h of incubation with nanoparticles (CaP/pHBsAg/SiO₂ and CaP/pHBsAg+CpG/SiO₂), Lipofectamine or PEI determined by ELISA. CaP/PEI/SiO₂ nanoparticles were used as control particles without plasmid to set the system detection baseline.

Polyethylenimine polymer is known to be a good transfection agent [224]. Different to Lipofectamine, where the interaction with the nucleic acid is based on a cationic

lipid, PEI is a cationic polymer. Analogous to Lipofectamine, an interaction of the negatively charged nucleic acid and the positive charge polymer generates the polyplexes. A polymer such as branched PEI (M_w 25 kDa) allows to have a highly protonated polymer at physiological conditions that will enhanced the interaction with the DNA [304].

The uptake mechanism for both systems (lipoplexes and polyplexes) is similar. Usually particles are taken up by the cells following an endocytosis mechanism. Once they are internalized, the particle has to be released into the cytosol before the endosome fuses with lysosomes. If this occurs, due to the lysosome acidic pH the nucleic acids loading is likely to be damage.

The pathway to release the polyplexes from the endosomes is triggered by an osmotic rupture of endosomes, caused by a charge gradient induced by the PEI's nitrogen protonation as the pH is lowered. Due to the increase in the positive charge inside the endosome, a Cl^- influx occurs to compensate the charge gradient in the endosome, which then leads to a water influx that finally causes that the endosome collapses [224, 305]. In a different way, the lipoplexes are released from the endosomes by a membrane destabilization caused by a lipid transfer or fusion from the lipoplex to the endosome membrane [305]. Once release in the cytoplasm the plasmid needs to reach the nucleus for transfection.

Similarly, calcium phosphate nanoparticles are taken up by the cells via endocytosis [133], and follow a slower process compared to lipoplexes absorption [46]. Due to the PEI loading in the nanoparticle, a comparable endosome rupture as polyplexes is expected to occur, and the release calcium ions helps to stabilized the gene vector and assists to complete the transfection [306]. As observed in Figure 67, after 24 h the HBsAg expression with Lipofectamine was higher as compared with PEI and calcium phosphate nanoparticles suggesting a faster delivery mechanism. After 48 h similar values for Lipofectamine and PEI were obtained and a higher amount with calcium phosphate nanoparticles when compared to 24 h.

The next step after the successful antigen expression by transfection is to verify the immune response induction. For this, the expression of costimulatory signals are

required to activate T cells and to cause the immune response [307]. *Ex vivo* stimulation of dendritic cells by pHBsAg loaded CaP NPs was studied for the expression of costimulatory molecules (CD80 and CD86). A nanoparticle comparison to determine the adjuvant influence in the activation was analyzed.

The results from flow cytometry are shown in Figure 68. CD80 was upregulated only by the SF containing nanoparticles but CD86 expression was stimulated by all the nanoparticles (loaded and not-loaded CaP NPs). This indicates that CaP NPs can upregulate CD86 without being dependent on the TLR-ligand loading.

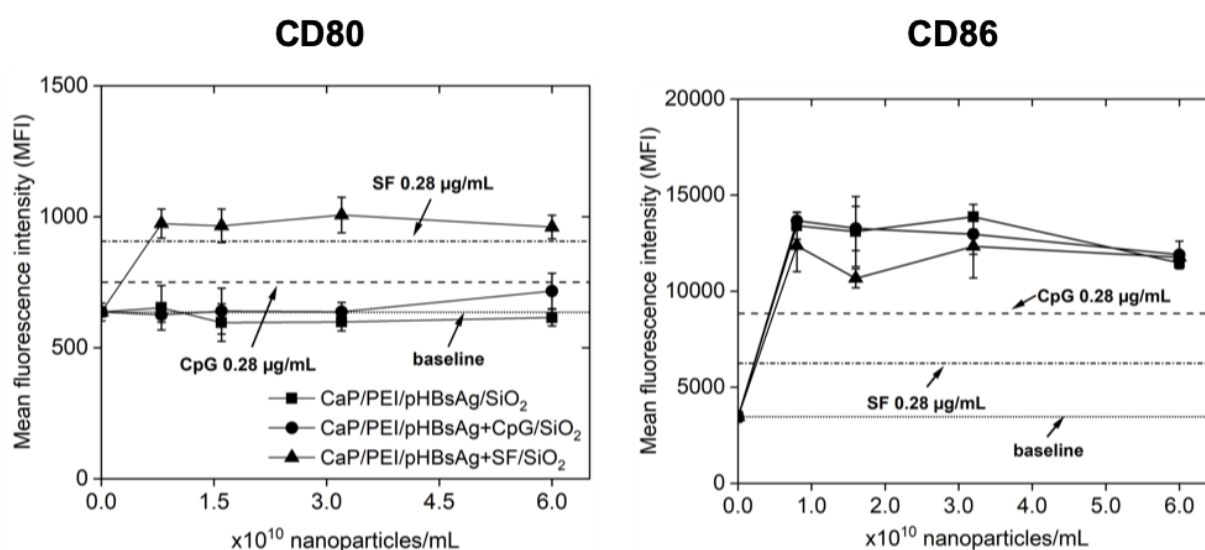


Figure 68 Activation of dendritic cells and expression of costimulatory signals (CD80 and CD86) by CaP/PEI/pHBsAg/SiO₂, CaP/PEI/pHBsAg+CpG/SiO₂, CaP/PEI/pHBsAg+SF/SiO₂. Dilution from the stock nanoparticles (Table 17) were assayed and a resultant adjuvant concentration per well of 0.03-0.27 $\mu\text{g mL}^{-1}$ was tested.

After the successful expression of HBs antigen in the *in vitro* experiments an *in vivo* immunization of C57BL/6 mice were performed using the pHBsAg loaded nanoparticles.

With the nanoparticles a dose of 42 μg plasmid was given to the mice by intramuscular injection (*i.m.*), and as a positive control 50 μg plasmid were injected (*i.m.*) followed by an electronic pulse (electroporation). After 5 days, the HBsAg expression increases more than the double compared to the base level (Figure 69). The baseline was set

by an immunized mice with unloaded nanoparticles, and is related to the mice and the ELISA detection method.

As observe from Figure 69, comparable results to the positive control by electroporation were obtained for pHBsAg and pHBsAg+CpG loaded nanoparticles. In general, these results evidence the *in vivo* transfection of loaded calcium phosphate nanoparticles and makes them suitable for further *in vivo* transfections assays.

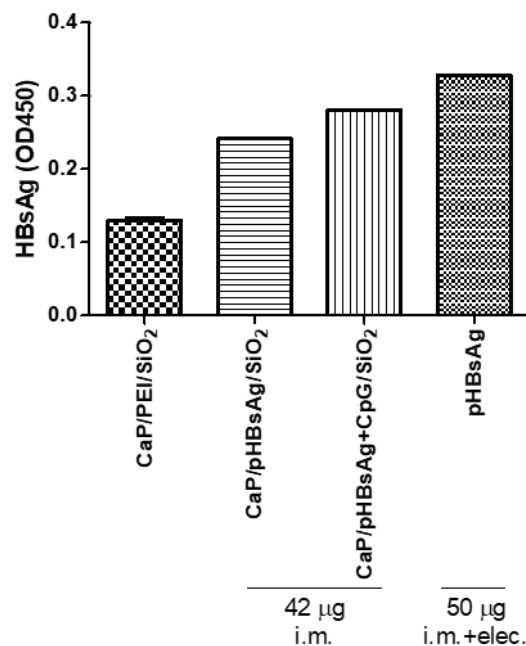


Figure 69: HBsAg expression *in vivo* in C57BL/6 mice 5 days post injection detected by ELISA. A positive control was pHBsAg plasmid delivered by i.m. followed by an electronic pulse. The detection baseline of the method was determined from animals immunized with calcium phosphate nanoparticles without plasmid.

As next step, the immune response induced by the loaded nanoparticles was studied. With C57/BL6 mice an immunization trial was performed with three immunization doses at a two week interval between each one. Fourteen days after the last immunization, the mice were sacrificed and the anti-HBs in the mouse serum detected by ELISA.

Figure 70 shows the anti-HBs IgG1 and IgG2a response after the immunization trial. As observed, an increased detection for anti-HBs IgG1 level is obtained for all the

loaded nanoparticles, as well, as for the pHBsAg control. Adjuvant loaded nanoparticles with CpG or *in situ* mixed with SF shows a higher antibody response. This Toll-like receptors ligands (TLR-ligands) are able to activate the immune response stimulating the antibody formation. In contrast, IgG2a level was not upregulated after the immunization doses.

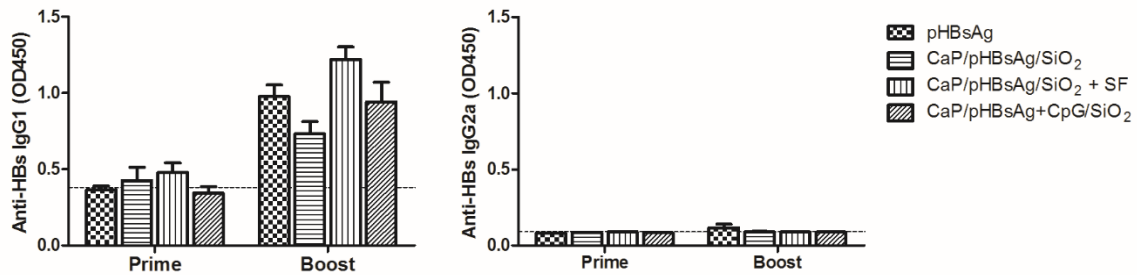


Figure 70: Antibody response after 14 days post the 3rd immunization with pHBsAg loaded nanoparticles. Anti-HBs IgG1 and anti-HBs IgG2a were detected at 1:100 by ELISA and the absorbance at 450 nm shows the relative expression of HBsAg in each group. The detection baseline is shown as a dash line using the serum of naïve mice.

8.5.3 Section summary

The nanoparticles plasmid loading was optimized to provide a higher dose per nanoparticle using a pEGFP as model. An appropriate loading in the calcium phosphate nanoparticle was achieved with a nominal pEGFP input of 150 μg per 1 mL nanoparticles ($1.59 \cdot 10^{+17}$). This gave around 130 pEGFP units per nanoparticle and a loading yield of near 90%. Nanoparticles loaded with pHBsAg were synthesized and the transfection studied with HeLa, C2C12 and BHK-21 cell lines. In all cases a good antigen expression was detected after 48 hours. Additionally, the NPs were able to upregulate CD86 and with SF-loaded NPs CD80 in *ex vivo* dendritic cells. *In vivo*, with C57BL/6 mice, the nanoparticles induced the HBsAg expression after 5 days. Moreover, the anti-HBs IgG1 response was increased after the third immunization with the pHBsAg loaded nanoparticles.

8.6 TNF- α gene silencing *in vitro* and *in vivo* with calcium phosphate nanoparticles

Calcium phosphate nanoparticles can be formulated to address a solution for a specific application. In a different way from vaccination, in the following section is demonstrated a successful direct topical application of an active calcium phosphate nanoparticle within the biomedicine scope.

In dentistry, especially after a restorative procedure, an extended inflammation can have a detrimental effect on the periodontal region. Of interested is the TNF- α cytokine which is related to the inflammation process [308-311]. As an alternative method, a localized gene silencing treatment together with the dental procedure can reduce this cytokine expression.

Due to its properties, calcium phosphate nanoparticles are an ideal siRNA carrier for this application. In the following section, a direct application of calcium phosphate nanoparticles loaded with TNF- α -siRNA is described and evaluated *in vitro* and *in vivo*.

8.6.1 siRNA loaded calcium phosphate nanoparticles

Calcium phosphate nanoparticles loaded with TNF- α siRNA and scrambled siRNA were prepared following the procedure described in section 7.7 which generates a nanoparticle structure of CaP/PEI/loading/SiO₂. In this case the siRNA loading is absorbed electrostatically to the calcium phosphate core and the external silica coating protects the loading from enzymatic degradation (*e.g.* RNAses). The nanoparticles had a positive ζ -potential due to the presence of PEI, which helps for the cellular uptake process. The nanoparticles characterization summary for the used materials in these experiments are shown in Table 18 and a representative DLS size distribution and SEM image in Figure 71.

Table 18: Properties of siRNA loaded calcium phosphate nanoparticles. Concentrations refer to stock solutions that were diluted before use in the experiments.

Sample (dispersion)	CaP/PEI/SiO ₂	CaP/PEI/ TNF- α - siRNA /SiO ₂	CaP/PEI/ scrambled- siRNA /SiO ₂
Solid particle diameter by SEM / nm	40	40	87
V (one nanoparticle; only CaP) / m ³	$3.35 \cdot 10^{-23}$	$3.35 \cdot 10^{-23}$	$3.45 \cdot 10^{-22}$
M (one nanoparticle; only CaP) / kg	$1.05 \cdot 10^{-19}$	$1.05 \cdot 10^{-19}$	$1.08 \cdot 10^{-18}$
W (Ca ²⁺) by AAS / kg m ⁻³	0.043	0.062	0.031
W (Ca ₅ (PO ₄) ₃ OH) / kg m ⁻³	0.108	0.155	0.078
N (nanoparticles) / m ⁻³	$1.03 \cdot 10^{18}$	$1.48 \cdot 10^{18}$	$7.25 \cdot 10^{16}$
W (siRNA) / kg m ⁻³	-	0.067	0.050
N (siRNA) / molecules m ⁻³	-	$3.01 \cdot 10^{21}$	$2.22 \cdot 10^{21}$
M (siRNA) per nanoparticle / kg	-	$4.55 \cdot 10^{-20}$	$6.84 \cdot 10^{-19}$
N (siRNA) molecules per nanoparticle	-	$2.04 \cdot 10^3$	$3.06 \cdot 10^4$
weight ratio siRNA to calcium phosphate	-	1 : 2.5	1 : 1.6
Hydrodynamic diameter by DLS / nm	188	225	251
PDI by DLS	0.21	0.34	0.46
Zeta potential by DLS / mV	+24	+23	+21
Endotoxins / EU mL ⁻¹	< 0.1	< 0.1	< 0.1

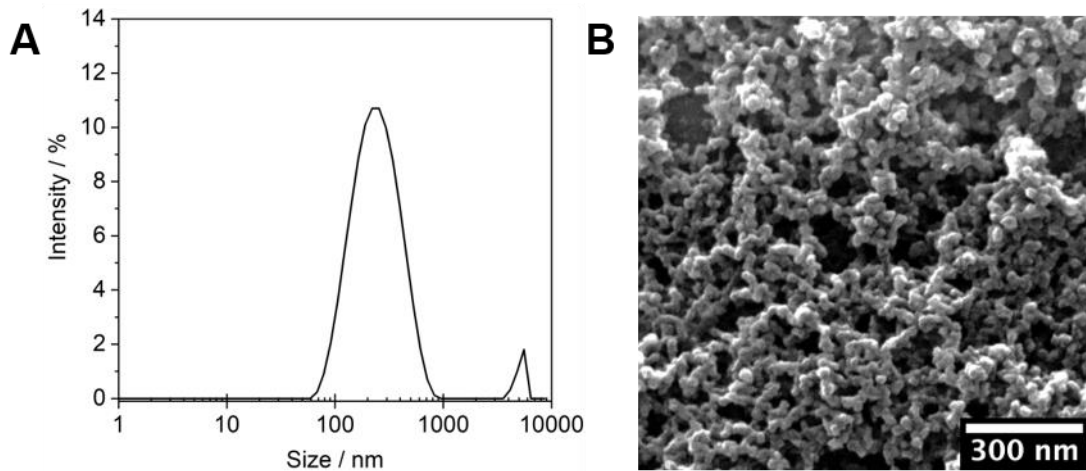


Figure 71 A: Particle size distribution by dynamic light scattering (DLS) and B: Scanning electron micrograph (SEM) of CaP/PEI/TNF- α -siRNA/SiO₂ nanoparticles.

8.6.2 *In vitro* studies with J774.2 macrophages

To assay for the gene silencing efficiency of these nanoparticles *in vitro* J774.2 macrophages were used. These macrophages are from mouse BALB/c origin and are semi-adherent cells with a population doubling time of 17 hours. With a lipopolysaccharides (LPS) stimulation is possible to upregulate the TNF- α expression to be detected and quantified by ELISA.

To follow the nanoparticle *in vitro* and to confirm the uptake by this cell line, clicked labelled calcium phosphate nanoparticles with Alexa Fluor® 488 were used. Figure 72 shows that the nanoparticles were successfully taken by the cells after 10 h. Additionally, Figure 73 shows a CLSM z-stacking reconstruction 3D view, in where is possible to confirm that the nanoparticles were inside the cell and not over it. These results agree with the time frame observed with other cells lines for the nanoparticles uptake [44].

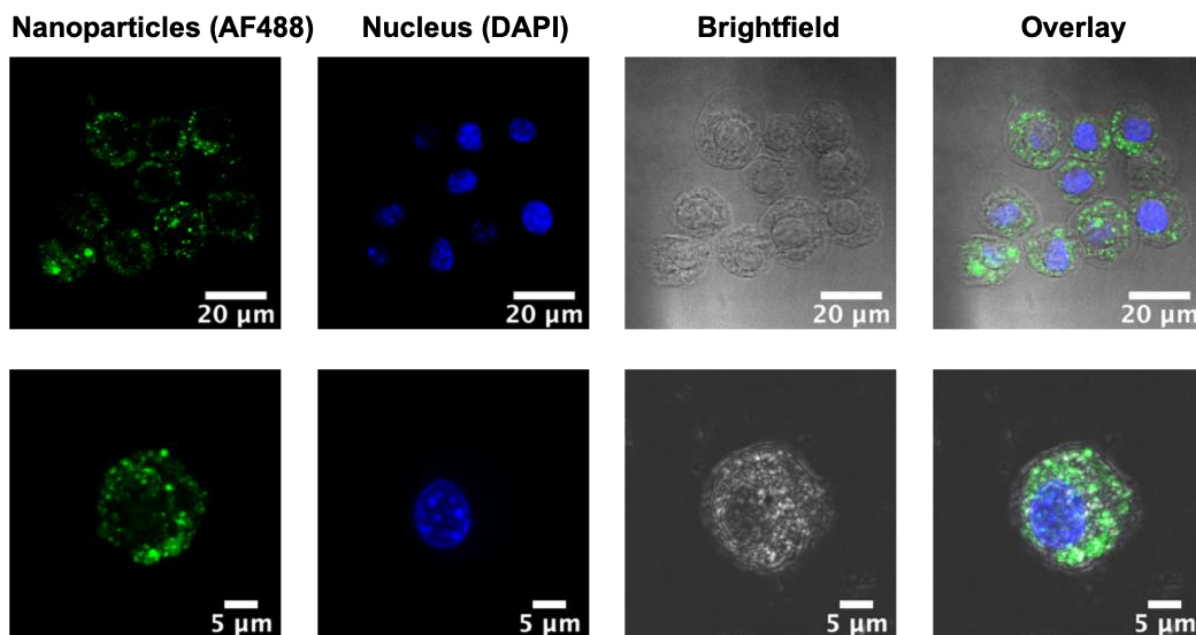


Figure 72: CLSM image of J774.2 cells incubated with fluorescent CaP/PEI/SiO₂-AF488 nanoparticles for 10 h. Brightfield illumination, 488 channel (nanoparticles in green), DAPI channel (cell nucleus in blue) and overlay. Top: Overview; bottom: close-up of one cell.

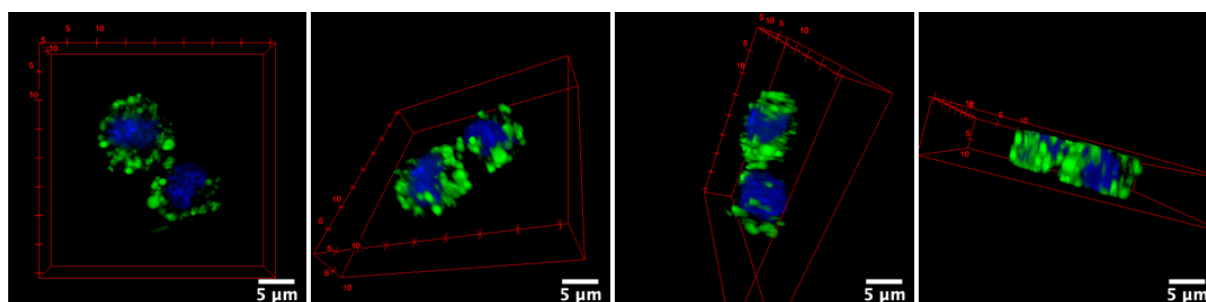


Figure 73: CLSM z-stack image of J774.2 cells incubated with fluorescent CaP/PEI/SiO₂-AF488 nanoparticles for 10 h. Nanoparticles in green (AF-488) and nucleus in blue (DAPI).

LPS from *Escherichia coli* O55:B5 were added to the cells to stimulate the cytokine TNF- α (Tumor necrosis factor) expression [312]. To find the LPS dose for the stimulation different concentration per well (0.1, 1, and 10 $\mu\text{g/mL}$) were studied. Figure 74 shows the normalized TNF- α expression after 4h of incubation with the LPS loading. For these conditions and with a 1 $\mu\text{g/mL}$ LPS concentration was possible to increase by a factor of 7 the cytokine expression. For further gene silencing expression this concentration was chosen.

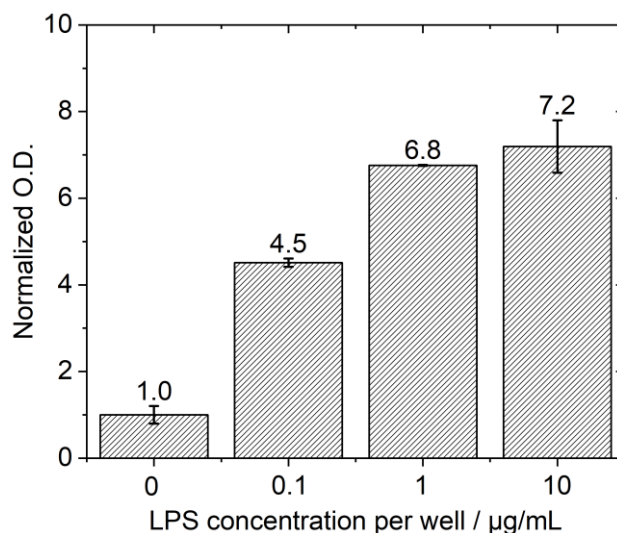


Figure 74: J774.2 macrophage TNF- α expression after 4 h incubation with different LPS concentration (*Escherichia coli* O55:B5). Cells were seeded the day before at 5.0×10^4 cells per well.

A MTT assay for the cell viability after the incubation with the nanoparticles and LPS stimulation was performed. Nanoparticles were incubated for a total of 9 hours with the cells before removing the medium for the MTT analysis. Figure 75 shows that up to a nanoparticle number of 2.1×10^{10} per well and LPS stimulated cells a cell viability above 65% is obtained and at this nanoparticle number a siRNA-TNF- α dose of $2.0 \mu\text{g mL}^{-1}$ was given. For a higher dosage, a larger number of nanoparticles should be given but the applicability is limited due to the decrease in the cell viability.

The gene silencing experiment was performed with a TNF- α -siRNA concentration of 0.5, 1, and $2 \mu\text{g mL}^{-1}$ after the addition of the nanoparticles. As positive control for silencing, Lipofectamine 2000® was used at the same TNF- α -siRNA concentration as for the nanoparticles, and a negative control with scramble siRNA loaded nanoparticles was used. Figure 75 shows the normalized TNF- α expression after the treatment. TNF- α expression was reduced by $12 \pm 2\%$ with the active nanoparticles and the silencing efficiency obtained was comparable to Lipofectamine, although no significant differences were observed within the groups.

Silencing efficiency is expected to vary between different cell lines [313, 314], in this case the obtained efficiency is lower compared to other macrophages [315]. Normally, macrophages are more resistant to transfection and gene silencing due to the release

of enzymes that can degrade nucleic acids after phagocytosis [316]. Moreover, J774 cell line is considered to be difficult to transfect [317, 318] and although transfection and silencing follow different pathways, the delivery of the nucleic acid (pDNA or siRNA) into the cytosol is required in both cases [136]. It has been observed that in difficult to transfect cell lines a lower gene silencing efficiency is normally obtained [319, 320].

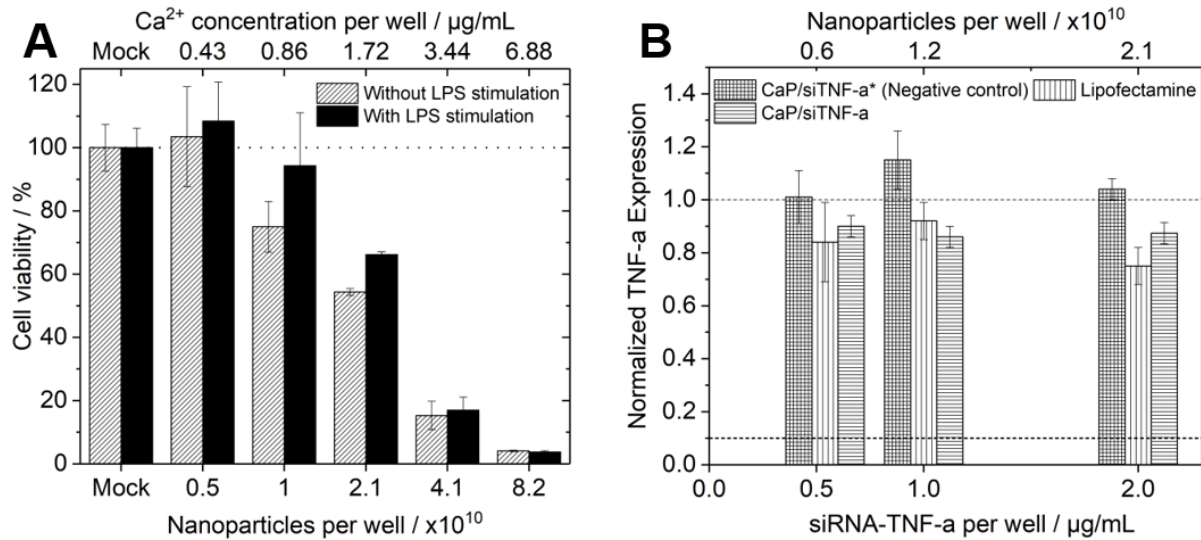


Figure 75: A: Cell viability of J774.2 monocytes after 9 hours incubation at different nanoparticles per well concentrations. **B:** Gene silencing efficiency for J774.2 monocytes after 6 h incubation with the nanoparticles or Lipofectamine 2000 and 4 h LPS ($1 \mu\text{g mL}^{-1}$) stimulation. The results are normalized to cells not treated with nanoparticles but stimulated with the same LPS concentration. Between the three groups, no significant differences were detected ($p < 0.05$).

With siRNA loaded calcium phosphate nanoparticles Neuhaus *et al.* had studied the TNF- α -siRNA silencing with MODE-K cells at the mRNA level [321]. In this case, a decrease of $45 \pm 10\%$ was observed for the active nanoparticles when compared to untreated LPS-stimulated cells. At the mRNA level the silencing can be followed before the expression of the cytokine, reducing the time required for the detection.

For the *in vivo* application in a rat periodontitis model an injectable substrate is required. Two main limitations of the direct application of the nanoparticles can emerge. The first one is related to the siRNA dosage, with a direct application of the active nanoparticles more material should be applied and the final siRNA would be too high. The second one is related to the material availability after the application. If the

nanoparticles are directly applied into the surgery cavity the material availability will be limited to a short time and its efficiency then decrease. To overcome these potential problems a matrix for the application is required. For this purpose a calcium phosphate based paste stabilized with carboxymethylcellulose (CMC) is used and the active nanoparticle dispersion is added into it.

Figure 76 shows the paste matrix TGA thermogram and SEM micrograph. From the TGA analysis, the matrix has a composition of near 69 wt.% calcium phosphate, 5.3 wt.% carboxymethylcellulose, and the remaining is water. The active paste was prepared by mixing the CaP/CMC matrix with the nanoparticles dispersion. To increase the siRNA content inside the paste, the nanoparticles stock dispersion was concentrated in a 57-fold. For this 1.25 mL nanoparticles stock dispersion was lyophilized and redispersed in 22 μ L water. From this concentrated dispersion 11 μ L were taken and mixed with 12.5 mg dry paste matrix. This lead to a mass ratio of approximate 54% paste matrix and 46% aqueous content (*i.e.*, the wt.% of the nanoparticles dispersion consists mainly of water). A presentative image of the final paste preparation is shown in Figure 77.

In the dental cavity was placed 1.6 mg of the paste per application, which provides a siRNA-TNF- α dosage of 5.4 μ g per site. As control material CaP/PEI/SiO₂ nanoparticles were used in the same ratios.

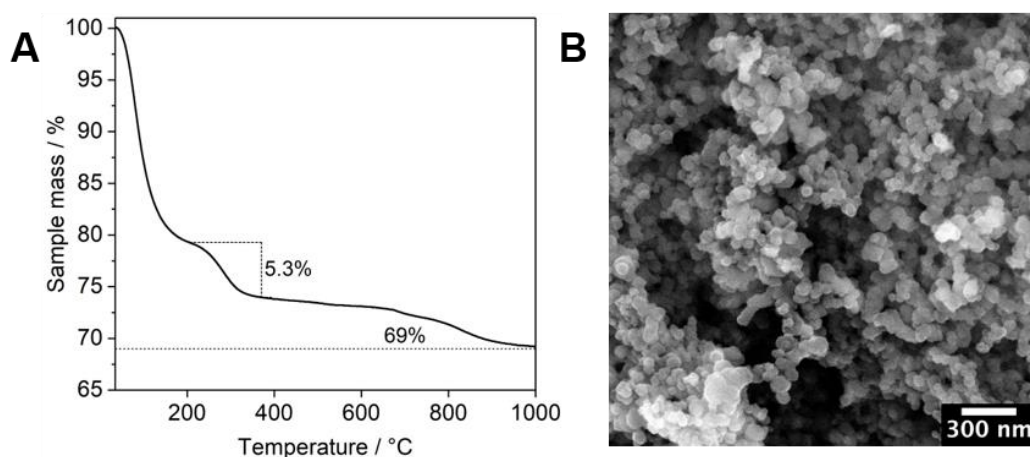


Figure 76: **A:** Thermogravimetric analysis (TGA) of the CaP/CMC paste matrix. **B:** SEM micrograph of the dried CaP/CMC paste matrix particles.

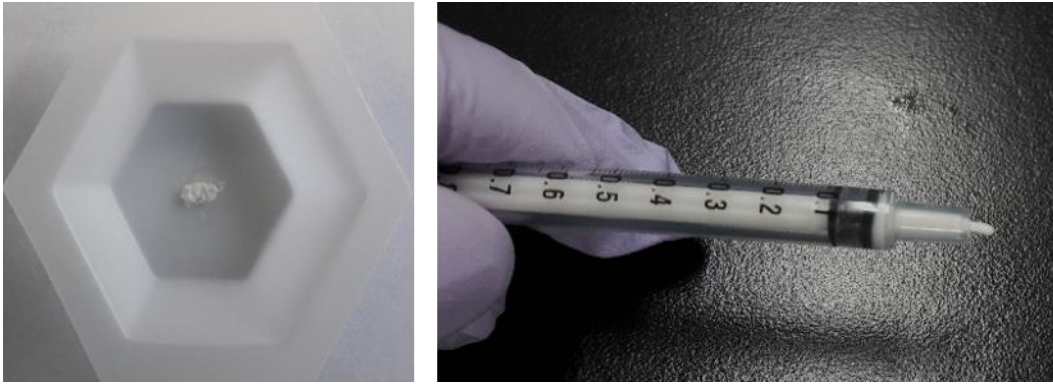


Figure 77 Calcium phosphate paste photograph after adding the nanoparticles dispersion to the paste matrix.

8.6.3 *In vivo* studies on a periodontitis model in rats

The *in vivo* studies on a periodontitis model in rats were carried out in Sendai, Japan by the group of Prof. Dr. Keiichi Sasaki and Dr. Taichi Tenkumo from Tohoku University. The main results are summarized in the following section.

The chronic periodontitis model in rats was first generated by doing a 1-mm-high bone defect by ultrasonication on the palatal sides of both maxillary first molars and afterwards sutured. After 7 days, a sandblasted stainless steel wire was reeled around the subgingival position for 14 days. Then on day 21st, the gingival-flap on the palatal side of both maxillary first molars was reflected and bone defect created by ultrasonication.

In the defect 1.6 mg calcium phosphate paste (active or non-active) was placed. The flap was sutured to prevent infection and material loss. In total, three different groups were prepared “CaP-positive” (CaP/PEI/TNF- α -siRNA/SiO₂), “CaP-negative” (CaP/PEI/SiO₂) and “Surgery-only” (without paste application). In total 90 rats were used in the study and the tissue was extracted after sacrificed on days 1, 3, 7, 10, and 21. Figure 78 shows the *in vivo* experimental timeline protocol.

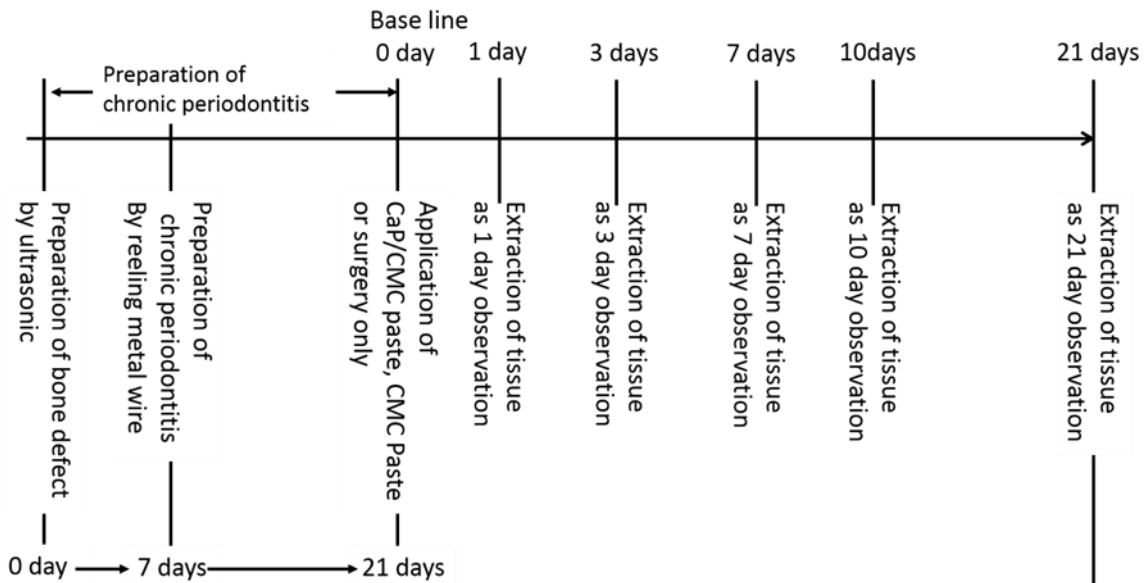


Figure 78: Timeline protocol of the *in vivo* experiment with a rat periodontitis model.

After the third day of the paste implantation the TNF- α mRNA expression decreases in the CaP-Positive group and was comparable to the surgery-only group as shown in Figure 79. As observed, the TNF- α mRNA expression was kept near one third to one half of the expression for the CaP-Negative group and a significant difference at the TNF- α protein level is also obtained (Figure 79, E).

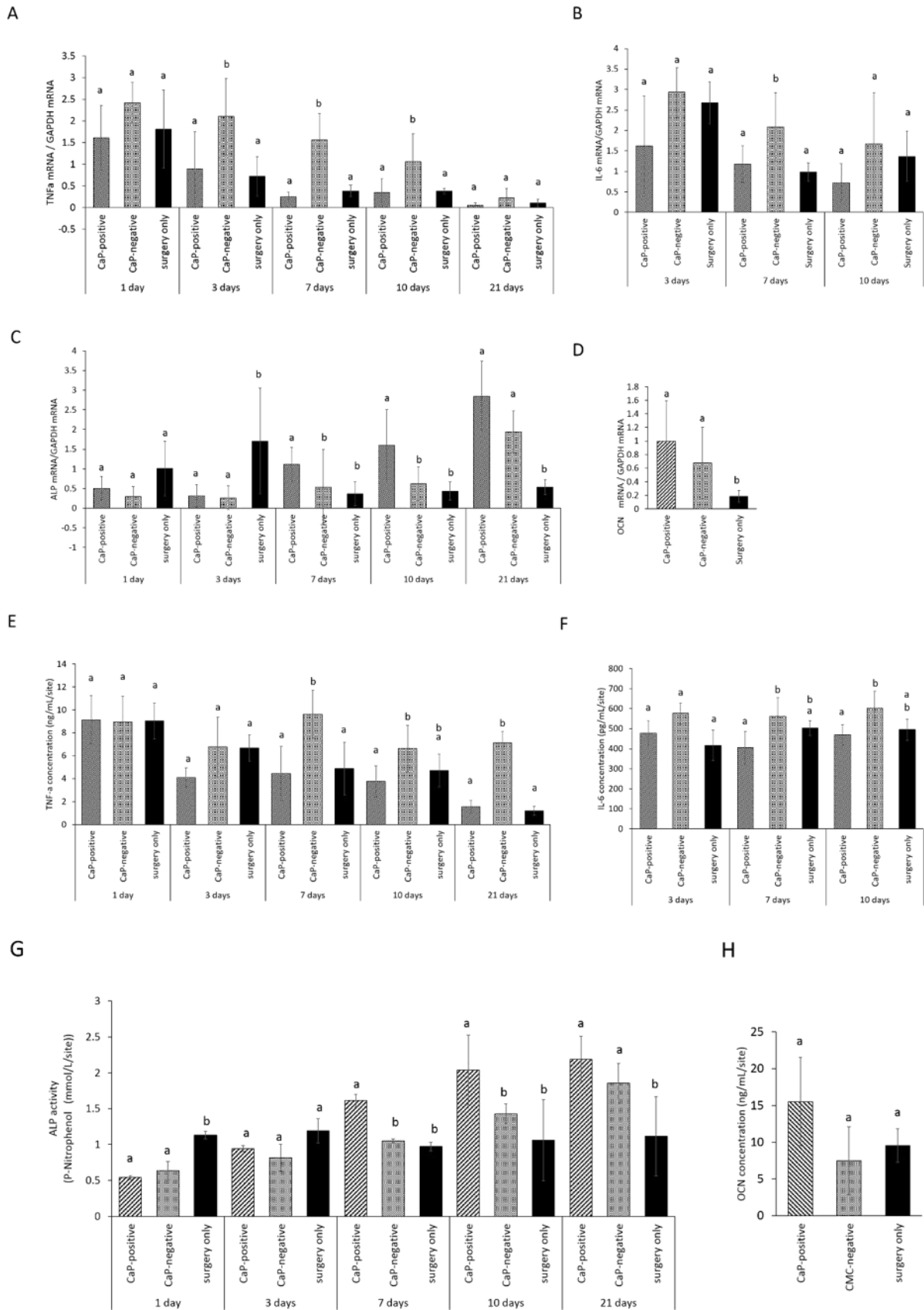


Figure 79: Biochemical analyses after implantation of CaP-positive or CaP-negative paste or surgery-only, respectively, in the experimental periodontitis site. A: TNF-α mRNA expression at 1, 3, 7, 10, or 21 d after implantation. B: IL-6 mRNA expression

at 3, 7, or 10 d after implantation. C: ALP mRNA expression at 1, 3, 7, 10, or 21 d after implantation. D: OCN mRNA expression at 21 d after implantation. E: Quantification of TNF- α protein in the supernatant by ELISA 1, 3, 7, 10, or 21 d after implantation. F: Quantification of IL-6 protein in the supernatant by ELISA 3, 7, or 10 d after implantation. G: Quantification of ALP protein in the supernatant by ELISA 1, 3, 7, 10, or 21 d after implantation. H: Quantification of OCN protein in the supernatant by ELISA 21 d after implantation. Significant differences ($p < 0.05$) between the groups at each time point are denoted by different superscript letters at the same time point (*i.e.*, bars with the same letter are not significantly different). Figure edited by Dr.Tenkumo *et al.*

For these parameters after the first day no differences were observed within the different groups. This time delay between the first three days is related to the time that is required for the nanoparticles release and cellular uptake. Different to *in vitro* experiments where the nanoparticles are added directly to the cell culture the uptake starts immediately and after a few hours the nanoparticles can be detected inside the cells. *In vivo* the cells have first to migrate into the material and the release nanoparticles can also be taken by the surrounding cells after the materials degradation [322-324].

From histological observations, inflammatory cells (*e.g.*, neutrophils, macrophages, red corpuscles) were detected without any severe inflammation nor necrosis. Positive stained TNF- α cells decrease with time as shown in Table 19. These observations are in agreement with the PCR and ELISA analysis mentioned before, for which after the third day of implantation the number of TNF- α expression decreases.

Table 19: Number of TNF- α -stained positive cells from immunohistochemical images.

Number of days after implantation / d	CaP-positive	CaP-negative	Surgery-only
1	932 \pm 50	1,072 \pm 252	695 \pm 146
3	671 \pm 48	710 \pm 128	524 \pm 119
7	430 \pm 97	578 \pm 141	367 \pm 74
10	356 \pm 40	454 \pm 94	296 \pm 92
21	253 \pm 111	348 \pm 52	172 \pm 30

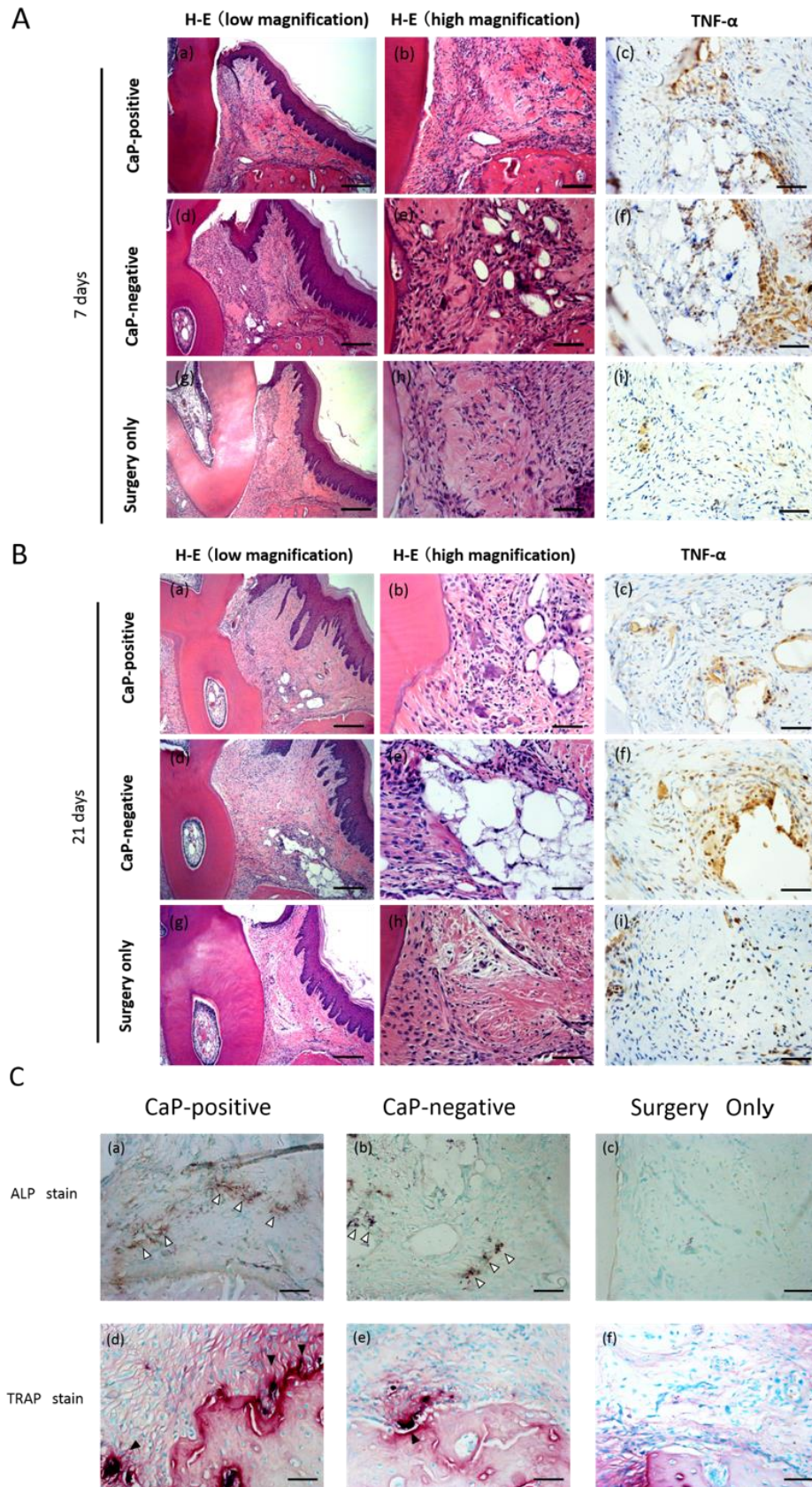


Figure 80: Immunohistochemical staining of periodontal tissue at A: 7 d, B and C: 21 d after implantation. Upper line shows CaP-positive group (a, b, and c); centre line shows CaP-negative group (d, e, and f); lower line shows surgery-only group (g, h,

and i). The left column shows haematoxylin and eosin (H&E) staining at low magnification; the centre column shows H&E staining at high magnification. The right column shows TNF- α staining. White arrowheads indicate BMP-2-positive areas. Asterisks indicate retained nHAC. Scale bars: 200 μm in the left column, 100 μm in the centre column, and 50 μm in the right column. C: Immunohistochemical staining of ALP and TRAP. The upper row shows ALP staining (a, b, and c); lower row shows TRAP staining (d, e, and f). The left column shows CaP-positive group (a, d); centre column shows CaP-negative group (b, e); the lower column shows surgery-only group (c, f). White arrowheads show ALP-stained areas; black arrowheads show TRAP-positive cells. Scale bars: 50 μm . Figure edited by Dr.Tenkumo *et al.*

In the PCR analysis, it was also observed that IL-6 mRNA was also downregulated after the TNF- α gene silencing. TNF- α can induce inflammation by phosphorylation of IKB α , JNK and p38 [325], and this transcription factors are associated with the IL-6 mRNA expression [326]. With the reduction of TNF- α expression the signaling pathway is inhibited, thus the IL-6 secretion is decreased.

Contrary to the observed low silencing efficiency *in vitro* with the J774 macrophages the performance *in vivo* was better. For *in vivo* experiments different cell lines that can release TNF- α are present and most of them are likely to uptake the calcium phosphate nanoparticles and later induce the gene silencing in contrast to *in vitro* where only a single cell strain was present.

With the application of the paste it was also observed that the ALP activity was higher when compared to the surgery-only group with a significant difference at day 21. Between both CaP-Positive and CaP-Negative groups significant differences at day 7 and 10 were observed. In the case of CaP-Positive, a higher ALP mRNA expression and ALP released was detected. TNF- α can inhibit the osteoblast activity which is reflected in this values [327]. These results are in agreement with the study from Pacios *et al.* [328]. In where TNF- α specific inhibition by injection therapy into periodontitis allowed to recover the bone metabolism of a diabetic rat (a higher inflammation) to a level comparable to non-diabetic rats.

When comparing at mRNA level for CaP-negative group at day 3 there is a significant increase of TNF- α mRNA and a decrease of ALP mRNA that will then be reflected at day 7 at the protein level. This time difference is expected for the *in vivo* mRNA expression and protein release biosynthesis [329].

From the biochemical analysis it was evidenced that the bone metabolism was triggered after the active paste treatment. At day 21 the OCN mRNA expression was significantly higher than surgery-only group, although at the protein level no significant levels were detected. Differently to ALP, which is expressed at early and middle stage of osteoblast differentiation, OCN is expressed at later stages.

At day 21, it was detected ALP and TRAP-stained cells in histological observations for CaP-positive and CaP-negative samples. Although, no direct new bone formation can be confirmed at this day, the biochemical pathway has been clearly activated. It will then be expected that the new bone formation will occur in a longer time. From μ CT analysis it was also not possible to confirm new bone at day 21, as no significant differences were observed between the linear distance of cement-enamel junction and bone cleft (Figure 81). Additionally, as the bone defect was horizontal the new bone formation can be restricted compared to a vertical defect.

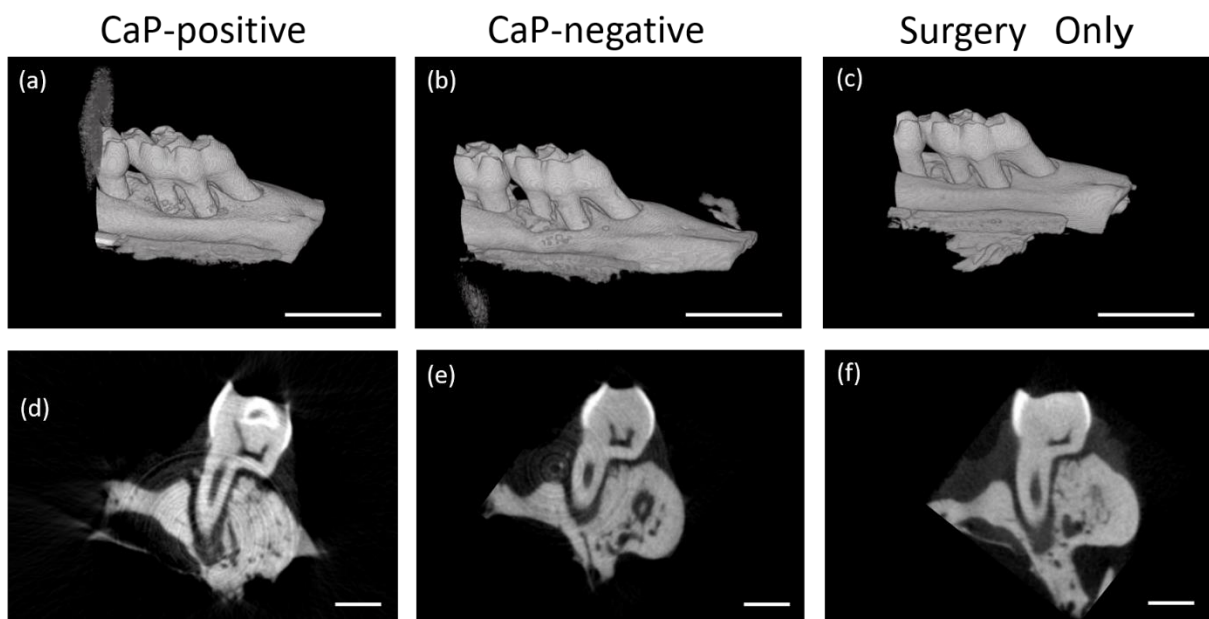


Figure 81: Representative μ CT images of the CaP-positive group (**a, d**), the CaP-negative group (**b, e**), and the surgery-only group (**c, f**) at 21 d after implantation into periodontal tissue. Scale bars: 2 mm in a, b, and c, and 1 mm in d, e, and f. Figure edited by Dr.Tenkumo *et al.*

8.6.4 Triple functional active paste

From the *in vivo* results it has been evidenced that after the application of the active paste in the periodontitis model the TNF- α release has decreased. Although no new bone formation has been observed the activation mechanism for bone formation has been induced at day 20, as observed from the upregulation of ALP mRNA and immunochemistry of histological images.

To enhance this process, a multifunctional paste was prepared to complement the TNF- α siRNA activity and the intrinsic bone formation stimulation of calcium phosphate nanoparticles. By including DNA plasmids for BMP-7 and VEGF expression into the calcium phosphate nanoparticles, those factors once transfected will enhance the bone growth and regeneration.

Previously, Chernousova *et al.* [223] have evaluated the transfection of BMP-7 and VEGF using calcium phosphate nanoparticles *in vitro* with different cell lines with a high transfection efficiency. Additionally, Schlickewei *et al.* studied *in vivo* for a critical-size bone defect the transfection of BMP-7 and VEGF-A in a rabbit model [49]. After four weeks of the implantation a significant difference in bone healing and bone mass between the active and control group was observed.

A set of calcium phosphate nanoparticles loaded independently with TNF- α -siRNA, pBMP-7 and pVEGF-A were prepared. With this modular approach, each nanoparticle contains only one type of nucleic acid, and the formulation in the paste matrix can be customized by changing the ratio between each one in the active paste as required. Like with the previous application, the paste matrix of CaP/CMC will be used as the substrate for the *in vivo* application.

When combined the three types of nanoparticles (TNF- α -siRNA, pBMP-7, and pVEGF-A) into the CaP/CMC substrate a triple functional active paste is developed. It will then reduce inflammation (reduce TNF- α expression) and induce bone formation and vascularization (increase BMP-7 and VEGF-A expression).

The nanoparticles characterization is shown in Table 20 and Figure 82 shows representative SEM micrographs of the synthesized nanoparticles.

The new *in vivo* experiments with these materials will be carried out by Prof. Dr. Keiichi Sasaki and Dr. Taichi Tenkumo research group at Tohoku University in Sendai, Japan.

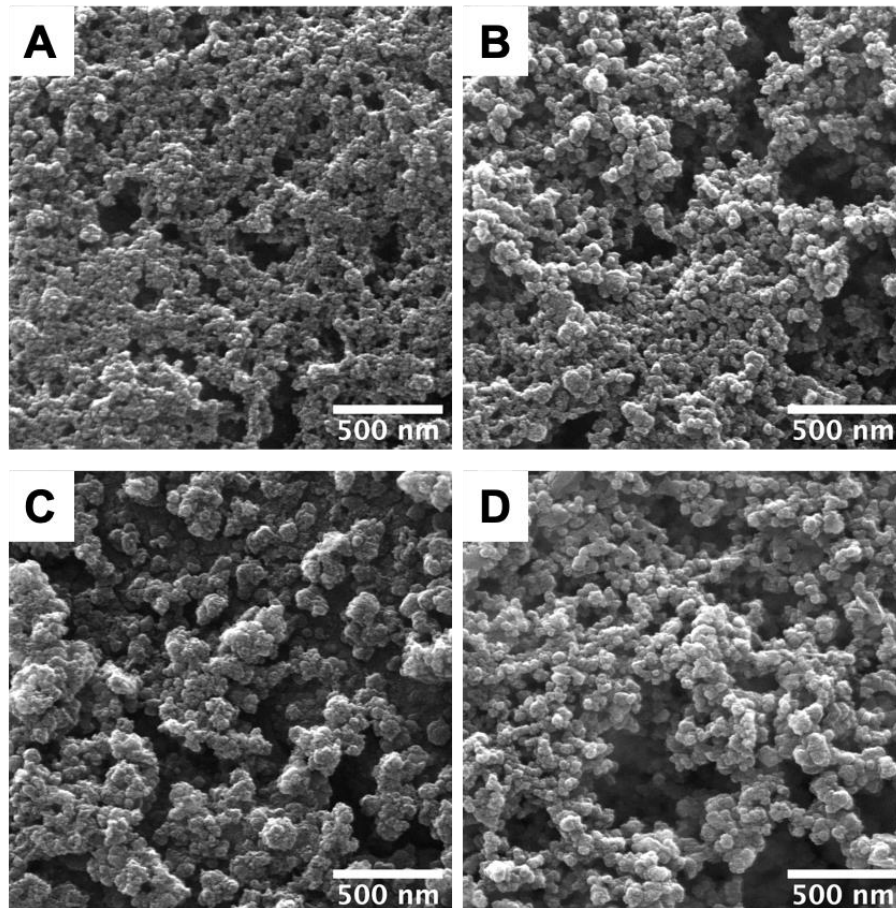


Figure 82: Scanning electron microscopy micrograph of calcium phosphate loaded nanoparticles. A) CaP/PEI/SiO₂, B) CaP/PEI/TNF- α -siRNA/SiO₂, C) CaP/PEI/pBMP-7/SiO₂, D) CaP/PEI/pVEGF-A/SiO₂.

Table 20: Characterization of loaded calcium phosphate nanoparticles for the triple active calcium phosphate paste. Concentrations refer to stock solutions.

Sample (dispersion)	CaP/PEI/ SiO ₂	CaP/PEI/ TNF- α - siRNA /SiO ₂	CaP/PEI/ pBMP-7/SiO ₂	CaP/PEI/ pVEGF-A /SiO ₂
Solid particle diameter by SEM / nm	59	56	57	58
<i>V</i> (one nanoparticle; only CaP) / m ³	1.07·10 ⁻²²	9.19·10 ⁻²³	9.69·10 ⁻²³	1.02·10 ⁻²²
<i>m</i> (one nanoparticle; only CaP) / kg	3.37·10 ⁻¹⁹	2.89·10 ⁻¹⁹	3.04·10 ⁻¹⁹	3.21·10 ⁻¹⁹
<i>W</i> (Ca ²⁺) by AAS / kg m ⁻³	0.072	0.066	0.073	0.068
<i>W</i> (Ca ₅ (PO ₄) ₃ OH) / kg m ⁻³	0.182	0.166	0.182	0.170
<i>N</i> (nanoparticles) / m ⁻³	5.38·10 ¹⁷	5.75·10 ¹⁷	6.00·10 ¹⁷	5.31·10 ¹⁷
<i>W</i> (loading) / kg m ⁻³	-	0.079	0.068	0.058
<i>N</i> (loading) / molecules m ⁻³	-	3.53·10 ²¹	1.10·10 ¹⁹	1.01·10 ¹⁹
<i>m</i> (loading) per nanoparticle / kg	-	1.37·10 ⁻¹⁹	1.13·10 ⁻¹⁹	1.09·10 ⁻¹⁹
<i>N</i> (loading) molecules per nanoparticle	-	6.1·10 ³	18	19
weight ratio loading to calcium phosphate	-	1 : 0.48	1 : 0.37	1 : 0.34
Hydrodynamic diameter by DLS / nm	246	220	187	312
PDI by DLS	0.28	0.37	0.25	0.35
Zeta potential by DLS / mV	+25	+23	+23	+29
Endotoxins / EU mL ⁻¹	< 0.1	< 0.1	< 0.1	< 0.1

8.6.5 Section summary

Nanoparticles loaded with siRNA-TNF- α were synthesized and evaluated *in vitro* and *in vivo*. The *in vitro* assays with J774 cell line showed a good cellular uptake and after stimulation with LPS a 12% reduction in the TNF- α cytokine expression was obtained. *In vivo* experiments with a rat periodontitis model and with a direct topical application of the nanoparticles embedded in a calcium phosphate paste matrix showed a significant TNF- α reduction after 3 days. Moreover, after 20 days the new bone formation mechanism was activated. To further extend the studies a triple active paste for *in vivo* was prepared using in addition to siRNA-TNF- α the DNA-plasmids for BMP-7 and VEGF-A proteins that enhance for bone formation and vascularization. The *in vivo* experiments for the triple active paste are currently in progress.

9 Summary and conclusions

With this thesis a new approach for the surface modification of calcium phosphate nanoparticles was developed and applications in biomedicine were evaluated. As initially mentioned, calcium phosphate nanoparticles are frequently used in biological applications as carriers for biomolecules or drugs. Although various synthetic, loading and modification methods are available in the literature, new and different applications require to redesign or introduce novel synthetic approaches.

Surface modification methods are a versatile way to modify the nanoparticles physical and chemical properties by binding molecules onto it. To guarantee a durable interaction, a covalent bond for surface modification is of high importance. In this direction, the concept of click chemistry, specifically the azide-alkyne reaction, was implemented as a surface modification method for calcium phosphate nanoparticles.

Stable azide-terminate calcium phosphate nanoparticles within a range of 50-100 nm core diameter (by SEM) were prepared with a high number of azide groups ($1.7 \cdot 10^5$ N₃ per nanoparticle) and low cytotoxicity. CuAAC click reaction was used for the surface modification. The nanoparticles were labeled with different dyes, such as FAM and AF488, where highly fluorescent nanoparticles (10^4 - 10^3 dye molecules per nanoparticle) were obtained with a hydrodynamic diameter (DLS) near 200 nm. Moreover, with this method two different molecules can react to the surface by a two-step reaction, as shown with FAM-TAMRA and FAM-Cy5 labeled nanoparticles.

As an alternative to CuAAC click reaction, the strain-promoted azide-alkyne cycloaddition reaction was also implemented. With the SPAAC approach the potential oxidative or toxicity copper related issues are avoided. Between both reactions, CuAAC allows a faster reaction on the nanoparticle but its applicability is limited to a 1 h reaction, although with SPAAC longer reaction times can take place. With an initial concentration of 13.8 μ M of dye molecule, by CuAAC after 1 h near $8.2 \cdot 10^3$ molecules were coupled to the surface, whereas by SPAAC it required 6 h to reach a similar amount. This difference in the reaction kinetics allows to control the surface labelling

density for both reactions. The reactions were performed at 8, 21, and 37 °C and comparable results were observed for CuAAC. However, for SPAAC higher temperatures were more favorable.

Not only traditional dyes were studied but also an aggregation-induced emission molecule was coupled to the nanoparticle surface. After the reaction, the AIE molecule properties were preserved and its behavior depended on the dispersion solvent. When dispersed in a solvent with > 37% water content the molecule emission is *on* and in DMSO rich conditions the emission is *off*. This type of functional molecules on the nanoparticles shows the potential application of nanoparticles for sensing conditions.

From the chemical point of view, the stable covalent triazole ring formation after the surface reaction allows a lasting surface modification, as demonstrated with the cellular uptake imaging and further biological experiments. For the first time, this system was imaged using fluorescent super-resolution microscopy methods (*e.g.* SIM, STORM), from which it was possible to determine that the nanoparticles are likely to remain as individual particles or low aggregated after cellular endocytosis.

Additionally, the influence the surface reaction had on the cell viability and potential molecular damage of sensitive loadings (*e.g.* DNA plasmid) was studied. It was demonstrated that after the CuAAC the loaded plasmid was no longer suitable for transfection, whereas with SPAAC reaction no functional damage was detected. Thus, SPAAC method is preferred for sensitive loadings as ROS oxidative damage is evaded.

The azide-terminated calcium phosphate nanoparticles are suitable for other alkyne-carrying molecules. An alkyne-derivate HIV-1 envelope glycoprotein was coupled at a specific position to the calcium phosphate nanoparticle, and compared to a non-specific coupling using sulfo-SMCC crosslinker. With the specific coupling near 570 proteins units were added, and for the non-specific 480 proteins. The coupling effect on the protein recognition was further evaluated at the immunological level. For this type of applications, the developed surface modification methodology based on alkyne-azide reaction is of high interest.

A second studied application of biomedical interest was in the field of vaccination for Hepatitis B. A loading optimization step was performed using pEGFP to increase the plasmid loading per nanoparticle as for *in vivo* transfection higher doses are required. A maximum loading for 1 mL NPs dispersion ($1.59 \cdot 10^{11}$ nanoparticles) was achieved with an initial plasmid input of 150 μg . With these conditions near 130 plasmid units were added to the core and represents a 90% loading efficiency. Nanoparticles loaded with pHBsAg successfully transfected HeLa, C2C12 and BHK-21 cell lines. *In vivo* transfection of C57BL/6 mice evidenced an increase in HBsAg expression after the fifth day of immunization.

In a different direction of the biomedicine field, a direct topical application of an active calcium phosphate nanoparticles paste based material was performed to reduce the TNF- α cytokine expression. For this, calcium phosphate nanoparticles loaded with siRNA-TNF- α were synthesized (40-90 nm core diameter by SEM, +23 mV ζ -potential). *In vitro* studies with J774 cell line were performed and a successful cellular uptake with a 12% TNF- α expression reduction was obtained.

The NPs were further studied in a rat periodontitis model, and the successful inflammation reduction was observed after 3 days. Additionally, an upregulation of ALP at the mRNA level and an increase in osteoclasts cells that evidenced the mechanism activation for bone formation after 20 days was detected. To take further advantage of this system, a triple active nanoparticle paste was developed with the additions of plasmids for bone formation induction (pBMP-7) and vascularization (pVEGF-A), as well as siRNA TNF- α for the inflammation reduction. This example proves the versatility of using active CaP NPs to attack specific problems in medicine.

As demonstrated in this thesis, the scope of calcium phosphate nanoparticles is very broad, and combined with an appropriate chemical surface modification method, like CuAAC and SPAAC, the application of CaP NPs can be extended. Thus, with an internal protected loading and an external chemically modified surface, the calcium phosphate nanoparticle system continues to be a highly versatile particle within the 50-100 nm range for biomedicine applications.

10 Zusammenfassung

In der vorliegenden Arbeit wurde ein neuer Ansatz zur Oberflächenmodifikation von Calciumphosphatnanopartikeln für die biomedizinische Anwendung entwickelt. Hierbei bieten sich diese anorganische Partikel an, da Calciumphosphatnanopartikel bereits als Trägermaterialien für Biomoleküle vielseitig erforscht wurden. Jedoch sind neue synthetische Ansätze notwendig, fernab von den bereits etablierten Modifikationsmethoden, umso maßgeschneidert neuen Herausforderungen der Biomedizin gerecht zu werden.

Die physikalischen und chemischen Eigenschaften von Nanopartikeln lassen sich durch die Kopplung von Molekülen an der Oberfläche manipulieren; eine dauerhafte Bindung dieser Moleküle lässt sich durch die kovalente Funktionalisierung an der Oberfläche gewährleisten. In der Arbeit wurde als Oberflächenmodifikation die Klickchemie, insbesondere die (Kupfer-katalysierte) Azid-Alkin-Cycloaddition, an der Calciumphosphatnanopartikeloberfläche etabliert.

Stabile Azid-funktionalisierte Calciumphosphatnanopartikel mit einem Kerndurchmesser zwischen 50-100 nm wurden mit einer großen Anzahl an Azidgruppen an der Oberfläche, welche die Zellviabilität nicht negativ beeinflussen, synthetisiert. Die Azidgruppen an der Oberfläche wurden mittels der CuAAC Klickreaktion mit diversen Alkin-modifizierten Fluorophoren z.B. FAM oder AF488 kovalent funktionalisiert. Diese Systeme wiesen hohe Fluoreszenzintensitäten (10^3 - 10^4 Fluorophore pro Nanopartikel) auf und besaßen einen hydrodynamischen Durchmesser von 200 nm. Eine zweistufige Reaktion ermöglichte die Oberflächenbeladung von zwei verschiedenen Molekülen, wie es bei den Systemen FAM-TAMRA und FAM-Cy5 gezeigt wurde.

Eine Alternative zur CuAAC Klickreaktion stellt die *Strain Promoted Alkyne-Azide Cycloaddition* (SPAAC) dar, welche auch an den Azid-funktionalisierten Nanopartikeln durchgeführt wurde. Einen besonderen Vorteil bietet die SPAAC, da hierbei auf kupferhaltige Katalysatoren verzichtet wird, welche oxidative oder toxische Probleme mit sich bringen können. Die CuAAC verläuft hingegen schneller, obwohl sich für die

Calciumphosphatnanopartikel eine Begrenzung von 1 h Reaktionszeit als optimal herausstellte und bei der SPAAC längere Reaktionszeiten notwendig sind. Zum Beispiel wurden nach 1 h mittels CuAAC circa $8,2 \cdot 10^3$ Moleküle an die Oberfläche geklickt, während die SPAAC 6 h benötigte um eine vergleichbare Anzahl zu erreichen. Dieser Unterschied begründet sich auf der Reaktionskinetik und erlaubt somit die Oberflächenladung zu kontrollieren. Die Reaktionen wurden bei 8, 21 und 37 °C verglichen. Für CuAAC wurden vergleichbare Ergebnisse erreicht, die SPAAC hingegen war bei höheren Temperaturen schneller.

Nicht nur traditionelle Fluorophore wurden an die Oberfläche der Nanopartikel funktionalisiert, sondern auch Moleküle die eine aggregationsinduzierte Emission (*aggregation-induced emission, AIE*) zeigten. Nach der Klickreaktion wurde eine AIE nachgewiesen, wobei dieses Verhalten vom Dispersionsmedium abhängig ist. In einem Lösungsmittel mit einem > 37% Wassergehalt ist die AIE zu beobachten und mit höheren DMSO Konzentrationen ist dieses Verhalten ausgeschaltet. Solch eine Art von funktionellen Molekülen auf den Nanopartikeln sind richtungsweisend für die Anwendung dieser in der Nanosensorik.

Der Triazolring stellt nach der Oberflächenreaktion eine dauerhafte Bindung auf den Nanopartikeln dar, die Stabilität dieser Systeme wurde auch mit zellulären Aufnahmen und weiteren biologischen Experimenten bestätigt. Erstmals wurde das System mit *fluorescence super-resolution microscopy* (e.g. SIM, STORM) abgebildet. Aus der Bildgebung zeigt sich, dass die Nanopartikeln nach der zellulären Aufnahme und Endozytose zu großen Anteilen als einzelne Partikel oder nur vereinzelt aggregiert vorliegen.

Zusätzlich wurde untersucht, ob die Systeme die Zellviabilität negativ beeinflussen oder molekulare Schäden an empfindlichen Biomolekülen (z.B. DNS-Plasmide) verursachen. Es zeigte sich, dass nach der CuAAC Reaktion die beladene Plasmid-DNS nicht mehr für die Transfektion geeignet ist, aber nach der SPAAC Reaktion wurden keine funktionellen Schäden festgestellt. Daher eignet sich die SPAAC Methode für empfindliche Biomoleküle, da oxidative Schäden durch ROS vermieden werden.

Die Azid-funktionalisierten Calciumphosphatnanopartikel ließen sich auch mit anderen Alkin-modifizierten Molekülen beladen. Ein Alkinderivat von HIV-1 *envelope glycoprotein* wurde an einer bestimmten Position an die Calciumphosphatnanopartikel gekoppelt und mit dem unspezifischen Crosslinker Sulfo-SMCC verglichen. Mit der spezifischen Kopplung wurden circa 570 Proteine an die Partikel gebunden, bei der unspezifischen Kopplung waren es circa 480 Proteine. Der Kopplungseffekt auf die Proteinerkennung wurde durch immunologische Reaktionen untersucht. Für diese Art von Anwendungen ist die entwickelte Oberflächenmodifikation auf Basis der Alkin-Azid-Reaktion von großem Interesse.

Eine weitere Anwendung der Nanopartikel in der Biomedizin wurde im Bereich der Impfung gegen Hepatitis B untersucht. Zunächst wurde die Beladung mit pEGFP optimiert, so dass die Plasmidanzahl pro Nanopartikel hoch genug war, da für die *in vivo* Transfektion höhere Dosen erforderlich sind. Eine maximale Beladung einer 1 mL Nanopartikeldispersion ($1,59 \cdot 10^{11}$ Nanopartikel) wurde mit einer anfänglichen Plasmidbeladung von 150 µg erreicht. Unter diesen Bedingungen wurden circa 130 Plasmide auf die Partikel beladen, das einer Beladungseffizienz von 90% entspricht. Die Nanopartikel, beladen mit pHBsAg, transfizierten erfolgreich HeLa, C2C12 und BHK-21 Zelllinien. *In vivo* Transfektion von C57BL/6 Mäusen zeigte einen Anstieg der HBsAg-Expression nach 5 Tagen der Immunisierung.

Eine direkte Anwendung der Partikel im Bereich der Biomedizin wurde auf Basis von Calciumphosphatnanopartikeln in einer aktiven Paste entwickelt, um die TNF- α Zytokin-Expression zu reduzieren. Hierzu wurden Nanopartikel mit siRNA-TNF- α synthetisiert (40-90 nm Kerndurchmesser bei REM, +23 mV ζ -Potential). *In vitro* Untersuchung mit J774 Zell Linie zeigten eine erfolgreiche zelluläre Aufnahme dieser und es wurde eine 12% TNF- α Expressionsreduktion erzielt.

Die aktive Paste wurde in einem Ratten-Parodontitis-Modell weiter untersucht und die erfolgreiche Entzündungsreduktion wurde nach 3 Tagen beobachtet. Zusätzlich wurde eine Hochregulation von ALP auf mRNA Ebene und ein Anstieg der Osteoklastenzellen festgestellt, dass somit die Aktivierung des Mechanismus zur Knochenbildung nach 20 Tagen belegt. Um dieses System weiter zu untersuchen,

wurde eine dreifach aktive Nanopartikelpaste mit Plasmiden für die Knochenbildungsinduktion (pBMP-7), Vaskularisation (pVEGF-A) und Entzündungsreduktion (siRNA-TNF- α) entwickelt. Dieses Beispiel zeigt die Vielfältigkeit der Calciumphosphatnanopartikel und den Einsatz dieser zur Lösung spezifischer Probleme in der Medizin.

Die vorliegende Arbeit zeigt die Vielfältigkeit der Calciumphosphatnanopartikel, welche durch geeignete Oberflächenmodifikationen, wie CuAAC und SPAAC, ein erhebliches Maß an Flexibilität gewinnen. Zusammenfassend lässt sich schlussfolgern, dass Calciumphosphatnanopartikel im Bereich von 50-100 nm, mit einer intern geschützten Ladung und einer extern chemisch modifizierten Oberfläche, erhebliche Vorteile im Bereich der Biomedizin mit sich bringen.

11 References

- [1] W. Habraken, P. Habibovic, M. Epple, M. Bohner, Calcium phosphates in biomedical applications: materials for the future?, *Materials Today* **2016**, *19*, 69-87.
- [2] K. Lin, C. Wu, J. Chang, Advances in synthesis of calcium phosphate crystals with controlled size and shape, *Acta Biomater.* **2014**, *10*, 4071-102.
- [3] S.V. Dorozhkin, Nanosized and nanocrystalline calcium orthophosphates, *Acta Biomater.* **2010**, *6*, 715-34.
- [4] M. Sadat-Shojai, M.T. Khorasani, E. Dinpanah-Khoshdargi, A. Jamshidi, Synthesis methods for nanosized hydroxyapatite with diverse structures, *Acta Biomater.* **2013**, *9*, 7591-621.
- [5] P. Gehr, R. Zellner, Biological Responses to Nanoscale Particles, Springer Nature Switzerland AG, Cham, Switzerland, **2019**.
- [6] R.A. Sperling, W.J. Parak, Surface modification, functionalization and bioconjugation of colloidal inorganic nanoparticles, *Philos. Trans. A Math. Phys. Eng. Sci.* **2010**, *368*, 1333-83.
- [7] S. Kango, S. Kalia, A. Celli, J. Njuguna, Y. Habibi, R. Kumar, Surface modification of inorganic nanoparticles for development of organic–inorganic nanocomposites—A review, *Prog. Polym. Sci.* **2013**, *38*, 1232-1261.
- [8] J.J. Giner-Casares, M. Henriksen-Lacey, M. Coronado-Puchau, L.M. Liz-Marzán, Inorganic nanoparticles for biomedicine: where materials scientists meet medical research, *Materials Today* **2016**, *19*, 19-28.
- [9] D.A. Richards, A. Maruani, V. Chudasama, Antibody fragments as nanoparticle targeting ligands: a step in the right direction, *Chem. Sci.* **2017**, *8*, 63-77.
- [10] W.R. Algar, T. Jeen, M. Massey, W.J. Peveler, J. Asselin, Small Surface, Big Effects, and Big Challenges: Toward Understanding Enzymatic Activity at the Inorganic Nanoparticle-Substrate Interface, *Langmuir* **2019**, *35*, 7067-7091.
- [11] K. Tripathi, J.D. Driskell, Quantifying Bound and Active Antibodies Conjugated to Gold Nanoparticles: A Comprehensive and Robust Approach To Evaluate Immobilization Chemistry, *ACS Omega* **2018**, *3*, 8253-8259.
- [12] N. Mustafaoglu, T. Kiziltepe, B. Bilgicer, Site-specific conjugation of an antibody on a gold nanoparticle surface for one-step diagnosis of prostate specific antigen with dynamic light scattering, *Nanoscale* **2017**, *9*, 8684-8694.

- [13] W. Hong, S. Lee, H.J. Chang, E.S. Lee, Y. Cho, Multifunctional magnetic nanowires: A novel breakthrough for ultrasensitive detection and isolation of rare cancer cells from non-metastatic early breast cancer patients using small volumes of blood, *Biomaterials* **2016**, *106*, 78-86.
- [14] H. Xu, Z.P. Aguilar, L. Yang, M. Kuang, H. Duan, Y. Xiong, H. Wei, A. Wang, Antibody conjugated magnetic iron oxide nanoparticles for cancer cell separation in fresh whole blood, *Biomaterials* **2011**, *32*, 9758-65.
- [15] A. Mukherjee, T. Darlington, R. Baldwin, C. Holz, S. Olson, P. Kulkarni, T.L. DeWeese, R.H. Getzenberg, R. Ivkov, S.E. Lupold, Development and screening of a series of antibody-conjugated and silica-coated iron oxide nanoparticles for targeting the prostate-specific membrane antigen, *ChemMedChem* **2014**, *9*, 1356-60.
- [16] M. Bouchoucha, É. Béliveau, F. Kleitz, F. Calon, M.-A. Fortin, Antibody-conjugated mesoporous silica nanoparticles for brain microvessel endothelial cell targeting, *J. Mater. Chem. B* **2017**, *5*, 7721-7735.
- [17] T. Mandal, M. Beck, N. Kirsten, M. Linden, C. Buske, Targeting murine leukemic stem cells by antibody functionalized mesoporous silica nanoparticles, *Sci. Rep.* **2018**, *8*, 989.
- [18] S.P. S.Verrier, R.Bareille, A.Jonczyk, J.Meyer, M.Dard, J.Amédée, Function of linear and cyclic RGD-containing peptides in osteoprogenitor cells adhesion process, *Biomaterials* **2002**, *23*, 585-596.
- [19] S.B. van der Meer, T. Knuschke, A. Frede, N. Schulze, A.M. Westendorf, M. Epple, Avidin-conjugated calcium phosphate nanoparticles as a modular targeting system for the attachment of biotinylated molecules in vitro and in vivo, *Acta Biomater.* **2017**, *57*, 414-425.
- [20] B. Pelaz, P. del Pino, P. Maffre, R. Hartmann, M. Gallego, S. Rivera-Fernandez, J.M. de la Fuente, G.U. Nienhaus, W.J. Parak, Surface Functionalization of Nanoparticles with Polyethylene Glycol: Effects on Protein Adsorption and Cellular Uptake, *ACS Nano* **2015**, *9*, 6996-7008.
- [21] K. Pombo Garcia, K. Zarschler, L. Barbaro, J.A. Barreto, W. O'Malley, L. Spiccia, H. Stephan, B. Graham, Zwitterionic-coated "stealth" nanoparticles for biomedical applications: recent advances in countering biomolecular corona formation and uptake by the mononuclear phagocyte system, *Small* **2014**, *10*, 2516-29.
- [22] Y. Qie, H. Yuan, C.A. von Roemeling, Y. Chen, X. Liu, K.D. Shih, J.A. Knight, H.W. Tun, R.E. Wharen, W. Jiang, B.Y. Kim, Surface modification of nanoparticles

enables selective evasion of phagocytic clearance by distinct macrophage phenotypes, *Sci. Rep.* **2016**, *6*, 26269.

[23] S. Richard, M. Boucher, A. Saric, A. Herbet, Y. Lalatonne, P.X. Petit, S. Mériaux, D. Boquet, L. Motte, Optimization of pegylated iron oxide nanoplatfoms for antibody coupling and bio-targeting, *J. Mater. Chem. B* **2017**, *5*, 2896-2907.

[24] J. Conde, J.T. Dias, V. Grazu, M. Moros, P.V. Baptista, J.M. de la Fuente, Revisiting 30 years of biofunctionalization and surface chemistry of inorganic nanoparticles for nanomedicine, *Front Chem.* **2014**, *2*, 48.

[25] M. Neumeier, L.A. Hails, S.A. Davis, S. Mann, M. Epple, Synthesis of fluorescent core-shell hydroxyapatite nanoparticles, *J. Mater. Chem.* **2011**, *21*, 1250-1254.

[26] D. Kozlova, S. Chernousova, T. Knuschke, J. Buer, A.M. Westendorf, M. Epple, Cell targeting by antibody-functionalized calcium phosphatenanoparticles, *J. Mater. Chem.* **2012**, *22*, 396-404.

[27] A. Purkayastha, J.B. Baruah, Review: Synthetic methodologies in siloxanes, *Appl. Organometal. Chem.* **2004**, *18*, 166-175.

[28] V. Sokolova, Z. Shi, S. Huang, Y. Du, M. Kopp, A. Frede, T. Knuschke, J. Buer, D. Yang, J. Wu, A.M. Westendorf, M. Epple, Delivery of the TLR ligand poly(I:C) to liver cells in vitro and in vivo by calcium phosphate nanoparticles leads to a pronounced immunostimulation, *Acta Biomater.* **2017**, *64*, 401-410.

[29] C. Zilker, D. Kozlova, V. Sokolova, H. Yan, M. Epple, K. Uberla, V. Temchura, Nanoparticle-based B-cell targeting vaccines: Tailoring of humoral immune responses by functionalization with different TLR-ligands, *Nanomedicine* **2017**, *13*, 173-182.

[30] V.V. Temchura, D. Kozlova, V. Sokolova, K. Uberla, M. Epple, Targeting and activation of antigen-specific B-cells by calcium phosphate nanoparticles loaded with protein antigen, *Biomaterials* **2014**, *35*, 6098-105.

[31] M. Kopp, U.W. Aufderhorst, M. Alt, U. Dittmer, A.M. Eis-Hubinger, B. Giebel, M. Roggendorf, M. Epple, A. Krawczyk, Induction of herpes simplex virus type 1 cell-to-cell spread inhibiting antibodies by a calcium phosphate nanoparticle-based vaccine, *Nanomedicine* **2019**, *16*, 138-148.

[32] C. Kim, J.F. Galloway, K.H. Lee, P.C. Searson, Universal antibody conjugation to nanoparticles using the Fcγ receptor I (FcγRI): quantitative profiling of membrane biomarkers, *Bioconjug. Chem.* **2014**, *25*, 1893-901.

[33] H.C. Kolb, M.G. Finn, K.B. Sharpless, Click Chemistry: Diverse Chemical Function from a Few Good Reactions, *Angew. Chem. Int. Ed.* **2001**, *40*, 2004-2021.

- [34] D.M. Patterson, L.A. Nazarova, J.A. Prescher, Finding the right (bioorthogonal) chemistry, *ACS Chem. Biol.* **2014**, *9*, 592-605.
- [35] C.S. McKay, M.G. Finn, Click chemistry in complex mixtures: bioorthogonal bioconjugation, *Chem Biol.* **2014**, *21*, 1075-101.
- [36] N.K. Devaraj, The Future of Bioorthogonal Chemistry, *ACS Cent. Sci.* **2018**, *4*, 952-959.
- [37] B.T. Worrell, J.A. Malik, V.V. Fokin, Direct evidence of a dinuclear copper intermediate in Cu(I)-catalyzed azide-alkyne cycloadditions, *Science* **2013**, *340*, 457-60.
- [38] K. Mg, K. V, H. F, History and Possible Uses of Nanomedicine Based on Nanoparticles and Nanotechnological Progress, *J. Nanomed. Nanotechnol.* **2015**, *06*, 1-7.
- [39] W. Ma, A. Saccardo, D. Roccatano, D. Aboagye-Mensah, M. Alkaseem, M. Jewkes, F. Di Nezza, M. Baron, M. Soloviev, E. Ferrari, Modular assembly of proteins on nanoparticles, *Nat. Commun.* **2018**, *9*, 1489.
- [40] T. Knuschke, O. Rotan, W. Bayer, S. Kollenda, J. Dickow, K. Sutter, W. Hansen, U. Dittmer, K.S. Lang, M. Epple, J. Buer, A.M. Westendorf, Induction of Type I Interferons by Therapeutic Nanoparticle-Based Vaccination Is Indispensable to Reinforce Cytotoxic CD8(+) T Cell Responses During Chronic Retroviral Infection, *Front Immunol.* **2018**, *9*, 614.
- [41] T. Knuschke, O. Rotan, W. Bayer, V. Sokolova, W. Hansen, T. Sparwasser, U. Dittmer, M. Epple, J. Buer, A.M. Westendorf, Combination of nanoparticle-based therapeutic vaccination and transient ablation of regulatory T cells enhances anti-viral immunity during chronic retroviral infection, *Retrovirology* **2016**, *13*, 24.
- [42] M. Kopp, O. Rotan, C. Papadopoulos, N. Schulze, H. Meyer, M. Epple, Delivery of the autofluorescent protein R-phycoerythrin by calcium phosphate nanoparticles into four different eukaryotic cell lines (HeLa, HEK293T, MG-63, MC3T3): Highly efficient, but leading to endolysosomal proteolysis in HeLa and MC3T3 cells, *PLoS One* **2017**, *12*, e0178260.
- [43] V. Sokolova, O. Rotan, J. Klesing, P. Nalbant, J. Buer, T. Knuschke, A.M. Westendorf, M. Epple, Calcium phosphate nanoparticles as versatile carrier for small and large molecules across cell membranes, *J. Nanopart. Res.* **2012**, *14*, 1-10.

- [44] B. Neuhaus, B. Tosun, O. Rotan, A. Frede, A.M. Westendorf, M. Epple, Nanoparticles as transfection agents: a comprehensive study with ten different cell lines, *RSC Adv.* **2016**, *6*, 18102-18112.
- [45] A. Frede, B. Neuhaus, T. Knuschke, M. Wadwa, S. Kollenda, R. Klopffleisch, W. Hansen, J. Buer, D. Bruder, M. Epple, A.M. Westendorf, Local delivery of siRNA-loaded calcium phosphate nanoparticles abates pulmonary inflammation, *Nanomedicine* **2017**, *13*, 2395-2403.
- [46] S. Chernousova, M. Epple, Live-cell imaging to compare the transfection and gene silencing efficiency of calcium phosphate nanoparticles and a liposomal transfection agent, *Gene Ther.* **2017**, *24*, 282-289.
- [47] V. Sokolova, L. Rojas-Sanchez, N. Bialas, N. Schulze, M. Epple, Calcium phosphate nanoparticle-mediated transfection in 2D and 3D mono- and co-culture cell models, *Acta Biomater.* **2019**, *84*, 391-401.
- [48] D.C. Tang, M. DeVit, S.A. Johnston, Genetic immunization is a simple method for eliciting an immune response, *Nature* **1992**, *356*, 152-4.
- [49] C. Schlickewei, T.O. Klatte, Y. Wildermuth, G. Laaff, J.M. Rueger, J. Ruesing, S. Chernousova, W. Lehmann, M. Epple, A bioactive nano-calcium phosphate paste for in-situ transfection of BMP-7 and VEGF-A in a rabbit critical-size bone defect: results of an in vivo study, *J. Mater. Sci. Mater. Med.* **2019**, *30*, 15.
- [50] A. Schlossbauer, D. Schaffert, J. Kecht, E. Wagner, T. Bein, Click chemistry for high-density biofunctionalization of mesoporous silica, *J. Am. Chem. Soc.* **2008**, *130*, 12558-12559.
- [51] S.V. Dorozhkin, Calcium orthophosphates: occurrence, properties, biomineralization, pathological calcification and biomimetic applications, *Biomatter* **2011**, *1*, 121-64.
- [52] S.V. Dorozhkin, M. Epple, Biological and medical significance of calcium phosphates, *Angew. Chem. Int. Ed.* **2002**, *41*, 3130-46.
- [53] M. Epple, Review of potential health risks associated with nanoscopic calcium phosphate, *Acta Biomater.* **2018**, *77*, 1-14.
- [54] C. Liu, H. He, Developments and Applications of Calcium Phosphate Bone Cements, Springer Nature, Singapore, Singapore, **2018**.
- [55] N. Eliaz, N. Metoki, Calcium Phosphate Bioceramics: A Review of Their History, Structure, Properties, Coating Technologies and Biomedical Applications, *Materials* **2017**, *10*, 1-104.

- [56] S.V. Dorozhkin, Calcium Orthophosphate-Based Bioceramics and Biocomposites, Wiley-VCH Verlag GmbH & Co. KGaA, Weinheim, Germany, **2016**.
- [57] J. Lu, H. Yu, C. Chen, Biological properties of calcium phosphate biomaterials for bone repair: a review, *RSC Adv.* **2018**, *8*, 2015-2033.
- [58] S.V. Dorozhkin, Bioceramics of calcium orthophosphates, *Biomaterials* **2010**, *31*, 1465-85.
- [59] M. Epple, K. Ganesan, R. Heumann, J. Klesing, A. Kovtun, S. Neumann, V. Sokolova, Application of calcium phosphate nanoparticles in biomedicine, *J. Mater. Chem.* **2010**, *20*, 18-23.
- [60] M. Okada, T. Matsumoto, Synthesis and modification of apatite nanoparticles for use in dental and medical applications, *Japanese Dental Science Review* **2015**, *51*, 85-95.
- [61] M. Miernicki, T. Hofmann, I. Eisenberger, F. von der Kammer, A. Praetorius, Legal and practical challenges in classifying nanomaterials according to regulatory definitions, *Nat. Nanotechnol.* **2019**, *14*, 208-216.
- [62] D.R. Boverhof, C.M. Bramante, J.H. Butala, S.F. Clancy, M. Lafranconi, J. West, S.C. Gordon, Comparative assessment of nanomaterial definitions and safety evaluation considerations, *Regul. Toxicol. Pharmacol.* **2015**, *73*, 137-50.
- [63] M. Boholm, R. Arvidsson, A Definition Framework for the Terms Nanomaterial and Nanoparticle, *NanoEthics* **2016**, *10*, 25-40.
- [64] S.E. Lohse, C.J. Murphy, Applications of colloidal inorganic nanoparticles: from medicine to energy, *J. Am. Chem. Soc.* **2012**, *134*, 15607-20.
- [65] H. Goesmann, C. Feldmann, Nanoparticulate functional materials, *Angew. Chem. Int. Ed.* **2010**, *49*, 1362-95.
- [66] S. Mo, X. Shao, Y. Chen, Z. Cheng, Increasing entropy for colloidal stabilization, *Sci. Rep.* **2016**, *6*, 36836.
- [67] B. Derjaguin, L. Landau, Theory of the stability of strongly charged lyophobic sols and of the adhesion of strongly charged particles in solutions of electrolytes, *Prog. Surf. Sci.* **1993**, *43*, 30-59.
- [68] E.J.W. Verwey, J.T.G. Overbeek, Theory of the Stability of Lyophobic Colloids, Elsevier Publishing Company, INC., Amsterdam, The Netherlands, **1948**.
- [69] Colloid Stability: The Role of Surface Forces, Part I. , Wiley-VCH Verlag GmbH & Co. KGaA, Weinheim, Germany, **2007**.

- [70] A. Sikora, D. Bartczak, D. Geißler, V. Kestens, G. Roebben, Y. Ramaye, Z. Varga, M. Palmi, A.G. Shard, H. Goenaga-Infante, C. Minelli, A systematic comparison of different techniques to determine the zeta potential of silica nanoparticles in biological medium, *Anal. Methods* **2015**, *7*, 9835-9843.
- [71] S. Bhattacharjee, DLS and zeta potential - What they are and what they are not?, *J. Control Release* **2016**, *235*, 337-351.
- [72] J. Lyklema, Fundamentals of Interface and Colloid Science, Volume IV Academic Press, London, UK, **2005**.
- [73] M. Kopp, S. Kollenda, M. Epple, Nanoparticle-Protein Interactions: Therapeutic Approaches and Supramolecular Chemistry, *Acc. Chem. Res.* **2017**, *50*, 1383-1390.
- [74] D. Ghosh, N. Chattopadhyay, Gold and silver nanoparticles based superquenching of fluorescence: A review, *J. Lumin.* **2015**, *160*, 223-232.
- [75] F. Pederzoli, G. Tosi, M.A. Vandelli, D. Belletti, F. Forni, B. Ruozi, Protein corona and nanoparticles: how can we investigate on?, *WIREs Nanomed. Nanobiotechnol.* **2017**, *9*, e1467.
- [76] J. Nakazawa, T.D. Stack, Controlled loadings in a mesoporous material: click-on silica, *J. Am. Chem. Soc.* **2008**, *130*, 14360-1.
- [77] P.d. Pino, B. Pelaz, Q. Zhang, P. Maffre, G.U. Nienhaus, W.J. Parak, Protein corona formation around nanoparticles – from the past to the future, *Mater Horiz* **2014**, *1*, 301-313.
- [78] D. Docter, D. Westmeier, M. Markiewicz, S. Stolte, S.K. Knauer, R.H. Stauber, The nanoparticle biomolecule corona: lessons learned - challenge accepted?, *Chem. Soc. Rev.* **2015**, *44*, 6094-121.
- [79] L. Vroman, A.L. Adams, Findings with the recording ellipsometer suggesting rapid exchange of specific plasma proteins at liquid/solid interfaces, *Surf. Sci.* **1969**, *16*, 438-446.
- [80] C.W. Tornøe, C. Christensen, M. Meldal, Peptidotriazoles on Solid Phase: [1,2,3]-Triazoles by Regiospecific Copper(I)-Catalyzed 1,3-Dipolar Cycloadditions of Terminal Alkynes to Azides, *J. Org. Chem.* **2002**, *67*, 3057-3064.
- [81] V.V. Rostovtsev, L.G. Green, V.V. Fokin, K.B. Sharpless, A stepwise Huisgen cycloaddition process: copper(I)-catalyzed regioselective "ligation" of azides and terminal alkynes, *Angew. Chem. Int. Ed.* **2002**, *41*, 2596-9.
- [82] R. Huisgen, 1,3-Dipolar Cycloadditions. Past and Future, *Angew. Chem. Int. Ed.* **1963**, *2*, 565-598.

- [83] R. Huisgen, Kinetics and Mechanism of 1,3-Dipolar Cycloadditions, *Angew. Chem. Int. Ed.* **1963**, *2*, 633-645.
- [84] M.F. Debets, C.W. van der Doelen, F.P. Rutjes, F.L. van Delft, Azide: a unique dipole for metal-free bioorthogonal ligations, *Chembiochem* **2010**, *11*, 1168-84.
- [85] E.M. Sletten, C.R. Bertozzi, Bioorthogonal chemistry: fishing for selectivity in a sea of functionality, *Angew. Chem. Int. Ed.* **2009**, *48*, 6974-98.
- [86] C.J. Pickens, S.N. Johnson, M.M. Pressnall, M.A. Leon, C.J. Berkland, Practical Considerations, Challenges, and Limitations of Bioconjugation via Azide-Alkyne Cycloaddition, *Bioconjug. Chem.* **2018**, *29*, 686-701.
- [87] D.C. Kennedy, C.S. McKay, M.C. Legault, D.C. Danielson, J.A. Blake, A.F. Pegoraro, A. Stolor, Z. Mester, J.P. Pezacki, Cellular consequences of copper complexes used to catalyze bioorthogonal click reactions, *J. Am. Chem. Soc.* **2011**, *133*, 17993-8001.
- [88] S. Li, H. Cai, J. He, H. Chen, S. Lam, T. Cai, Z. Zhu, S.J. Bark, C. Cai, Extent of the Oxidative Side Reactions to Peptides and Proteins During the CuAAC Reaction, *Bioconjug. Chem.* **2016**, *27*, 2315-2322.
- [89] N.J. Agard, J.A. Prescher, C.R. Bertozzi, A strain-promoted [3 + 2] azide-alkyne cycloaddition for covalent modification of biomolecules in living systems, *J. Am. Chem. Soc.* **2004**, *126*, 15046-7.
- [90] A.T. Blomquist, L.H. Liu, Many-membered Carbon Rings. VII. Cycloöctyne, *J. Am. Chem. Soc.* **1953**, *75*, 2153-2154.
- [91] G. Wittig, A. Krebs, Zur Existenz niedergliedriger Cycloalkine, I, *Chemische Berichte* **1961**, *94*, 3260-3275.
- [92] C.G. Gordon, J.L. Mackey, J.C. Jewett, E.M. Sletten, K.N. Houk, C.R. Bertozzi, Reactivity of biarylazacyclooctynones in copper-free click chemistry, *J. Am. Chem. Soc.* **2012**, *134*, 9199-208.
- [93] J.M. Baskin, J.A. Prescher, S.T. Laughlin, N.J. Agard, P.V. Chang, I.A. Miller, A. Lo, J.A. Codelli, C.R. Bertozzi, Copper-free click chemistry for dynamic in vivo imaging, *Proc. Natl. Acad. Sci. USA* **2007**, *104*, 16793-7.
- [94] V. Vidova, Z. Spacil, A review on mass spectrometry-based quantitative proteomics: Targeted and data independent acquisition, *Anal. Chim. Acta* **2017**, *964*, 7-23.

- [95] N.E. Mbuja, J. Guo, M.A. Wolfert, R. Steet, G.J. Boons, Strain-promoted alkyne-azide cycloadditions (SPAAC) reveal new features of glycoconjugate biosynthesis, *Chembiochem* **2011**, *12*, 1912-21.
- [96] M.F. Debets, S.S. van Berkel, S. Schoffelen, F.P. Rutjes, J.C. van Hest, F.L. van Delft, Aza-dibenzocyclooctynes for fast and efficient enzyme PEGylation via copper-free (3+2) cycloaddition, *Chem. Commun.* **2010**, *46*, 97-9.
- [97] J.C. Jewett, E.M. Sletten, C.R. Bertozzi, Rapid Cu-free click chemistry with readily synthesized biarylazacyclooctynones, *J. Am. Chem. Soc.* **2010**, *132*, 3688-90.
- [98] X. Ning, J. Guo, M.A. Wolfert, G.J. Boons, Visualizing metabolically labeled glycoconjugates of living cells by copper-free and fast Huisgen cycloadditions, *Angew. Chem. Int. Ed.* **2008**, *47*, 2253-5.
- [99] K. Chenoweth, D. Chenoweth, W.A. Goddard, 3rd, Cyclooctyne-based reagents for uncatalyzed click chemistry: A computational survey, *Org. Biomol. Chem.* **2009**, *7*, 5255-8.
- [100] J. Dommerholt, F. Rutjes, F.L. van Delft, Strain-Promoted 1,3-Dipolar Cycloaddition of Cycloalkynes and Organic Azides, *Top. Curr. Chem. (Z)* **2016**, *374*, 16.
- [101] S. Chassaing, V. Bénétou, P. Pale, When CuAAC 'Click Chemistry' goes heterogeneous, *Catal. Sci. Technol.* **2016**, *6*, 923-957.
- [102] N.W. Li, W.H. Binder, Click-chemistry for nanoparticle-modification, *J. Mater. Chem.* **2011**, *21*, 16717-16734.
- [103] H.S. Mader, M. Link, D.E. Achatz, K. Uhlmann, X. Li, O.S. Wolfbeis, Surface-modified upconverting microparticles and nanoparticles for use in click chemistries, *Chemistry* **2010**, *16*, 5416-24.
- [104] B. Uszczyńska, T. Ratajczak, E. Frydrych, H. Maciejewski, M. Figlerowicz, W.T. Markiewicz, M.K. Chmielewski, Application of click chemistry to the production of DNA microarrays, *Lab Chip* **2012**, *12*, 1151-6.
- [105] G. Yi, J. Son, J. Yoo, C. Park, H. Koo, Application of click chemistry in nanoparticle modification and its targeted delivery, *Biomater. Res.* **2018**, *22*, 13.
- [106] C.E. Evans, P.A. Lovell, Click chemistry as a route to surface functionalization of polymer particles dispersed in aqueous media, *Chem. Commun.* **2009**, *17*, 2305-7.
- [107] G. Rousseau, H. Fensterbank, K. Baczko, M. Cano, E. Allard, C. Larpent, Azido-Coated Nanoparticles: A Versatile Clickable Platform for the Preparation of

Fluorescent Polystyrene Core–PAMAM Shell Nanoparticles, *Macromolecules* **2012**, *45*, 3513-3522.

[108] K. Ouadahi, E. Allard, B. Oberleitner, C. Larpent, Synthesis of azide-functionalized nanoparticles by microemulsion polymerization and surface modification by click chemistry in aqueous medium, *J. Polym. Sci. A* **2012**, *50*, 314-328.

[109] J. Olejniczak, G. Collet, V.A. Nguyen Huu, M. Chan, S. Lee, A. Almutairi, Biorthogonal click chemistry on poly(lactic-co-glycolic acid)-polymeric particles, *Biomater. Sci.* **2017**, *5*, 211-215.

[110] J.F. Lutz, G. Nanotechnology for Life Science Research, 1,3-dipolar cycloadditions of azides and alkynes: a universal ligation tool in polymer and materials science, *Angew. Chem. Int. Ed.* **2007**, *46*, 1018-25.

[111] V. Castro, H. Rodriguez, F. Albericio, CuAAC: An Efficient Click Chemistry Reaction on Solid Phase, *ACS Comb. Sci.* **2016**, *18*, 1-14.

[112] T. Freichel, S. Eierhoff, N.L. Snyder, L. Hartmann, Toward Orthogonal Preparation of Sequence-Defined Monodisperse Heteromultivalent Glycomacromolecules on Solid Support Using Staudinger Ligation and Copper-Catalyzed Click Reactions, *J. Org. Chem.* **2017**, *82*, 9400-9409.

[113] A.H. El-Sagheer, T. Brown, Click chemistry with DNA, *Chem. Soc. Rev.* **2010**, *39*, 1388-405.

[114] A.H. El-Sagheer, T. Brown, Click nucleic acid ligation: applications in biology and nanotechnology, *Acc. Chem. Res.* **2012**, *45*, 1258-67.

[115] P. Saha, D. Panda, J. Dash, The application of click chemistry for targeting quadruplex nucleic acids, *Chem. Commun.* **2019**, *55*, 731-750.

[116] C. Uttamapinant, A. Tangpeerachaikul, S. Grecian, S. Clarke, U. Singh, P. Slade, K.R. Gee, A.Y. Ting, Fast, cell-compatible click chemistry with copper-chelating azides for biomolecular labeling, *Angew. Chem. Int. Ed.* **2012**, *51*, 5852-6.

[117] J. Zayas, M. Annoual, J.K. Das, Q. Felty, W.G. Gonzalez, J. Miksovská, N. Sharifai, A. Chiba, S.F. Wnuk, Strain Promoted Click Chemistry of 2- or 8-Azidopurine and 5-Azidopyrimidine Nucleosides and 8-Azidoadenosine Triphosphate with Cyclooctynes. Application to Living Cell Fluorescent Imaging, *Bioconjug. Chem.* **2015**, *26*, 1519-32.

- [118] M. Dolci, J.-F. Bryche, C. Leuvrey, S. Zafeiratos, S. Gree, S. Begin-Colin, G. Barbillon, B.P. Pichon, Robust clicked assembly based on iron oxide nanoparticles for a new type of SPR biosensor, *J. Mater. Chem. C* **2018**, *6*, 9102-9110.
- [119] S. Ranjbar, P. Riente, C. Rodriguez-Esrich, J. Yadav, K. Ramineni, M.A. Pericas, Polystyrene or Magnetic Nanoparticles as Support in Enantioselective Organocatalysis? A Case Study in Friedel-Crafts Chemistry, *Org. Lett.* **2016**, *18*, 1602-5.
- [120] M.D. de Tercero, M. Bruns, I.G. Martínez, M. Türk, U. Fehrenbacher, S. Jennewein, L. Barner, Continuous Hydrothermal Synthesis of In Situ Functionalized Iron Oxide Nanoparticles: A General Strategy to Produce Metal Oxide Nanoparticles With Clickable Anchors, *Part. Part. Syst. Charact.* **2013**, *30*, 229-234.
- [121] J.I. Cutler, D. Zheng, X. Xu, D.A. Giljohann, C.A. Mirkin, Polyvalent oligonucleotide iron oxide nanoparticle "click" conjugates, *Nano Lett.* **2010**, *10*, 1477-80.
- [122] R.M. Fratila, M. Navascuez, J. Idiago-López, M. Eceiza, J.I. Miranda, J.M. Aizpurua, J.M. de la Fuente, Covalent immobilisation of magnetic nanoparticles on surfaces via strain-promoted azide-alkyne click chemistry, *New J. Chem.* **2017**, *41*, 10835-10840.
- [123] J.B. Haun, N.K. Devaraj, S.A. Hilderbrand, H. Lee, R. Weissleder, Bioorthogonal chemistry amplifies nanoparticle binding and enhances the sensitivity of cell detection, *Nat. Nanotechnol.* **2010**, *5*, 660-5.
- [124] A. Nouredine, M. Gary-Bobo, L. Lichon, M. Garcia, J.I. Zink, M. Wong Chi Man, X. Cattoen, Bis-clickable Mesoporous Silica Nanoparticles: Straightforward Preparation of Light-Actuated Nanomachines for Controlled Drug Delivery with Active Targeting, *Chemistry* **2016**, *22*, 9624-30.
- [125] C. Tissandier, N. Diop, M. Martini, S. Roux, O. Tillement, T. Hamaide, One-pot synthesis of hybrid multifunctional silica nanoparticles with tunable coating by click chemistry in reverse w/o microemulsion, *Langmuir* **2012**, *28*, 209-18.
- [126] E.W. Elliott, 3rd, A.L. Ginzburg, Z.C. Kennedy, Z. Feng, J.E. Hutchison, Single-Step Synthesis of Small, Azide-Functionalized Gold Nanoparticles: Versatile, Water-Dispersible Reagents for Click Chemistry, *Langmuir* **2017**, *33*, 5796-5802.
- [127] S.B. van der Meer, K. Loza, K. Wey, M. Heggen, C. Beuck, P. Bayer, M. Epple, Click Chemistry on the Surface of Ultrasmall Gold Nanoparticles (2 nm) for Covalent Ligand Attachment Followed by NMR Spectroscopy, *Langmuir* **2019**, *35*, 7191-7204.

- [128] J. Zhao, M.H. Stenzel, Entry of nanoparticles into cells: the importance of nanoparticle properties, *Polym. Chem.* **2018**, *9*, 259-272.
- [129] S. Behzadi, V. Serpooshan, W. Tao, M.A. Hamaly, M.Y. Alkawareek, E.C. Dreaden, D. Brown, A.M. Alkilany, O.C. Farokhzad, M. Mahmoudi, Cellular uptake of nanoparticles: journey inside the cell, *Chem. Soc. Rev.* **2017**, *46*, 4218-4244.
- [130] G.J. Doherty, H.T. McMahon, Mechanisms of endocytosis, *Annu. Rev. Biochem.* **2009**, *78*, 857-902.
- [131] S. Kumari, S. Mg, S. Mayor, Endocytosis unplugged: multiple ways to enter the cell, *Cell Res.* **2010**, *20*, 256-75.
- [132] S. Gordon, Phagocytosis: An Immunobiologic Process, *Immunity* **2016**, *44*, 463-475.
- [133] V. Sokolova, D. Kozlova, T. Knuschke, J. Buer, A.M. Westendorf, M. Epple, Mechanism of the uptake of cationic and anionic calcium phosphate nanoparticles by cells, *Acta Biomater.* **2013**, *9*, 7527-35.
- [134] F. Recillas-Targa, Multiple strategies for gene transfer, expression, knockdown, and chromatin influence in mammalian cell lines and transgenic animals, *Mol. Biotechnol.* **2006**, *34*, 337-54.
- [135] S.D. Patil, D.G. Rhodes, D.J. Burgess, DNA-based therapeutics and DNA delivery systems: a comprehensive review, *AAPS J* **2005**, *7*, E61-77.
- [136] T.K. Kim, J.H. Eberwine, Mammalian cell transfection: the present and the future, *Anal. Bioanal. Chem.* **2010**, *397*, 3173-8.
- [137] J.M. Meacham, K. Durvasula, F.L. Degertekin, A.G. Fedorov, Physical methods for intracellular delivery: practical aspects from laboratory use to industrial-scale processing, *J. Lab. Autom.* **2014**, *19*, 1-18.
- [138] M.A. Kotterman, T.W. Chalberg, D.V. Schaffer, Viral Vectors for Gene Therapy: Translational and Clinical Outlook, *Annu. Rev. Biomed. Eng.* **2015**, *17*, 63-89.
- [139] K. Lundstrom, Viral Vectors in Gene Therapy, *Diseases* **2018**, *6*, 1-20.
- [140] L. Kaestner, A. Scholz, P. Lipp, Conceptual and technical aspects of transfection and gene delivery, *Bioorg. Med. Chem. Lett.* **2015**, *25*, 1171-6.
- [141] N. Agrawal, P.V. Dasaradhi, A. Mohammed, P. Malhotra, R.K. Bhatnagar, S.K. Mukherjee, RNA interference: biology, mechanism, and applications, *Microbiol. Mol. Biol. Rev.* **2003**, *67*, 657-85.
- [142] N. Li, H. Yang, Z. Yu, Y. Li, W. Pan, H. Wang, B. Tang, Nuclear-targeted siRNA delivery for long-term gene silencing, *Chem. Sci.* **2017**, *8*, 2816-2822.

- [143] J.K. Lam, M.Y. Chow, Y. Zhang, S.W. Leung, siRNA Versus miRNA as Therapeutics for Gene Silencing, *Mol. Ther. Nucleic Acids* **2015**, *4*, e252.
- [144] G. Sun, S.Y. Yeh, C.W. Yuan, M.J. Chiu, B.S. Yung, Y. Yen, Molecular Properties, Functional Mechanisms, and Applications of Sliced siRNA, *Mol. Ther. Nucleic Acids* **2015**, *4*, e221.
- [145] M. Ha, V.N. Kim, Regulation of microRNA biogenesis, *Nat. Rev. Mol. Cell Biol.* **2014**, *15*, 509-24.
- [146] D.H. Kim, J.J. Rossi, Strategies for silencing human disease using RNA interference, *Nat. Rev. Genet.* **2007**, *8*, 173-84.
- [147] R.W. Carthew, E.J. Sontheimer, Origins and Mechanisms of miRNAs and siRNAs, *Cell* **2009**, *136*, 642-55.
- [148] D.G. Sashital, J.A. Doudna, Structural insights into RNA interference, *Curr Opin Struct Biol.* **2010**, *20*, 90-97.
- [149] F. Wahid, A. Shehzad, T. Khan, Y.Y. Kim, MicroRNAs: synthesis, mechanism, function, and recent clinical trials, *Biochim. Biophys. Acta* **2010**, *1803*, 1231-43.
- [150] J.R. Dunkelberger, W.C. Song, Complement and its role in innate and adaptive immune responses, *Cell Res.* **2010**, *20*, 34-50.
- [151] C.J. Eaves, Hematopoietic stem cells: concepts, definitions, and the new reality, *Blood* **2015**, *125*, 2605-13.
- [152] Y. Zhang, S. Gao, J. Xia, F. Liu, Hematopoietic Hierarchy - An Updated Roadmap, *Trends Cell. Biol.* **2018**, *28*, 976-986.
- [153] E. Laurenti, B. Gottgens, From haematopoietic stem cells to complex differentiation landscapes, *Nature* **2018**, *553*, 418-426.
- [154] J. Parkin, B. Cohen, An overview of the immune system, *The Lancet* **2001**, *357*, 1777-1789.
- [155] D.D. Chaplin, Overview of the immune response, *J. Allergy Clin. Immunol.* **2010**, *125*, S3-23.
- [156] S.E. Turvey, D.H. Broide, Innate immunity, *J. Allergy Clin. Immunol.* **2010**, *125*, S24-32.
- [157] G. Liu, Y. Zhao, Toll-like receptors and immune regulation: their direct and indirect modulation on regulatory CD4⁺ CD25⁺ T cells, *Immunology* **2007**, *122*, 149-56.
- [158] F.A. Bonilla, H.C. Oettgen, Adaptive immunity, *J. Allergy Clin. Immunol.* **2010**, *125*, S33-40.

- [159] H.W. Schroeder, Jr., L. Cavacini, Structure and function of immunoglobulins, *J. Allergy Clin. Immunol.* **2010**, *125*, S41-52.
- [160] K. Chen, A. Cerutti, The function and regulation of immunoglobulin D, *Curr. Opin. Immunol.* **2011**, *23*, 345-52.
- [161] G. Vidarsson, G. Dekkers, T. Rispens, IgG subclasses and allotypes: from structure to effector functions, *Front Immunol.* **2014**, *5*, 520.
- [162] V. Irani, A.J. Guy, D. Andrew, J.G. Beeson, P.A. Ramsland, J.S. Richards, Molecular properties of human IgG subclasses and their implications for designing therapeutic monoclonal antibodies against infectious diseases, *Mol. Immunol.* **2015**, *67*, 171-82.
- [163] J.M. Woof, M.A. Kerr, The function of immunoglobulin A in immunity, *J. Pathol.* **2006**, *208*, 270-82.
- [164] J.M. Woof, M.W. Russell, Structure and function relationships in IgA, *Mucosal Immunol.* **2011**, *4*, 590-7.
- [165] H.C. Oettgen, Fifty years later: Emerging functions of IgE antibodies in host defense, immune regulation, and allergic diseases, *J. Allergy Clin. Immunol.* **2016**, *137*, 1631-1645.
- [166] S.L. Nutt, P.D. Hodgkin, D.M. Tarlinton, L.M. Corcoran, The generation of antibody-secreting plasma cells, *Nat. Rev. Immunol.* **2015**, *15*, 160-71.
- [167] N.E. Harwood, F.D. Batista, Early events in B cell activation, *Annu. Rev. Immunol.* **2010**, *28*, 185-210.
- [168] M. Seifert, R. Kuppers, Human memory B cells, *Leukemia* **2016**, *30*, 2283-2292.
- [169] J. Mercer, U.F. Greber, Virus interactions with endocytic pathways in macrophages and dendritic cells, *Trends Microbiol.* **2013**, *21*, 380-8.
- [170] F.A. Rey, S.M. Lok, Common Features of Enveloped Viruses and Implications for Immunogen Design for Next-Generation Vaccines, *Cell* **2018**, *172*, 1319-1334.
- [171] J. Grove, M. Marsh, The cell biology of receptor-mediated virus entry, *J. Cell Biol.* **2011**, *195*, 1071-82.
- [172] E. Barrow, A.V. Nicola, J. Liu, Multiscale perspectives of virus entry via endocytosis, *Viol. J.* **2013**, *10*, 177.
- [173] G.J. Kotwal, S. Hatch, W.L. Marshall, Viral infection: an evolving insight into the signal transduction pathways responsible for the innate immune response, *Adv. Virol.* **2012**, *2012*, 131457.

- [174] H. Changotra, A. Vij, Rotavirus virus-like particles (RV-VLPs) vaccines: An update, *Rev. Med. Virol.* **2017**, *27*, 1-11.
- [175] A. Zeltins, Construction and characterization of virus-like particles: a review, *Mol. Biotechnol.* **2013**, *53*, 92-107.
- [176] M.J. Rohovie, M. Nagasawa, J.R. Swartz, Virus-like particles: Next-generation nanoparticles for targeted therapeutic delivery, *Bioeng. Transl. Med.* **2017**, *2*, 43-57.
- [177] P. Ratnatilaka Na Bhuket, J.A. Luckanagul, P. Rojsitthisak, Q. Wang, Chemical modification of enveloped viruses for biomedical applications, *Integr. Biol.* **2018**, *10*, 666-679.
- [178] Y. Shen, T. Hao, S. Ou, C. Hu, L. Chen, Applications and perspectives of nanomaterials in novel vaccine development, *Medchemcomm* **2018**, *9*, 226-238.
- [179] V. Sokolova, A.M. Westendorf, J. Buer, K. Überla, M. Epple, The potential of nanoparticles for the immunization against viral infections, *J. Mater. Chem. B* **2015**, *3*, 4767-4779.
- [180] P.M. Carvalho, M.R. Felicio, N.C. Santos, S. Goncalves, M.M. Domingues, Application of Light Scattering Techniques to Nanoparticle Characterization and Development, *Front Chem.* **2018**, *6*, 237.
- [181] H. Kato, Size Determination of Nanoparticles by Dynamic Light Scattering, in: S.C. Singh, H. Zeng, C. Guo, W. Cai (Eds.), *Nanomaterials: Processing and Characterization with Lasers*, Wiley-VCH Verlag GmbH & Co. KGaA, Weinheim, Germany, **2012**.
- [182] P. Yadav, S. Chacko, G. Kumar, R. Ramapanicker, V. Verma, Click chemistry route to covalently link cellulose and clay, *Cellulose* **2015**, *22*, 1615-1624.
- [183] M.M. Domingues, P.S. Santiago, M.A. Castanho, N.C. Santos, What can light scattering spectroscopy do for membrane-active peptide studies?, *J. Pept. Sci.* **2008**, *14*, 394-400.
- [184] M. Sauer, J. Hofkens, J. Enderlein, *Handbook of Fluorescence Spectroscopy and Imaging: From Ensemble to Single Molecules*, Wiley-VCH Verlag & Co. KGaA, Weinheim, Germany, **2010**.
- [185] Z. Gao, Y. Hao, M. Zheng, Y. Chen, A fluorescent dye with large Stokes shift and high stability: synthesis and application to live cell imaging, *RSC Adv.* **2017**, *7*, 7604-7609.
- [186] B.H. Stuart, *Infrared Spectroscopy: Fundamentals and Applications*, John Wiley & Sons Ltd, West Sussex, UK, **2004**.

- [187] Thermal analysis of polymers: fundamentals and applications, John Wiley & Sons, Inc., New Jersey, USA, **2009**.
- [188] J. Ayache, L. Beaunier, J. Boumendil, G. Ehret, D. Laub, Sample Preparation Handbook for Transmission Electron Microscopy, Springer Science+Business Media, New York, USA, **2010**.
- [189] C.G.H. Walker, I. Konvalina, F. Mika, L. Frank, I. Müllerová, Quantitative comparison of simulated and measured signals in the STEM mode of a SEM, *Nuclear Inst. and Methods in Physics Research B* **2018**, *415*, 17-24.
- [190] W. Sigle, Analytical transmission electron microscopy, *Annu. Rev. Mater. Res.* **2005**, *35*, 239-314.
- [191] B. Cao, H. Xu, C. Mao, Transmission electron microscopy as a tool to image bioinorganic nanohybrids: the case of phage-gold nanocomposites, *Microsc. Res. Tech.* **2011**, *74*, 627-35.
- [192] S. De Carlo, J.R. Harris, Negative staining and cryo-negative staining of macromolecules and viruses for TEM, *Micron* **2011**, *42*, 117-31.
- [193] P.M. Kelly, C. Aberg, E. Polo, A. O'Connell, J. Cookman, J. Fallon, Z. Krpetic, K.A. Dawson, Mapping protein binding sites on the biomolecular corona of nanoparticles, *Nat. Nanotechnol.* **2015**, *10*, 472-9.
- [194] P. Ercius, O. Alaidi, M.J. Rames, G. Ren, Electron Tomography: A Three-Dimensional Analytic Tool for Hard and Soft Materials Research, *Adv. Mater.* **2015**, *27*, 5638-5663.
- [195] O. Ersen, I. Florea, C. Hirlimann, C. Pham-Huu, Exploring nanomaterials with 3D electron microscopy, *Materials Today* **2015**, *18*, 395-408.
- [196] P.L. Stewart, Cryo-electron microscopy and cryo-electron tomography of nanoparticles, *WIREs Nanomed. Nanobiotechnol.* **2017**, *9*, e1417.
- [197] R.F. Thompson, M. Walker, C.A. Siebert, S.P. Muench, N.A. Ranson, An introduction to sample preparation and imaging by cryo-electron microscopy for structural biology, *Methods* **2016**, *100*, 3-15.
- [198] L. Schermelleh, R. Heintzmann, H. Leonhardt, A guide to super-resolution fluorescence microscopy, *J. Cell Biol.* **2010**, *190*, 165-75.
- [199] L. Schermelleh, A. Ferrand, T. Huser, C. Eggeling, M. Sauer, O. Biehlmaier, G.P.C. Drummen, Super-resolution microscopy demystified, *Nat. Cell Biol.* **2019**, *21*, 72-84.

- [200] J. Jonkman, C.M. Brown, Any Way You Slice It-A Comparison of Confocal Microscopy Techniques, *J. Biomol. Tech.* **2015**, *26*, 54-65.
- [201] S.W. Paddock, Principles and Practices of Laser Scanning Confocal Microscopy, *Molecular Biotechnology* **2000**, *16*, 127-150.
- [202] J. Demmerle, C. Innocent, A.J. North, G. Ball, M. Muller, E. Miron, A. Matsuda, I.M. Dobbie, Y. Markaki, L. Schermelleh, Strategic and practical guidelines for successful structured illumination microscopy, *Nat. Protoc.* **2017**, *12*, 988-1010.
- [203] E. Wegel, A. Gohler, B.C. Lagerholm, A. Wainman, S. Uphoff, R. Kaufmann, I.M. Dobbie, Imaging cellular structures in super-resolution with SIM, STED and Localisation Microscopy: A practical comparison, *Sci. Rep.* **2016**, *6*, 27290.
- [204] M.G.L. Gustafsson, Surpassing the lateral resolution limit by a factor of two using structured illumination microscopy, *Journal of Microscopy* **2000**, *198*, 82-87.
- [205] B. Huang, M. Bates, X. Zhuang, Super-resolution fluorescence microscopy, *Annu. Rev. Biochem.* **2009**, *78*, 993-1016.
- [206] J.R. Allen, S.T. Ross, M.W. Davidson, Single molecule localization microscopy for superresolution, *J Optics-Uk* **2013**, *15*, 1-15.
- [207] G.T. Dempsey, J.C. Vaughan, K.H. Chen, M. Bates, X. Zhuang, Evaluation of fluorophores for optimal performance in localization-based super-resolution imaging, *Nat. Methods* **2011**, *8*, 1027-36.
- [208] M.J. Rust, M. Bates, X. Zhuang, Sub-diffraction-limit imaging by stochastic optical reconstruction microscopy (STORM), *Nat. Methods* **2006**, *3*, 793-5.
- [209] M. Lehmann, G. Lichtner, H. Klenz, J. Schmoranzer, Novel organic dyes for multicolor localization-based super-resolution microscopy, *J. Biophotonics* **2016**, *9*, 161-70.
- [210] M.T. Hoffman, J. Sheung, P.R. Selvin, Fluorescence imaging with one nanometer accuracy: in vitro and in vivo studies of molecular motors, *Methods Mol. Biol.* **2011**, *778*, 33-56.
- [211] T. Mosmann, Rapid colorimetric assay for cellular growth and survival: Application to proliferation and cytotoxicity assays, *Journal of Immunological Methods* **1983**, *65*, 55-63.
- [212] H. Wang, F. Wang, X. Tao, H. Cheng, Ammonia-containing dimethyl sulfoxide: an improved solvent for the dissolution of formazan crystals in the 3-(4,5-dimethylthiazol-2-yl)-2,5-diphenyl tetrazolium bromide (MTT) assay, *Anal. Biochem.* **2012**, *421*, 324-6.

- [213] C.R. Raetz, Bacterial endotoxins: extraordinary lipids that activate eucaryotic signal transduction, *J. Bacteriol.* **1993**, *175*, 5745-53.
- [214] C. Galanos, M.A. Freudenberg, Bacterial endotoxins: biological properties and mechanisms of action, *Mediators Inflamm* **1993**, *2*, S11-6.
- [215] H. Bosshart, M. Heinzemann, Targeting bacterial endotoxin: two sides of a coin, *Ann. N.Y. Acad. Sci.* **2007**, *1096*, 1-17.
- [216] P. Kalita, A. Bholra, N. Goel, V. Sritharan, S. Gupta, Heterogeneous endotoxin detection bioassay using drug–nanoparticle bioconjugates: an optimization study, *Mol. Syst. Des. Eng.* **2017**, *2*, 470-477.
- [217] G.K. Lindsay, P.F. Roslansky, T.J. Novitsky, Single-step, chromogenic Limulus amoebocyte lysate assay for endotoxin, *J. Clin. Microbiol.* **1989**, *27*, 947-51.
- [218] S.D. Gan, K.R. Patel, Enzyme immunoassay and enzyme-linked immunosorbent assay, *J. Invest. Dermatol.* **2013**, *133*, 1-3.
- [219] P. Hornbeck, S.E. Winston, S.A. Fuller, Enzyme-linked immunosorbent assays (ELISA), *Curr. Protoc. Mol. Biol.* **1991**, *15*, 11.2.1-11.2.22.
- [220] W. Stöber, A. Fink, E. Bohn, Controlled growth of monodisperse silica spheres in the micron size range, *J. Colloid Interface Sci.* **1968**, *26*, 62-69.
- [221] C. Wu, W. Deng, L. Deng, L. Cao, B. Qin, S. Li, Y. Wang, R. Pei, D. Yang, M. Lu, X. Chen, Amino acid substitutions at positions 122 and 145 of hepatitis B virus surface antigen (HBsAg) determine the antigenicity and immunogenicity of HBsAg and influence in vivo HBsAg clearance, *J. Virol.* **2012**, *86*, 4658-69.
- [222] J. Yang, Y. Zhao, P. Li, Y. Yang, E. Zhang, M. Zhong, Y. Li, D. Zhou, Y. Cao, M. Lu, F. Shao, H. Yan, Sequence determinants of specific pattern-recognition of bacterial ligands by the NAIP-NLRC4 inflammasome, *Cell Discov.* **2018**, *4*, 22.
- [223] S. Chernousova, J. Klesing, N. Soklakova, M. Epple, A genetically active nano-calcium phosphate paste for bone substitution, encoding the formation of BMP-7 and VEGF-A, *RSC Adv.* **2013**, *3*, 11155-11161.
- [224] O. Boussif, F. Lezoualc'h, M.A. Zanta, M.D. Mergny, D. Scherman, B. Demeneix, J.P. Behr, A versatile vector for gene and oligonucleotide transfer into cells in culture and in vivo: polyethylenimine, *Proc. Natl. Acad. Sci. USA* **1995**, *92*, 7297-301.
- [225] A. Baker, M. Saltik, H. Lehrmann, I. Killisch, V. Mautner, G. Lamm, G. Christofori, M. Cotten, Polyethylenimine (PEI) is a simple, inexpensive and effective reagent for condensing and linking plasmid DNA to adenovirus for gene delivery, *Gene Ther.* **1997**, *4*, 773-82.

- [226] C. Malloggi, D. Pezzoli, L. Magagnin, L. De Nardo, D. Mantovani, E. Tallarita, G. Candiani, Comparative evaluation and optimization of off-the-shelf cationic polymers for gene delivery purposes, *Polym. Chem.* **2015**, *6*, 6325-6339.
- [227] M. Thomas, A.M. Klibanov, Enhancing polyethylenimine's delivery of plasmid DNA into mammalian cells, *Proc. Natl. Acad. Sci. USA* **2002**, *99*, 14640-5.
- [228] L. Rojas-Sánchez, V. Sokolova, S. Riebe, J. Voskuhl, M. Epple, Covalent Surface Functionalization of Calcium Phosphate Nanoparticles with Fluorescent Dyes by Copper-Catalysed and by Strain-Promoted Azide-Alkyne Click Chemistry, *ChemNanoMat* **2019**, *5*, 436-446.
- [229] Y. Han, Z. Lu, Z. Teng, J. Liang, Z. Guo, D. Wang, M.Y. Han, W. Yang, Unraveling the Growth Mechanism of Silica Particles in the Stober Method: In Situ Seeded Growth Model, *Langmuir* **2017**, *33*, 5879-5890.
- [230] E. Lieber, C.N.R. Rao, T.S. Chao, C.W.W. Hoffman, Infrared Spectra of Organic Azides, *Anal. Chem.* **1957**, *29*, 916-918.
- [231] E. Lieber, C.N.R. Rao, A.E. Thomas, E. Oftedahl, R. Minnis, C.V.N. Nambury, Infrared spectra of acid azides, carbamyl azides and other azido derivatives, *Spectrochimica Acta* **1963**, *19*, 1135-1144.
- [232] A. Antonakos, E. Liarokapis, T. Leventouri, Micro-Raman and FTIR studies of synthetic and natural apatites, *Biomaterials* **2007**, *28*, 3043-54.
- [233] F. Rubio, J. Rubio, J.L. Oteo, A FT-IR Study of the Hydrolysis of Tetraethylorthosilicate (TEOS), *Spectrosc. Lett.* **1998**, *31*, 199-219.
- [234] M.I. Tejedor-Tejedor, L. Paredes, M.A. Anderson, Evaluation of ATR-FTIR Spectroscopy as an "in Situ" Tool for Following the Hydrolysis and Condensation of Alkoxysilanes under Rich H₂O Conditions, *Chem. Mater.* **1998**, *10*, 3410-3421.
- [235] M. Markovic, B.O. Fowler, M.S. Tung, Preparation and Comprehensive Characterization of a Calcium Hydroxyapatite Reference Material, *J. Res. Natl. Inst. Stand. Technol.* **2004**, *109*, 553-68.
- [236] V. Hong, S.I. Presolski, C. Ma, M.G. Finn, Analysis and optimization of copper-catalyzed azide-alkyne cycloaddition for bioconjugation, *Angew. Chem. Int. Ed.* **2009**, *48*, 9879-83.
- [237] S.I. Presolski, V.P. Hong, M.G. Finn, Copper-Catalyzed Azide-Alkyne Click Chemistry for Bioconjugation, *Curr. Protoc. Chem. Biol.* **2011**, *3*, 153-162.

- [238] V.O. Rodionov, S.I. Presolski, D.D. Diaz, V.V. Fokin, M.G. Finn, Ligand-accelerated Cu-catalyzed azide-alkyne cycloaddition: a mechanistic report, *J. Am. Chem. Soc.* **2007**, *129*, 12705-12.
- [239] J. Klesing, S. Chernousova, M. Epple, Freeze-dried cationic calcium phosphatenanorods as versatile carriers of nucleic acids (DNA, siRNA), *J. Mater. Chem.* **2012**, *22*, 199-204.
- [240] W. Ngamcherdtrakul, T. Sangvanich, M. Reda, S. Gu, D. Bejan, W. Yantasee, Lyophilization and stability of antibody-conjugated mesoporous silica nanoparticle with cationic polymer and PEG for siRNA delivery, *Int. J. Nanomedicine* **2018**, *13*, 4015-4027.
- [241] P. Fonte, S. Soares, F. Sousa, A. Costa, V. Seabra, S. Reis, B. Sarmiento, Stability study perspective of the effect of freeze-drying using cryoprotectants on the structure of insulin loaded into PLGA nanoparticles, *Biomacromolecules* **2014**, *15*, 3753-65.
- [242] A.S. Picco, L.F. Ferreira, M.S. Liberato, G.B. Mondo, M.B. Cardoso, Freeze-drying of silica nanoparticles: redispersibility toward nanomedicine applications, *Nanomedicine (Lond)* **2018**, *13*, 179-190.
- [243] C.C. Carcouet, M.W. van de Put, B. Mezari, P.C. Magusin, J. Laven, P.H. Bomans, H. Friedrich, A.C. Esteves, N.A. Sommerdijk, R.A. van Benthem, G. de With, Nucleation and growth of monodisperse silica nanoparticles, *Nano Lett.* **2014**, *14*, 1433-8.
- [244] C.J. Moore, H. Montón, R. O'Kennedy, D.E. Williams, C. Nogués, C. Crean, V. Gubala, Controlling colloidal stability of silica nanoparticles during bioconjugation reactions with proteins and improving their longer-term stability, handling and storage, *J. Mater. Chem. B* **2015**, *3*, 2043-2055.
- [245] Y. Fu, N.S. Finney, Small-molecule fluorescent probes and their design, *RSC Adv.* **2018**, *8*, 29051-29061.
- [246] M. Panigrahi, S. Dash, S. Patel, B.K. Mishra, Syntheses of cyanines: a review, *Tetrahedron* **2012**, *68*, 781-805.
- [247] P.L. Southwick, L.A. Ernst, E.W. Tauriello, S.R. Parker, R.B. Mujumdar, S.R. Mujumdar, H.A. Clever, A.S. Waggoner, Cyanine dye labeling reagents--carboxymethylindocyanine succinimidyl esters, *Cytometry* **1990**, *11*, 418-30.

- [248] S.I. Presolski, V. Hong, S.H. Cho, M.G. Finn, Tailored ligand acceleration of the Cu-catalyzed azide-alkyne cycloaddition reaction: practical and mechanistic implications, *J. Am. Chem. Soc.* **2010**, *132*, 14570-6.
- [249] J. Mei, N.L. Leung, R.T. Kwok, J.W. Lam, B.Z. Tang, Aggregation-Induced Emission: Together We Shine, United We Soar!, *Chem. Rev.* **2015**, *115*, 11718-940.
- [250] D. Ding, K. Li, B. Liu, B.Z. Tang, Bioprobes based on AIE fluorogens, *Acc. Chem. Res.* **2013**, *46*, 2441-53.
- [251] J. Luo, Z. Xie, J.W. Lam, L. Cheng, H. Chen, C. Qiu, H.S. Kwok, X. Zhan, Y. Liu, D. Zhu, B.Z. Tang, Aggregation-induced emission of 1-methyl-1,2,3,4,5-pentaphenylsilole, *Chem. Commun.* **2001**, *18*, 1740-1.
- [252] S. Riebe, C. Vallet, F. van der Vight, D. Gonzalez-Abadelo, C. Wolper, C.A. Strassert, G. Jansen, S. Knauer, J. Voskuhl, Aromatic Thioethers as Novel Luminophores with Aggregation-Induced Fluorescence and Phosphorescence, *Chemistry* **2017**, *23*, 13660-13668.
- [253] S. Riebe, M. Saccone, J. Stelzer, A. Sowa, C. Wolper, K. Soloviova, C.A. Strassert, M. Giese, J. Voskuhl, Alkylated Aromatic Thioethers with Aggregation-Induced Emission Properties-Assembly and Photophysics, *Chem Asian J.* **2019**, *14*, 814-820.
- [254] Y. Moriyama, D. Ohta, K. Hachiya, Y. Mitsui, K. Takeda, Fluorescence behavior of tryptophan residues of bovine and human serum albumins in ionic surfactant solutions: A comparative study of the two and one tryptophan(s) of bovine and human albumins, *J. Protein Chem.* **1996**, *15*, 265-272.
- [255] V.D. Suryawanshi, L.S. Walekar, A.H. Gore, P.V. Anbhule, G.B. Kolekar, Spectroscopic analysis on the binding interaction of biologically active pyrimidine derivative with bovine serum albumin, *J. Pharm. Anal.* **2016**, *6*, 56-63.
- [256] C.B. Berde, B.S. Hudson, R.D. Simoni, L.A. Sklar, Human serum albumin. Spectroscopic studies of binding and proximity relationships for fatty acids and bilirubin, *J. Biol. Chem.* **1979**, *254*, 391-400.
- [257] K.A. Majorek, P.J. Porebski, A. Dayal, M.D. Zimmerman, K. Jablonska, A.J. Stewart, M. Chruszcz, W. Minor, Structural and immunologic characterization of bovine, horse, and rabbit serum albumins, *Mol. Immunol.* **2012**, *52*, 174-82.
- [258] S. Dominguez-Medina, S. McDonough, P. Swanglap, C.F. Landes, S. Link, In situ measurement of bovine serum albumin interaction with gold nanospheres, *Langmuir* **2012**, *28*, 9131-9.

- [259] O. Koniev, A. Wagner, Developments and recent advancements in the field of endogenous amino acid selective bond forming reactions for bioconjugation, *Chem. Soc. Rev.* **2015**, *44*, 5495-551.
- [260] E. Mavropoulos, A.M. Costa, L.T. Costa, C.A. Achete, A. Mello, J.M. Granjeiro, A.M. Rossi, Adsorption and bioactivity studies of albumin onto hydroxyapatite surface, *Colloids Surf. B Biointerfaces* **2011**, *83*, 1-9.
- [261] B.E. Givens, Z. Xu, J. Fiegel, V.H. Grassian, Bovine serum albumin adsorption on SiO₂ and TiO₂ nanoparticle surfaces at circumneutral and acidic pH: A tale of two nano-bio surface interactions, *J. Colloid Interface Sci.* **2017**, *493*, 334-341.
- [262] S.E. Lehman, I.A. Mudunkotuwa, V.H. Grassian, S.C. Larsen, Nano-Bio Interactions of Porous and Nonporous Silica Nanoparticles of Varied Surface Chemistry: A Structural, Kinetic, and Thermodynamic Study of Protein Adsorption from RPMI Culture Medium, *Langmuir* **2016**, *32*, 731-42.
- [263] H.T. Phan, S. Bartelt-Hunt, K.B. Rodenhausen, M. Schubert, J.C. Bartz, Investigation of Bovine Serum Albumin (BSA) Attachment onto Self-Assembled Monolayers (SAMs) Using Combinatorial Quartz Crystal Microbalance with Dissipation (QCM-D) and Spectroscopic Ellipsometry (SE), *PLoS One* **2015**, *10*, e0141282.
- [264] S. Narayan, A. Rajagopalan, J.S. Reddy, A. Chadha, BSA binding to silica capped gold nanostructures: effect of surface cap and conjugation design on nanostructure–BSA interface, *RSC Adv.* **2014**, *4*, 1412-1420.
- [265] F. Oesterhelt, M. Rief, H.E. Gaub, Single molecule force spectroscopy by AFM indicates helical structure of poly(ethylene-glycol) in water, *New J Phys* **1999**, *1*, 6.1-6.11.
- [266] B. Jachimaska, K. Tokarczyk, M. Łapczyńska, A. Puciul-Malinowska, S. Zapotoczny, Structure of bovine serum albumin adsorbed on silica investigated by quartz crystal microbalance, *Colloids and Surfaces A: Physicochem. Eng. Aspects* **2016**, *489*, 163-172.
- [267] P.G. Squire, P. Moser, C.T. O'Konski, The hydrodynamic properties of bovine serum albumin monomer and dimer, *Biochemistry* **1968**, *7*, 4261-72.
- [268] S.W. Hell, S.J. Sahl, M. Bates, X. Zhuang, R. Heintzmann, M.J. Booth, J. Bewersdorf, G. Shtengel, H. Hess, P. Tinnefeld, A. Honigmann, S. Jakobs, I. Testa, L. Cognet, B. Lounis, H. Ewers, S.J. Davis, C. Eggeling, D. Klenerman, K.I. Willig, G.

- Vicidomini, M. Castello, A. Diaspro, T. Cordes, The 2015 super-resolution microscopy roadmap, *J. Phys. D: Appl. Phys.* **2015**, *48*, 1-35.
- [269] F. Cardarelli, L. Digiacomio, C. Marchini, A. Amici, F. Salomone, G. Fiume, A. Rossetta, E. Gratton, D. Pozzi, G. Caracciolo, The intracellular trafficking mechanism of Lipofectamine-based transfection reagents and its implication for gene delivery, *Sci. Rep.* **2016**, *6*, 25879.
- [270] B. Dalby, S. Cates, A. Harris, E.C. Ohki, M.L. Tilkins, P.J. Price, V.C. Ciccarone, Advanced transfection with Lipofectamine 2000 reagent: primary neurons, siRNA, and high-throughput applications, *Methods* **2004**, *33*, 95-103.
- [271] G.R. Abel, Jr., Z.A. Calabrese, J. Ayco, J.E. Hein, T. Ye, Measuring and Suppressing the Oxidative Damage to DNA During Cu(I)-Catalyzed Azide-Alkyne Cycloaddition, *Bioconjug. Chem.* **2016**, *27*, 698-704.
- [272] B.D. Monnery, M. Wright, R. Cavill, R. Hoogenboom, S. Shaunak, J.H.G. Steinke, M. Thanou, Cytotoxicity of polycations: Relationship of molecular weight and the hydrolytic theory of the mechanism of toxicity, *Int. J. Pharm.* **2017**, *521*, 249-258.
- [273] S.M. Moghimi, P. Symonds, J.C. Murray, A.C. Hunter, G. Debska, A. Szewczyk, A two-stage poly(ethylenimine)-mediated cytotoxicity: implications for gene transfer/therapy, *Mol. Ther.* **2005**, *11*, 990-5.
- [274] Y. Liu, J. Pan, Y. Cai, N. Grigorieff, S.C. Harrison, B. Chen, Conformational States of a Soluble, Uncleaved HIV-1 Envelope Trimer, *J. Virol.* **2017**, *91*, 1-15.
- [275] P. Zhu, E. Chertova, J. Bess, Jr., J.D. Lifson, L.O. Arthur, J. Liu, K.A. Taylor, K.H. Roux, Electron tomography analysis of envelope glycoprotein trimers on HIV and simian immunodeficiency virus virions, *Proc. Natl. Acad. Sci. USA* **2003**, *100*, 15812-7.
- [276] D.R. Burton, J.R. Mascola, Antibody responses to envelope glycoproteins in HIV-1 infection, *Nat. Immunol.* **2015**, *16*, 571-6.
- [277] J. Ingale, A. Stano, J. Guenaga, S.K. Sharma, D. Nemazee, M.B. Zwick, R.T. Wyatt, High-Density Array of Well-Ordered HIV-1 Spikes on Synthetic Liposomal Nanoparticles Efficiently Activate B Cells, *Cell Rep.* **2016**, *15*, 1986-99.
- [278] S.K. Sharma, N. de Val, S. Bale, J. Guenaga, K. Tran, Y. Feng, V. Dubrovskaya, A.B. Ward, R.T. Wyatt, Cleavage-independent HIV-1 Env trimers engineered as soluble native spike mimetics for vaccine design, *Cell Rep.* **2015**, *11*, 539-50.

- [279] J. Guenaga, N. de Val, K. Tran, Y. Feng, K. Satchwell, A.B. Ward, R.T. Wyatt, Well-ordered trimeric HIV-1 subtype B and C soluble spike mimetics generated by negative selection display native-like properties, *PLoS Pathog.* **2015**, *11*, e1004570.
- [280] S.C. Harrison, Viral membrane fusion, *Virology* **2015**, *479-480*, 498-507.
- [281] M. Kielian, Mechanisms of Virus Membrane Fusion Proteins, *Annu. Rev. Virol.* **2014**, *1*, 171-89.
- [282] R. Wyatt, J. Sodroski, The HIV-1 envelope glycoproteins: fusogens, antigens, and immunogens, *Science* **1998**, *280*, 1884-8.
- [283] D. Rabuka, J.S. Rush, G.W. deHart, P. Wu, C.R. Bertozzi, Site-specific chemical protein conjugation using genetically encoded aldehyde tags, *Nat. Protoc.* **2012**, *7*, 1052-67.
- [284] P. Wu, W. Shui, B.L. Carlson, N. Hu, D. Rabuka, J. Lee, C.R. Bertozzi, Site-specific chemical modification of recombinant proteins produced in mammalian cells by using the genetically encoded aldehyde tag, *Proc. Natl. Acad. Sci. USA* **2009**, *106*, 3000-5.
- [285] M.S. Klausen, M.C. Jespersen, H. Nielsen, K.K. Jensen, V.I. Jurtz, C.K. Sonderby, M.O.A. Sommer, O. Winther, M. Nielsen, B. Petersen, P. Marcatili, NetSurfP-2.0: Improved prediction of protein structural features by integrated deep learning, *Proteins* **2019**, *87*, 520-527.
- [286] J. Oscherwitz, F. Yu, K.B. Cease, A heterologous helper T-cell epitope enhances the immunogenicity of a multiple-antigenic-peptide vaccine targeting the cryptic loop-neutralizing determinant of *Bacillus anthracis* protective antigen, *Infect. Immun.* **2009**, *77*, 5509-18.
- [287] S.M. Russell, F.Y. Liew, T cells primed by influenza virion internal components can cooperate in the antibody response to haemagglutinin, *Nature* **1979**, *280*, 147-148.
- [288] V. Temchura, K. Uberla, Intrastructural help: improving the HIV-1 envelope antibody response induced by virus-like particle vaccines, *Curr. Opin. HIV AIDS* **2017**, *12*, 272-277.
- [289] C.A. Bresk, T. Hofer, S. Wilmschen, M. Krismer, A. Beierfuss, G. Effantin, W. Weissenhorn, M.J. Hogan, A.P.O. Jordan, R.S. Gelman, D.C. Montefiori, H.X. Liao, J.E. Schmitz, B.F. Haynes, D. von Laer, J. Kimpel, Induction of Tier 1 HIV Neutralizing Antibodies by Envelope Trimers Incorporated into a Replication Competent Vesicular Stomatitis Virus Vector, *Viruses* **2019**, *11*, 1-20.

- [290] H. Elsayed, G. Nabi, W.J. McKinstry, K.K. Khoo, J. Mak, A.M. Salazar, M. Tenbusch, V. Temchura, K. Uberla, Intrastructural Help: Harnessing T Helper Cells Induced by Licensed Vaccines for Improvement of HIV Env Antibody Responses to Virus-Like Particle Vaccines, *J. Virol.* **2018**, *92*, 1-15.
- [291] G. Nabi, M.S. Genannt Bonsmann, M. Tenbusch, O. Gardt, D.H. Barouch, V. Temchura, K. Uberla, GagPol-specific CD4(+) T-cells increase the antibody response to Env by intrastructural help, *Retrovirology* **2013**, *10*, 117.
- [292] S. Ranasinghe, D.Z. Soghoian, M. Lindqvist, M. Ghebremichael, F. Donaghey, M. Carrington, M.S. Seaman, D.E. Kaufmann, B.D. Walker, F. Porichis, HIV-1 Antibody Neutralization Breadth Is Associated with Enhanced HIV-Specific CD4+ T Cell Responses, *J. Virol.* **2015**, *90*, 2208-20.
- [293] M. Storcksdieck genannt Bonsmann, T. Niezold, V. Temchura, F. Pissani, K. Ehrhardt, E.P. Brown, N.Y. Osei-Owusu, D. Hannaman, H. Hengel, M.E. Ackerman, H. Streeck, G. Nabi, M. Tenbusch, K. Uberla, Enhancing the Quality of Antibodies to HIV-1 Envelope by GagPol-Specific Th Cells, *J. Immunol.* **2015**, *195*, 4861-72.
- [294] P. Panina-Bordignon, A. Tan, A. Termijtelen, S. Demotz, G. Corradin, A. Lanzavecchia, Universally immunogenic T cell epitopes: promiscuous binding to human MHC class II and promiscuous recognition by T cells, *Eur. J. Immunol.* **1989**, *19*, 2237-42.
- [295] P.L. Felgner, T.R. Gadek, M. Holm, R. Roman, H.W. Chan, M. Wenz, J.P. Northrop, G.M. Ringold, M. Danielsen, Lipofection: a highly efficient, lipid-mediated DNA-transfection procedure, *Proc. Natl. Acad. Sci. USA* **1987**, *84*, 7413-7.
- [296] E. Nature 1989; 337: 387–388. Dodds, M.G. Dunckley, K. Naujoks, U. Michaelis, G. Dickson, Lipofection of cultured mouse muscle cells: a direct comparison of Lipofectamine and DOSPER, *Gene Ther.* **1998**, *5*, 542-51.
- [297] B. Neuhuber, D.I. Huang, M.P. Daniels, C.E. Torgan, High efficiency transfection of primary skeletal muscle cells with lipid-based reagents, *Muscle Nerve* **2002**, *26*, 136-40.
- [298] B. Balci, P. Dincer, Efficient transfection of mouse-derived C2C12 myoblasts using a matrigel basement membrane matrix, *Biotechnol. J.* **2009**, *4*, 1042-5.
- [299] O. Akbari, N. Panjwani, S. Garcia, R. Tascon, D. Lowrie, B. Stockinger, DNA vaccination: transfection and activation of dendritic cells as key events for immunity, *J. Exp. Med.* **1999**, *189*, 169-78.

- [300] C. Volpi, F. Fallarino, M.T. Pallotta, R. Bianchi, C. Vacca, M.L. Belladonna, C. Orabona, A. De Luca, L. Boon, L. Romani, U. Grohmann, P. Puccetti, High doses of CpG oligodeoxynucleotides stimulate a tolerogenic TLR9-TRIF pathway, *Nat. Commun.* **2013**, *4*, 1852.
- [301] M. Stoker, I. Macpherson, Syrian Hamster Fibroblast Cell Line Bhk21 and Its Derivatives, *Nature* **1964**, *203*, 1355-7.
- [302] I. Macpherson, M. Stoker, Polyoma transformation of hamster cell clones—an investigation of genetic factors affecting cell competence, *Virology* **1962**, *16*, 147-151.
- [303] L.E. Guskey, H.M. Jenkin, Adaptation of BHK-21 cells to growth in shaker culture and subsequent challenge by Japanese encephalitis virus, *Appl. Microbiol.* **1975**, *30*, 433-8.
- [304] S. Choosakoonkriang, B.A. Lobo, G.S. Koe, J.G. Koe, C.R. Middaugh, Biophysical characterization of PEI/DNA complexes, *J. Pharm. Sci.* **2003**, *92*, 1710-22.
- [305] A. Elouahabi, J.M. Ruyschaert, Formation and intracellular trafficking of lipoplexes and polyplexes, *Mol. Ther.* **2005**, *11*, 336-47.
- [306] A.M.I. Lam, P.R. Cullis, Calcium enhances the transfection potency of plasmid DNA–cationic liposome complexes, *Biochim. Biophys. Acta* **2000**, *1463*, 279-290.
- [307] J.G. Damoiseaux, H. Yagita, K. Okumura, P.J. van Breda Vriesman, Costimulatory molecules CD80 and CD86 in the rat; tissue distribution and expression by antigen-presenting cells, *J. Leukoc. Biol.* **1998**, *64*, 803-9.
- [308] T. Horiuchi, H. Mitoma, S. Harashima, H. Tsukamoto, T. Shimoda, Transmembrane TNF-alpha: structure, function and interaction with anti-TNF agents, *Rheumatology* **2010**, *49*, 1215-28.
- [309] W.M. Chu, Tumor necrosis factor, *Cancer Lett.* **2013**, *328*, 222-5.
- [310] G.D. Kalliolias, L.B. Ivashkiv, TNF biology, pathogenic mechanisms and emerging therapeutic strategies, *Nat. Rev. Rheumatol.* **2016**, *12*, 49-62.
- [311] K.J. Tracey, A. Cerami, Tumor necrosis factor: a pleiotropic cytokine and therapeutic target, *Annu. Rev. Med.* **1994**, *45*, 491-503.
- [312] D.M. Mosser, X. Zhang, Activation of murine macrophages, *Curr. Protoc. Immunol.* **2008**, *83*, 14.2.1-14.2.8.
- [313] N. Smith, P.O. Vidalain, S. Nisole, J.P. Herbeuval, An efficient method for gene silencing in human primary plasmacytoid dendritic cells: silencing of the TLR7/IRF-7 pathway as a proof of concept, *Sci. Rep.* **2016**, *6*, 29891.

- [314] H. Kasai, K. Inoue, K. Imamura, C. Yuvienco, J.K. Montclare, S. Yamano, Efficient siRNA delivery and gene silencing using a lipopolypeptide hybrid vector mediated by a caveolae-mediated and temperature-dependent endocytic pathway, *J. Nanobiotechnology* **2019**, *17*, 11.
- [315] S.S. Kim, C. Ye, P. Kumar, I. Chiu, S. Subramanya, H. Wu, P. Shankar, N. Manjunath, Targeted delivery of siRNA to macrophages for anti-inflammatory treatment, *Mol. Ther.* **2010**, *18*, 993-1001.
- [316] K. Jensen, J.A. Anderson, E.J. Glass, Comparison of small interfering RNA (siRNA) delivery into bovine monocyte-derived macrophages by transfection and electroporation, *Vet. Immunol. Immunopathol.* **2014**, *158*, 224-32.
- [317] T.J. Van De Parre, W. Martinet, D.M. Schrijvers, A.G. Herman, G.R. De Meyer, mRNA but not plasmid DNA is efficiently transfected in murine J774A.1 macrophages, *Biochem. Biophys. Res. Commun.* **2005**, *327*, 356-60.
- [318] X. Zhang, J.P. Edwards, D.M. Mosser, The expression of exogenous genes in macrophages: obstacles and opportunities, *Methods Mol. Biol.* **2009**, *531*, 123-43.
- [319] T. Stroh, U. Erben, A.A. Kuhl, M. Zeitz, B. Siegmund, Combined pulse electroporation--a novel strategy for highly efficient transfection of human and mouse cells, *PLoS One* **2010**, *5*, e9488.
- [320] V. Capel, D. Vllasaliu, P. Watts, S. Stolnik, Insight into the relationship between the cell culture model, cell trafficking and siRNA silencing efficiency, *Biochem. Biophys. Res. Commun.* **2016**, *477*, 260-5.
- [321] B. Neuhaus, A. Frede, A.M. Westendorf, M. Epple, Gene silencing of the pro-inflammatory cytokine TNF- α with siRNA delivered by calcium phosphate nanoparticles, quantified by different methods, *J. Mater. Chem. B* **2015**, *3*, 7186-7193.
- [322] Y. Kuboki, Q. Jin, H. Takita, Geometry of Carriers Controlling Phenotypic Expression in BMP-Induced Osteogenesis and Chondrogenesis, *J. Bone Joint Surg. Am.* **2001**, *83*, S105-S115.
- [323] S. Srouji, D. Ben-David, R. Lotan, E. Livne, R. Avrahami, E. Zussman, Slow-release human recombinant bone morphogenetic protein-2 embedded within electrospun scaffolds for regeneration of bone defect: in vitro and in vivo evaluation, *Tissue Eng. Part A* **2011**, *17*, 269-77.
- [324] S. Takemoto, N. Morimoto, Y. Kimura, T. Taira, T. Kitagawa, K. Tomihata, Y. Tabata, S. Suzuki, Preparation of collagen/gelatin sponge scaffold for sustained release of bFGF, *Tissue Eng. Part A* **2008**, *14*, 1629-38.

-
- [325] H. Wajant, K. Pfizenmaier, P. Scheurich, Tumor necrosis factor signaling, *Cell Death Differ.* **2003**, *10*, 45-65.
- [326] H. Kinoshita, Y. Hirata, H. Nakagawa, K. Sakamoto, Y. Hayakawa, R. Takahashi, W. Nakata, K. Sakitani, T. Serizawa, Y. Hikiba, M. Akanuma, W. Shibata, S. Maeda, K. Koike, Interleukin-6 mediates epithelial-stromal interactions and promotes gastric tumorigenesis, *PLoS One* **2013**, *8*, e60914.
- [327] S.A. Hienz, S. Paliwal, S. Ivanovski, Mechanisms of Bone Resorption in Periodontitis, *J. Immunol. Res.* **2015**, *2015*, 615486.
- [328] S. Pacios, J. Kang, J. Galicia, K. Gluck, H. Patel, A. Ovaydi-Mandel, S. Petrov, F. Alawi, D.T. Graves, Diabetes aggravates periodontitis by limiting repair through enhanced inflammation, *FASEB J.* **2012**, *26*, 1423-30.
- [329] Y. Liu, A. Beyer, R. Aebersold, On the Dependency of Cellular Protein Levels on mRNA Abundance, *Cell* **2016**, *165*, 535-50.

12 Appendix

12.1 Publications

Covalent surface functionalization of calcium phosphate nanoparticles with fluorescent dyes by copper-catalysed and by strain-promoted azide-alkyne click chemistry. L.Rojas-Sánchez, V.Sokolova, S.Riebe, J.Voskuhl, M.Epple. *ChemNanoMat* **2019**, 5, 436-446.

Calcium phosphate nanoparticle-mediated transfection in 2D and 3D mono- and co-culture cell models. V.Sokolova, L.Rojas-Sánchez, N.Białas, N. Schulze, M.Epple. *Acta Biomaterialia* **2019**, 84, 391-401.

Calcium phosphate nanoparticle-based vaccines as a platform for improvement of HIV-1 Env antibody responses by intrastructural help. D. Damm, L. Rojas-Sánchez, H. Theobald, V. Sokolova V, R.T. Wyatt, K. Überla, M. Epple, V. Temchura *Nanomaterials* **2019**, 9, 1389.

Reduction of inflammatory periodontitis in rats by TNF- α gene silencing with a topically applied siRNA-loaded calcium phosphate paste. T. Tenkumo, L. Rojas-Sánchez, J.R. Vanegas Sáenz, M. Miyashita, N. Yoda, T. Ogawa, O. Prymak, V. Sokolova, K. Sasaki, M. Epple *Submitted*.

12.2 Contributions to conferences

Click chemistry for the covalent surface modification of calcium phosphate nanoparticles. L.Rojas-Sánchez, M.Epple. CRC 1093 International Symposium "Supramolecular Chemistry on Proteins". Essen, 20-21 September, 2017. **(Poster contribution)**

Click chemistry for the covalent surface modification of calcium phosphate nanoparticles. L.Rojas-Sánchez, M.Epple. Annual Meeting of the German Society for Biomaterials. Würzburg, 9-11 November, 2017. **(Oral contribution)**

Click chemistry as new approach for the selective surface modification of calcium phosphate nanoparticles. L.Rojas-Sánchez, V.Sokolova, M.Epple. 29th Annual Congress of the European Society for Biomaterials. Maastricht, 9-13 September, 2018. **(Poster contribution)**

Click chemistry for the surface modification of calcium phosphate nanoparticles. L.Rojas-Sánchez, V.Sokolova, S.Riebe, J.Voskuhl, M.Epple. 13. Winterseminar der Medizinischen Fakultät der Universität Duisburg-Essen. Pichl, 11-13 February, 2019. **(Oral contribution)**

Fluorescent covalently labelled calcium phosphate nanoparticles by click chemistry for cellular imaging. L.Rojas-Sánchez, V.Sokolova, S.Riebe, J.Voskuhl, M.Epple. 70. Mosbacher Kolloquium of the German Society for Biochemistry and Molecular Biology (GBM) - "High-resolution imaging of cells and molecules", Mosbach, 4-6 April, 2019. **(Poster contribution)**

A comparison between CuAAC and SPAAC labelling methods for calcium phosphate nanoparticle surface modification L.Rojas-Sánchez, M.Epple. CRC 1093 International Symposium "Supramolecular Principles in Biological Systems". Essen, 10-12 September, 2019. **(Poster contribution)**

12.3 Curriculum vitae

The Curriculum vitae is not included in the online version for privacy reasons.

Der Lebenslauf ist in der Online-Version aus Gründen des Datenschutzes nicht enthalten.

12.4 Acknowledgements

First, I want to thank Prof. Dr. Matthias Epple for receiving me into his research group and giving me the opportunity to work in an interesting and active research topic, as well as all the provided access to the required facilities and materials. Additionally, I thank him for all his support and motivation during these years, and for the great opportunities to join international collaborative research projects and other scientific events.

Next, I am thankful to the technical and administrative staff Carola, Sabine K., Ursula, Sabine B., Kerstin, Robin, Mr. Boukercha and Dietrich for all their support and nice time we shared during these years. I thank Dr. Sokolova and Dr. Prymak for the collaborative research work. To all the PhD students in the group I thank them for the pleasant working atmosphere. Specially, I will like to thank Selina, Karolin, Sebastian, Dr. Grasmik, Dr. Loza, and Dr. Pappert for their great support, good mood and shared experiences. Also, I thank Mrs. Qianmin Chen for the work together.

Additionally, I will like to thank Dr. Anthony Squire, Mrs. Alexandra Brenzel, Dr. Johannes Koch and Dr. Nina Schulze from the light microscopy imaging facilities (IMCES and ICCE) for their support with the different microscopy techniques, and to Mr. Bernd Walkenfort and Dr. Mike Hasenberg for the TEM imaging.

I will also want to thank the research colleagues: from Organic Chemistry Prof. Dr. Jens Voskuhl and Mr. Steffen Riebe; from University Hospital Erlangen Mr. Dominik Damm, PD Dr. Vladimir Temchura and Prof. Dr. Klaus Überla; from Tohoku University in Sendai, Japan Dr. Taichi Tenkumo, Dr. Toru Ogawa, Dr. Makiko Miyashita, Dr. Juan Ramón Vanegas, Dr. Nobuhiro Yoda, and Prof. Dr. Keiichi Sasaki; and from Wuhan Institute of Virology, China Dr. Maohua Zhong, Dr. Ejuan Zhang and Prof. Dr. Huimin Yan.

Also, I am thankful to the MICITT from Costa Rica for the PhD scholarship that I received which gave me the opportunity to study abroad.

I will like to thank my family for their great and constant support and motivation that kept me always going forward, as well as to the good friends I made in Essen.

Finally, I truly thank Irene for her unique support, motivation and all the shared memories of these years in Germany. This experience would not have been the same without her.

12.5 Eidesstattliche Erklärung

Hiermit versichere ich, die vorliegende Arbeit mit dem Titel

“Calcium phosphate nanoparticle surface modification by click chemistry and applications in biomedicine”

selbst verfasst und keine außer den angegebenen Hilfsmitteln und Quellen verwendet zu haben.

Zudem erkläre ich, dass ich die Arbeit in dieser oder einer ähnlichen Form bei keiner anderen Fakultät eingereicht habe.

Essen, den

Leonardo Rojas Sánchez